INVESTIGATION OF *Cryptocarya nigra* EXTRACTS AS A GREEN CORROSION INHIBITOR ON MILD STEEL AND ITS PHYTOCHEMICAL STUDIES

MAS FAIZ BIN MAS ROSEMAL HAKIM

FACULTY OF SCIENCE
UNIVERSITY OF MALAYA
KUALA LUMPUR

2019

INVESTIGATION OF *Cryptocarya nigra* EXTRACTS AS A GREEN CORROSION INHIBITOR ON MILD STEEL AND ITS PHYTOCHEMICAL STUDIES

MAS FAIZ BIN MAS ROSEMAL HAKIM

DISSERTATION SUBMITTED IN FULFILMENT OF THE REQUIREMENTS FOR THE DEGREE OF MASTER OF SCIENCE

DEPARTMENT OF CHEMISTRY
FACULTY OF SCIENCE
UNIVERSITY OF MALAYA
KUALA LUMPUR

2019

UNIVERSITY OF MALAYA

ORIGINAL LITERARY WORK DECLARATION

Name of Candidate: **MAS FAIZ BIN MAS ROSEMAL HAKIM**

Matric no. : **SMA 170001**

Name of Degree : **MASTER OF SCIENCE**

Title of Project Paper/Research Report/Dissertation/Thesis ("this Work"):

INVESTIGATION OF *Cryptocarya nigra* EXTRACTS AS A GREEN CORROSION INHIBITOR ON MILD STEEL AND ITS PHYTOCHEMICAL STUDIES

Field of Study: **ORGANIC CHEMISTRY**

I do solemnly and sincerely declare that:

(1) I am the sole author/writer of this Work;
(2) This Work is original;
(3) Any use of any work in which copyright exists was done by way of fair dealing and for permitted purposes and any excerpt or extract from, or reference to or reproduction of any copyright work has been disclosed expressly and sufficiently and the title of the Work and its authorship have been acknowledged in this Work;
(4) I do not have any actual knowledge nor do I ought reasonably to know that the making of this work constitutes an infringement of any copyright work;
(5) I hereby assign all and every rights in the copyright to this Work to the University of Malaya ("UM"), who henceforth shall be owner of the copyright in this Work and that any reproduction or use in any form or by any means whatsoever is prohibited without the written consent of UM having been first had and obtained;
(6) I am fully aware that if in the course of making this Work, I have infringed any copyright whether intentionally or otherwise, I may be subject to legal action or any other action as may be determined by UM.

Candidate's Signature Date:

Subscribed and solemnly declared before,

Witness's Signature Date:

Name :

Designation:

INVESTIGATION OF *Cryptocarya nigra* EXTRACTS AS A GREEN CORROSION INHIBITOR ON MILD STEEL AND ITS PHYTOCHEMICAL STUDIES

ABSTRACT

Three crude extracts; hexane (CNHE), dichloromethane (CNDE) and methanol (CNME) from the bark of *Cryptocarya nigra* were investigated for their corrosion inhibition properties on mild steel in 1M HCl media. CNDE showed the highest inhibition efficiency for the electrochemical impedance (EIS) and potentiodynamic polarization (PDP) experiments, respectively. Further identification, fractionation and purification of the active compounds from CNDE were analyzed under positive mode using liquid chromatography-mass spectrometer-ion trap-time of flight (LCMS-IT-TOF), column chromatography (CC) and preparative thin layer chromatography (PTLC). Structural elucidation of the seven known compounds named (+)-*N*-methylisococlaurine **1**, atherosperminine-*N*-oxide **2**, atherosperminine **3**, 2-hydroxyatherosperminine **4**, argentinine **5**, (+)-*N*-methyllaurotetanine **6** and (+)-laurotetanine **7** were successfully accomplished *via* optical polarimeter, UV-Vis spectrophotometer, FITR, 1D and 2D NMR spectroscopy (COSY, HMBC, HSQC). **1**, **3** and **6** were evaluated for their corrosion inhibition potentials and found to be in the ascending order of **1**< **3**< **6** at their respective optimum concentrations. EIS and PDP experiments showed that **6** reduced the corrosion rate significantly through charge transfer mechanisms. ΔG_{ads} values calculated from the Langmuir adsorption isotherm plots for CNDE and **6** suggested that they adsorbed on the mild steel surface dominantly *via* physisorption mechanism. Scanning electron microscopy micrographs and elemental composition studies confirmed the improvement of the surface morphologies by the formation of protective films over the metal surface.

Keywords: *Cryptocarya nigra*, Lauraceae, Alkaloid, Corrosion inhibitors, Mild steel

KAJIAN EKSTRAK *Cryptocarya nigra* SEBAGAI PERENCAT PENGARATAN SEMULA JADI KE ATAS KELULI LEMBUT DAN KAJIAN FITOKIMIA

ABSTRAK

Tiga ekstrak mentah; heksana (CNHE), diklorometana (CNDE) dan methanol (CNME) dari kulit *Cryptocarya nigra* dikaji untuk kebolehan perencatan mereka pada keluli lembut dalam media 1M HCl. CNDE menunjukkan kecekapan perencatan tertinggi bagi eksperimen impedens elektrokimia (EIS) dan polarisasi potensiometer (PDP). Pengenal pastian, fraksinasi dan penulenan sebatian aktif dari CNDE dianalisa di bawah mod positif cecair kromatografi spectrometer jisim-perangkap ion-takrifan masa (LCMS-IT-TOF), turus pemisah berperingkat (CC) dan turus pemisahan lapisan tipis preparatif (PTLC). Pengenalpastian struktural molekular tujuh sebatian iaitu (+)-*N*-methylisococlaurine **1**, atherosperminine-*N*-oksida **2**, atherosperminine **3**, 2-hydroxyatherosperminine **4**, argentinine **5**, (+)-*N*-methyllaurotetanine **6** dan (+)-laurotetanine **7** berjaya dicapai melalui kaedah polarimeter optik, spektrofotometer UV-Vis, FITR, spektroskopi NMR 1D dan 2D (COSY, HMBC, HSQC). **1**, **3** dan **6** dinilai untuk potensi perencatan kakisan dan didapati berada dalam urutan naik **1**< **3**< **6** pada kepekatan optima masing-masing. Eksperimen EIS dan PDP menunjukkan **6** mengurangkan kadar kakisan melalui mekanisme pemindahan caj. Nilai ΔG_{ads} dari plot isoterma penjerapan Langmuir untuk CNDE dan **6** mencadangkan bahawa mereka menjerap pada permukaan keluli ringan dengan lebih tinggi melalui mekanisme penjerapan fizikal. Mikrograf mikroskop permukaan elektron dan kajian komposisi unsur mengesahkan penambaikan morfologi permukaan terhasil daripada pembentukan filem pelindung di permukaan logam.

Kata kunci: *Cryptocarya nigra*, Lauraceae, Alkaloid; Perencat pengaratan, Keluli lembut

ACKNOWLEDGEMENTS

Praise and glory to Allah S.W.T, the source of all wisdom and strength as everything is under His grace and blessing. I would like to take this opportunity to express my heartfelt gratitude to my supervisor, Prof. Dr. Khalijah Awang for her kindly good supervision, constant comfort and enthusiasm throughout the course of this study. I owed special thanks to Dr. Azeana Zahari for her endless advice, encouragement and for sharing immense knowledge just to bring out the best in me. I am very indebted with their patience and honoured with their confidence in my ability. Their golden values have inspired me to see things positively in many aspects. My second recognition goes to the Institute Postgraduate Studies (IPS) for giving me the opportunity to pursue my postgraduate studies in UM. I appreciate the continuous administrative help from the Head of Chemistry Department, Prof Sharifuddin.

Next, I also wish to extend my appreciation words to Mr.Teo, Mr.Din and Mr.Rafly (staffs of the Herbarium), Ms. Norzalida and Mrs. Dara Fiona (for handling NMR) along with my other professional seniors and colleagues Dr, Nurul, Dr. Norsita, Dr. Liew Sook Yee and phytochemistry laboratory members especially; Dr. Devi, Ms. Aimi, Dr. Chong, Dr. Chan, Ms. Hazrina, Ms. Haslinda, Mrs. Julia, Ms.Tien, Ms. Shelly, Ms. Rosalind, Ms. Maryam, Mr. Hafiz, and Mr. Azrul for their warm presence, teachings, supports and friendships. They helped me to steer my way through many complexities and ambiguities of research.

Finally, I would like to convey my deepest gratitude to my beloved parents, Prof. Madya Dr. Mas Rosemal Hakim, Dr. Hazariah, and to all my family members for the continuous inspirations, ideas, understandings and endurance that are greatly treasured throughout this project. They have always been there for me no matter where I am with all those unconditional moral supports. Without them, I would have not able to finish this course. Thank you for making my research life meaningful.

TABLE OF CONTENTS

LIST OF FIGURES

LIST OF TABLES

LIST OF SCHEMES

LIST OF SYMBOLS AND ABBREVIATIONS

α	:	Alpha
β	:	Beta
δ	:	Chemical Shift
λ	:	Wavelength
µL	:	Microliter
µM	:	Micromolar
cm^{-1}	:	Per centimeter
^{13}C-NMR	:	13-Carbon NMR
1D-NMR	:	One Dimension Nuclear Magnetic Resonance
^{1}H-NMR	:	Proton NMR
2D-NMR	:	Two Dimension Nuclear Magnetic Resonance
CC	:	Column chromatography
$CDCl_3$	:	Deuterated chloroform
CH_2Cl_2	:	Dichloromethane
$CHCl_3$	:	Chloroform
CNDE	:	*Cryptocarya nigra* dichloromethane extract
CNHE	:	*Cryptocarya nigra* hexane extract
CNME	:	*Cryptocarya nigra* methanol extract
COSY	:	^{1}H-^{1}H Correlation Spectroscopy
d	:	Doublet
dd	:	Doublet of doublet
DEPT	:	Distortions Enhancement Polarization Transfer
g	:	Gram
HCl	:	Hydrochloric acid

HMBC	:	Heteronuclear Multiple Bond Coherence
HSQC	:	Heteronuclear Single Quantum Correlation
Hz	:	Hertz
IR	:	Infra-red
J	:	Coupling constant
kg	:	Kilogram
LCMS	:	Liquid Chromatography-Mass Spectroscopy
M	:	Molar
m	:	Multiplet
m/z	:	Mass per charge
MeOD	:	Deuterated methanol
MeOH	:	Methanol
MHz	:	MegaHertz
mL	:	Milliliter
NH_3	:	Ammonia
NMR	:	Nuclear Magnetic Resonance
OCH_3	:	Methoxy group
OH	:	Hydroxyl group
pH	:	Power of hydrogen
ppm	:	Part per million
Q	:	Quaternary carbon
s	:	Singlet
t	:	Triplet
TLC	:	Thin layer chromatography
UV	:	Ultra-violet

CHAPTER 1: INTRODUCTION

1.1 General

Malaysia is one of the oldest continents globally known to have rich and diversified ecosystems. For example, The Royal Belum reserve forest in the Perak State of Peninsular Malaysia has been recognized to be the largest virgin tropical rainforests in the world where it existed 130 million years ago (Kanniah *et al.*, 2018). This makes it even older than the Amazon and Congo forest (Schwabe *et al.*, 2014). Kelantan which is stated in the northeast of Peninsular Malaysia has the largest area of reserved forest approximately 1.5 million hectares, and one of the popular recreational areas is the Ulu Sat reserve forest (Lim, N.W., Yong *et al*, 2010). These forests are protected under the Malaysian National Forestry Act and Northern Corridor Implementation Authority and has been declared as spots for ecotourism. These authentic locations hosted a myriad of interesting research wonders of more than 15,000 plant species to be explored (Nasrullah, Zahari *et al.*, 2013).

Among the prevalent species available, *Cryptocarya nigra* was specifically selected for this work due for its capacity to yield many types of interesting chemical constituents with various activities (Wan Othman *et al.*, 2017). This plant is widely distributed in Sumatra and Borneo and it is locally known in Peninsular Malaysia as '*Medang*'. *Cryptocarya* is an almost pantropical genus (absent from central Africa), with the majority of species in tropical Asia The genus *Cryptocarya* belonged to the family Lauraceae which comprises more than 350 species of which 17 of them were recorded in the recent taxonomic study in Malaysia (Nishida, S., Kok *et al.*, 2016).

A survey of the literature on phytochemical and pharmacological studies, *Cryptocarya* is a prolific producer of flavonoids (Custodio & Junior, 2014), chalcones, lactones, α-pyrones and alkaloids (Wang*, 2018). Anti-plasmodial, anti-oxidant (Zahari *et al.*, 2016),

anti-cholinesterase (Wan *et al.*, 2016), anti-bacterial (Omar *et al.*, 2013) and anti-cytotoxic (Kurniadewi *et al.*, 2010) activity studies particularly on alkaloids have been published from this species. However, to date, no work on *Cryptocarya* as a potential source of corrosion inhibitor has been reported. This research has been inspired by the fact that anti-oxidant secondary metabolites containing polyphenolic groups such as alkaloids, may assist in the protection of metal towards corrosion (Raja, Fadaeinasab, *et al.*, 2013).

Corrosion is the deterioration of a metal surface due to, in many cases, unavoidable slow continuous oxidation and reduction reactions. The prevention of this undesired phenomenon would be more practical and achievable than complete elimination. An average cost of $ 2.5 trillion, approximately 3.4 % of the world's domestic product annually worldwide suffered from the impact of corrosion according to a study done by NACE International (Verma, Ebenso, & Quraishi, 2017). Acidic media which are widely used in industrial acid cleaning, acid descaling, and acid pickling require the use of corrosion inhibitors to restrain corrosion on metallic materials (Verma, Ebenso *et al.*, 2018). Hence, the study of corrosion prevention particularly on mild steel using new corrosion inhibitors is of tremendous interest not only in the industrial sectors but has caught the attention of the academics. Over the years, considerable efforts have been focused on finding suitable green corrosion inhibitors of organic origin such as tea leave extracts (Hamdan, Suryanto, & Haider, 2018), *Ginkgo* leaf extract (Qiang, Zhang, Tan *et al.*, 2018), *Musa pradisica* peel extract (Ji, Anjum, Sundaram *et al.*, 2015), sweet melon peel extract (Saeed *et al.*, 2019), *Saraca Ashoka* extract (Saxena, Prasad, Haldhar *et al.,* 2018) and *Uncaria* gambir extracts (Hussin & Kassim, 2011) to be incorporated in various corrosive media. The most important feature of an extract to behave as an efficient acid inhibitor are those containing organic compounds with oxygen, nitrogen, sulphur and/or phosphorus in their structures. Their extent of inhibition depends on the effective

organic groups attached and increases in the order: oxygen < nitrogen < sulphur < phosphorus (Abd El Haleem, Abd El Wanees *et al.,* 2013). Diverse types of organic compounds were reported as excellent corrosion inhibitors for mild steel in hydrochloric media (Krishnan *et al.*, 2018; Mo, Luo, Li *et al.* 2016; Olasunkanmi, Kabanda *et al.*, 2016). The reported compounds' efficiencies as corrosion inhibitors were mainly governed by their molecular structures and the nature of the adsorbed layers formed on the metal surface (Lai *et al.*, 2017).

In view of the above together with our continuing affords in searching for eco-friendly material particularly plant-based compounds (Raja, Qureshi *et al.,* 2013), our group investigated corrosion inhibition properties of *Cryptocarya nigra* for the first time. This research was inspired by the fact that extracts containing alkaloids have been reported to exert prominent inhibitory effects as they were proven beyond doubt to be good electron donors, and the property contributed in the prevention of corrosion process. On all accounts, *Cryptocarya nigra* dichloromethane extract (CNDE) showed good corrosion inhibition action on mild steel in 1M HCl. It was chosen to be further purified *via* various chromatographic techniques and has accounted for 7 pure alkaloids. The rest of this dissertation will be discussing into detail for each of the procedure and results obtained.

1.2 Phytochemicals as a source of corrosion inhibitors

Over 295,000 species of angiosperm estimated existed on this planet, 74,000 of them are monocots and 210,000 are eudicots (Christenhusz & Byng, 2016). Apart from fuel, fibre, food, traditional supply of medicines, plants have recently been familiar to be an excellent alternative in preventing corrosion since they could be incorporated in various acidic solutions (Khan *et al.*, 2015). Plants have been an exemplary source of secondary metabolites with high chemical diversity and have given rise to the continuing interests in natural products research. Most of the corrosion inhibitors today are originated from

plants, in the way or another. Plants of the tropical rainforests, particularly in Malaysia have high chemical diversity and thus offers a promising potential source of new useful natural product discovery.

To protect metals or alloys from corrosion, approaches such as isolating the structure from aggressive media using coatings or compensating for the loss of electrons from the corroded structure were employed throughout the years. Scientists have explored the use of organic and inorganic compounds that adsorb on the metallic surface in order to restrain the oxidation-reduction process. However, most of the investigated corrosion inhibitors were toxic and bring environmental hazards upon disposal. Therefore, there is an essential need to utilize plant-based material as green corrosion inhibitors. Plant extracts are deemed to be rich in active chemical compounds that could reduce the corrosion rate by adsorption and replacing hydrogen ions/water molecules on the metal surface (Olasunkanmi *et al.*, 2016) through the following equation:

$$\text{Inhibitor} + n\text{H}_{ads} / n\text{H}_2\text{O} \rightarrow \text{Inhibitor}_{ads} + \text{H}_2 / \text{H}_2\text{O} \qquad (1.1)$$

Green inhibitors have an interesting adsorptive property, known as site-blocking ability (Aliofkhazraei, M., 2018). This property helps to put an end to further oxidation of iron or reduction of oxygen during the corrosion process. Having said all the above, we continued the search for possible green corrosion inhibitors in Malaysia for the betterment of our future generations.

1.3 Lauraceae family: General appearance and morphology

The family Lauraceae is classified in the Subclass Magnolite under the Order, Laurales (Ian R C Bick & Potier, 1972). The family is pantropical, including about 50 genera with a probable number of 2500 to 3500 species worldwide, principally from warm to tropical region, Southeast Asia and Brazil (Al-Tameme, 2016). Trees of the Laurel family

predominate in the world's Laurel forests, which occur in a few humid subtropicals and mildly temperate regions of the northern and southern region hemisphere, including the Macaronesian islands, southern Japan, Madagascar, and central Chile.

In the Lowlands of Malaysia, few members of Lauraceae may reach 30 m tall, but commonly they appeared as small trees of the canopy. In the Highlands, the term "Oak laurel forest" is given to this vegetation which lies at altitude 1200-1600 m (Custodio & Junior, 2014). The timber of Lauraceae is light hardwood with trademark name '*Medang*' or '*Tejur*' and of great commercial importance for manufacturing. They are suitable for interior decorative work such as interior design, panelling, furniture and cabinet making. The heavier species could be utilized for medium construction undercover. The family of Lauraceae provide many useful economic products.

1.4 Classification of tribe

Lauraceae family are characterized by many primitive and archaic features. The determination is dependent on a combination of characters, for instance, the type of leaves, root, bark and branches, wood stems, fruits, flowers and other observable patterns. This classification is according to Malayan seed plants. They were classified based on both inflorescences structures and wood anatomy which divides the Lauraceae family into two sub-families; Lauroideae and Cassythoideae as shown in Scheme 1.1.

Kingdom : Plantae **Division** : Magnoliophyta

Class : Magnoliopsida **Order** : Laurales

Family : Lauraceae

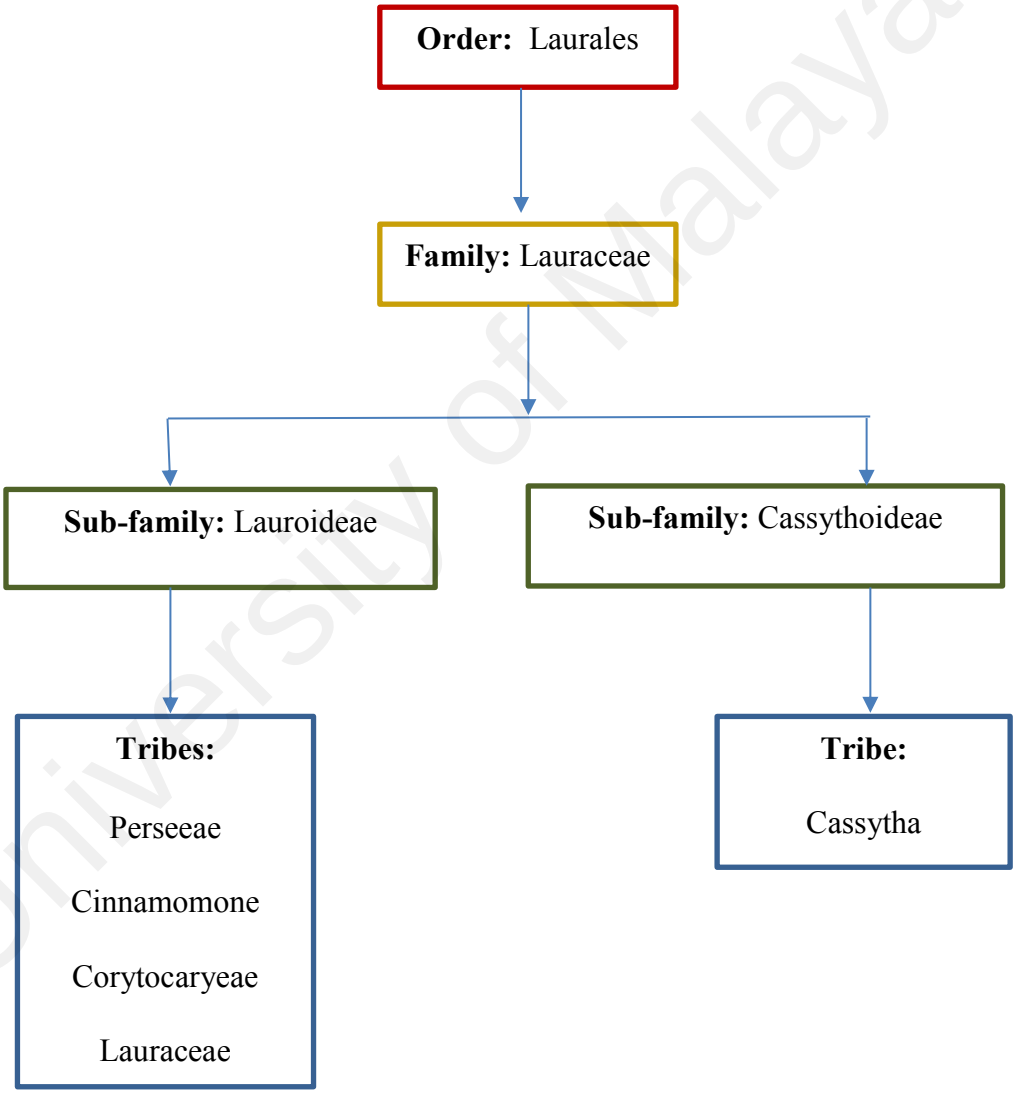

Scheme 1.1: Classification of family Lauraceae.

1.5 The genus *Cryptocarya*

The genus *Cryptocarya* originated from a Greek word *krypto* which means, to hide, while *karya* means a walnut tree. Sometimes they are called mountain laurels or mountain walnuts. It belonged to the laurel family, Lauraceae, comprises more than 350 species and 17 species are found in Malaysia (Nasrullah *et al.*, 2013). *Cryptocarya* can be distinguished from other laurel genera by its bisexual trimerous flower, which very typical in shape (usually slender, apically narrowed tube, and immersed ovary, six equals to subequal petals, nine fertile stamens with di-sporangia anthers, staminal glands only in the third androecial whorl). The flowers are bisexual (perianth tube turbinate or ovoid), lobes 6, stamens, stamens usually 9 and by the characteristic fruit that is enclosed by the accrescent flower tube (Gomes-Bezerra, Gomes-Silveira *et al.*, 2018). The fruits entirely included in the enlarge perianth tube leaving only a minute opening at apex. The leaves are alternate, pinnate nerved, rarely trinerved. Inflorescences in axillary or subterminal panicles.

1.6 *Cryptocarya nigra*

Cryptocarya nigra is a medium-sized tree up to 10 m tall with about 15 cm diameters. The bark is white-grey brown and smooth. The inner bark is pinkish red and mottled white while the young twigs of this species are velvety hairy. *Cryptocarya nigra* leaves are spirally simple, thick coriaceous from lanceolate or elliptic-ovate (Nasrullah *et al.*, 2013). Their apex shortly pointed, asymmetric, base obtuse with 8.0-14.5 cm x 5.0-6.5 cm. The upper surface is bright green with glaucous colour below it. The young leaves have secondary nerves 7 – 11 pairs which are raised below and faint above it. The tertiary nerves are in scalar form. The petioles are up to 1.5 cm long. *Cryptocarya nigra* flowers are yellow with inflorescence in axillaries and terminal panicles.

Figure 1.1: Leaves of *Cryptocarya nigra*.

Figure 1.2: Bark of *Cryptocarya nigra*.

1.7 Problem statement

Mild steel in acidic solutions has been commonly used in industrial applications such as acidic cleaning, pickling and descaling process. Nowadays, corrosion in acidic media is a challenge to scientist and engineers. Viewing this issue, corrosion inhibitors is one of the best methods for metal protection against corrosion. Researches carried out throughout the globalization years have established that organic compounds containing heteroatoms such as O, N and S, acted as good corrosion inhibitors (Saeed *et al.*, 2019; Sanaei, Ramezanzadeh *et al.*, 2019). However, hazardous substances were used during the synthesis of these inhibitors which led to the production of toxic byproducts for human beings as well as to the environment. In addition to that, the synthesis of these organic compounds is expensive and cost ineffective. This controversy urged the need for the utilization of green corrosion inhibitors.

Green corrosion inhibitors are obtained from plant sources which are biodegradable, eco-friendly and non-toxic (Marzorati, Verotta *et al.*, 2018; Peter, Obot *et al.*, 2015). The planarity molecular geometry resulted from the multiple π-bonds of these natural compounds provides good corrosion inhibition properties. Many phytochemical constituents of plant extracts including alkaloids (Raja, Qureshi, *et al.*, 2013), flavonoid (Prabakaran, Kim *et al.,* 2016), amino acids (Barouni *et al.*, 2008) and tannins (Yamuna & Anthony, 2015) have molecular and electronic structure structures similar to those of the conventional corrosion inhibitors and was found to possess the ability to inhibit corrosion of metal. This research work reports the corrosion inhibition process of *Cryptocarya nigra* for the first time and has been inspired in a bid to conserve our environment and maintain the integrity of global engineering structures and materials. The dichloromethane extract (CNDE) from the bark of this species showed excellent inhibition potentials on mild steel in 1M HCl *via* analysis conducted by electrochemical

impedance study and potentiodynamic polarization experiments. This extract was reported to yield several interesting constituents, particularly alkaloids therefore have developed a considerable interest to investigate for their potential use as green corrosion inhibitors.

1.8 Objective of study

Overall, this project involved plant extraction and isolation of chemical constituents from *Cryptocarya nigra* (bark) sample. The plant extracts were later analyzed for their potential as green corrosion inhibitor. The objectives of this study are as follows:

1) To extract the bark of *Cryptocarya nigra* using hexane, dichloromethane and methanol solvents.
2) To fractionate, isolate and purify active compounds from dichloromethane crude extract (CNDE) using a combination of various chromatographic methods such as liquid chromatography-mass spectrometer-ion trap-time of flight (LCMS-IT-TOF), thin layer chromatography (TLC), and column chromatography (CC).
3) To elucidate the chemical structures of the pure compounds by means of complementary spectroscopic techniques such as NMR spectroscopy (^{1}H-NMR, ^{13}C-NMR, COSY, DEPT, HMBC, HSQC), FTIR spectroscopy and UV-Vis spectrophotometer and optical polarimeter.
4) To examine and compare the effectiveness between the crude extracts and the active pure compounds as green corrosion inhibitors *via* electrochemical impedance study (EIS) and potentiodynamic polarization experiment (PDP).
5) To evaluate the adsorption isotherm associated with the corrosion inhibition mechanism for the studied extracts and pure compounds.
6) To study the surface morphology and elemental compositions of the mild steel under the inhibitory effect of the extracts/compounds using SEM-EDX analysis.

CHAPTER 2: LITERATURE REVIEW

2.1 General chemical aspect

Plant compounds are divided into primary and secondary metabolites. Primary metabolites are directly involved in growth and development or other primary functions. Secondary metabolites are organic compounds produced by plants which are not directly involved in the normal growth, development or reproduction of an organism. Unlike primary metabolites, absence of secondary metabolites does not result in immediate death, but rather in a long-term impairment of the organism's survivability or perhaps no significant change at all. Secondary metabolites play an important role in plant defence against herbivores, other interspecies defences and as pollinator attractants. Human use secondary metabolites as medicines, flavourings, pigments and recreational drugs (Bourgaud, Gravot *et al.*, 2001).

Secondary metabolites can be distinguished based on their chemical structures, precursor molecules or biosynthetic pathways. The progressive analysis of exact structural formulas and biosynthetic pathways for secondary metabolites has developed over the past 30 years with the use of modern analytical techniques like spectroscopy, chromatography, mass spectrometry, electrophoresis, isotope techniques and enzymology (Alvarez-Rivera, Ballesteros-Vivas *et al.*, 2019). Secondary metabolites can be classified into three major classes according to Croteau *et al.* (2000); terpenoids (55 %), alkaloids (27 %), and phenolic compounds (18 %) (Figure 2.1).

Among the secondary metabolites produced by plants, alkaloids appeared to be a very prominent class of defence compound. More than 12,000 alkaloids from 150 families have been identified in plants and around 20 % of flowering plants contain alkaloids (Richard, Temsamani *et al.*, 2013). In plants, alkaloids generally exist as salts of organic

acids like acetic, malic, lactic, citric, oxalic, tannic and other acids. During the last 20 to 30 years, the analysis of secondary plant products has made a progressive head away. The elucidation of exact structural formulas, and most importantly their biosynthetic pathways were made possible by the aid of analytical methods such as chromatography, electrophoresis, enzymology, spectroscopy and isotope techniques (Patel, 2017). The general secondary metabolite synthetic pathways are shown in Scheme 2.1. Shikimate route has been the most common one.

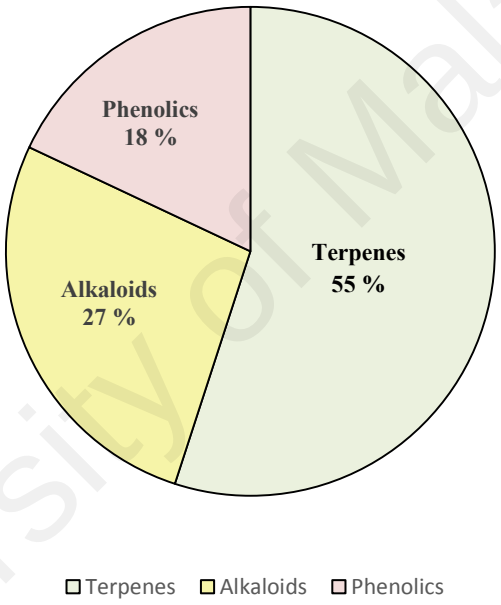

Figure 2.1: Pie chart representing the major groups of plant secondary metabolites.

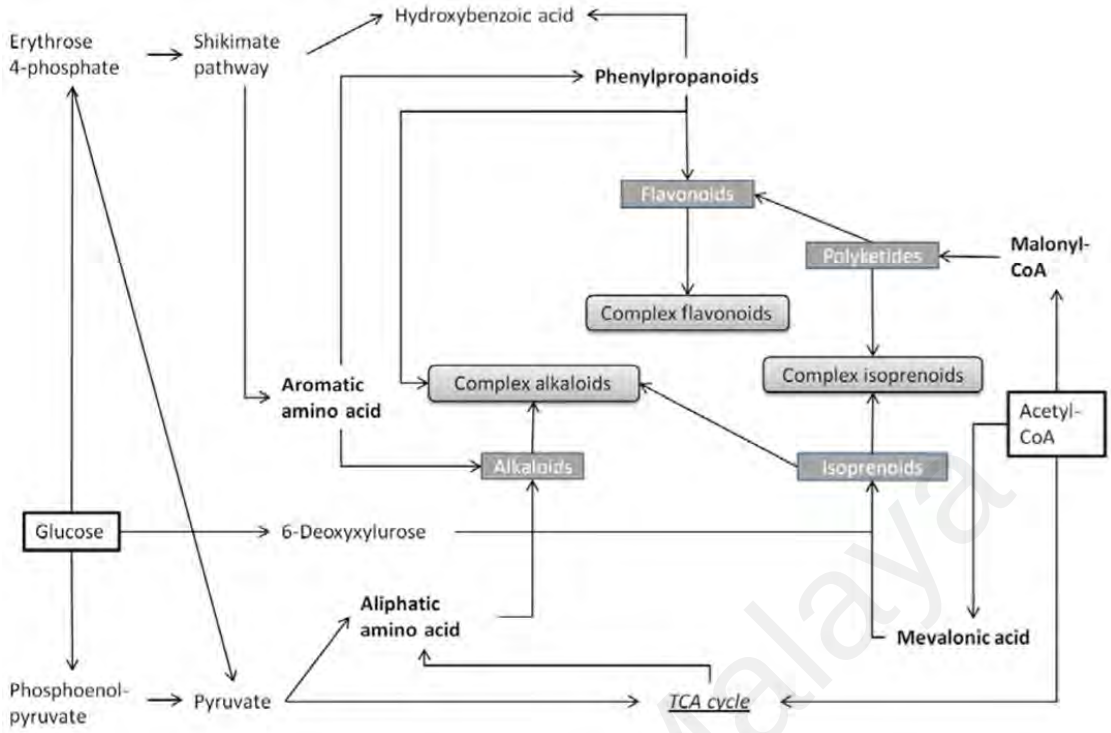

Scheme 2.1: Secondary metabolites synthetic pathway (Verpoorte, 2002)**.**

Due to high interest, researchers from all over the world are working towards finding better extraction and isolation techniques of these valuable compounds. Similar to other secondary metabolites, the first purification of alkaloid was revolutionized from paper chromatography (Eddy, 2009). It was the easiest to handle, fast and cheap. However today, alkaloids are being exploited for various purposes thanks to the advancement of science and technology (Kaur, Kapoor *et al.*, 2015).

2.2 Alkaloids

The nature of alkaloids was not understood until the early part of the nineteenth century, where Friedrich Serturner, an apothecary's assistant from Westphalia, first isolated morphine, one of the most important alkaloids in the applied science. This was a significant lead in the chemistry of pharmacology. The term "alkaloid" was first coined in 1819 by Carl F. W. Meissner, an apothecary from Halle as observed that these compounds appeared "like alkali", and so named them alkaloids (Castro-Saavedra *et al.*,

2016). Later, alkaloid defined by Nowacki (1965), is a molecule containing nitrogen, connected to at least two carbon atoms and one ring.

Alkaloids are synthesized from one of the few common amino acids, lysine, tyrosine and tryptophan. Some weak basic alkaloids, such as nicotine, occur freely in nature while a few alkaloids occur as glycosides of sugar such as glucose, rhamnose and galactose (Ramawat, Dass, & Mathur, 2009). Figure 2.2 shows some of the well-known alkaloids up to date. The biological properties of various alkaloids have also led to their use as pharmaceuticals, narcotics, stimulants and poisons (Table 2.1).

Table 2.1: Major known alkaloids in plants.

Compounds	Source	Effect and uses
Morphine	*Papaver somniferum*	Analgestic
Camptothecin	*Camptotheca acuminate*	Anticancer
Atropine	*Hyoscyamus niger*	Prevention of intestinal spasms
Vinblastine	*Catharanthus roseus*	Anticancer
Codeine	*Papaver somniferum*	Analgestic, antitussive
Caffeine	*Coffea arabica*	Stimulant, natural pesticides
Nicotine	*Nicotina tabacum*	Stimulant, tranquillizer
Cocaine	*Erythroxylon coca*	Stimulant of the central nervous system, local anaesthetic

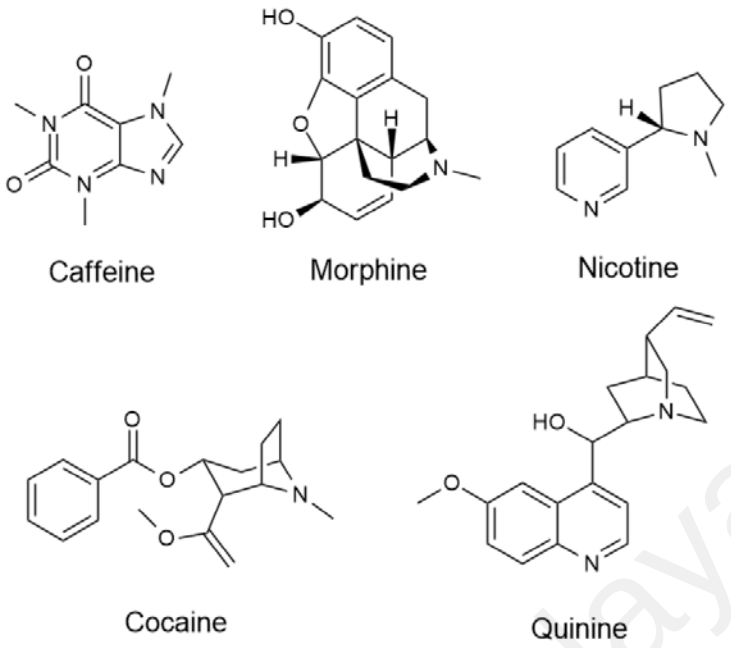

Figure 2.2: Examples of alkaloids.

2.3 Classification of alkaloids

Alkaloids are a group of chemical compounds characterized by carbon rings that have nitrogen atom(s) and by the fact they are usually basic on the pH scale. They are classified based on chemical, taxonomic, biological, and molecular construction. From structural point of view, alkaloids are divided according to their shapes and origins. They are categorized into three broad groups according to their biosynthesis origins, which are:

1) 'True Alkaloids' contain nitrogen in the heterocycle and originates from amino acids. Their characteristics examples are nicotine, morphine, and hygrine.
2) 'Protoalkaloids' are compounds originated from amino acid but the nitrogen atoms are not part of the heterocyclic bond. Such alkaloids include compounds derived from L—tyrosine and L-tryptophan. Mescaline, hordenine and serotonine are good examples of these kinds of alkaloids.
3) 'Pseudoalkaloids' are nitrogen-containing compounds but are not derived from amino acids. This group includes terpene-, purine-like and steroid-like alkaloids such as caffeine, theobromine, theacrine, and theophylline.

The true alkaloids can be further classified into different types of basic skeletons. This is the most popular methods for alkaloids classification. Classification also can be done based on other factors such as; biogenesis, structural relationships, botanical origin and spectroscopic criteria.

2.4 Alkaloids of *Cryptocarya*

Interest in Lauraceae, a pantropical family with 67 genera and 2500-3500 species, is of considerable interest to both taxonomists and natural product chemists (Van der Werff, H. 2017; Drewes, Horn, & Mavi, 1997). *Cryptocarya* is a genus of evergreen trees belonging to the laurel family, Lauraceae. The genus includes more 350 species distributed through the Neotropic, Afrotropic, Indomalaya and Australasia ecozones. This family have been known for a long time to contain a rich source of secondary metabolites with interesting biological activities. Most of the alkaloids isolated from this family have been found stem bark as well as in leaves and roots. The Lauraceae alkaloids represent a large number with over 300 different alkaloids have been isolated, and still expanding the group of biogenetically related isoquinoline alkaloids that are found exclusively in plants belonging to this family. About 287 structures of alkaloids distributed among all the genera within this family have been reported. Subsequently, these isoquinolines were divided into subclasses inclusive of 148 aporphines, 47 benzylisoquinolines, 23 pavines, 21 bisbenzylisoquinolines, 21 proaporphines, 18 morphinandienones, 4 phenanthrenes and 5 simple isoquinolines. The most frequently detected alkaloids in the Lauraceae are those with the aporphine skeleton. . Previous studies have revealed that *Cryptocarya* genus is a rich source of secondary metabolites such as flavonoids, pyrones, lignans, terpenoids and alkaloids (Castro-Saavedra *et al.*, 2016; Suzuki *et al.*, 2017; Wan Othman *et al.*, 2016). Species of *Cryptocarya* are known to yield various types of alkaloids in which majority are from isoquinolune type such as aporphine,

benzylisoquinoline, phenanthroindolizidine, pavine and many more. Phytochemical studies on several species of *Cryptocarya* have been reported and the isolated compounds are tabulated in Table 2.2.

Table 2.2: Alkaloids Isolated from the Genus of *Cryptocarya*.

Plant	Alkaloids isolated
Cryptocarya angulata (Cooke & Haynes, 1954)	atherosperminine **3** isocorydine **29** roemerine **32**
Cryptocarya chinensis (Lin, Wu, & Wu, 2001) (Gao, Wang, Zhu, & Ye, 2011)	(+)-eschscholtzidine-*n*-oxide **35** (-)-12-hydroxycrychine **36** (-)-12-hydroxy-*o*-methylcaryachine **37** (-)-*n*-demethylcrychine **38** caryachine **39** (-)-isocaryachine-*n*-oxide **40** isocryprochine **41** isoamuronine **42** (+)-8,9-dihydrostepharine **43**
Cryptocarya crassinervia (Awang *et al.*, 2008) (Saidi *et al.*, 2011)	2-hydroxyatherosperminine **4** 2-methoxyatherosperminine **22** 2-methoxyatherosperminine *n*-oxide **23** *n*-demethyl-2-methoxyatherosperminine **24**
Cryptocarya densiflora Blume *Cryptocarya infectoria* *Cryptocarya griffithiana* (Wan *et al.*, 2016)	(+)-laurotetanine **7** 2-methoxyatherosperminine **22** (-)-antofine **25** (-)-densiindolizidine **26** (+)-nornantenine **31** dicentrinone **33** prodensiflorin A **43**

Cryptocarya ferrea (Saidi, Awang *et al.*, 2010)	(+)-lirioferine **27** (+)-norlirioferine **28** (-)-*o*-methylisopiline **34**
Cryptocarya longifolia (Bick, Sinchai *et al.*, 1981)	laurotetanine **6** cocalurine **12** longifolinine **15** reticuline **19** thalifoline **48**
Cryptocarya nigra (Nasrullah *et al.*, 2013)	*n*-methylisococlaurine **1** atherosperminine **3** noratherosperminine **21** isocorydine **29** norisococlaurine **30**
Cryptocarya phyllostemon (Cave *et al.*, 1989)	(+)-phyllocryptine **18** (-)-antotine **25** (-)-phyllosteminine **45** (+)-phyllosteminine **46**
Cryptocarya rugulosa (Saidi, Morita, Litaudon, 2011)	codamine **13** norcinnamolaurine **16** reticuline **19** reticuline-*N*-oxide **20**
Cryptocarya strictifolia (Juliawaty, Kitajima *et al.*, 2000)	armepavine **11** laudanidine **14** orientaline **17**

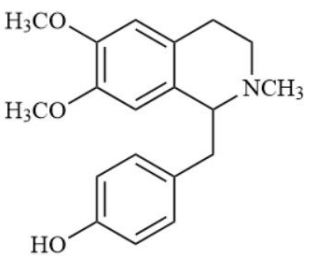

Armepavine **11**

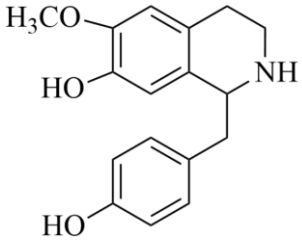

(+)-Coclaurine **12**

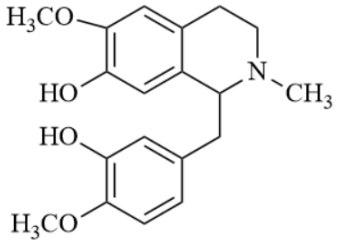

Codamine **13**

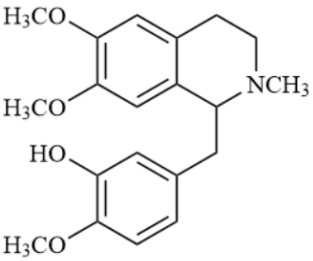

Laudanidine **14**

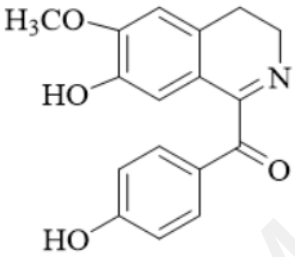

Longifolinine **15**

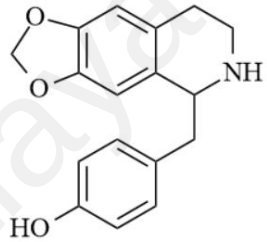

(+)-Norcinnamolaurine **16**

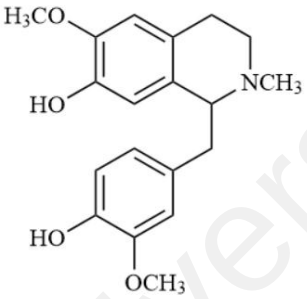

Orientaline **17**

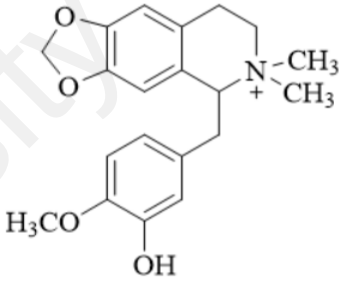

(+)-Phyllocryptine **18**

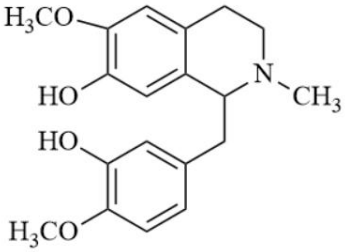

Reticuline **19**

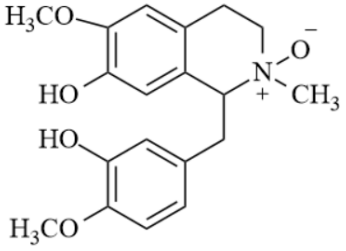

Reticuline-*N*-oxide **20**

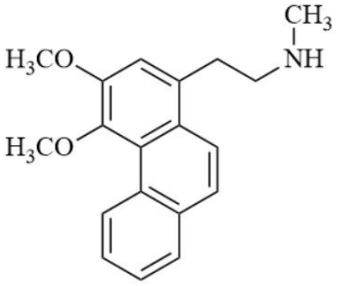

Noratherosperminine **21**

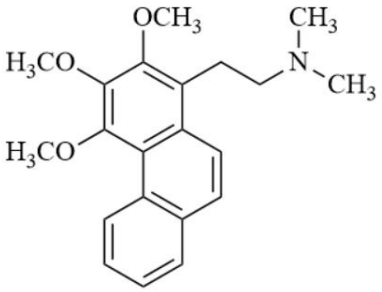

2-methoxyatherosperminine **22**

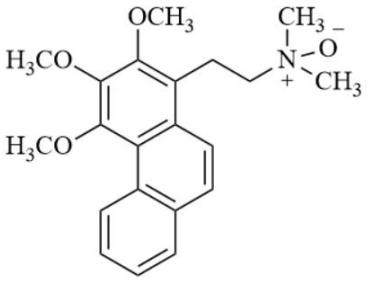

2-methoxyatherosperminine-*N*-oxide **23**

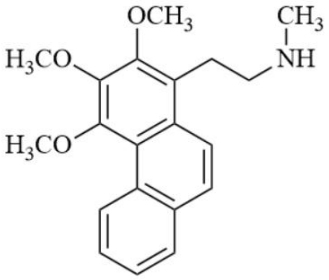

N-demethyl-2-methoxyatherosperminine **24**

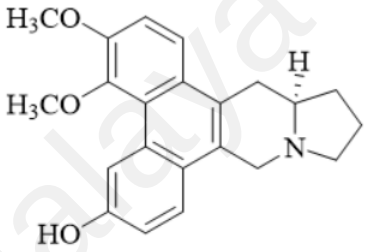

(-)-Densiindolizidine **26**

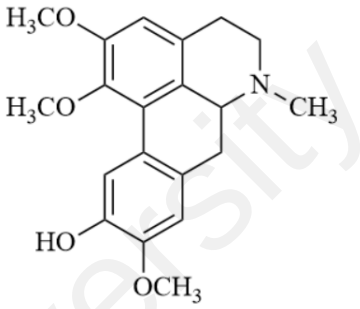

(+)-Lirioferine **27**

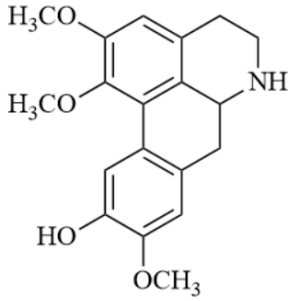

(+)-Norlirioferine **28**

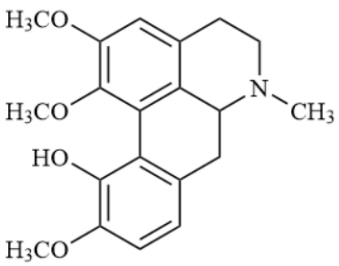

Isocorydine **29**

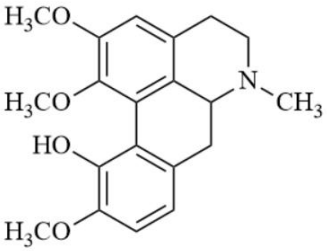

Norisocorydine **30**

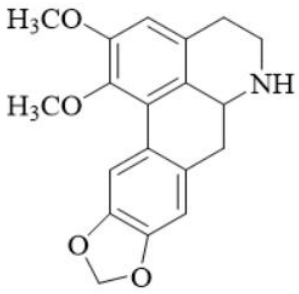

Nornantenine **31**

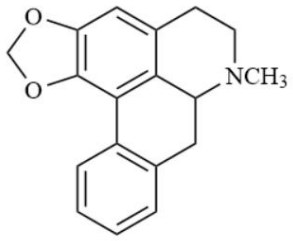

Roemarine **32**

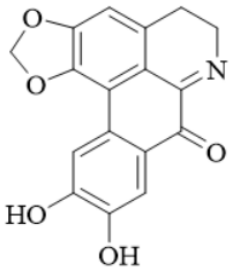

Dicentrinone **33**

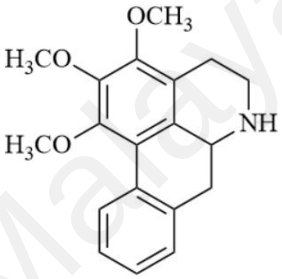

(-)-O-methylisopiline **34**

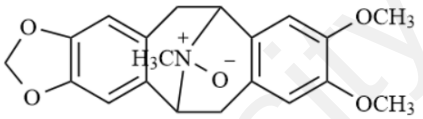

(+)-Eschscholtzidine-*N*-oxide **35**

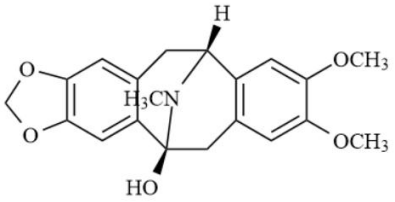

(-)-12-hydroxy-O-methylcaryachine **36**

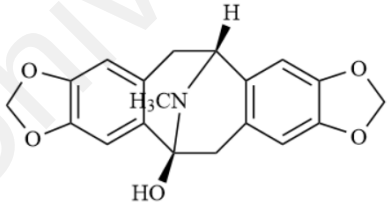

(-)-12-hydroxycrychine **37**

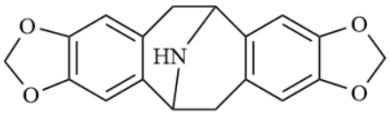

(-)-*N*-demethylcrychine **38**

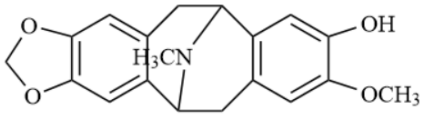

(±)-Caryachine **39**

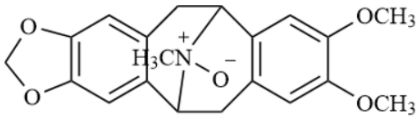

(±)-Isocaryachine-*N*-oxide **40**

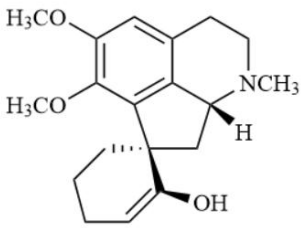

Isocryprochine **41**

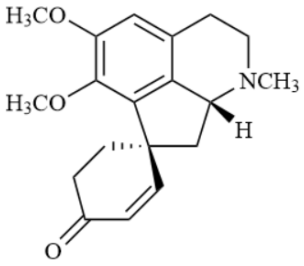

Isoamuronine **42**

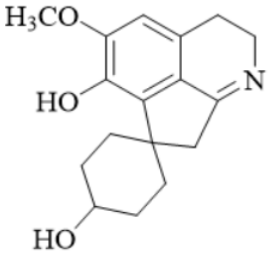

Prodensiflorin A **43**

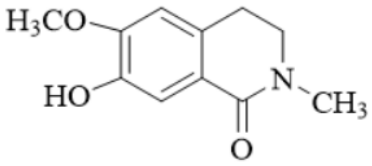

Thalifoline **48**

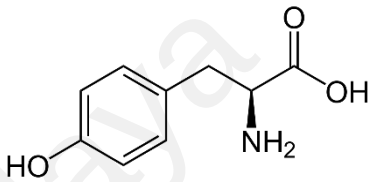

Tyrosine **49**

From Table 2.2 and the chemical compounds shown above, Lauraceae is a prolific producer of alkaloids having a fair number of *Cryptocarya* species rich with structurally diverse isoquinoline alkaloids (Castro-Saavedra et al., 2016). The production of those phytochemicals from the Lauraceae plants has been the subject of myriad comprehensive articles. Although their biogenesis and metabolism have been analyzed in many cases throughout the past 70 years, the function of alkaloids is still vague and equivocal by the chemist. Biogenesis is the experimental study of the formation of secondary metabolites. Thus, biogenesis is the hypothetical speculation on the precursor-product relationship in a biosynthetic pathway. Most alkaloids of Lauraceae, are isoquinoline type derived from tetrahydribenzylisoquinoline which originated from tyrosine **49** (Zahari, A., 2016; Shamma, M., 2012). The phenanthrene alkaloids are usually found in the same plant families as aporphines, from which they are biogenetically derived. Both types of alkaloids are closely related and co-occur in most species. Aporphine alkaloids are the largest group within the isoquinoline alkaloids and it has a twisted biphenyl ring system. Altogether, isoquinoline and phenanthrene type alkaloids are derived from the aporphine

type alkaloid through similar biogenesis route. Meticulous study on the chemical constituents of this species has led to the identification of alkaloids with interesting pharmacological properties and therefore has driven the goal for this research work.

2.5 Corrosion background

Our world is dealing with one of the naturally occurring disaster, corrosion. The term corrosion or mostly known as rust was derived from the Latin word '*corrosus' or* '*rodere*' which defines gnawing, that is, consumed or eaten away (Sastri & Editor, 2011). Corrosion will cause physical damage, reducing functionalities of an object and thus shorten their shelf life. Figure 2.3 below shows the corrosion cycle that we have been facing throughout our technological years.

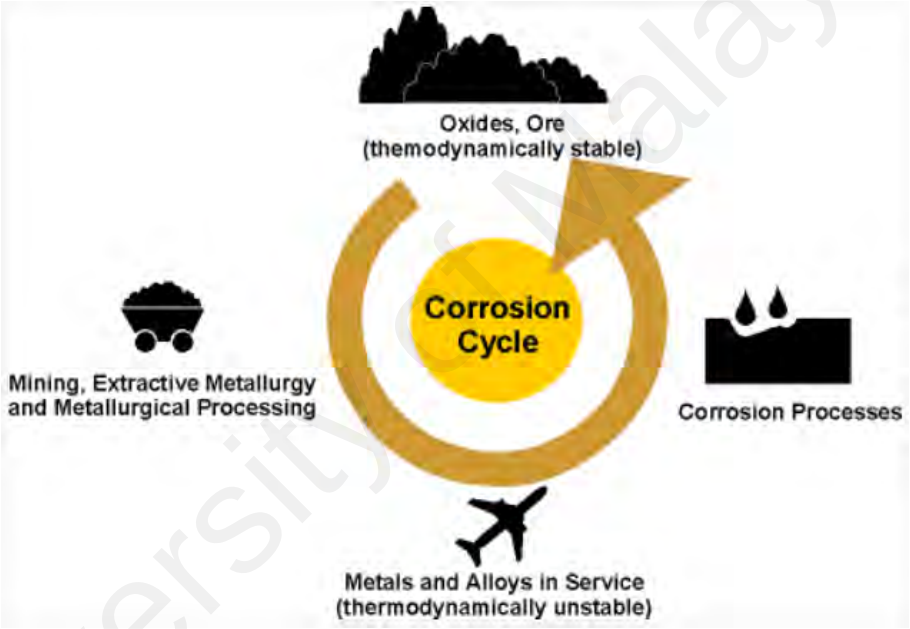

Figure 2.3: Corrosion cycle of steel (Corrosion-club.com, accessed 1st March 2019).

Previously, there were only a few scientists who showed some interest in the corrosion study until Robert Boyle came across the corrosion mechanism in his essay "*Mechanical Origin of Corrosiveness*" (Groysman, A., & Brodsky, N., 2006). Early in 19th century, the corrosion concept was explained more in detail from the electrochemical perspective. Later in the year 1933, Michael Faraday established a quantitative relationship between chemical actions and electric current. Faraday's first and second law are the basis for the calculation of corrosion rates in metals (Newman & Sieradzki, 1999).

2.6 Corrosion of iron

Iron plays an important role in our present era of rapid development. Problems that are mostly encountered by the industrial sectors are corrosion of metals composed majorly from iron. The driving force as though why metal corrodes no matter how hard we try to prevent it is because of its thermodynamic unstable nature. A neutral iron atom has an electronic configuration of [Ar] $3d^6$ $4s^2$, whereby the element is not achieving any electronic stability. It tends to release 3 valence electrons from its 3d and 4s shells in order to gain half-electronic stability, making all the valence electrons in 3d shells arranged singularly and of the same spin direction, hence lowering its orbital energy. It is necessary to provide a certain amount of energy to prevent oxidation of iron from Fe to Fe^{3+} or to revert Fe^{3+} to Fe. It is, therefore, when the iron is exposed to the natural environment, they will most likely be converted back to the original states in which they were found (Fe^{2+}/Fe^{3+}) (S.-S. Wang & Frankel, 2017). The electronic configurations for both neutral (Fe) and rusted iron (Fe^{3+}) are shown in Figure 2.4 below.

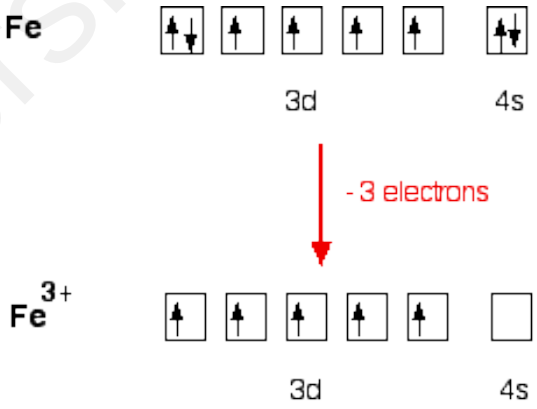

Figure 2.4: Electronic configuration of Fe and Fe^{3+}.

In the presence of water and oxygen, metallic iron is thermodynamically unstable and corrosion proceeds according to the electrochemical mechanism shown in Figure 2.5 (Grundmeier, Schmidt, & Stratmann, 2000). The redox reaction of corrosion occurs both

in anodic and cathodic terminal sides of the metal surface. More than one oxidation and reduction processes may occur.

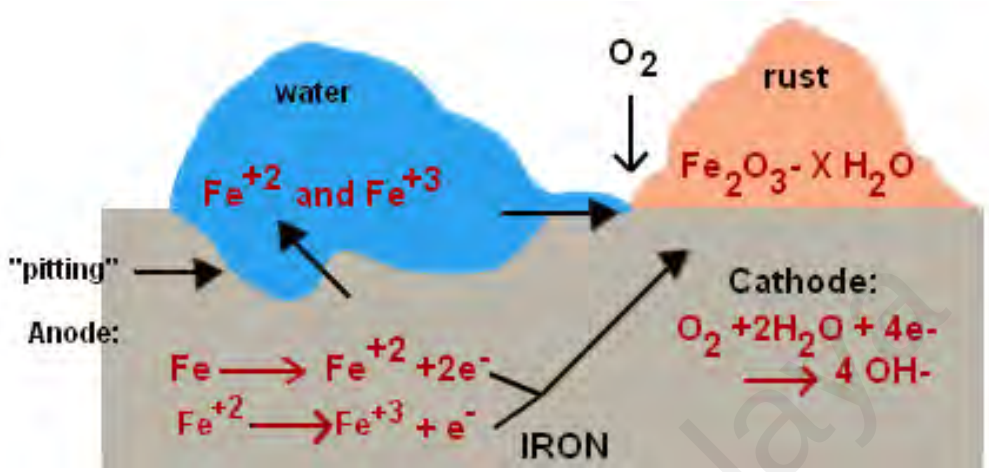

Figure 2.5: Electrochemical mechanism of corrosion.

2.7 Consequences of corrosion

The importance of corrosion studies has drastically inclined ever since the industrialization era. The first area of significance is focused on the economic aspects including the objective of reducing material losses resulting from the corrosion of pipes, tanks, metal components of machines, ships, bridges and marine structures. The second sphere is the safety of operating equipment resulting in catastrophic consequences because of corrosion. Examples of these events are pressure vessels, boilers, metallic containers for radioactive materials, turbine blades, bridge cables, aeroplane parts, and automotive steering mechanisms. The third dimension of corrosion studies is the conservation of materials as applied primarily to metal resources. It is very well known that the supply of metals is limited, and their wastage includes corresponding losses of energy and water reserves associated with the production and fabrication of metal constructions. The humanitarian efforts required for the design and repair of corroded equipment can easily be utilized for other socially useful purposes. Figure 2.6 shows a

division of corrosion impact on the world's economy, in accordance with 2015 GDP (NACE, 2015).

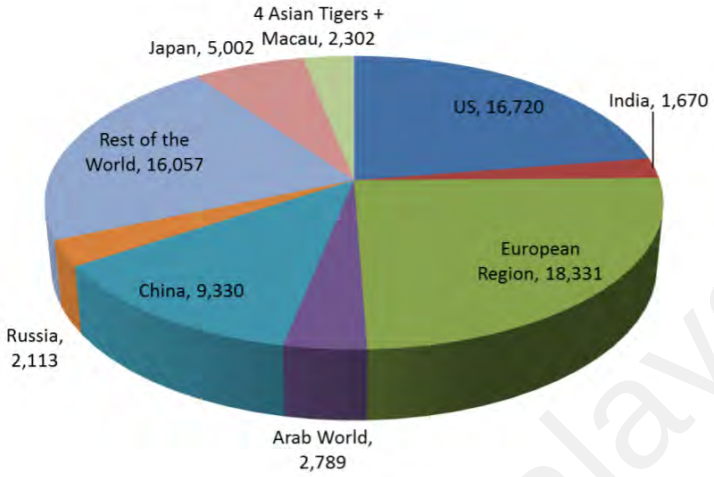

Figure 2.6: Global cost of corrosion on the world's economy (NACE, 2015).

Economic losses due to corrosion are classified into two; direct losses and indirect losses (François, R., Laurens *et al.*, 2018). The direct losses are the cost of replacing the corroded structures and machines or their components such as condenser tubes, mufflers, pipelines and metal roofing including labour cost. Direct losses also include the extra cost of using corrosion resistant metals and alloys instead of carbon steel where the latter does have adequate mechanical properties but not enough corrosion resistance. The cost of galvanizing, nickel plating on steel of dehumidification of storage rooms for metal equipment also accounts for direct losses.

Indirect losses, which are more difficult to access, may either be economic or social. These may include contamination of the product, loss of valuable product from a corroded container, damage of adjacent equipment, decreased safety and production (e.g. Sudden failure of equipment may cause fire, explosion or release of toxic products) and change of appearance. Indirect losses are in fact very difficult to access in the event of loss of health or life through explosion, unpredictable failure of chemical equipment or the wreckage of aeroplanes, trains or automobiles through sudden failure by corrosion of

critical components. To sum up, it can be said that corrosion is a potent force which incurs an economic loss, depletes resources and causes untimely failures of industrial plants, equipment and their constituents (Talbot, D. E., & Talbot, J. D, 2018).

2.8 Corrosion equation

Corrosion regarding iron metal, steel or other iron alloys usually known as **rusting** in which ferrous is converted to hydrous ferric oxides. Therefore, nonferrous metals corrode rather than rust. The general ionic and chemical equations for iron rusting are shown in Scheme 2.2 below:

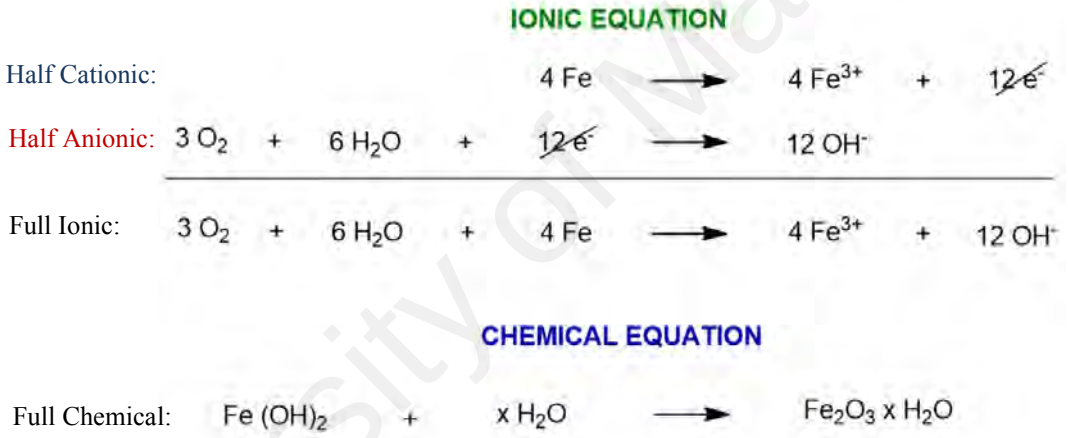

Scheme 2.2: General ionic and chemical equation for corrosion of iron.

The term "corrosion" is presently confined to surface degradation due to chemical attacks. While "erosion" is termed for the protective layers, which occurs when protective mechanisms have been overlooked, broken down, or have been exhausted, leaving the metal vulnerable to physicochemical attacks.

Silver articles tarnish and finally turn black in the atmosphere; here, the transformation of silver to its black sulphide does not amount to a serious loss of costly metal, but steps must be taken to restore the lustrous surface. A similar loss of appearance due to corrosion

is also mentioned in the dulling of brass and in the fogging of nickel (Tezeghdenti, Etteyeb *et al.*, 2017).

2.9 Corrosion control

Metal corrosion could be prevented by using various protection methods. These methods of protection could be suggested based on the environment in which metal is exposed. In industries, the following methods were used for corrosion control (Gillanders, Williams *et al.,* 2009):

a) material selection and design
b) change of environment
c) changing interfacial potential
d) protective coatings
e) corrosion inhibitors

2.10 Corrosion inhibitors

Corrosion inhibitors are those inorganics, organic or naturally occurring compounds which interact with the metal or the corrosive environment in such a way by:

i. adsorbing as a film on the metal surface, or
ii. inducing the formation of a thick product, or
iii. changing the environment (medium) characteristics by producing protonating precipitates, or
iv. by inactivating an aggressive constituent so that it reduces the corrosion rate to a certain extent

Therefore, corrosion inhibitors can be divided into two broad categories, namely;

a) those that facilitate the formation of a protective oxide film by an oxidizing effect, and,

b) those that inhibit corrosion by selectively adsorbing on the metal surface and creating a barrier that prevents access of corrosive agents to the metal surface.

Almost all organic molecules containing heteroatoms such as nitrogen, sulphur, phosphorus, and oxygen (Inzunza *et al.*, 2013) showed significant inhibition efficiency. The inhibition efficiency should follow the sequence O < N < S < P. Current data explains the phenomenon that most organic inhibitors adsorbed on the surface of the metal by displacing water molecules, hence forming a compact barrier.

The adsorption mechanism of the inhibitors is generally divided into physical adsorption (physisorption) and chemical adsorption (chemisorption). Physisorption is a phenomenon where the functional groups of the inhibitor being protonated by the corrosive environment, therefore, forming an excess positive or negative charge(s) at the end terminal of the heteroatoms. These excess charges then bind onto the positively charge iron surfaces through electrostatic interactions. However, no bond formation nor breaking is involved throughout the process. The strength of this type of mechanism depends on the aggressiveness of the corrosive media and dependent on the adsorbed species on the iron surface (Ikeuba, Ita *et al.*, 2015). The higher the acidity or alkalinity of the corrosive media, the higher the protonation rate of the functional groups. The example given, in HCl, iron surface is being oxidized by the chloride ions, Cl^- leading to the formation of ferric chloride, $FeCl_2$. The presence of the negatively charged Cl^- promotes the attraction of the protonated functional groups of the inhibitor, indirectly acting as a bridge interconnecting with the iron surface. The protonated groups will then reduce the Fe^{2+} back to its original state, Fe by forming a homogenous monolayer of protection. This type of mechanism occurs dominantly when the Gibbs free energy of adsorption, ΔG_{ads} calculated on the metal surface to be < -20 $kJmol^{-1}$.

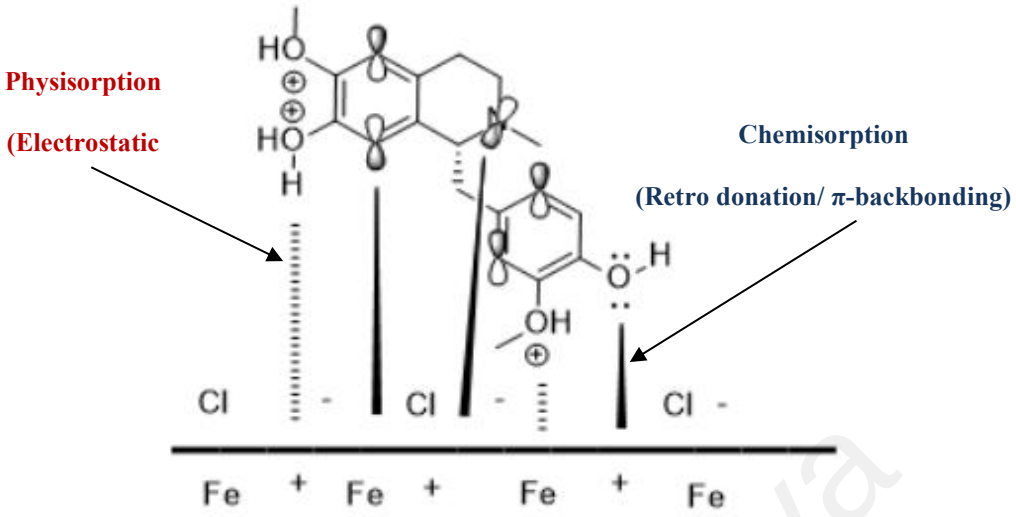

Figure 2.7: The schematic illustration of different adsorption modes by alkaloids at mild steel/ 1M HCl interface.

Chemisorption in the other hand is the case where the lone pair electrons from the functional groups and the multiple heterocyclic π-electrons in the aromatic rings of the inhibitors binds onto the iron surface through coordinative bonds. These electron rich sites could donate their electron into the empty *d*-orbital of the metal lattice through comprehensive back-donation bonds forming a stable metal-inhibitor complex. The chemisorption bond strength depends on the density of the donor atom or functional group and on the polarizability of the group. If the carbon in the ring system carries such groups like $–NH_2$, $-NO_2$, -CHO, or –COOH as a substituent, this will improve the corrosion inhibition effects (Yamuna & Anthony, 2015). The strength of this mechanism is characterized by the energy of the highest occupied molecular orbital, E_{HOMO} and the energy of the lowest unoccupied molecular orbital, E_{LUMO} of the functional groups on the inhibitor molecule as well the energy gap between both energy levels. The inhibition efficiency increases with the increase in E_{HOMO}, and the decrease in E_{LUMO} and the energy gap (ΔE) (Madkour, Kaya *et al.*, 2016; Qiang *et al.*, 2018). The aggressiveness of the corrosive media plays an important role in allowing the inhibitor to bind onto the metal surface through chemisorption mode. This type of mechanism involves bond formation

and is consistent under low molarity acidic media with ΔG_{ads} > -40 $kJmol^{-1}$. Chemisorption occurs spontaneously at a very favourable condition where it takes a longer time to form a stable, better and stronger monolayer of protection on the metal surface. The schematic illustration for the general physisorption and chemisorption mechanisms are displayed in Figure 2.7.

Green inhibitors can be classified into different groups based on many factors. In view of the electrochemical process, they could be classified as anodic inhibitors, cathodic inhibitors and mixed inhibitors. On the basis of the environment, these can be classified as acid (inorganic, organic inhibitors), neutral and alkaline inhibitors (Parthipan *et al.*, 2017).

The adsorption of electrons released from the anodic reaction by oxidant species is the cathodic reaction which could involve either oxygen reduction in basic and neutral solutions or hydrogen evolution due to the reduction of hydrogen ions in acidic medium. The driving force for the corrosion is the thermodynamic instability of the metal in its surrounding environment. The electrode potential of a metal is a measure of its propensity to corrode. The metals corrode faster when dissolution potential is negative. Various factors shall be considered while selecting inhibitors, which are:

1. long range efficiency,
2. temperature and concentration effects of inhibitor performance,
3. toxicity and pollution aspects,
4. economically and technically competitiveness with other considered corrosion inhibitors.

2.11 Corrosion study

Corrosion process is a spontaneous electrochemical reaction that occurs on the metal surface in the presence of oxygen and water. Electron flow from the anodic site towards the cathodic region of the metal surface could be studied from several established techniques mentioned below. The electrochemical experiments were conducted at the School of Chemical Sciences, University of Science Malaysia (USM), Penang, Malaysia while the surface morphological analysis using SEM-EDX was conducted at Medical Faculty, University of Malaya.

2.11.1 Weight loss technique

Theoretically, corrosion process occurs naturally when a specimen of mild steel or coupon is exposed to a corrosive environment for a certain duration. The weight loss taking place along the period of exposure is expressed as corrosion rate. The advantage of this weight loss technique is that it is applicable to all environment, easy to monitor, corrosion deposits can be observed, corrosion can be easily being determined and calculated. Besides, the inhibitor efficiency can be easily assessed by this method. Despite all the advantages and understanding of the technique, this experiment is time-consuming and less sensitive as it would not indicate any variations in the corrosion rates that occur during the test (Hussin & Kassim, 2011). Therefore, this technique is not applied to this research.

2.11.2 Electrochemical impedance study (EIS)

EIS is a well-established and a powerful electrochemical experiment in the corrosion studies. Surface properties, electrode kinetics and mechanistic information can be obtained from the impedance diagram which consists of Bode plot and Nyquist plot. EIS is usually measured by applying an alternate current (AC) potential to an electrochemical

cell and measuring the current through the cell. The terms resistance and impedance are both denoted to opposition to the flow of electrons or current. Two circuit elements, which are the capacitor and inductor, will impede the flow of electrons in AC circuits.

This technique applies a small amplitude signal, usually a voltage between 5 to 50 mV to a specimen over a range of frequencies. Normally for corrosion systems, the frequency range being set is 0.0001 Hz to 100,000 Hz since most of the relevant information regarding the corrosion reaction occurs over this range (Ribeiro & Abrantes, 2016). The EIS instrument records the real (resistive) and imaginary (capacitive) components of the impedance response, $Z^{'}$ and $Z^{''}$ respectively. An important part of the EIS analysis is to create an equivalent circuit of the system using resistors and capacitors whether in series or in parallel. The physical behaviour of the corrosion system can be stimulated and quantified with this circuit to insight into the important processes in the corrosion systems.

2.11.3 Potentiodynamic polarization measurements (PDP)

The characterization of a metal specimen by its current and potential relationship is generally studied via this electrochemical technique. It enables us to determine the corrosion rate in the passive region, corrosion potential, corrosion current density of the system and can be used to determine types of inhibitors and their characteristics. This method works by the concept of, whenever a specimen is immersed in a corrosive medium, both oxidation and reduction process occurs simultaneously on its surface. A specimen is at its corrosion potential, E_{corr} when it is in contact with a corrosive liquid and it assumes a potential to a reference electrode. At E_{corr}, the rate of oxidation is exactly equal to the rate of reduction and the specimen is at equilibrium with the environment (Figure 3.5).

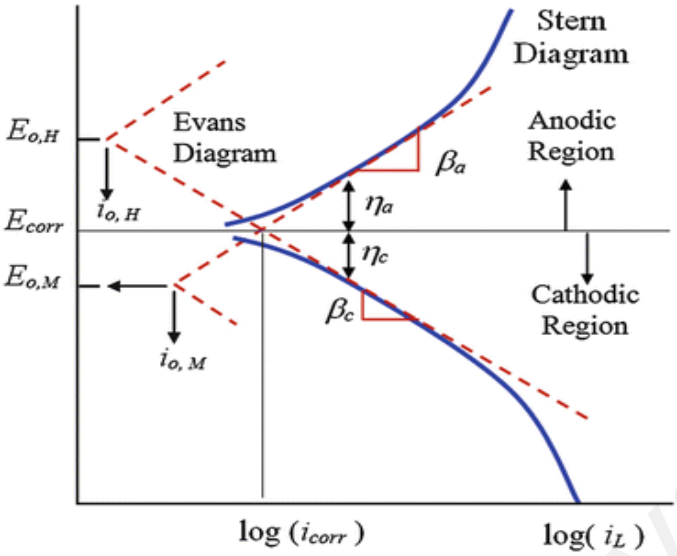

Figure 2.8: A hypothetical Tafel plot.

2.12 Adsorption isotherm

Adsorption of the organic compounds on the mild steel surface can be described as either physical or chemical adsorption. Both types of interaction are influenced by the nature and charge (potential of zero charge Eq=0) of the metal, the chemical structure of the inhibitor as well as the type of the corrosive electrolyte. However, basic information on the interaction between the inhibitor and the metal surface can be provided by the adsorption isotherm, which, in turns depends on the degree of electrode surface coverage (Θ). This quantity can be calculated from the values of current density running through the steel in the uninhibited (i_0) and the inhibited (i_1) solutions according to the equation (Bahrami, Hosseini, & Pilvar, 2010):

$$\Theta = 1 - \left(\frac{i_0}{i_1}\right) \qquad (2.1)$$

To evaluate the adsorption process of *Cryptocarya nigra* inhibitors on the mild steel surface, Langmuir, Temkin and Frumkin adsorption isotherm were obtained according to the following equations:

$$\text{Langmuir: } \frac{\theta}{1-\theta} = KC \qquad (2.2)$$

$$\text{Temkin: } \log\left(\frac{\theta}{C}\right) = \log K - g\Theta \qquad (2.3)$$

$$\text{Frumkin: } \log\left(\frac{\theta}{(1-\theta)C}\right) = \log K + g\Theta \qquad (2.4)$$

Where Θ is the surface coverage (% IE), K is the adsorption-desorption equilibrium constant, C represents the inhibitor concentration and g is the adsorbate interaction parameter. Considering that the double-layer capacitance is proportional to the surface not covered by the inhibitor, the fraction of the surface covered by adsorbed molecules was determined according to the ratio:

$$\Theta = \left(1 - \frac{C_{dl}^{0}}{C_{dl}}\right) \times 100 \qquad (2.5)$$

Where C^0_{dl} and C_{dl} are the double layer capacitance determined, respectively without and with the presence of corrosion inhibitor in the solution. The free-energy of adsorption (ΔG^0_{ads}) was calculated from the slope of the Langmuir isotherm, which showed the best correlation with the experimental data, according to the equation:

$$K = \left(\frac{1}{55.5}\right) \exp\left(\frac{-G_{ads}^{0}}{RT}\right) \qquad (2.6)$$

55.5 is the water concentration, R is the universal gas constant and T is the thermodynamic temperature.

2.13 Scanning electron microscope (SEM) analysis

A type of electron microscope that produces images of a sample by scanning the surface with a focused beam of electrons. The electrons interact with the atoms on the surface of the sample, producing various signals that describe the surface topography and

composition of the sample. Specimens are observed in high or low vacuum condition under an inert nitrogen environment. The sample size should fit the specimen stage and may require special preparation to increase their electrical conductivity and to stabilize them so that they can withstand the high vacuum conditions and the high energy beam of electrons.

CHAPTER 3: METHODOLOGY

3.1 Plant material

The bark of *Cryptocarya nigra* was collected at Hutan Simpan Ulu Sat, Machang, Kelantan (Malaysia) by Mr. Teo, Mr. Rafly and Mr. Din from the phytochemical group before being deposited at the Herbarium of the Department of Chemistry, University of Malaya, Kuala Lumpur, Malaysia for research reservations. The voucher specimen was given code number KL 5272.

Table 3.1: Plant description and locality.

Voucher specimen	Species	Part of plant	Locality and date of collection
KL 5272	*Cryptocarya nigra* Kosterm	Bark	Ulu Sat Reserved Forest, Machang, Kelantan

3.2 Solvent and chemicals

Sephadex LH-20 (Pharmacia Fine Chemicals, Upsala, Sweden), Kiesel gel 60 (Merck, 7734; 9385); silica gel (Sigma Co., S-9258), lichro prep RP-18 (Merck). Solvent systems for extraction process were n-Hexane, CH_2Cl_2 and MeOH, distilled prior to use. All solvents are of AR grade except that were used for folk extraction. TLC plates were developed using 60 F_{254} plates (Merck, Art.5719) with various combination of solvent systems: (a) n-hexane: CH_2Cl_2; (b) n-hexane: EtOAc; (c) CH_2Cl_2–MeOH. Alkaloid spots were confirmed by spraying dragendorff's reagent and visualized under ultra-violet light (254 and 365 nm), while aromatic compounds by vanillin solution with heating at 80 °C.

3.3 Instrumentation

The 1D and 2D NMR spectra were acquired in deuterated chloroform, $CDCl_3$ (Merck, Germany) with trimethyl silane (TMS) as the internal standard using Bruker AVN 400 FT NMR, Bruker AVN 600 FT NMR, JEOL ECA 400 FT NMR spectrometer systems. Data were analyzed *via* Mestrec Nova, Top Spin and DELTA software packages. Chemical shifts were reported in ppm and internally referenced to the solvent signals as in Table 3.2:

Table 3.2: NMR shifts of selected deuterated solvents.

Solvents	Chemical formula	^{1}H shift(s) in ppm (multiplicity)	^{13}C shift(s) in ppm (multiplicity)	Peak for trace of water (ppm)
chloroform	$CDCl_3$	7.26 (*1*)	77.00 (*3*)	1.5
methanol	CD_3OD	3.30 (*5*)	49.05 (*7*)	4.72
		7.20 (*1*)	123.44 (*3*)	
pyridine	C_5D_5N	7.56 (*1*)	135.51 (*3*)	5.0
		8.71 (*1*)	179.68 (*3*)	

High-resolution liquid chromatography-mass spectrometry-ion trap-time of flight mass spectrometry (LCMS-IT-TOF) spectra were obtained using Agilent 6530 Accurate-Mass Q-TOF ESI LC/MS with ZORBAX Eclipse XDB-C18 Rapid Resolution HT (4.6 mm i.d x 50 mm x 1.8 µm column). HPLC grade methanol, acetonitrile and deionized water were used as mobile phase solvents. All solvents and samples were filtered with a 0.2 µm nylon membrane filter (WHATMAN) prior to LCMS analysis. The ultraviolet spectra were recorded on a Shimadzu UV-250 using HPLC grade methanol as a solvent with mirror UV cell. The Fourier Transform Infrared (FT-IR) spectra were obtained

through Perkin Elmer 1600 using spectroscopic grade chloroform as solvent. Optical rotations of the compounds were determined by JASCO DIP-1000 automatic digital polarimeter and A JASCO P-1020 polarimeter.

3.4 Chromatography

Separation and purification process was performed using various chromatography techniques such as thin layer chromatography (TLC) and column chromatography (CC). The TLC plates were activated at 60 ^{o}C for one hour and stored in the desiccator until needed.

3.4.1 Thin layer chromatography (TLC)

Aluminium supported silica gel 60 F_{254} plates (Merck) were used to see the spots of the isolated compound. UV Light Model UVGL-58 Mineral light Lamp 230V~50/60 Hz (254 and 365 nm) was used to examine spots or bands on the TLC followed by spraying with the dragendroff's reagent.

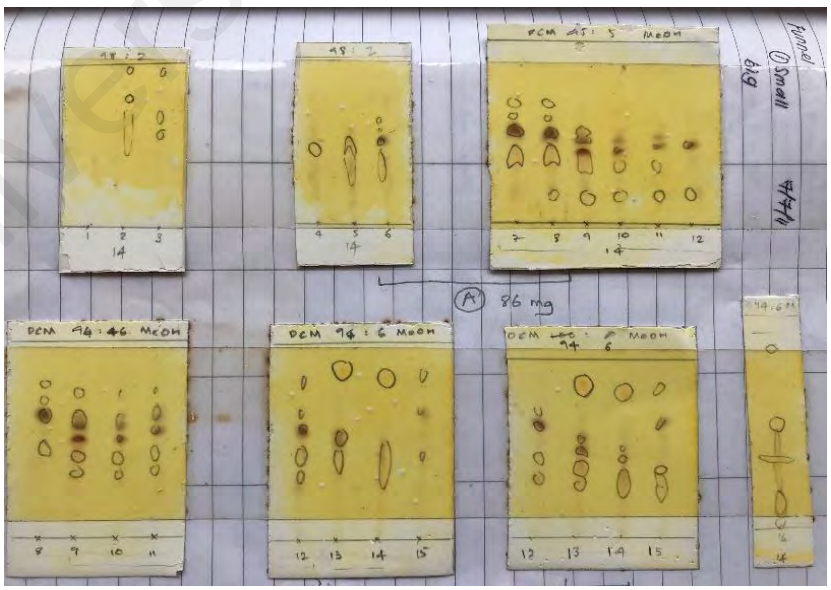

Figure 3.1: Series of TLC plates sprayed with dragendorff's reagent for alkaloid identification (orange spots).

3.4.2 Column chromatography (CC)

Silica gel 60 (63-200 µm-70-230 mesh ASTM) and silica gel 60 (40-63 µm-70-230 mesh ASTM) were used for column chromatography. The column was prepared by pouring slurry 60 g of silica gel (approximately 30:1 silica gel to sample ratio) in dichloromethane solvent system into a glass column of appropriate size with gentle tapping to remove trapped air bubbles. CNDE was initially dissolved in a minimum amount of solvent and loaded on top of the packed column. The extract was eluted with appropriate solvent systems (CH_2Cl_2-MeOH) of gradual increasing polarity at a slow consistent flow rate. Fractions were collected in either test tubes or conical flasks and evaporated for the next step. Fractions with similar TLC profile (having the same R_f values) were pooled together to obtain the sub-fractions which then subjected to further purification process.

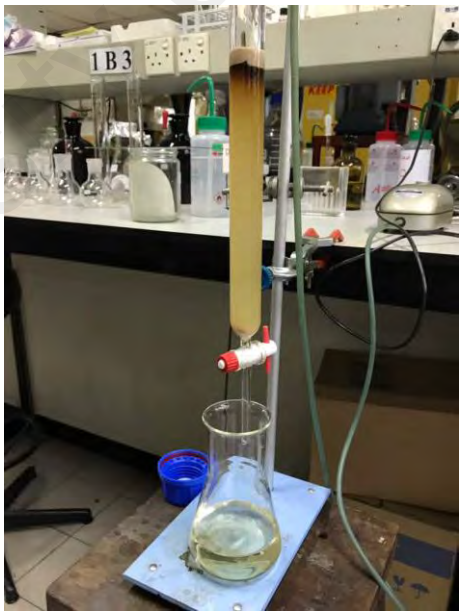

Figure 3.2: Column chromatography used for the fractionation of CNDE.

3.5 Detector reagent

Mayers reagent and dragendorffs reagent were applied for the detection and identification of the compounds from the spots seen on the TLC plates.

3.5.1 Mayers reagent (Potassium Mercuric Iodide)

A solution of mercury (II) chloride (1.4 g) in distilled water (60 mL) was poured into a solution of potassium iodide (5.0 g) in distilled water (40 mL). The potassium tetraiodomercurate (II), [K_2HgI_4] solution was then made up to 100 mL level. A positive result is indicated by the formation of a white precipitate when the aqueous layer (acidified) is treated with 2 to 3 drops of Mayer's reagent.

$$HgCl_{2\,(l)} + KI_{(l)} \rightarrow 2\,K^+ \left[I,\ Hg(I)(I),\ I \right]^{2-} + 2KCl \qquad (3.1)$$

3.5.2 Dragendorff's reagent (Potassium Bismuth Iodide)

Bismuth (III) nitrate (0.85 g) in a mixture of glacial acetic acid (10 mL) and distilled water (40 mL) were prepared in a beaker as solution A. Potassium Iodide (8.0 g) in distilled water (200 mL) in a separate beaker as solution B. Stock solution was prepared by mixing solution A and solution B in equal volumes. The stock solution (20 mL) was then diluted in a mixture of acetic acid (20 mL) and distilled water (60 mL) to prepare the spray reagent. A positive test result is indicated by the formation of orange-red precipitate or spots, indicating the presence of nitrogen-containing compounds on the TLC plates.

3.6 Extraction of *Cryptocarya nigra*

Extraction was carried out by conventional solvent percolation (soaking) method. Thorough descriptions of the procedures are provided in the subsections below.

3.6.1 Extraction of bark

The grounded and dried stem bark of *Cryptocarya nigra* (2.5 kg) was first defatted with hexane (15 L) at room temperature for 3 days. This procedure was repeated three times for a collective of 72 hours to remove wax, chlorophyll, terpenoids and flavonoids. The *Cryptocarya nigra* hexane extract (CNHE) were collected, combined, and the solvents were evaporated out. The dried plant materials were then moistened with 25% NH_4OH (100 mL) and left for 2 hours; this step was to aggregate the nitrogen-containing compounds in the plant. The sample was then macerated with dichloromethane (15 L) thrice for 3 days period. After filtration, the supernatant obtained was concentrated under reduced pressure using a rotary evaporator to a volume of 500 mL, tested for alkaloid content using TLC and confirmed by spraying with dragendorff's reagent. The extracts were finally concentrated and dried to yield 11.50 g of *Cryptocarya nigra* dichloromethane extract (CNDE). The residues were soaked again with methanol solvent (17 L) for a period of 3 days at room temperature to obtain 8.95 g of *Cryptocarya nigra* methanol extract (CNME).

3.6.2 Acid-base extraction for alkaloids

Approximately 5 g of the CNDE was taken and extracted with a solution of 5% hydrochloric acid in a separating funnel. This is to protonate the alkaloids so that they dissolve in the acidic aqueous layer, while other remaining chemical constituents stay in the organic layer. The acidic aqueous layer was then basified with 10 % ammonia solution until pH 11 and then re-extracted with dichloromethane solvent. The crude fraction (0.85

g) was obtained as a dark gummy residue after washing the combined dichloromethane extracts with distilled water, drying over anhydrous sodium sulphate and evaporation under pressure. The focus of this was to concentrate and extract the alkaloidal contents from the CNDE. The percentage yield recovered from the acid-base extraction was only 17 %.

3.7 Isolation and purification

The alkaloid extract of CNDE was subjected to exhaustive column chromatography (CC) over silica gel using CH_2Cl_2 and MeOH solvent systems (100:0, 99:1, 98:2, 97:3, 96:4, 95:5, 94:6, 90:10, 85:25, 75:25, 50:50) and finally 100% methanol as eluent to obtain 288 small fractions. The alkaloid spots were first detected by UV light (254 and 365 nm) and confirmed by spraying with dragendorff's reagent. Fractions of similar orange stains on the TLC plates, having the same R_f values were combined into 10 subfractions. The combined groups were then purified separately and successfully in stages to obtain seven compounds using column chromatography and preparative thin layer chromatography. Table 3.2 describes the combination of the subfractions according to their solvent systems. The isolation and purification procedures are summarized in Scheme 3.1 and the pure alkaloids are listed in Table 3.4. The structures of the isolated compounds were elucidated with the aid of spectroscopic methods such as 1D NMR (^1H, ^{13}C and DEPT), 2D NMR (COSY, NOESY, HSQC and HMBC), FTIR and LCMS-IT-TOF, in comparison with the literature values. Overall research flow is simplified in Scheme 3.2.

Table 3.3: Solvent systems for the combination of the subfractions.

Subfraction	Dichloromethane (CH_2Cl_2)	Methanol (MeOH)
1	98	2
2	97	3
3	96	4
4	95	5
5	93	7
6	92	8
7	90	10
8	85	15
9	80	10
10	70	30

Table 3.4: Solvent systems for the isolation and purification of the pure alkaloids.

Alkaloids	Solvent system (CH_2Cl_2: MeOH)	Weight (mg)
(+)-*N*-methylisococlaurine **1**	98:2	16.5
(+)-*N*-methyllaurotetanine **6**	97:3	20.2
(+)-Laurotetanine **7**	97:3	9.4
Atherosperminine **3**	95:5	23.4
Argentinine **5**	95:5	7.5
2-hydroxyatherosperminine **4**	90:10	5.5
Atherosperminine *N*-oxide **2**	90:10	8.3

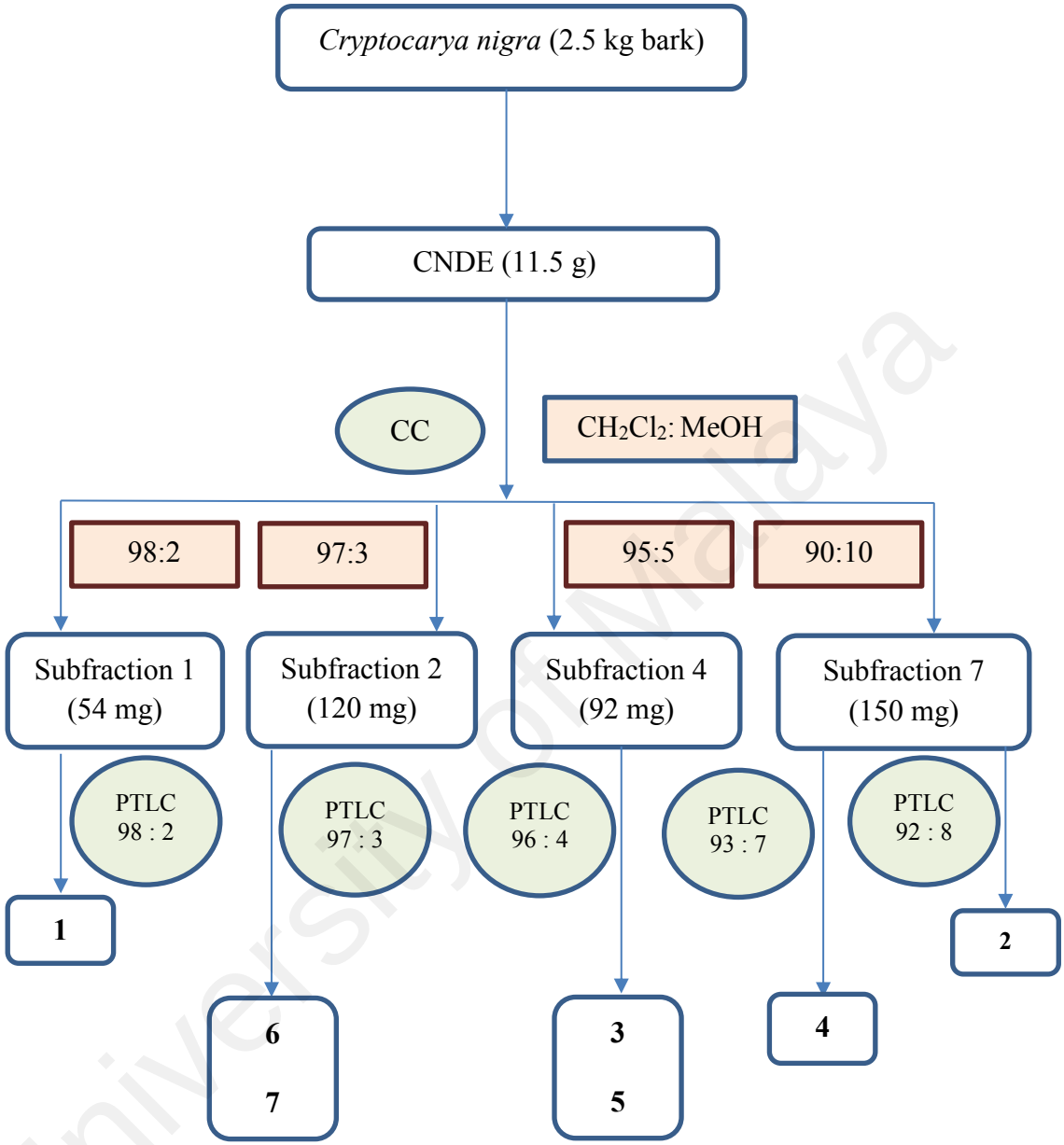

CC : column chromatography

PTLC : preparative thin later chromatography

Scheme 3.1: Isolation and purification of alkaloids from the bark of *Cryptocarya nigra*.

Flow Chart of Research Activities

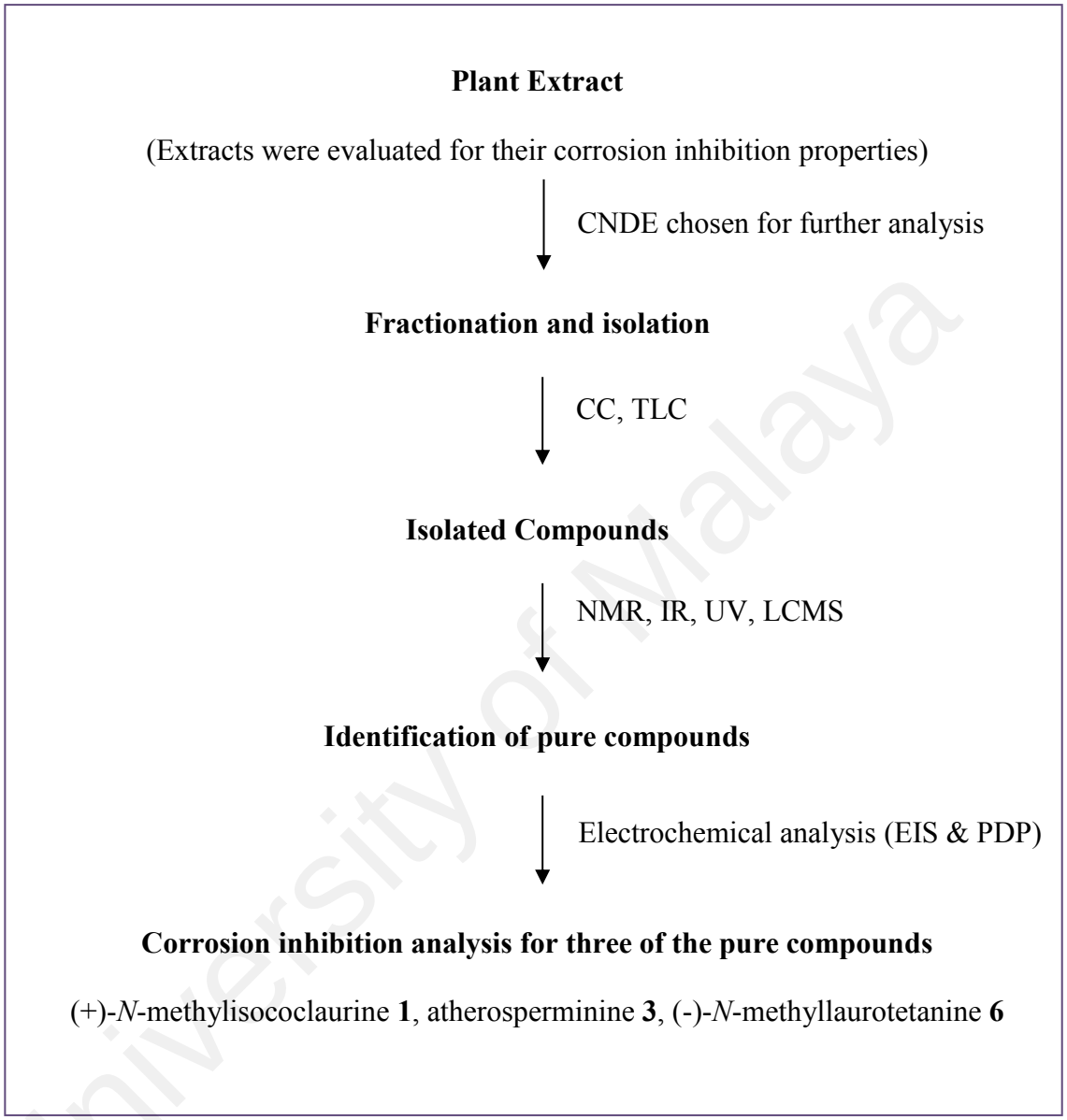

Scheme 3.2: Description of overall research methodology.

3.8 Physical and spectral data of the isolated compounds

Compound 1 : **(+)-*N*-methylisococlaurine**

Physical appearance : Light yellowish amorphous solid

Mass ($gmol^{-1}$) : 299.3710

$[\alpha]_D^{27}$: +29.4

Molecular formula : $C_{18}H_{21}NO_3$

IR υ_{max} (cm^{-1}) : 3370, 2357, 1500, 1250

^1H NMR and ^{13}C NMR : See Table 4.3

Compound 2 **: Atherosperminine-*N*-oxide**

Physical appearance : Brownish amorphous solid

Mass ($gmol^{-1}$) : 325.1500

$[\alpha]_D^{27}$: 0

Molecular formula : $C_{20}H_{23}NO$

IR υ_{max} (cm^{-1}) : 2920, 2870, 1620, 1460, 1380, 1255

^1H NMR and ^{13}C NMR : See Table 4.4

Compound 3 **: Atherosperminine**

Physical appearance : Brownish amorphous solid

Mass ($gmol^{-1}$) : 309.1510

$[\alpha]_D^{27}$: 0

Molecular formula : $C_{20}H_{23}NO_2$

IR υ_{max} (cm^{-1}) : 2917, 2849, 1604, 1512, 1223

^1H NMR and ^{13}C NMR : See Table 4.5

Compound 4 **: 2-Hydroxyatherosperminine**

Physical appearance : Brownish amorphous solid

Mass ($gmol^{-1}$) : 325.1700

$[\alpha]_D^{27}$: 0

Molecular formula : $C_{20}H_{23}NO_3$

IR υ_{max} (cm^{-1}) : 3412, 1643, 1450

^1H NMR and ^{13}C NMR : See Table 4.6

Compound 5 **: Argentinine**

Physical appearance : Light brownish amorphous solid

Mass ($gmol^{-1}$) : 295.1520

$[\alpha]_D^{27}$: 0

Molecular formula : $C_{19}H_{21}NO_2$

IR υ_{max} (cm^{-1}) : 3440, 2930, 1590, 1490, 1290

^{1}H NMR and ^{13}C NMR : See Table 4.7

Compound 6 : (+)-*N*-methyllaurotetanine

Physical appearance : Dark brown amorphous solid

Mass ($gmol^{-1}$) : 341.3070

$[\alpha]_D^{27}$: +45

Molecular formula : $C_{20}H_{23}NO_4$

IR υ_{max} (cm^{-1}) : 3120, 1600, 1444, 1258

^{1}H NMR and ^{13}C NMR : See Table 4.8

Compound 7 : (+)-Laurotetanine

Physical appearance : Dark brown amorphous solid

Mass ($gmol^{-1}$) : 327.2070

$[\alpha]_D^{27}$: +37

Molecular formula : $C_{19}H_{21}NO_4$

IR υ_{max} (cm^{-1}) : 3429, 2920, 2097, 1653, 1464

^{1}H NMR and ^{13}C NMR : See Table 4.9

3.9 Corrosion inhibition study

This section elaborates the experimental part of the corrosion inhibition activity. Sample preparation and description of the analysis are stated accordingly below.

3.9.1 Specimen and electrolyte preparation

Mild steel (MS) specimens scanned under X-ray Fluorescence (XRF) (C=0.205 %, Si=0.06 wt %, Mn=0.55 wt %, S=0.047 wt %, P=0.039 wt % and Fe remaining) were used throughout this experiment. The electrochemical study implied MS with an exposed area of 3.142 cm^2, while specimens' size of 2.3 x 0.2 x 2.3 cm was used for the SEM analysis. The surface of the MS specimens was mechanically abraded before analysis using different grades (200, 400, 800, and 1200) of emery papers. The solution used was made of AR grade hydrochloric acid. The electrolytes were diluted with distilled water into various concentrations ranging from 10 ppm to 1000 ppm.

Figure 3.3: Preparation of mild steel specimens.

3.9.2 Electrochemical studies

The electrochemical studies were carried out using Gamry Instruments reference 600 (potentiostat/galvanostat/ZRA), in a conventional three-electrode system. The MS

specimen was placed as the working electrode, while the Pt electrode and saturated calomel electrode (SCE) served as auxiliary and reference electrodes, respectively. All polarization and impedance curves were recorded at room temperature (30 ± 2°C) at the pH range of 0.7-0.8 in 1M HCl solution. The working electrode was immersed in the test solution for 30 min with a signal amplitude perturbation of 5 mV until a steady state open-circuit potential E_{ocp} attained. The fitting of the impedance data in an equivalent electrical impedance circuit was accomplished by using GAMRY Echem Analyst software package 5.50. The same software was implemented to extrapolate the Tafel slopes. Experiments were carried out in duplicate to ensure reproducibility of results and the electrochemical setup is shown in Figure 3.4.

Figure 3.4: Three electrode system set up for electrochemical analysis

3.9.2.1 Electrochemical impedance study (EIS)

AC impedance measurements were carried out at potential amplitude of 10mV, peak-to-peak (AC signal) in open circuit, with 10 points per decade and the frequency ranging from 10,000 Hz to 0.1 Hz. The impedance results obtained are represented as Nyquist plots. Inhibition efficiency, IE (%) is calculated from the charge transfer resistance (R_{ct}) values by using the following equation (Ribeiro & Abrantes, 2016):

$$IE\ (\%) = (1 - \frac{\boldsymbol{R_{ct\ (0)}}}{\boldsymbol{R_{ct\ (1)}}}) \times 100 \qquad (3.2)$$

Where $R_{ct(0)}$ is the charge transfer resistance of MS without inhibitor, $R_{ct(i)}$ is the charge transfer resistance of MS with inhibitor.

3.9.2.2 Potentiodynamic polarization study (PDP)

Potentiodynamic polarization measurements were carried out by scanning the electrode from -800 mV to -200 mV (vs SCE) with a scan rate of 0.5 mV s^{-1}. The linear Tafel segments were chosen (approximately 10-40 mV from the corrosion potential, E_{corr}, of the anodic and cathodic curves) and were extrapolated to E_{corr} several times to obtain reproducible corrosion current density (i_{corr}) values. Below shows the calculation of IE (%) from the I_{corr} values (Bandy, 1980):

$$IE\ (\%) = (1 - \frac{i_{corr(1)}}{i_{corr(0)}}) \times 100 \qquad (3.3)$$

Where $i_{corr(0)}$ is the corrosion current density of MS without inhibitor, i_{corr1} is the corrosion current density of MS with inhibitor.

3.10 Scanning Electron Microscope-Energy Dispersive X-Ray (SEM-EDX)

The surface morphological changes were monitored by using SEM LEO SUPRA 50VP – Scanning Electron Microscope, at an accelerating voltage of 15 keV. For this study, MS plates were carefully polished to a 1500 grit surface finish using silicon carbide paper and immersed in 1M HCl medium in the presence of an optimum concentration of inhibitors for 24 hours. Then the specimens were cleaned with distilled water, dried in cold air blaster before analyzed under SEM-EDX instrument.

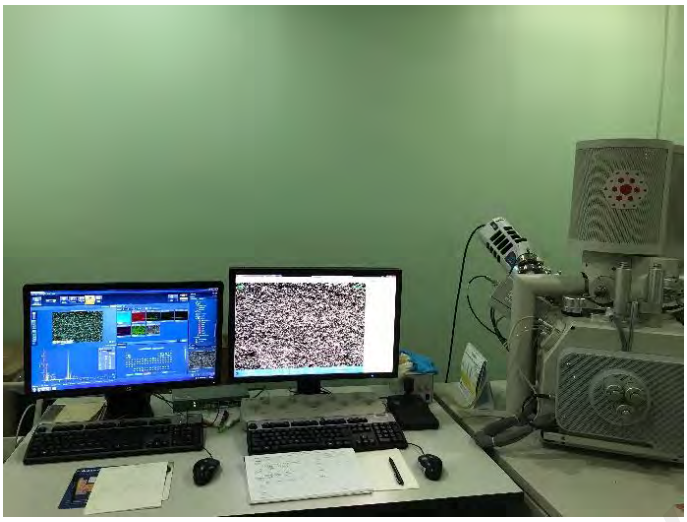

Figure 3.5: Scanning electron microscopy instrument at the Faculty of Medicine, UM.

CHAPTER 4: RESULTS AND DISCUSSIONS

4.1 Extraction

The bark of *Cryptacarya nigra* (2.5 kg) was extracted using three different solvents to give three different crude extracts; *Cryptocarya nigra* hexane extract (CNHE), *Cryptocarya nigra* dichloromethane extract (CNDE) and *Cryptocarya nigra* methanol extract (CNME). The details of the maceration process are described in Chapter 3 and the percentage yields of the collected crude extracts are calculated and depicted in Figure 4.1.

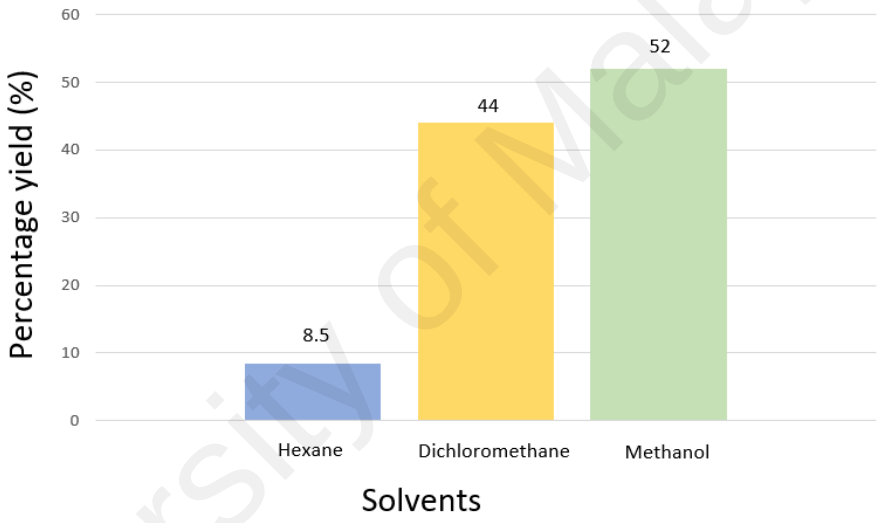

Figure 4.1: Percentage yield of different *Cryptocarya nigra* crude extracts.

The three crude extracts were studied under Nuclear Magnetic Resonance (NMR) spectroscopy to identify the possible compounds present prior to further purification steps and the results are shown in Figure 4.2, Figure 4.3 and Figure 4.4, respectively. Alkaloids, benzylic and phenolic moieties are mainly observed to occupy the semi to polar solvent portions; dichloromethane and methanol due to their polar structures having electronegative elements such as N, S and O.

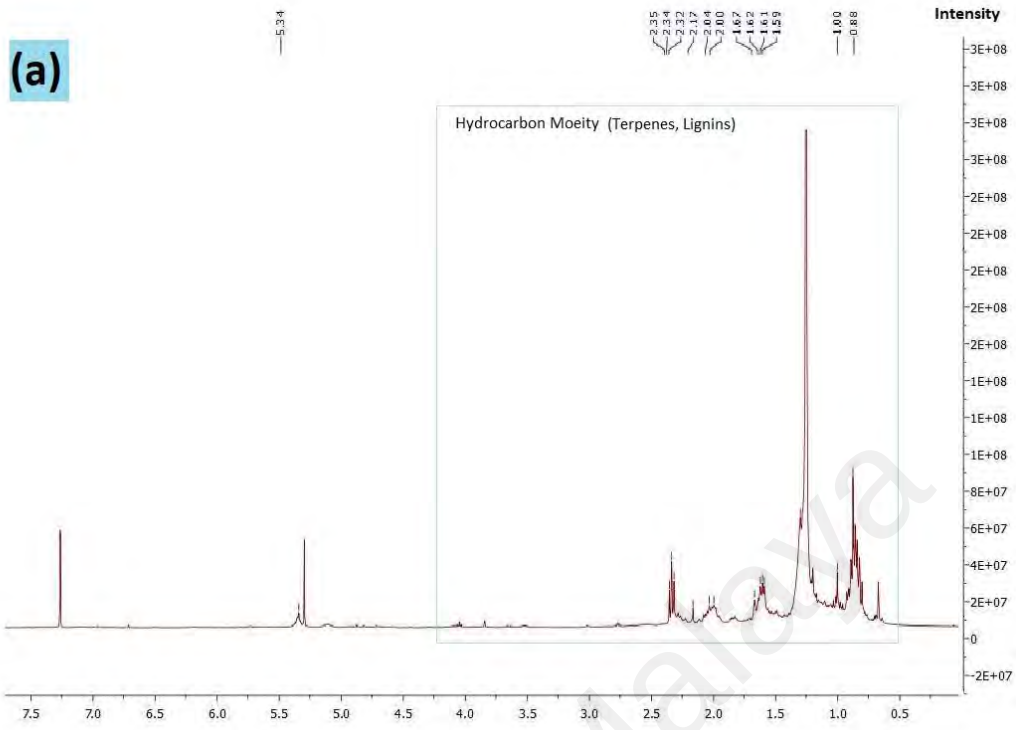

Figure 4.2: NMR spectra for *Cryptocarya nigra* hexane extract (CNHE).

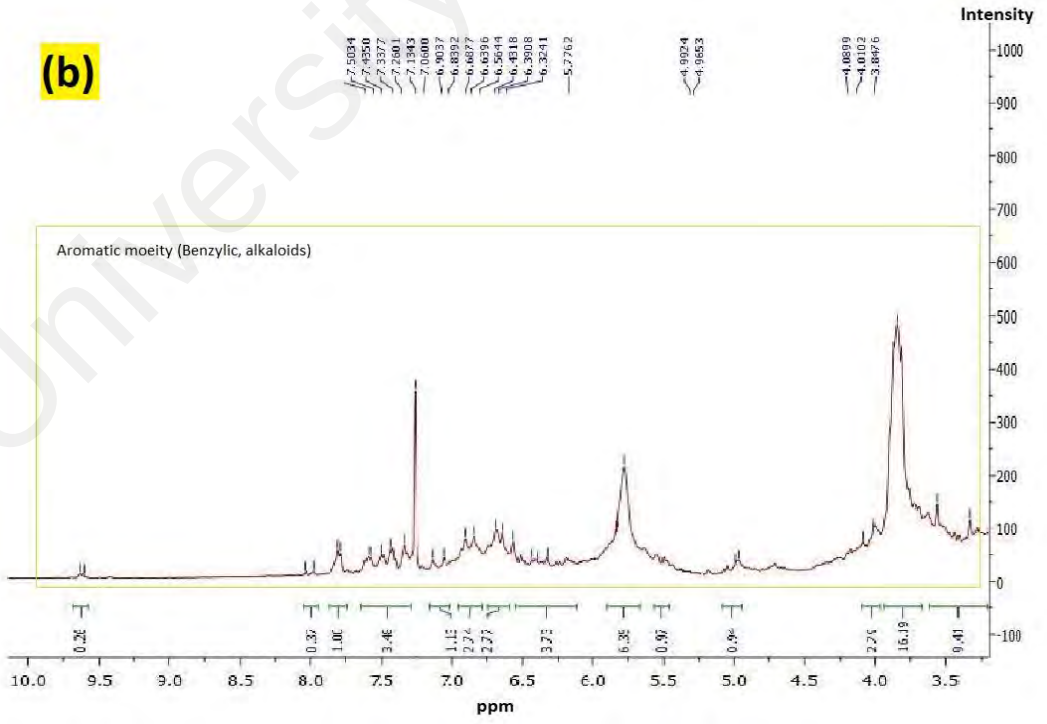

Figure 4.3: NMR spectra for *Cryptocarya nigra* dicloromethane extract (CNDE).

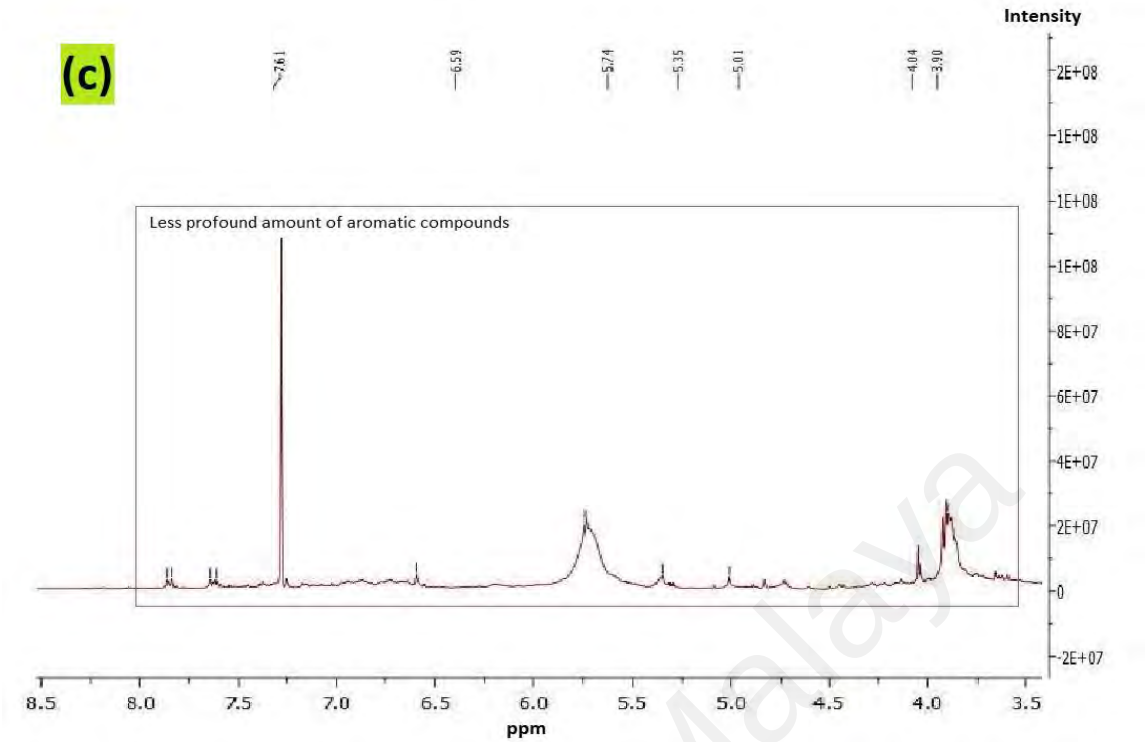

Figure 4.4: NMR spectra for *Cryptocarya nigra* methanol extract (CNME).

The crude extracts were subjected to Fourier Transform Infrared (FTIR) spectroscopy to study the absorption bands of the chemical functional groups present in each of the extracts. The values are tabulated in Table 4.1.

Table 4.1: FTIR peaks assignment for *Cryptocarya nigra* extracts.

Frequency range (cm^{-1})			**Peak assignment**	**Vibration modes**
CNHE	**CNDE**	**CNME**		
-	3430 (s)	3430 (s)	N-H	Stretching
-	3220 (b)	3220 (b)	-OH	Stretching
2920	2920 (s)	2920 (s)	C-H	Stretching
-	-	1730 (s)	C=O	Stretching
1605	1605 (m)	1605 (m)	C=C	Stretching
1247	1247 (m)	1247 (m)	C-O	Bending
758	758 (s)	758 (s)	O-H	Bending

Based on Table 4.1, all the extracts showed peaks at 2920 cm^{-1} and 1060 cm^{-1} which were due to the stretching and bending modes of C-H moiety. CNDE and CNME displayed strong absorption bands at 3430 cm^{-1} and 3220 cm^{-1} due to the presence of N-H and O-H stretching emerged from the possible alkaloids and polyphenolic compounds. These functional groups could be responsible for the corrosion inhibitive action through either chemisorption or physisorption mechanisms to prevent oxidation of metals. Hence from both NMR and FTIR analysis on the crude extracts, CNDE and CNME could be a promising source of green corrosion inhibitors.

4.2 Chemical constituents in *Cryptocarya nigra* (Lauraceae)

Cryptocarya nigra Kosterm (Lauraceae), coded KL 5272 was collected from Hutan Simpan Ulu Sat, Machang, Kelantan by the phytochemical group of the Chemistry Department, University of Malaya. Alkaloids from the bark of this species were extracted by the general procedure as described in the experimental section in early Chapter 3. High resolution liquid chromatography mass spectrometry-ion trap-time of flight mass spectrometry (LCMS-IT-TOF) was used to observe the possible chemical constituents of CNDE before further purification steps were done. The refined LC profile spectra under positive mode (+1) and molecular mass fragmentation at retention time R_t = 1.4856 of CNDE are depicted in Figure 4.5 and Figure 4.6, respectively.

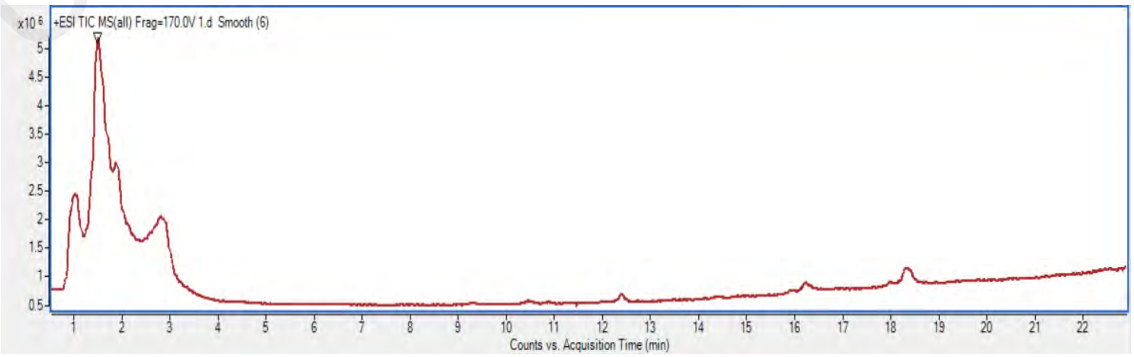

Figure 4.5: Refined LC profile spectra of CNDE under positive mode (+1).

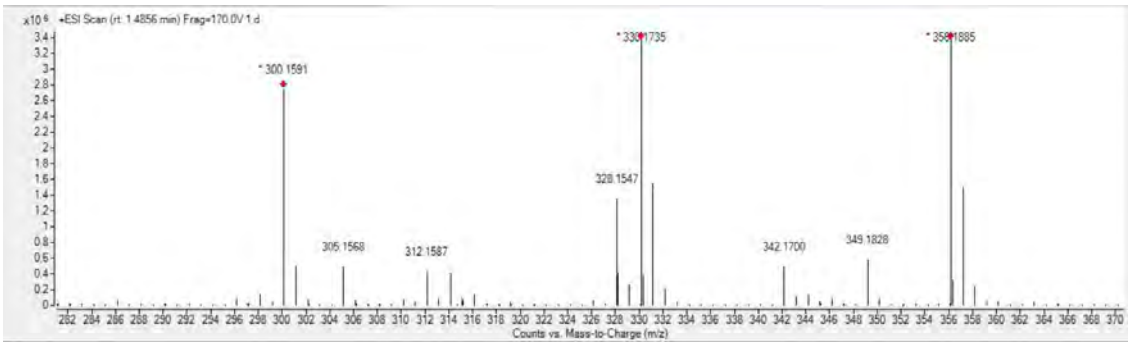

Figure 4.6: Molecular mass fragmentations at R_t = 1.4856.

These figures evidenced the presence of multiple interesting compounds that may potentiate the corrosion inhibitory effect of the extract. The build-in analyzer allowed us to determine the subsequent structure assignation of the compounds and calculate the elemental composition of the protonated molecules and the fragment ions at a high degree of accuracy (<5 ppm error) (X. Wu, Ding, Zhong *et al.*, 2013).

The *Cryptocarya nigra* dichloromethane extract (CNDE) was later subjected through extensive column chromatography (CC), and preparative thin layer chromatography (PTLC) to yield seven known pure compounds; one benzylisoquinoline, four phenanthrenes and two aporphine alkaloids. The following subchapters shall discuss briefly and concisely on the structural elucidation for each of the isolated compounds. The alkaloids isolated are listed in Table 4.2.

Table 4.2: Compounds isolated from CNDE.

Compounds	Name	Skeletal Type	Page
1	(+)-*N*-methylisococlaurine	Benzyl isoquinoline	63
2	Atherospermine *N*-oxide	Phenanthrene	75
3	Atherospermine	Phenanthrene	90
4	2-Hydroxyatherosperminine	Phenanthrene	101
5	Argentinine	Phenanthrene	112
6	(+)-*N*-methyllaurotetanine	Aporphine	123
7	(+)-Laurotetanine	Aporphine	134

Their structures were established through several complementary spectroscopic methods; UV, IR, MS, 1D (^{1}H-NMR, ^{13}C-NMR, DEPT-135) and 2D-NMR (COSY, HSQC, HMBC, NOESY) and upon comparison with those reported in the literature (Awang *et al.*, 2008; Nasrullah *et al.*, 2013; Saidi *et al.*, 2010; Thakur *et al.*, 2012; Wan Othman *et al.*, 2016). Among the compounds isolated, three alkaloids; **1**, **3** and **6** having different skeletal structures were analyzed for their corrosion inhibition activity on mild steel in 1M HCl. **1** is a benzyl isoquinoline with two hydroxyls and one methoxyl group. **3** is a phenanthrene with only two methoxyl groups. While **6** is an aporphine with one hydroxyl and three methoxyl groups.

4.2.1 (+)-*N*-methylisococlaurine **1**

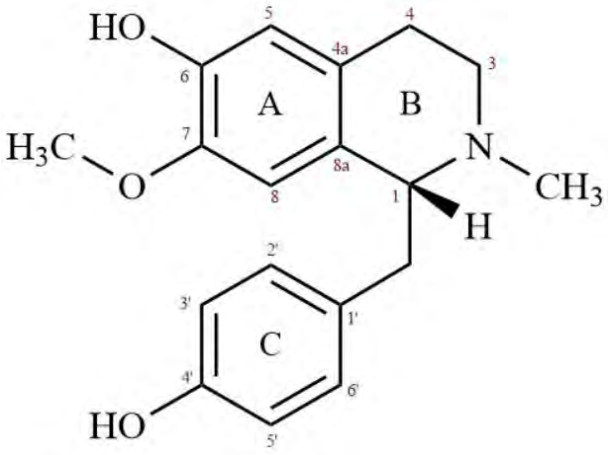

IUPAC:
(R)-1-(4-hydroxybenzyl)-7-methoxy-2-methyl-1,2,3,4-tetrahydroisoquinoline-6-ol)

Compound **1** was isolated as a light yellowish amorphous with $[\alpha]_D^{27}$ = +29.4° (c 1.0, α Methanol). A pseudomolecular ion peak at m/z 300.1573, $[M+H]^+$ was attained from the positive mode LCMS-IT-TOF spectrum (Figure 4.8) corresponded to the possible molecular formula of $C_{18}H_{21}NO_3$, with nine degrees of unsaturation. Strong absorption bands at 3370 (broad), 2890 (strong), 2257 (weak) and 1250 cm^{-1} from the IR spectrum (Figure 4.9) indicated the presence of O-H, C=C-H, C-N and C-O stretching, respectively. The characteristic UV adsorption peak of a benzyl isoquinoline moiety was observed at λ_{max} 302 nm (Custodio & Junior, 2014).

The ^{1}H NMR spectrum (Figure 4.10) has the basic pattern recognition of a benzylisoquinoline type revealing a total of twenty-one proton signals agreeing to the chemical formula $C_{18}H_{21}NO_3$. From the HSQC spectrum (Figure 4.14), two singlets representing three protons each at δ 2.42 and δ 3.78 could be assigned to *N*-CH_3 and 7-OCH_3 groups respectively. There were seven aliphatic protons in the region between δ 2.54 – 3.66 and a total of six aromatic protons located at the lower field region of the spectra. Looking at the aliphatic protons, the most deshielded one was H-1 because it is positioned vicinal to the N atom. Due to the electron withdrawing effect of the latter, H-

1 resonated at δ 3.66 (*t*, *J*= 6.8 Hz). The other adjacent proton to H-1, which is H-α_a appeared at δ 2.99 (*dd*, J_v= 2.88 Hz, J_g= 6.8 Hz) and δ 2.78 (*m*). The signal of H-α_b has overlapped with that of H-3b and H-4a at δ 2.74 as multiplets. Two of the aromatic protons, H-8 and H-5 appearing as two singlets at δ 6.31 and δ 6.47 suggested that they were located *para* to one another. Another four aromatic protons appeared at δ 6.59 (2H, *d*, *J*=8.5, H-3' and H-5') and δ 6.90 (2H, *d*, *J*=8.5, H-2' and H-6') as doublets. In fact, the correlation of vicinal protons H-α/H-α, H-2'/H-3', H-5'/H-6' and H-3/H-4 were observed in the COSY spectrum (Figure 4.13).

The ^{13}C NMR spectrum (Figure 4.11) supported the molecular formula deduced from the mass spectrum, accounting for all the eighteen carbons. DEPT-135 spectrum (Figure 4.12) exhibited one methoxyl, one *N*-methyl, three methylenes, seven methines, and six quaternary carbons. The signals at δ 55.86 and δ 46.66 were correlated to 7-OMe and *N*-Me, meanwhile, two overlapping signals appeared at δ 130.4 and δ 115.5 corresponded to C-2'/C-6' and C-3'/C-5' respectively. The HSQC spectrum (Figure 4.14) displayed the cross-peaks of H-5/C-5 and H-8/C-8 at δ_H 6.47/ δ_C 110.59 and δ_H 6.31/ δ_C 113.9 ppm respectively. The graphical correlation between the carbons and hydrogens observed in COSY and HMBC is depicted in Figure 4.7 below.

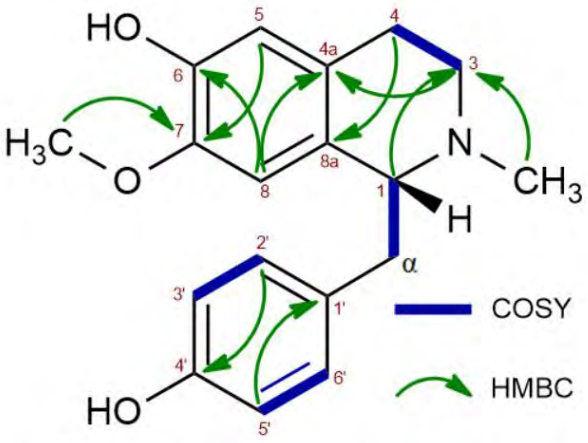

Figure 4.7: ^{1}H-^{1}H and ^{1}H-^{13}C correlations observed in COSY and HMBC spectra of **1**

The HMBC spectrum (Figure 4.15) revealed the correlation between C-7 and -OMe, C-4' to H-2' and H-6'. Another hydroxyl group positioned at C-6 was confirmed from the cross peaks between H-8 to C-6. The *N*-Me group showed strong correlation with C-3 and C-1. Long range ^{3}J coupling of H-5 to one of the C-4 protons is clearly seen in the HMBC spectrum. Thorough analysis from the combination of techniques has confirmed that compound **1** to be (+)-*N*-methylisococlaurine.

Table 4.3: NMR spectroscopy parameters and values of **1** (Nasrullah *et al.*, 2013).

	^{1}H NMR	**HSQC**	**DEPT-135**	**HMBC**	**Literature**
Position	**δ_H, pattern, *J* (Hz)**	**δ_C**	**Type ^{13}C**	**neighbor**	**δ_H , pattern**
1	3.6420, *t*, *J*= 6.8	64.8	(-CH)	4a , 3 , 8	3.63, *J*=6.5, *t*
3	H_a: 3.17-3.11, *m* H_b: 2.79-2.78, *m*	44.6	(-CH_2)	4a , 1	H_a= 3.01-2.96, *m* H_b=2.52-2.65, *m*
4	H_a: 2.79-2.78, *m* H_b: 2.54-2.52, *m*	24.7	(-CH_2)	8a , 5	H_a= 2.52-2.65, *m* H_b=2.25-2.40, *m*
4a	-	125.2	Q	1 , 3 , 6	-
5	6.4698, *s*	110.8	-CH	8a , 4 , 7	6.51, *s*
6	-	145.3	Q	4a , 8	-
7	-	143.5	Q	8a , 5	-
8	6.3055, *s*	113.9	-CH	4a , 1 , 8	6.29, *s*
8a	-	130.1	Q	4 , 5 , 7	-
α	**α_a**: 2.9915, *dd* J_v=8.0, J_g= 4.5 **α_b**: 2.74-2.71, *m*	40.8	-CH_2	8a, 2', 6'	α_a: 2.9715, *dd* α_b: 2.72-2.65, *m*
1'	-	131.1	Q	3' , 5'	-
2'	6.9004, *d*, J_o= 8.5	130.4	-CH	α , 4' , 6'	6.88, *d*
3'	6.5910, *d*, J_o= 8.5	115.5	-CH	1' , 5'	6.57, *d*
4'	-	154.6	Q	6 ' , 2'	-
5'	6.5910, *d*, J_o= 8.5	115.5	-CH	1' , 5'	6.54, *d*
6'	6.9004, *d*, J_o= 8.5	130.4	-CH	α , 6' , 4'	6.88, *d*
7OMe	3.7825, *s*	55.9	-CH_3	6 , 8	3.74, *s*
N–Me	2.4152, *s*	42.3	-CH_3	1 , 3	2.37, *s*

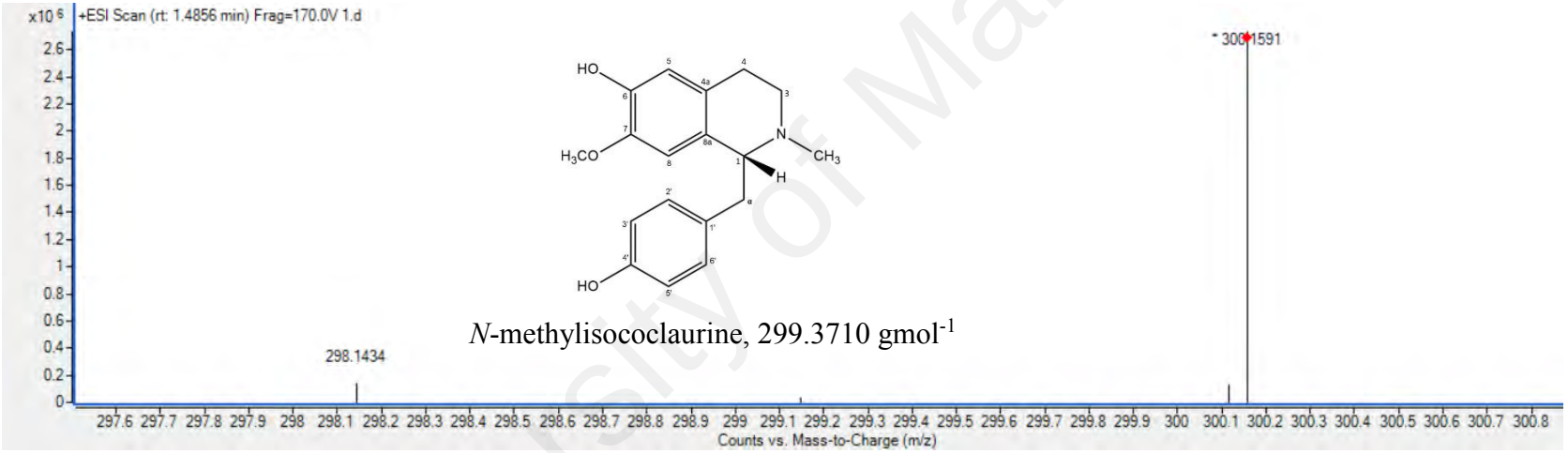

N-methylisococlaurine, 299.3710 gmol^{-1}

Figure 4.8: MS spectrum of **1** at *m/z* 300.1591.

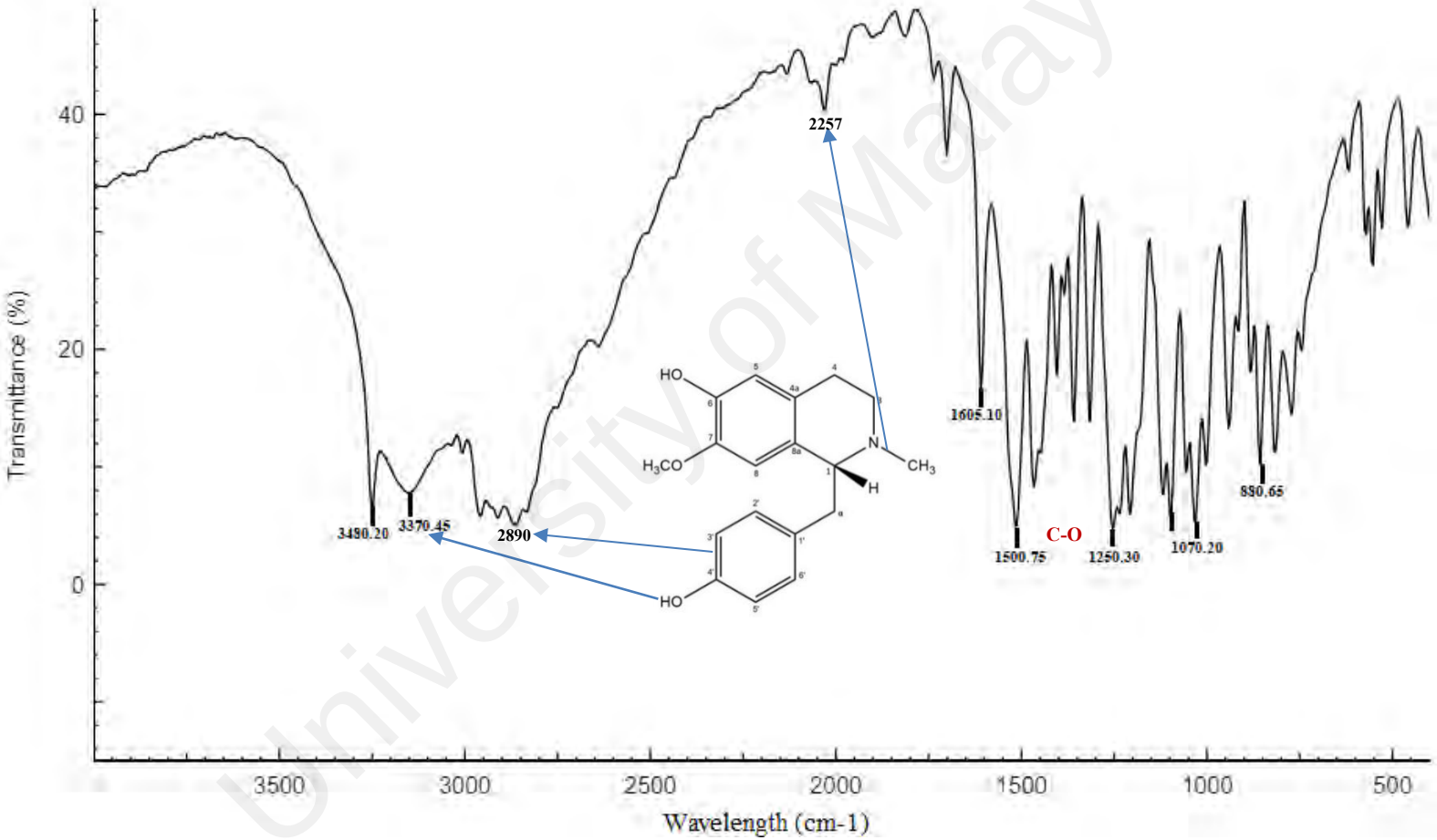

Figure 4.9: FTIR spectrum of **1**.

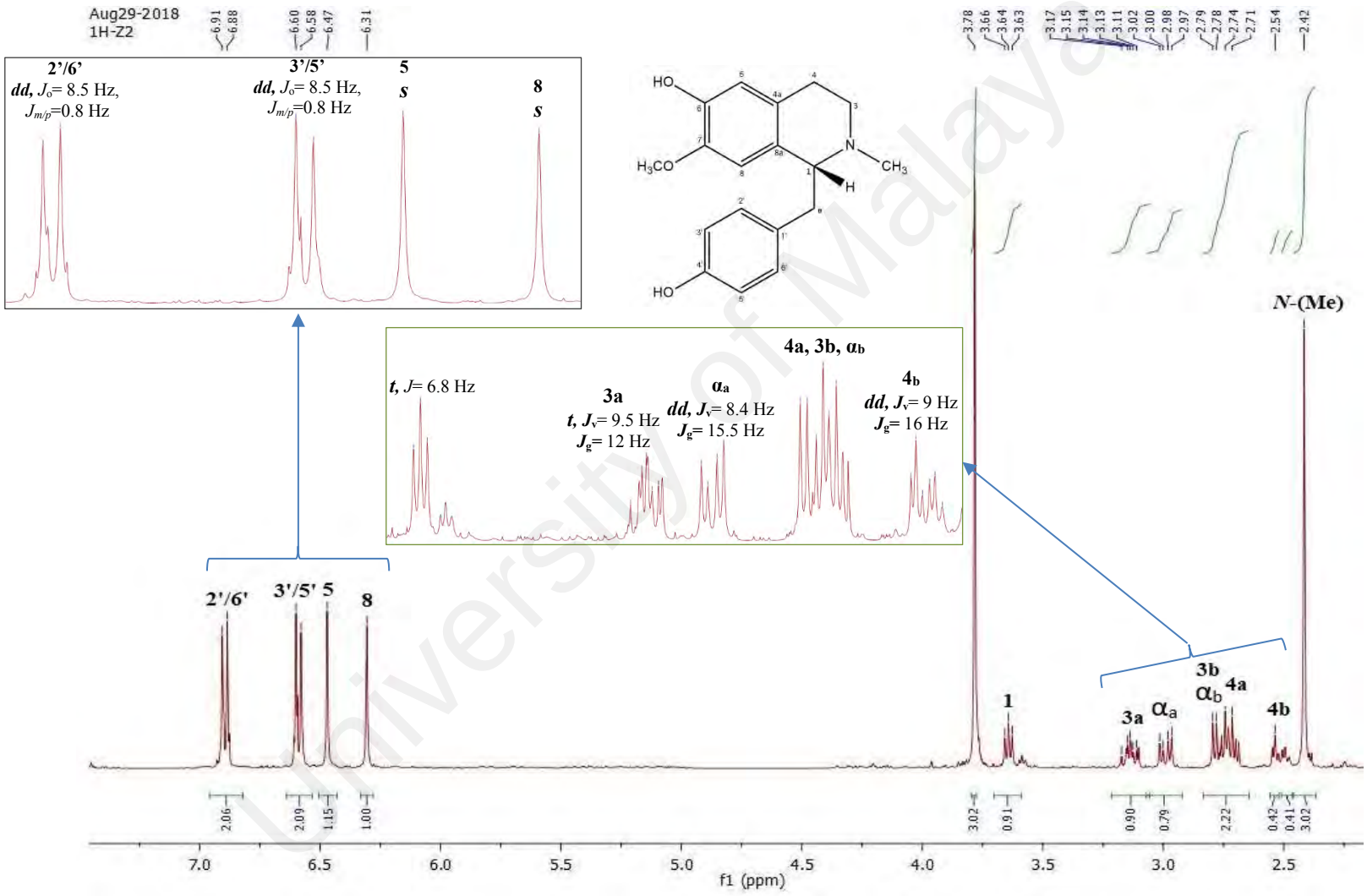

Figure 4.10: ^{1}H NMR spectrum of **1**.

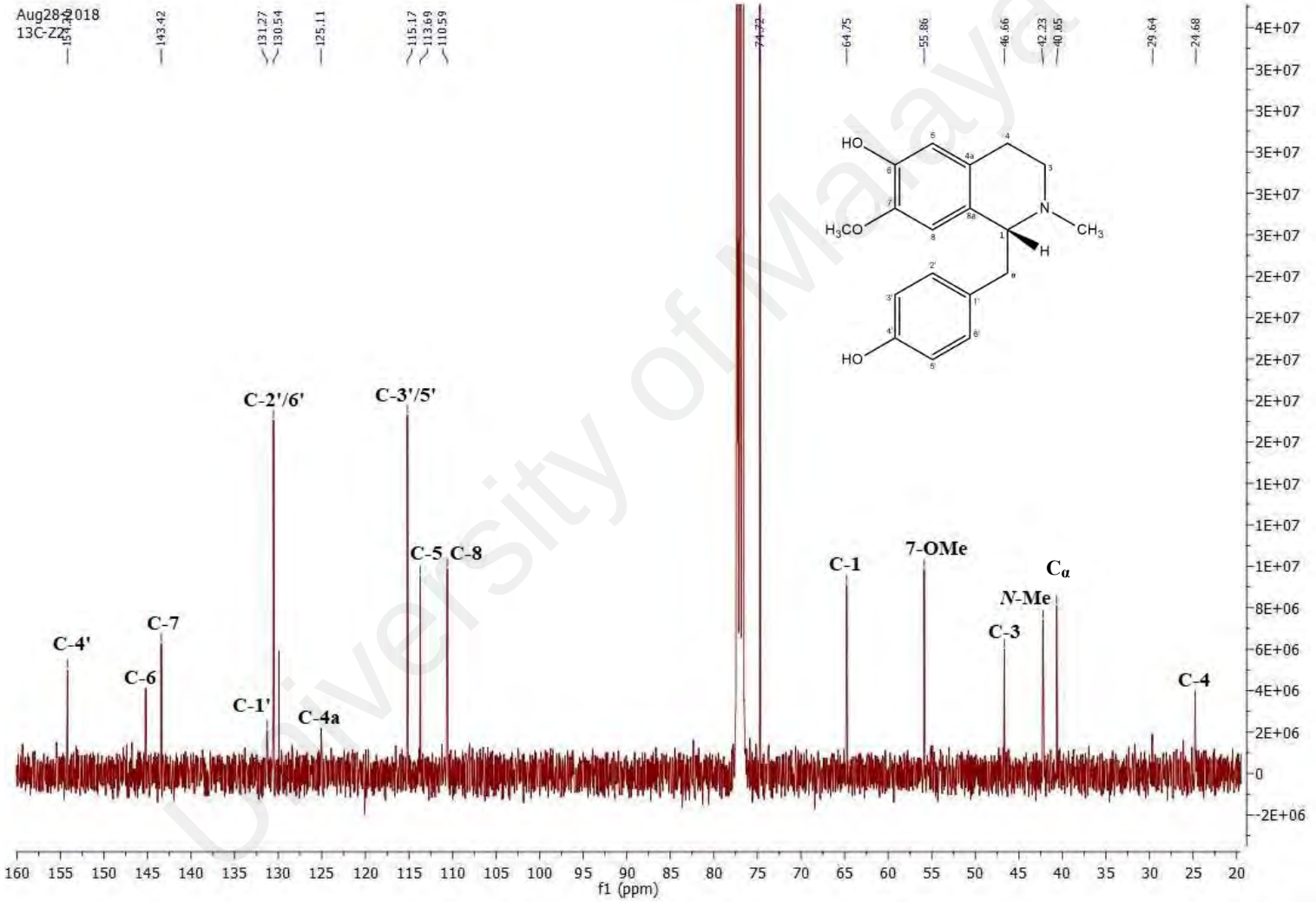

Figure 4.11: ^{13}C NMR spectrum of **1**.

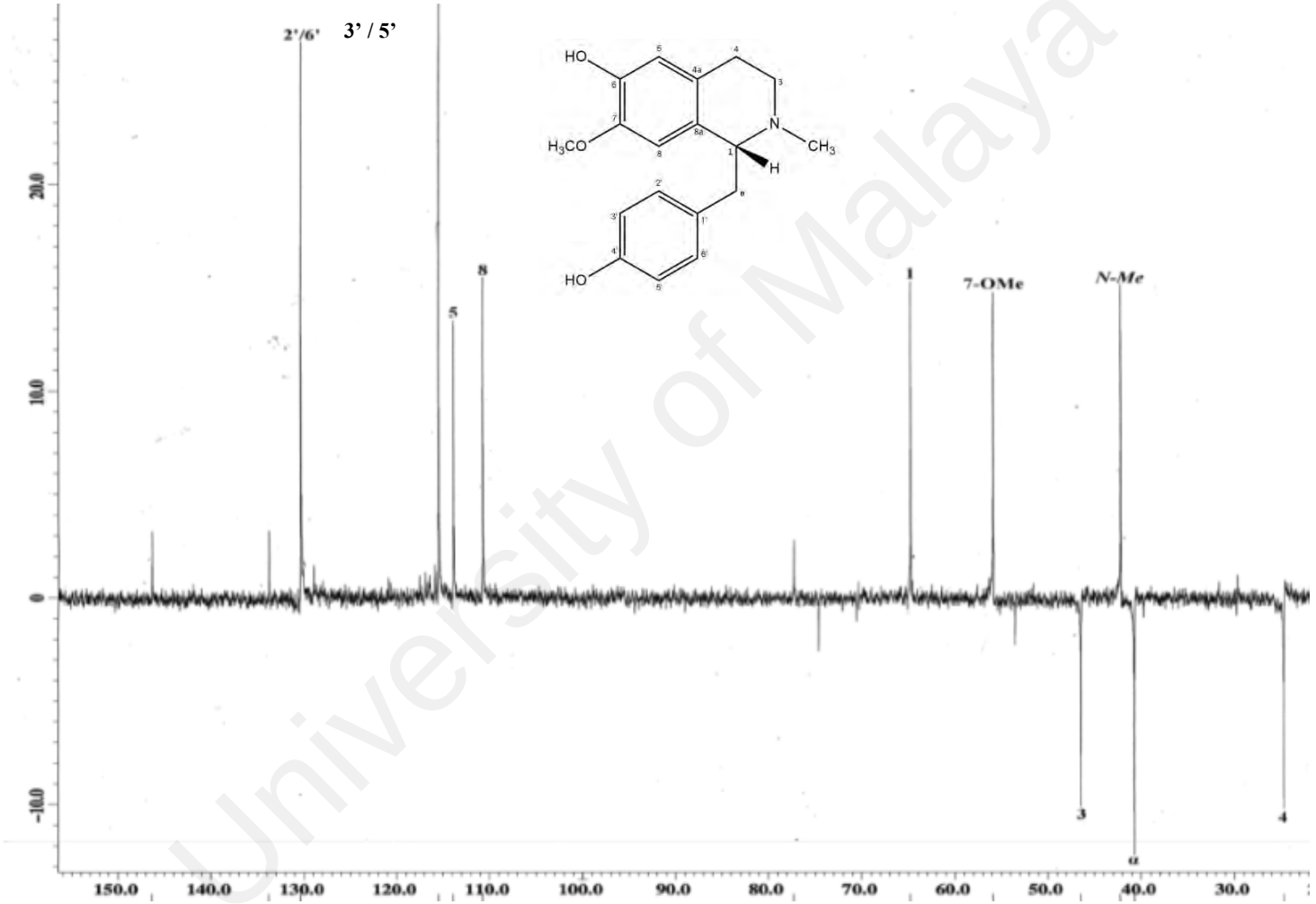

Figure 4.12: DEPT-135 spectrum of **1**.

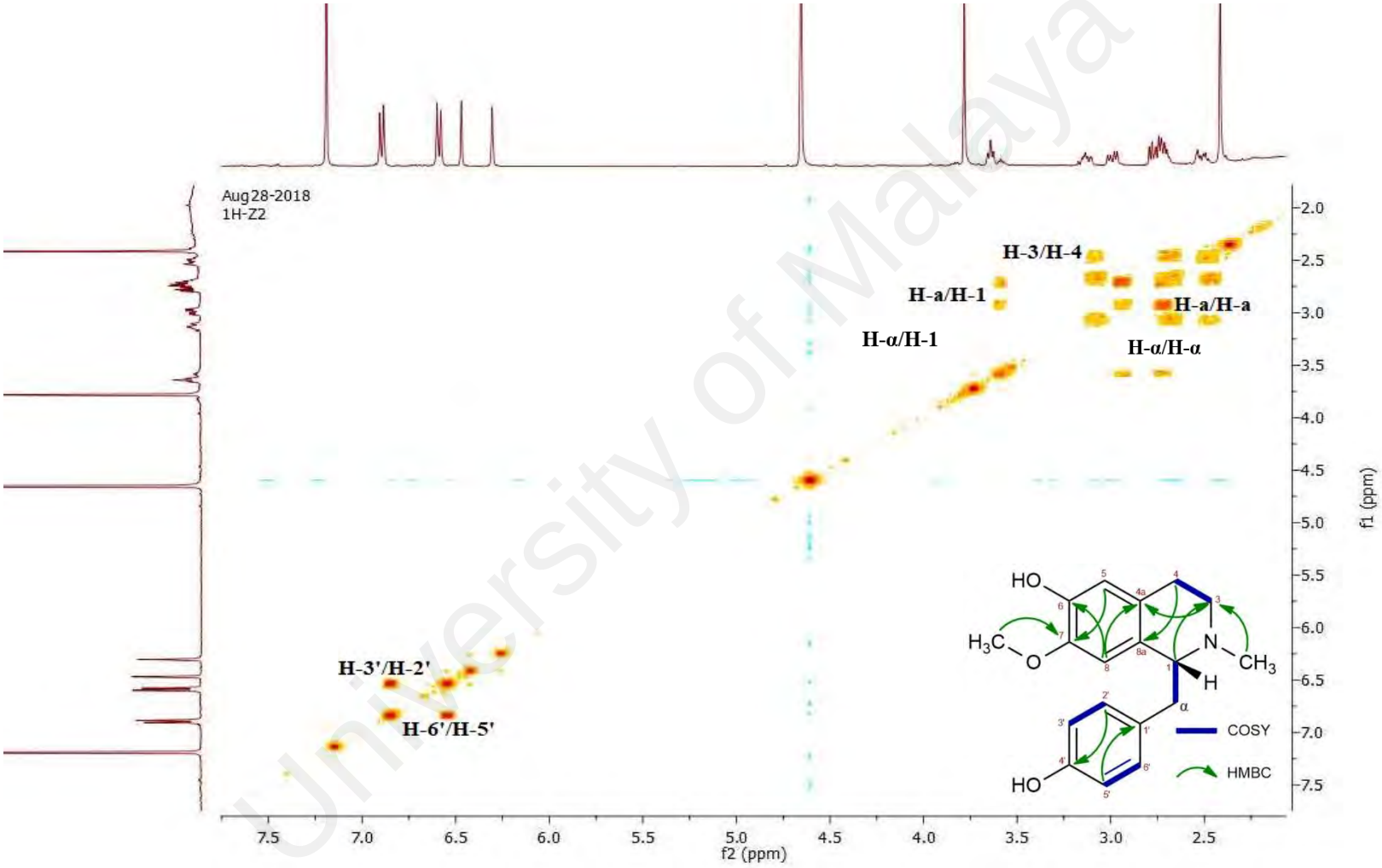

Figure 4.13: COSY spectrum of **1**.

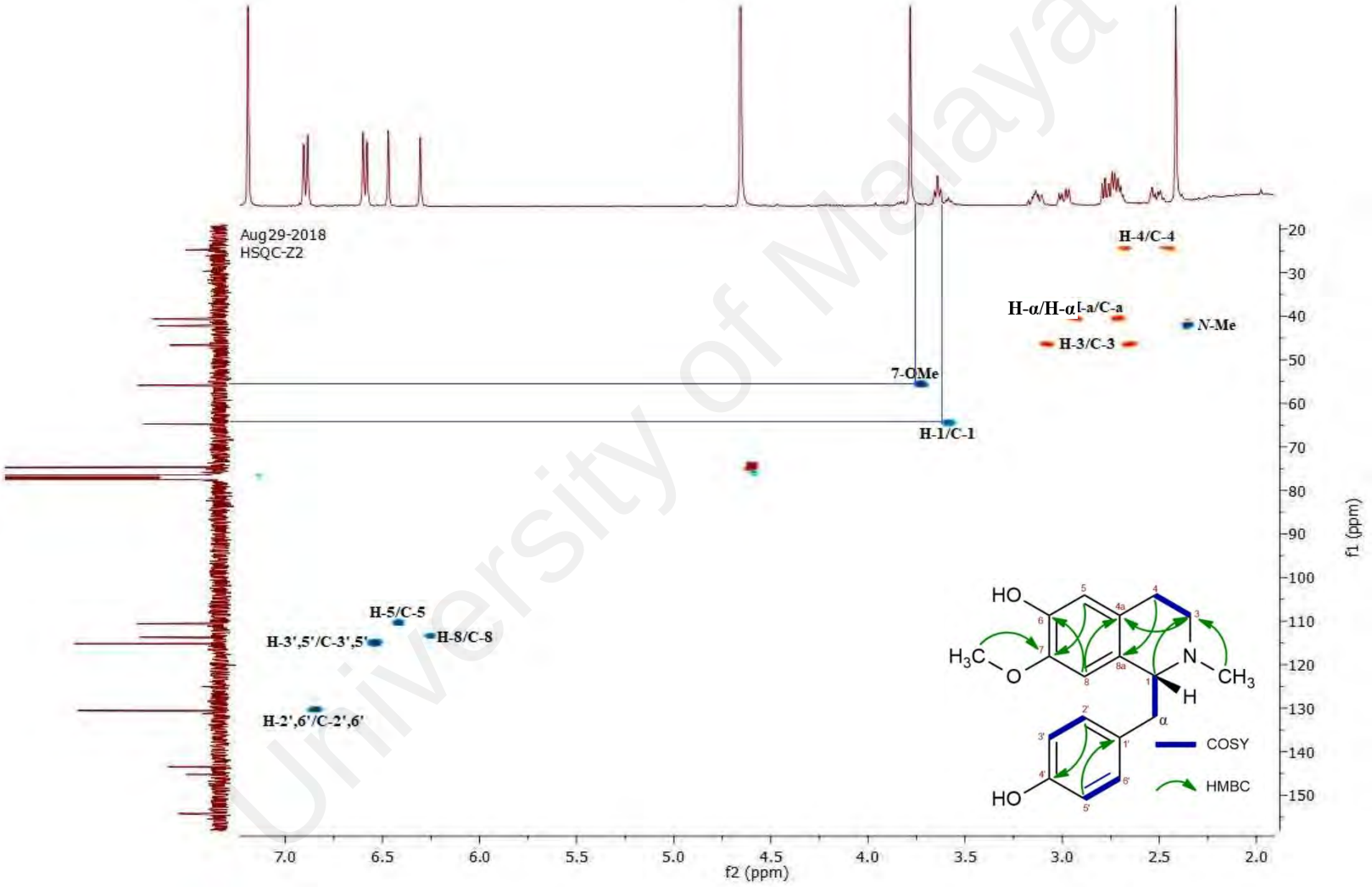

Figure 4.14: HSQC spectrum of **1**.

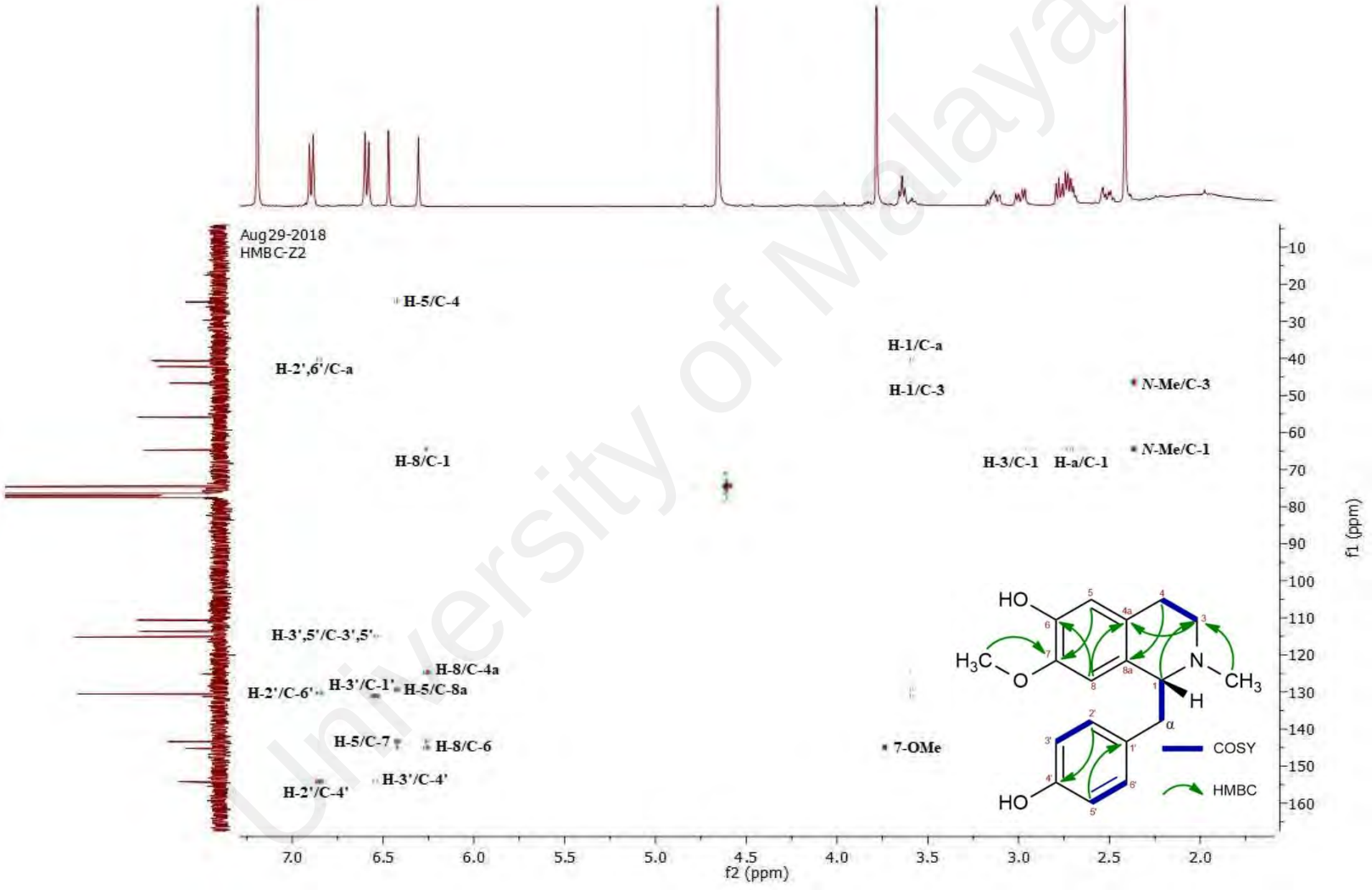

Figure 4.15: HMBC spectrum of **1**.

4.2.2 Atherosperminine *N*-oxide **2**

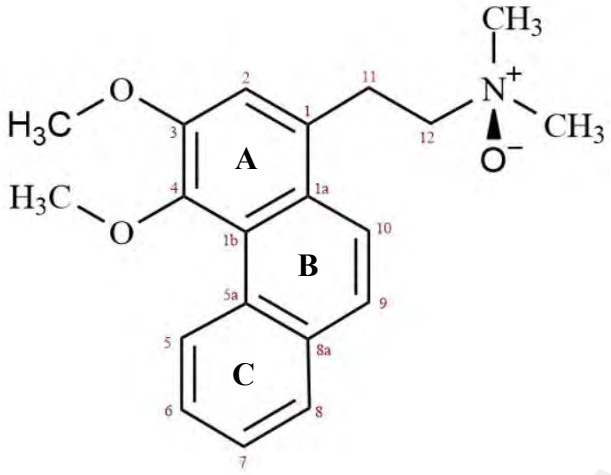

IUPAC: 2-(3,4-dimethoxyphenanthren-1-yl)-*N,N*-dimethylethanamine oxide

Compound **2** was isolated as an optically inactive brownish amorphous solid with $[\alpha]_D^{27}$= 0º (c 1.0, Methanol). LCMS-IT-TOF spectrum showed a pseudomolecular ion peak at m/z 326.1752 $[M+H]^+$ that is associated with the molecular formula $C_{20}H_{23}NO_3$ accounting for 10 degrees of unsaturation (Figure 4.17). The UV spectrum showed the presence of multiple absorption bands at 220, 310 and 344 nm typical for a phenanthrene type alkaloid (Wan *et al.*, 2016). The IR spectrum (Figure 4.18) displayed presence of strong vibrational bands at 2920 (C-H stretching), 2870 (=C-H stretching), 1620 and 1460 (C=C stretching), 1380 (N-O stretching), and 1255 (C-O stretching) cm^{-1} respectively.

The ^1H NMR spectrum (Figure 4.19) revealed an inclusive of twenty-three proton integrations, with sixteen protons in the higher region and seven aromatic protons at the lower region of the spectrum. The protons were arranged in an aporphine pattern. Expansion of the higher field region of the spectrum (Figure 4.20) showed two methoxyl groups, 4-OMe and 3-OMe resonated at δ 3.91 and δ 4.03, respectively. The dimethyl ammonium oxide O-*N*-$(Me)_2$ group was observed to form an intense resonance peak at δ 3.34, rather deshielded to where a dimethyl amino substituent should be. This case could be resulted from the attachment of oxygen on the nitrogen atom forming *N*-oxide,

indirectly causing the chemical shift to be resonating towards the lower field region. The quaternary ammonium group ($O\text{-}N^{+}\text{-}(CH_3)_2$) has less shielding effect due the absence of nitrogen lone pairs. Two identical triplet peaks at δ 3.57 and δ 3.78 could be attributed to the aliphatic protons H-12 and H-11, respectively. The ethylene substituent ($\text{-}CH_2\text{-}CH_2\text{-}$) are placed next to the quaternary nitrogen and thus deshielding them towards higher chemical environment.

Looking at the lower field region (Figure 4.21), a singlet peak resonated at δ 7.24 could be best assigned to H-2 due to its isolated position in ring A. H-8 and H-10 formed beautiful doublet of doublet signals at δ 7.86 (J_o= 16.8; Hz H-10/H-9 and H-8/H-7) and (J_m = 9.16 Hz; H-8/H-6) as they were *ortho*-connected to a single neighbouring proton in ring C and B, respectively. A distinctive doublet signal was observed at δ 9.66 corresponded to H-5 having coupling constants of J_o= 8.28 Hz with respect to the neighbouring *ortho* H-6. The COSY spectrum (Figure 4.25) confirmed the correlation between vicinal protons H-12/H-11, H-5/H-6, H-9/H-10 and H-7/H-8.

The ^{13}C NMR spectrum (Figure 4.22) showed twenty carbon peaks hence establishing the molecular formula $C_{20}H_{23}NO_2$. It has one dimethyl ammonium oxide, two methoxyl, two methylenes, seven methines and seven quaternary carbon signals. The methylene carbons, C-11 and C-12 could be assigned to signals at δ 27.97 and δ 71.13 as they showed inverted resonation in DEPT-135 spectrum (Figure 4.24). The two methyl groups on the quaternary *N*-oxide has a slightly higher carbon resonance peak at δ 58.72 due to their chemically deshielded environment. The other carbon signals in the lower field region of the spectrum representing all the aromatic and quaternary carbons were described precisely in (Figure 4.23). The graphical representation for the proton-carbon short range (^1J) and long range (^3J) correlations is shown in Figure 4.16 below.

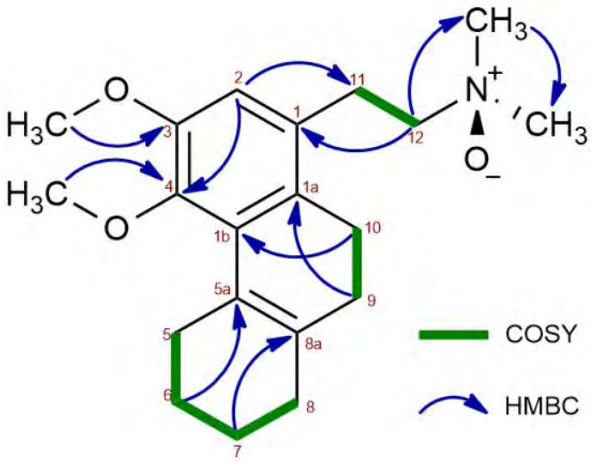

Figure 4.16: ^{1}H-^{1}H and ^{1}H-^{13}C correlations observed in COSY and HMBC spectra of **2**.

The 2D-NMR experiments; HSQC and HMBC (Figure 4.5 and Figure 4.6) allowed us to assign the protons to their respective carbons at high accuracy. The complete assignments for all the proton and carbon signals assured that compound **2** is atherosperminine-*N*-oxide. Their spectroscopic values are tabulated in Table 4.4.

Table 4.4: NMR Spectroscopy parameters and values of **2** (Lu, Wu *et al.*, 1985; Wu, Kao *et al.*, 1990).

	^{1}H NMR	**HSQC**	**DEPT-135**	**HMBC**	**Literature**
Position	**δ_H, pattern, *J* (Hz)**	**δ_C**	**Type ^{13}C**	**neighbor**	**δ_H, pattern**
1	-	130.01	Q	3, 12, 1b, 10	-
1a	-	125.46	Q	2, 4, 5a, 11	-
1b	-	126.10	Q	3, 1, 8a, 10	-
2	7.3320, *s*	115.42	CH	1a, 4, 11	7.35, *s*
3	-	151.02	Q	3-OMe	-
4	-	146.63	Q	4-OMe	-
5	9.6554, *d*, J_o=8.28	128.27	CH	1b, 8a, 7	9.67, *m*
5a	-	132.71	Q	6, 8, 9, 1a, 4	-
6	7.5922-7.6644, *m*	126.81	CH	5a, 8	7.56-7.64, *m*
7	7.5922-7.6644, *m*	126.81	CH	5, 8a	7.56-7.64, *m*
8	7.8689, *dd*, J_o= 16.8, J_m= 9.2	128.09	8	6, 5a, 9	7.84-7.86, *dd*,

8a	-	129.38	Q	5, 7, 10, 1b	-
9	7.5922-7.6644, *m*	126.52	CH	1a, 5a, 8	7.56-7.64, *m*
10	7.8689, *dd*, J_o= 16.8, J_m= 9.2	121.61	CH	1, 1b, 8a	7.86, *d*
11	3.7828, *t*, J_v= 7.9, J_g= 16.6	27.97	(-CH_2)	2, 1a	3.26-3.34, *m*
12	3.5724, *t*, J_v= 7.8, J_g= 16.0	71.13	(-CH_2)	1, *N*-Me	2.65-2.70, *m*
3 –OMe	4.0295, *s*	56.67	CH_3	3	4.04, *s*
4 – OMe	3.9191, *s*	59.82	CH_3	4	3.92, *s*
O-N^+-$(Me)_2$	3.3357, *s*	58.72	CH_3	12. *N*-Me	2.41, *s*

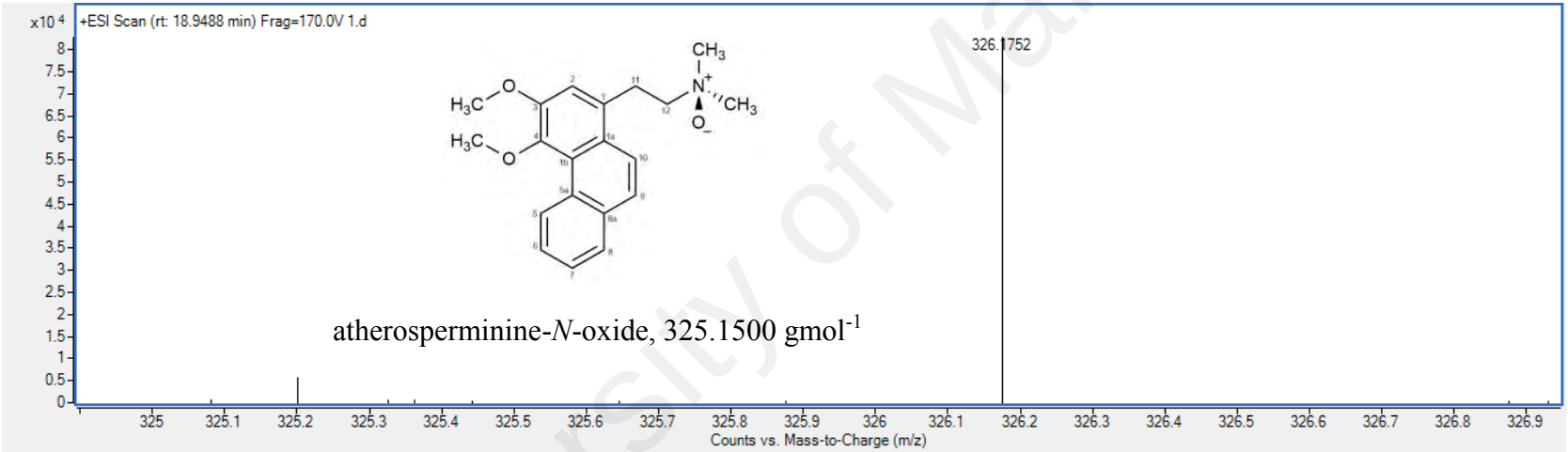

Figure 4.17: MS spectrum of **2**.

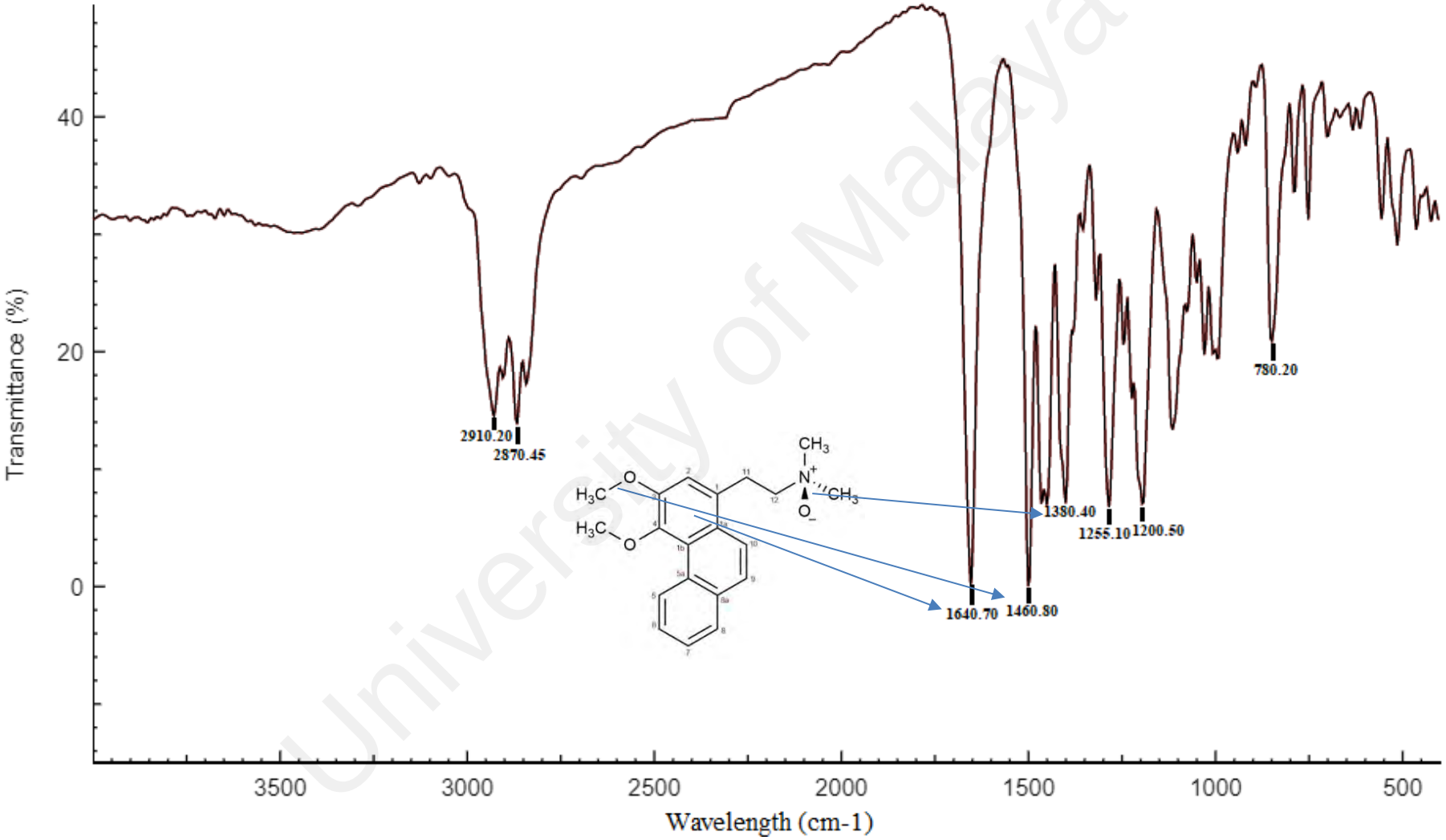

Figure 4.18: FTIR spectrum of **2**.

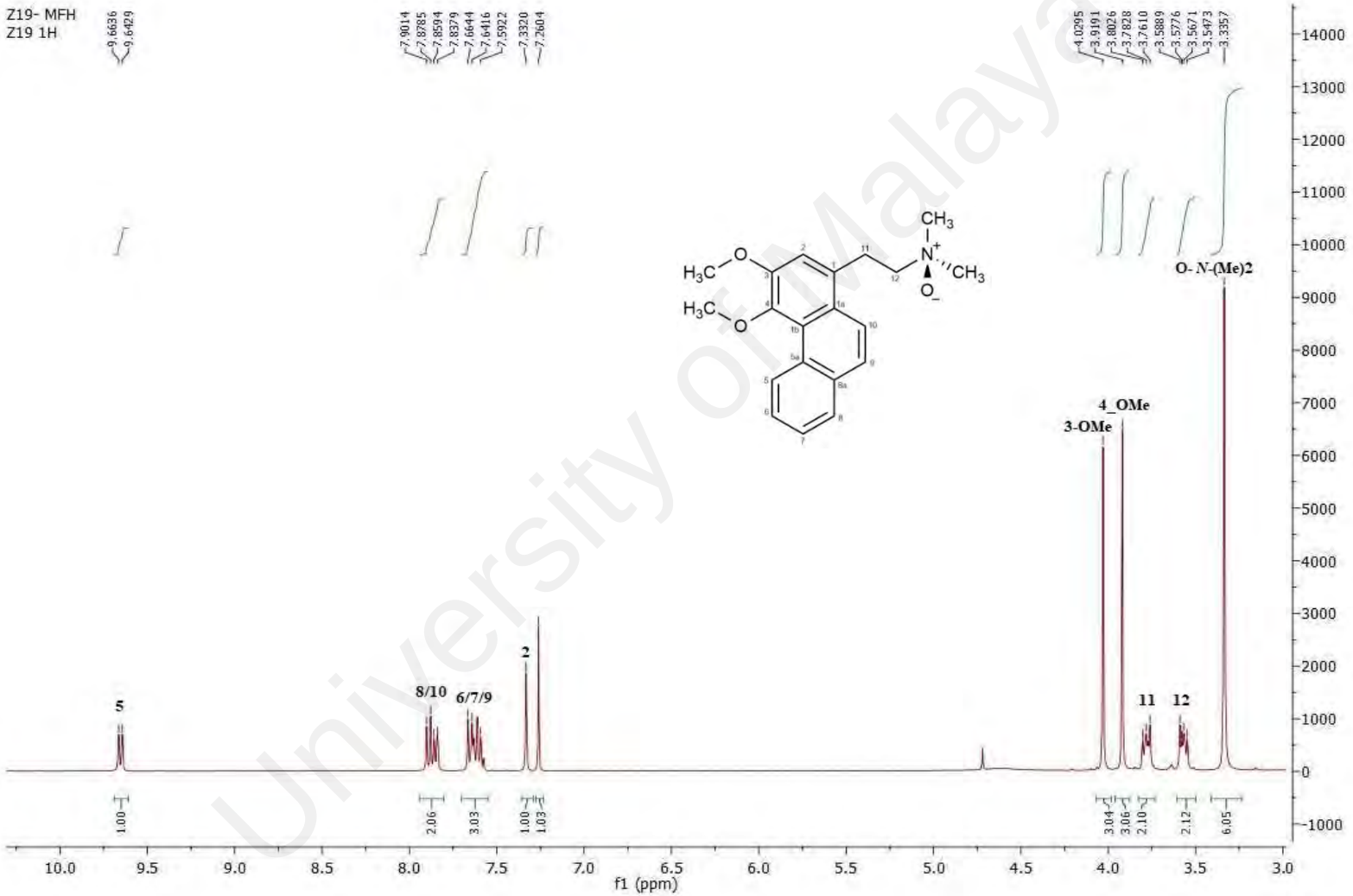

Figure 4.19: ^{1}H NMR spectrum of **2**.

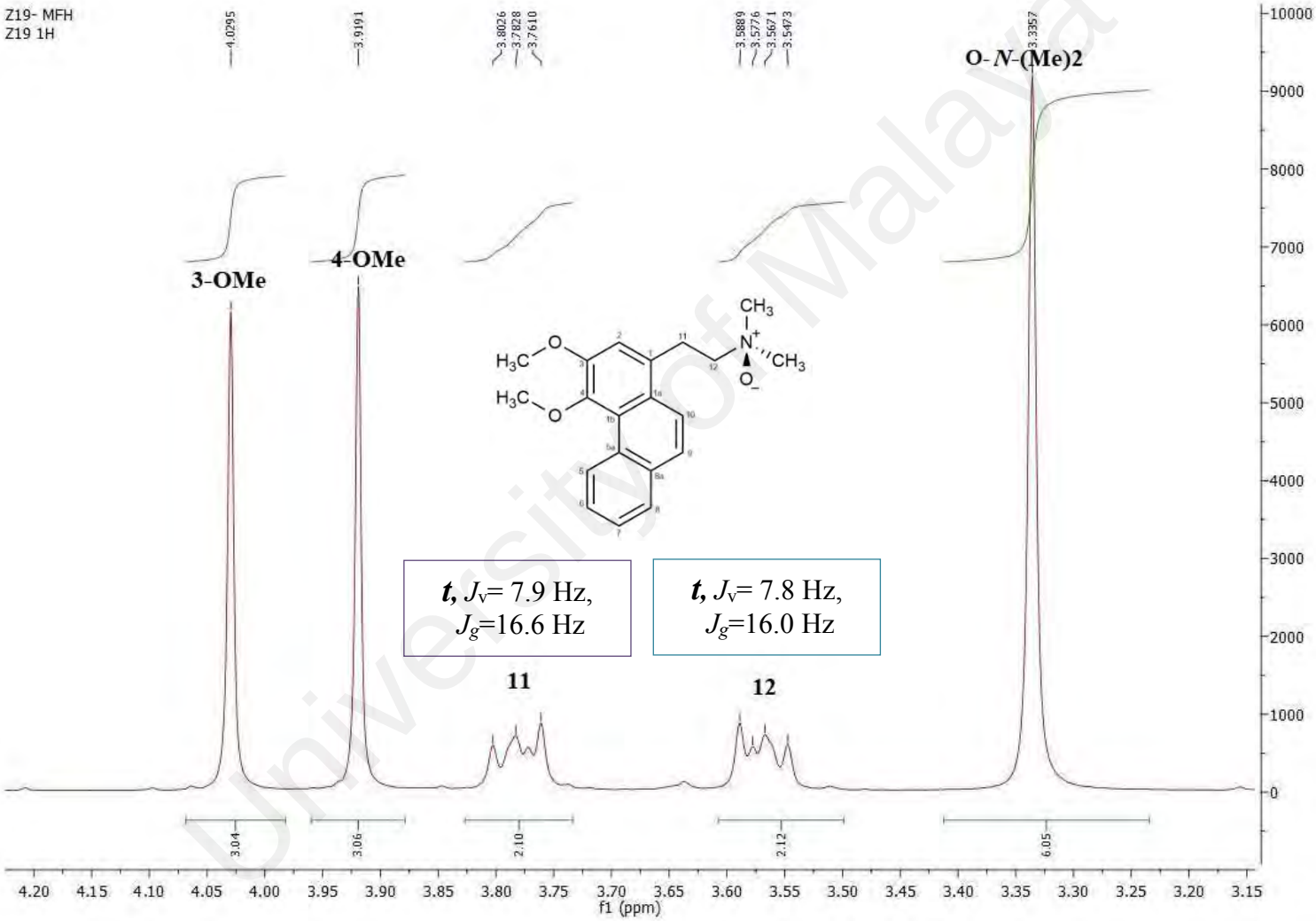

Figure 4.20: ^{1}H NMR spectrum of **2** (δ 3.15 – δ 4.20).

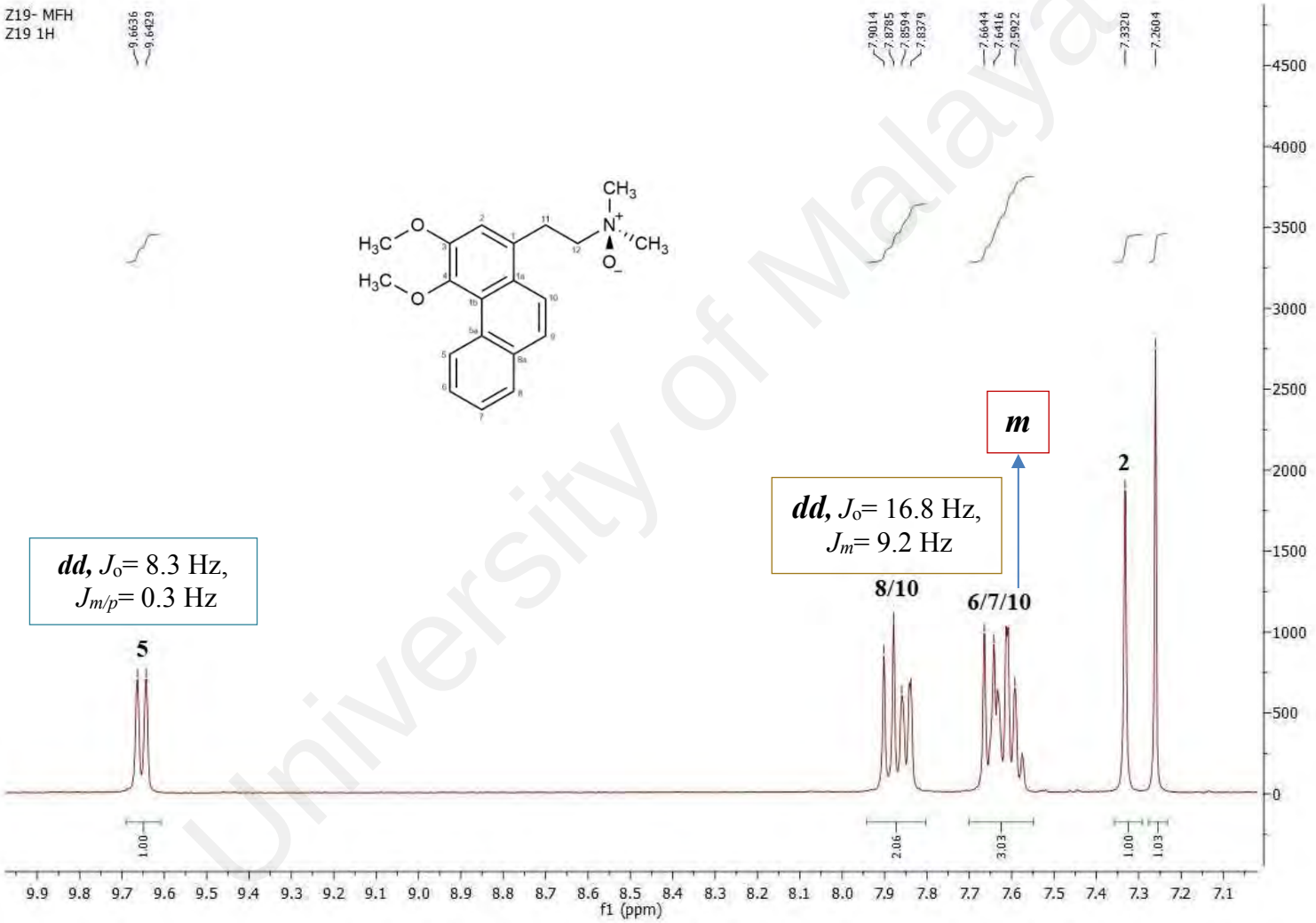

Figure 4.21: ^{1}H NMR spectrum of **2** (δ 7.10 – δ 9.90).

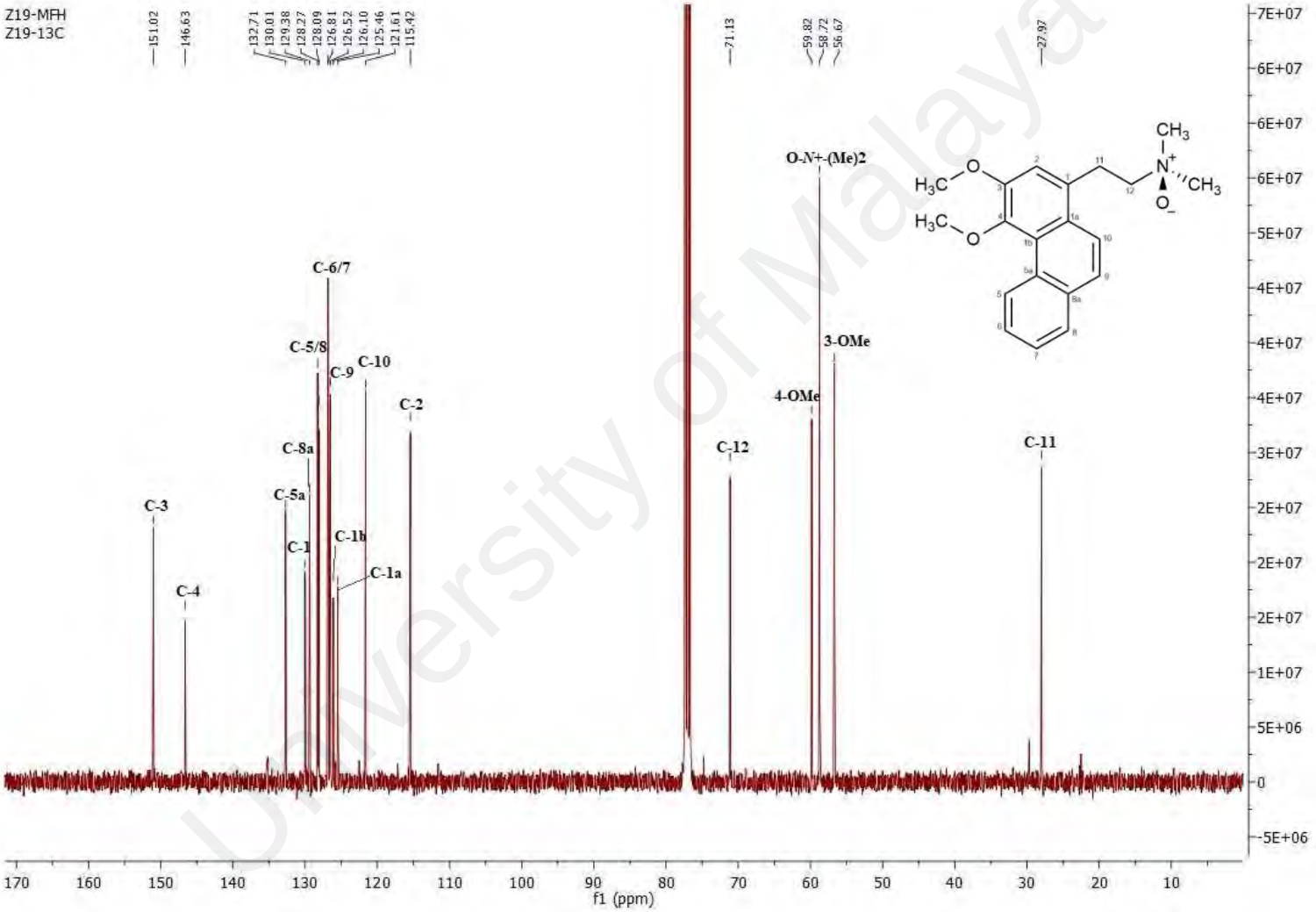

Figure 4.22: ^{13}C NMR spectrum of **2**.

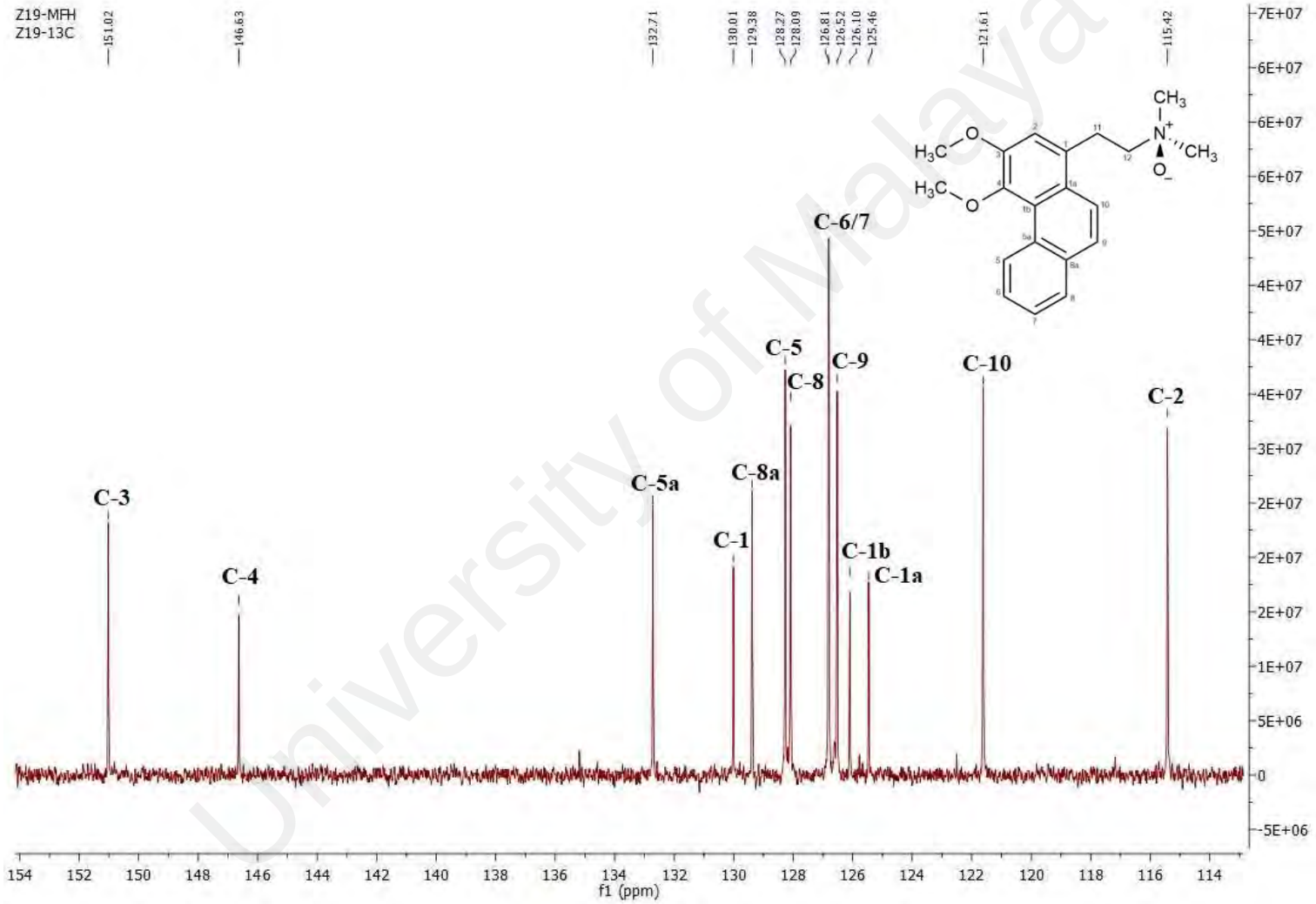

Figure 4.23: ^{13}C NMR spectrum of **2** (δ 114 – δ 155).

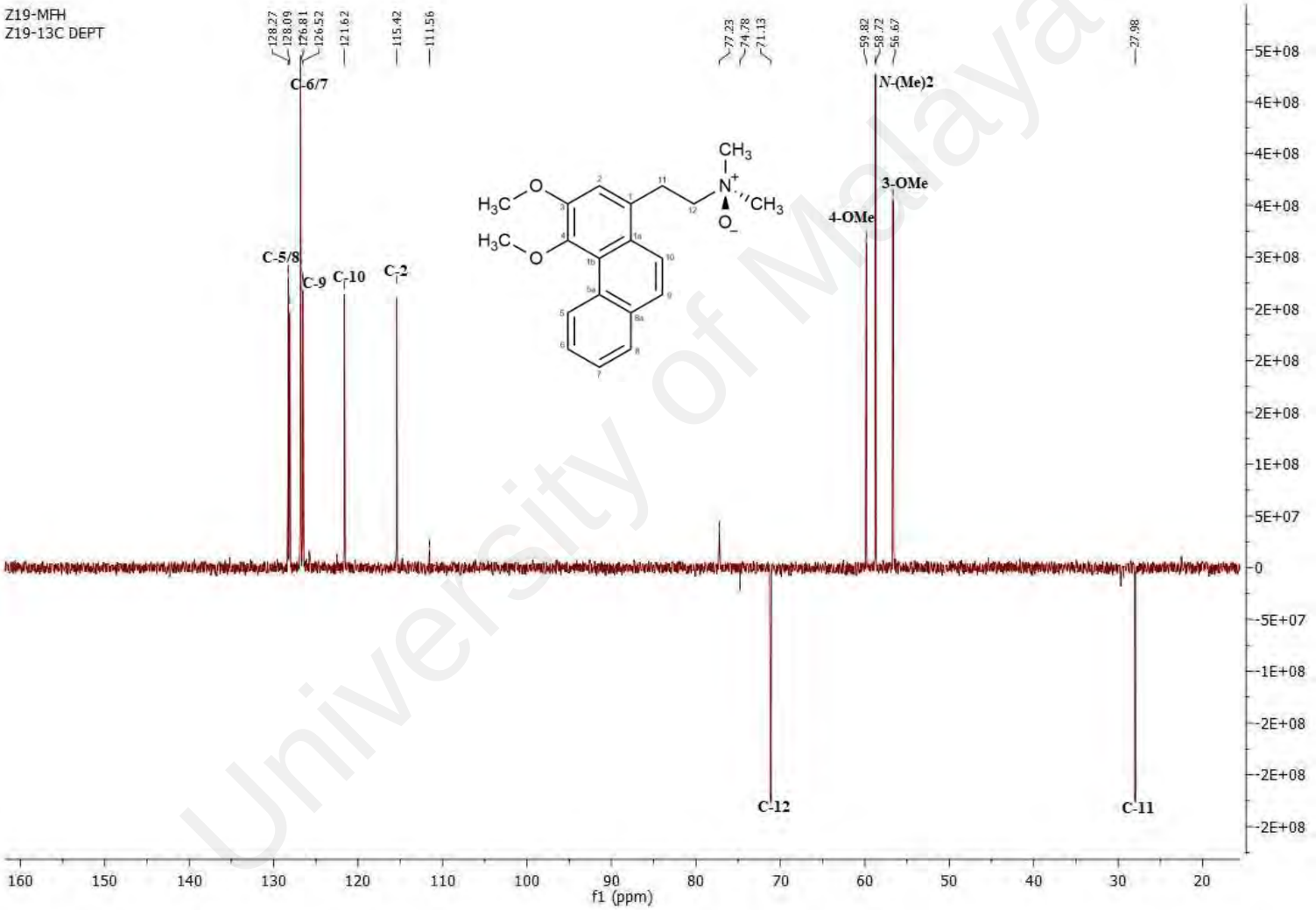

Figure 4.24: DEPT-135 spectrum of **2.**

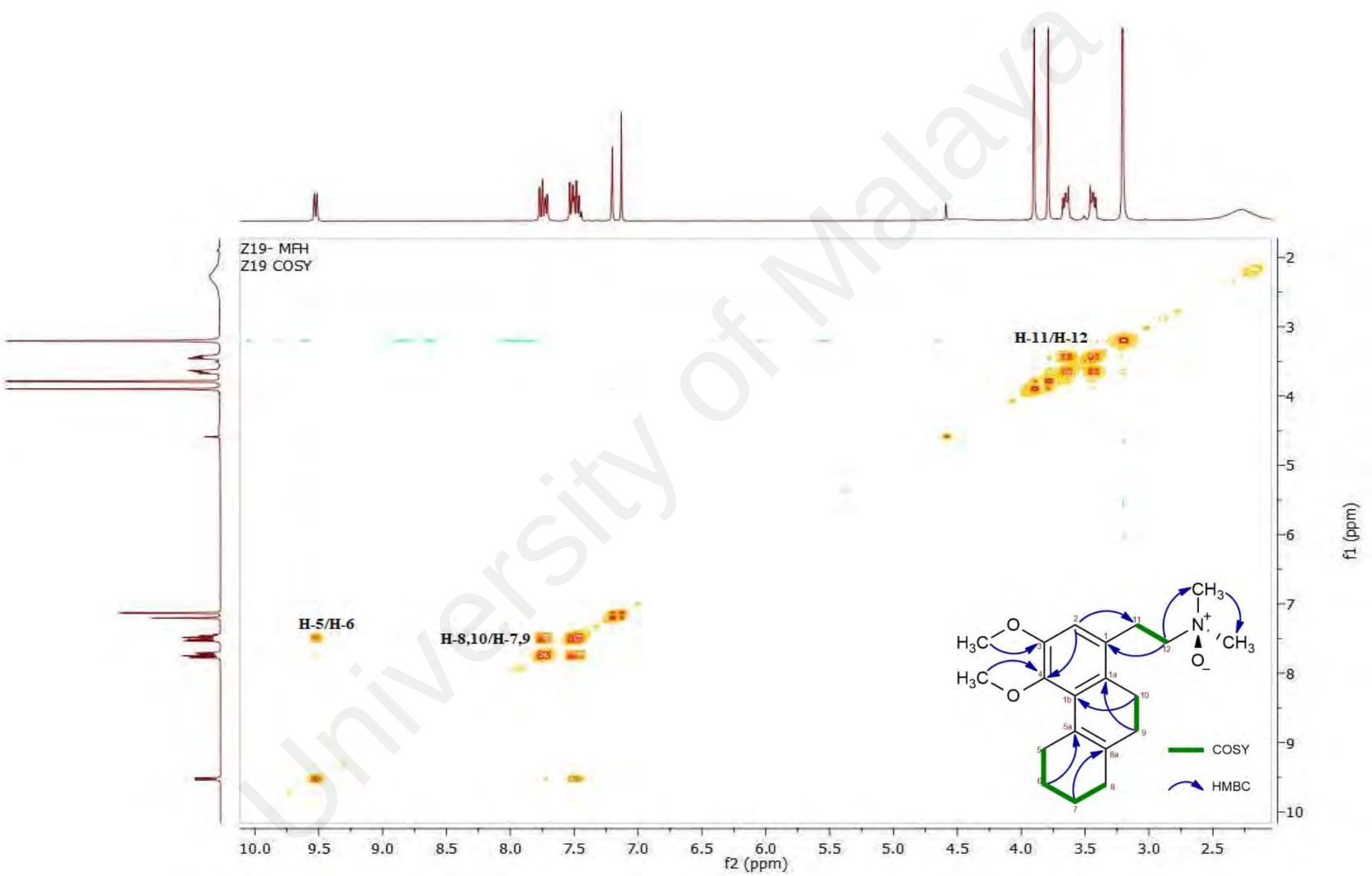

Figure 4.25: COSY spectrum of **2**.

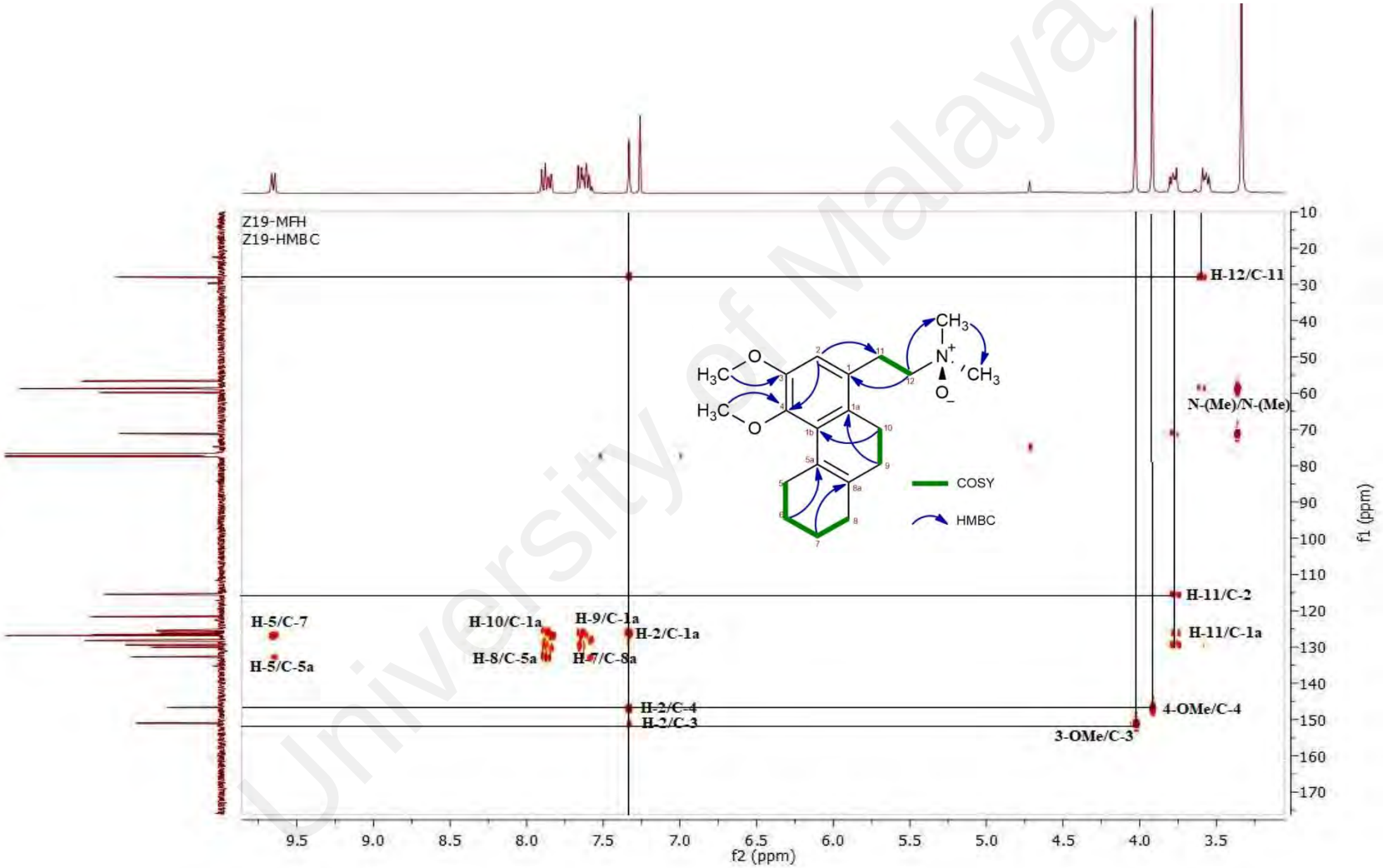

Figure 4.26: HSQC spectrum of **2**.

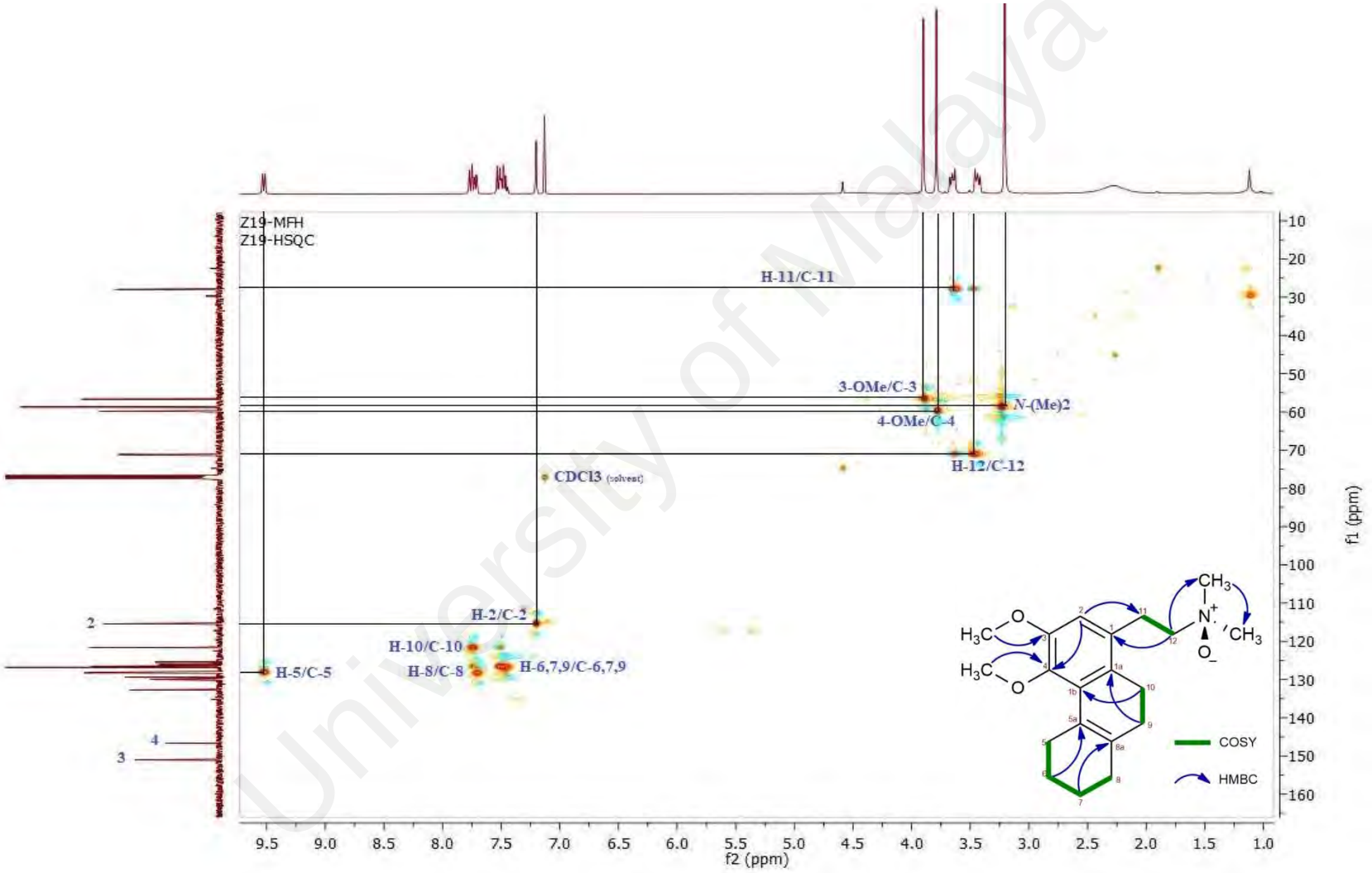

Figure 4.27: HMBC spectrum of **2**.

4.2.3 Atherosperminine **3**

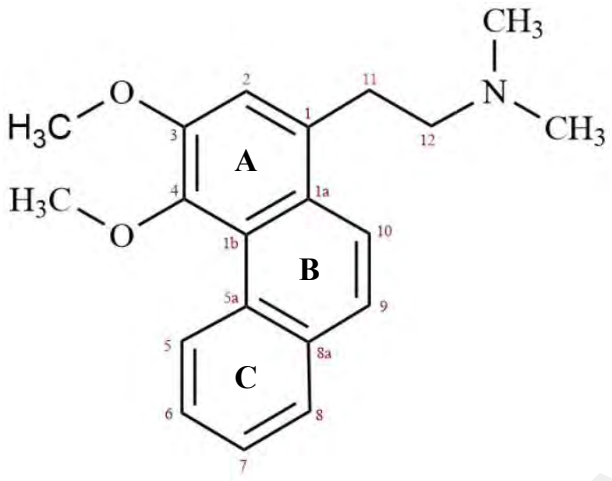

IUPAC: 2-(3,4-dimethoxyphenanthrene-1-yl)-*N, N*-dimethylethanamine

Compound **3** was isolated as an optically inactive brownish amorphous solid with $[\alpha]_D^{27}$= 0° (c 1.0, Methanol). A pseudomolecular ion peak at m/z 310.1802 $[M+H]^+$ was retrieved from the LCMS-IT-TOF spectrum (Figure 4.29). This mass was associated with the molecular formula of $C_{20}H_{23}NO_2$ with 10 degrees of unsaturation. The UV spectrum showed the presence of multiple absorption bands at 220, 227, 306 and 344 nm like that of compound **2**. The IR spectrum (Figure 4.30) of this alkaloid evidenced strong vibrational bands at 2917 (C-H stretching), 2849 (=C-H stretching), 2362 (C-N stretching), 1604 and 1512 (C=C stretching), and 1223 (C-O stretching) cm^{-1} respectively. However, unlike compound **2,** no noticeable IR peaks were seen at the region of 1300~1400 cm^{-1}, indicating the absence of N-O stretching.

The ^1H NMR spectrum (Figure 4.31) displayed a summation of twenty-three protons that match to a typical phenanthrene alkaloid. Two methoxyl groups, 4-OMe and 3-OMe resonated at δ 3.92 and δ 4.04 while the *N*-$(Me)_2$ peak resonated at δ 2.42. The two identical triplet peaks at δ 2.71 and δ 3.32 were attributed to the aliphatic protons H-12 and H-11, respectively. The protons at the high field region of compound **3** have lower chemical shifts as compared to compound **2.** All other protons in the low field region

appeared to be similarly arranged. The COSY spectrum (Figure 4.34) exhibited the vicinal proton correlations of H-12/H-11, H-5/H-6, H-9/H-10 and H-7/H-8. There were twenty carbon peaks seen from the ^{13}C NMR spectrum (Figure 4.32) with one *N*-$(Me)_2$, two methoxyl, two methylenes, seven methines and seven quaternary carbon signals. The methylene carbons, C-11 and C-12 could be typically observed at δ 32.43 and δ 60.93 further verified by the -CH_2 signals developed from DEPT-135 spectrum (Figure 4.33). It was also observed that the *N*-$(Me)_2$ peak appeared at a lower chemical shift of δ 45.38 rather than what was in ^{13}C spectrum of compound **2**. The other proton-carbon cross peaks are described precisely in the 2D-NMR experiments (Figure 4.35 and Figure 4.36) and shown graphically in Figure 4.28 below. Complete assignments for all the proton and carbon correlations have confirmed that compound **3** as atherosperminine. Their spectroscopic values are specified in Table 4.5.

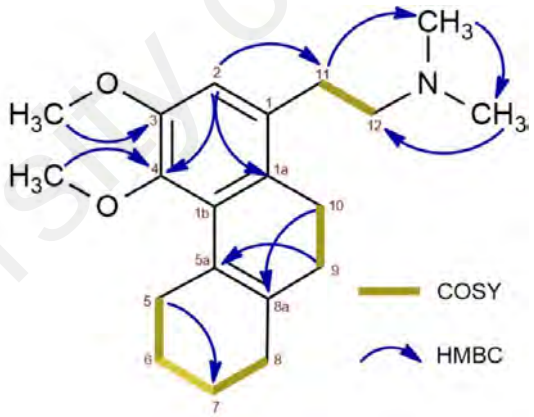

Figure 4.28: ^{1}H-^{1}H and ^{1}H-^{13}C correlation observed in COSY and HMBC spectra of **3.**

Table 4.5: NMR Spectroscopy parameters and values of **3** (Nasrullah *et al.*, 2013; Y.-C. Wu *et al.*, 1990).

	^{1}H NMR	HSQC	DEPT-135	HMBC	Literature
Position	**δ_H, pattern, *J* (Hz)**	**δ_C**	**Type ^{13}C**	**neighbor**	**δ_H, pattern**
1	-	130.10	Q	3, 1b, 10	-
1a	-	125.21	Q	2, 5a, 11	-
1b	-	126.10	Q	1, 5, 8a	-
2	7.2389, *s*	114.80	CH	1a, 4, 11	7.25, *s*
3	-	150.86	Q	1b, 3-OMe	-
4	-	145.97	Q	1a, 4-OMe	-
5	9.6596, *d*, J_o=8.4	128.12	CH	1b, 8a, 7	9.67, *m*
5a	-	132.78	Q	6, 8, 9, 1a	-
6	7.5615-7.6337, *m*	126.56	CH	5a, 8	7.56-7.64, *m*
7	7.5615-7.6337, *m*	126.56	CH	5, 8a	7.56-7.64, *m*
8	7.8347-7.8665, *m*	128.12	8	6, 5a, 9	7.84-7.86, *dd*, J_1= 7.3, J_2= 2.0
8a	-	133.02	Q	5, 10, 1b	-
9	7.5615-7.6337, *m*	125.75	CH	1a, 5a, 8	7.56-7.64, *m*
10	7.8347-7.8665, *m*	122.50	CH	1, 1b, 8a	7.86, *d*, J=9.3
11	3.2954, *t*, J_v= 8.0, J_o= 16.5	32.43	(-CH_2)	2, 1a	3.26-3.34, *m*
12	2.6921, *t*, J_v= 7.8, J_o= 16.0	60.93	(-CH_2)	1, *N*-Me	2.65-2.70, *m*
3 –OMe	4.0380, *s*	56.60	CH_3	3	4.04, *s*
4 – OMe	3.9158, *s*	59.90	CH_3	4	3.92, *s*
N-$(Me)_2$	2.4167, *s*	45.38	CH_3	11, 12	2.41, *s*

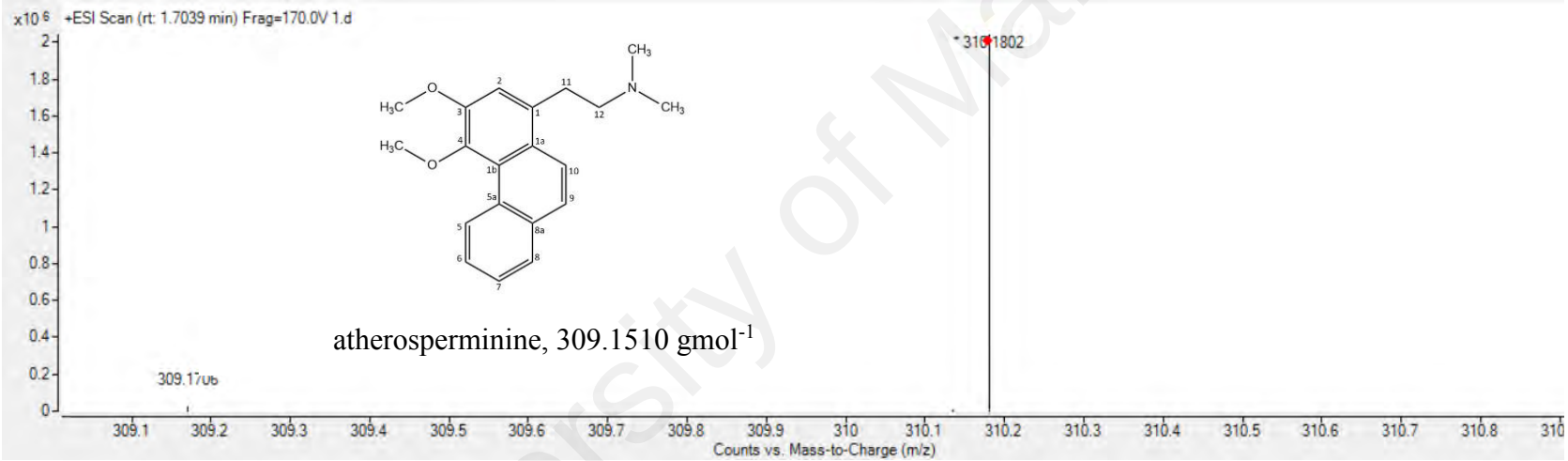

Figure 4.29: MS spectrum of **3** at *m/z* 310.1802.

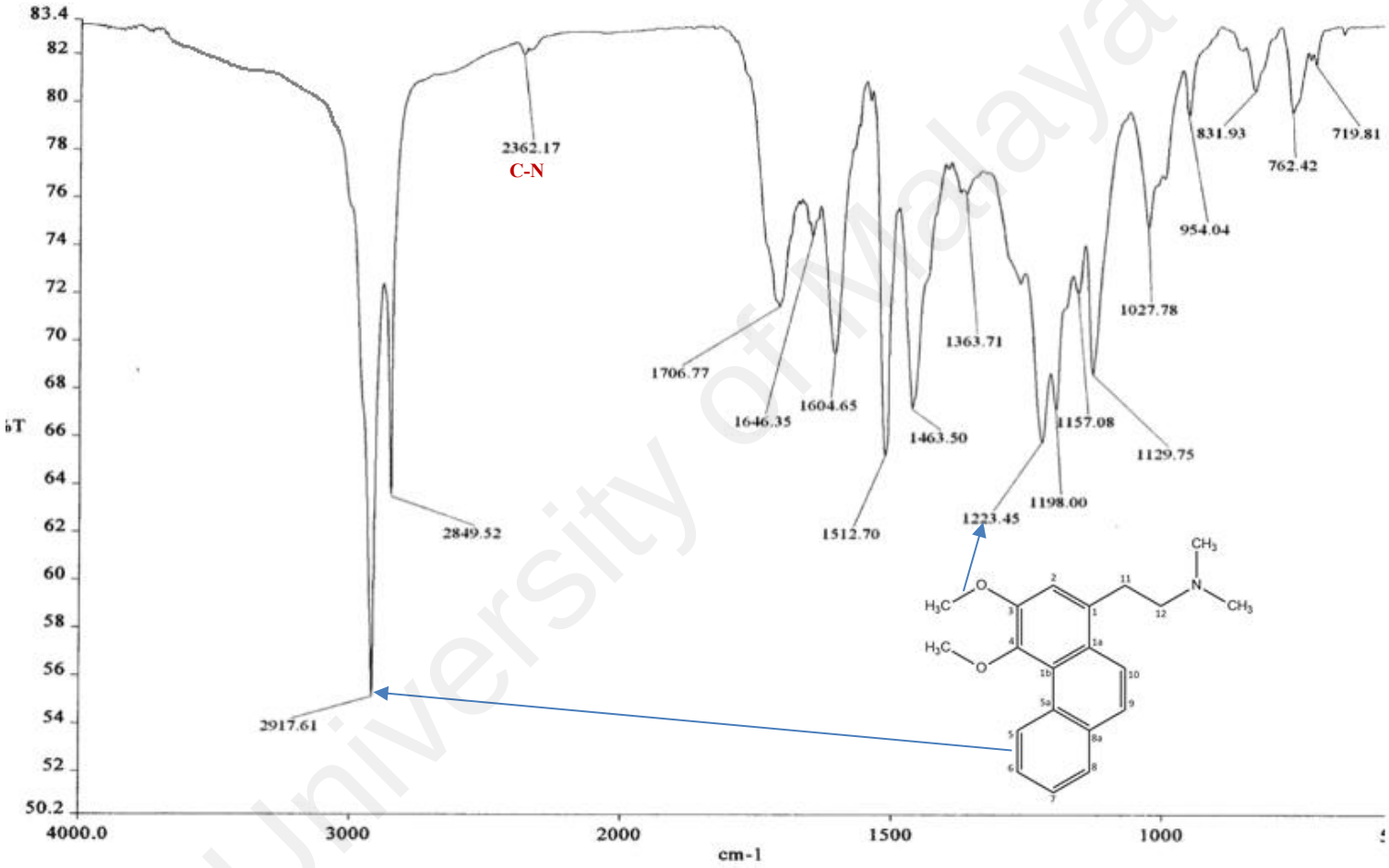

Figure 4.30: FTIR spectrum of **3**.

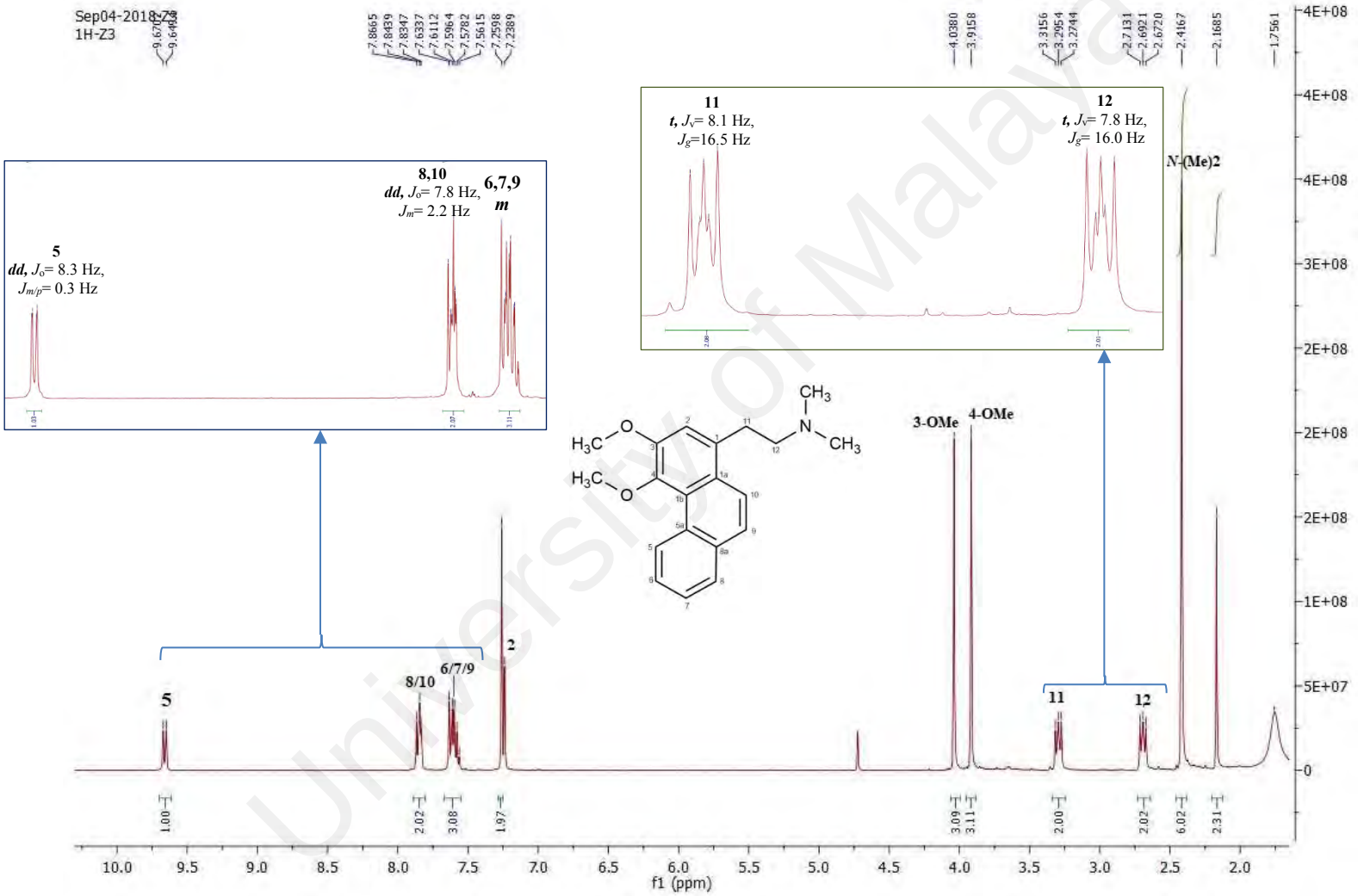

Figure 4.31: ^{1}H NMR spectrum of **3**.

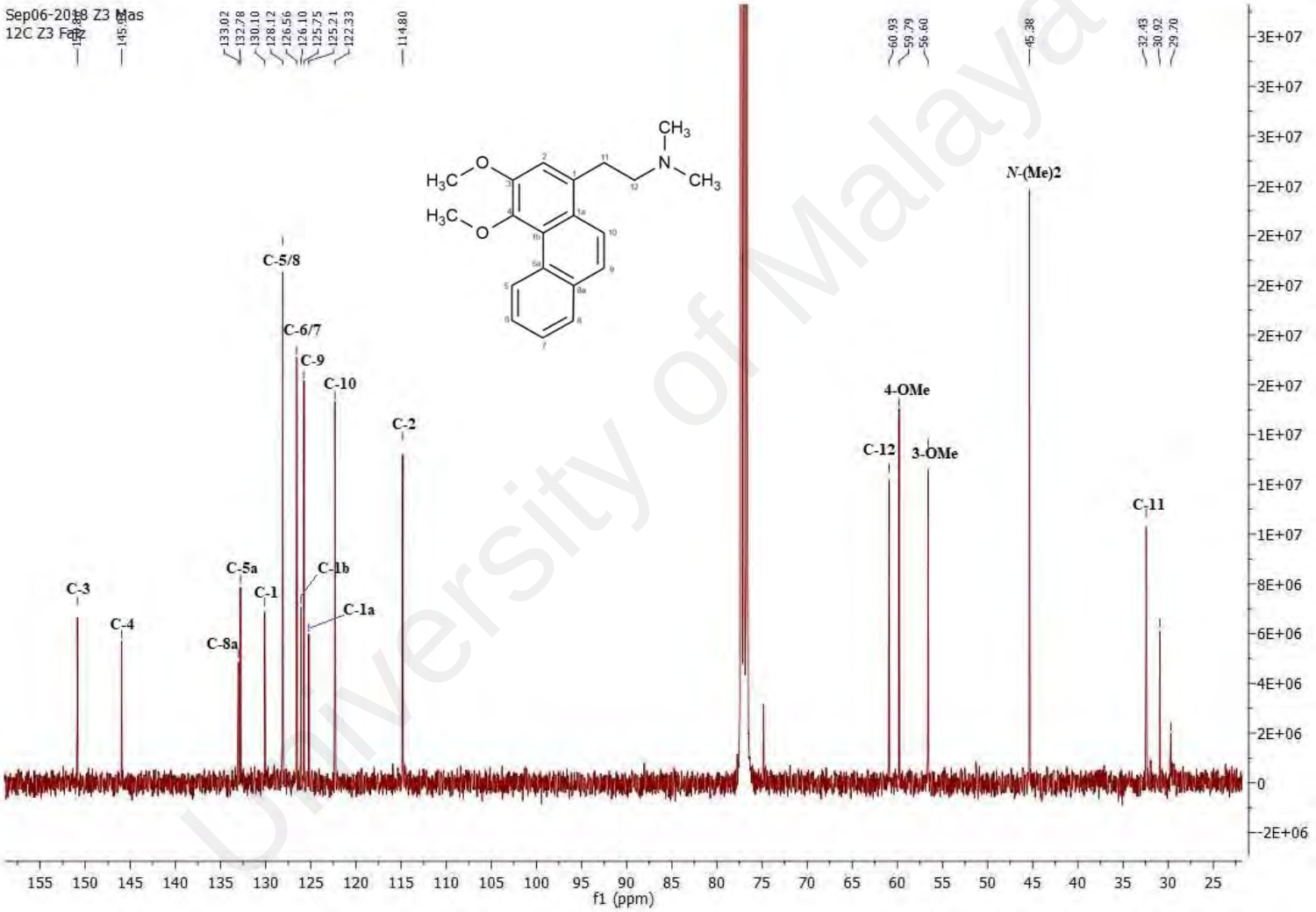

Figure 4.32: ^{13}C NMR spectrum of **3**.

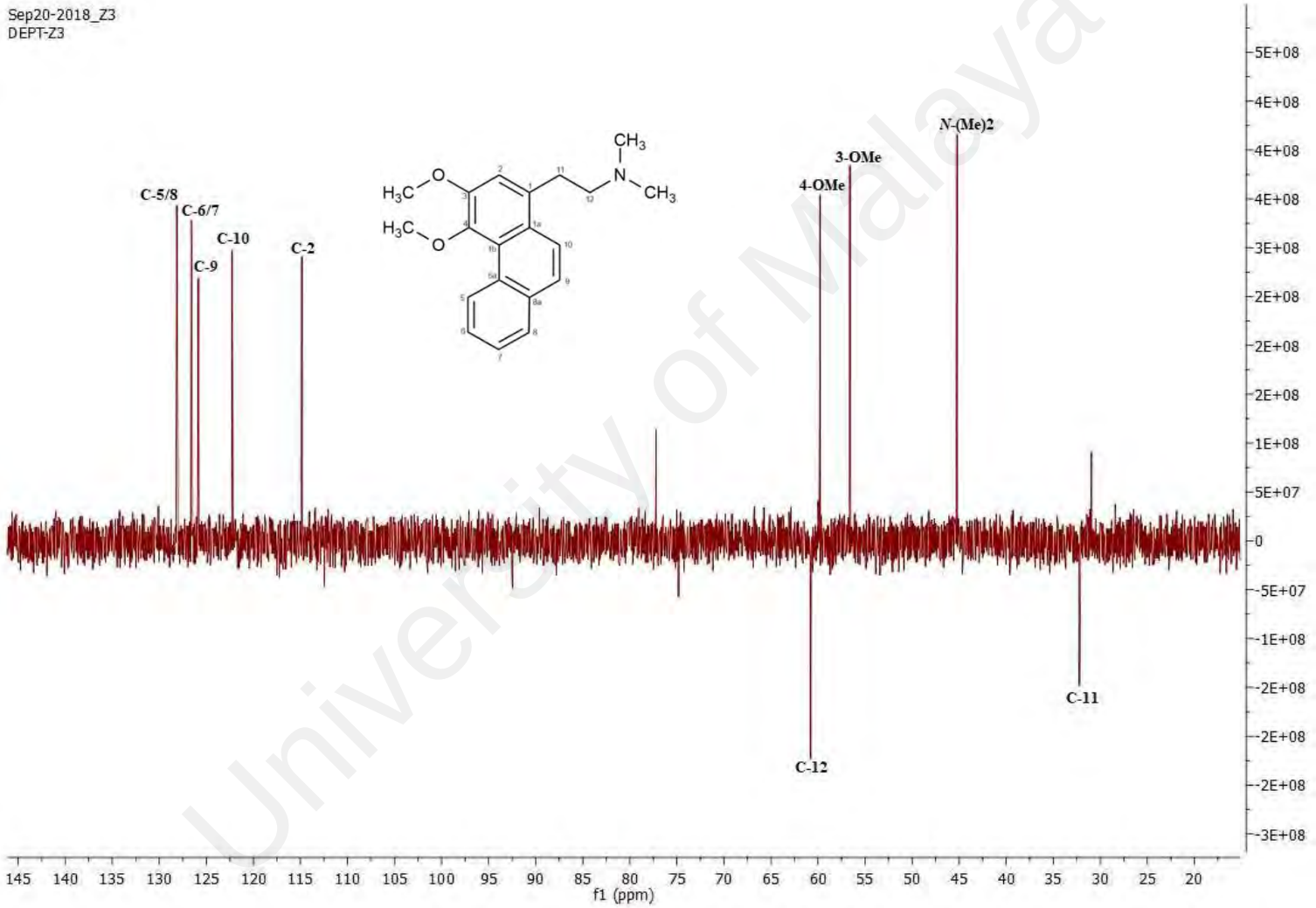

Figure 4.33: DEPT-135 spectrum of **3**.

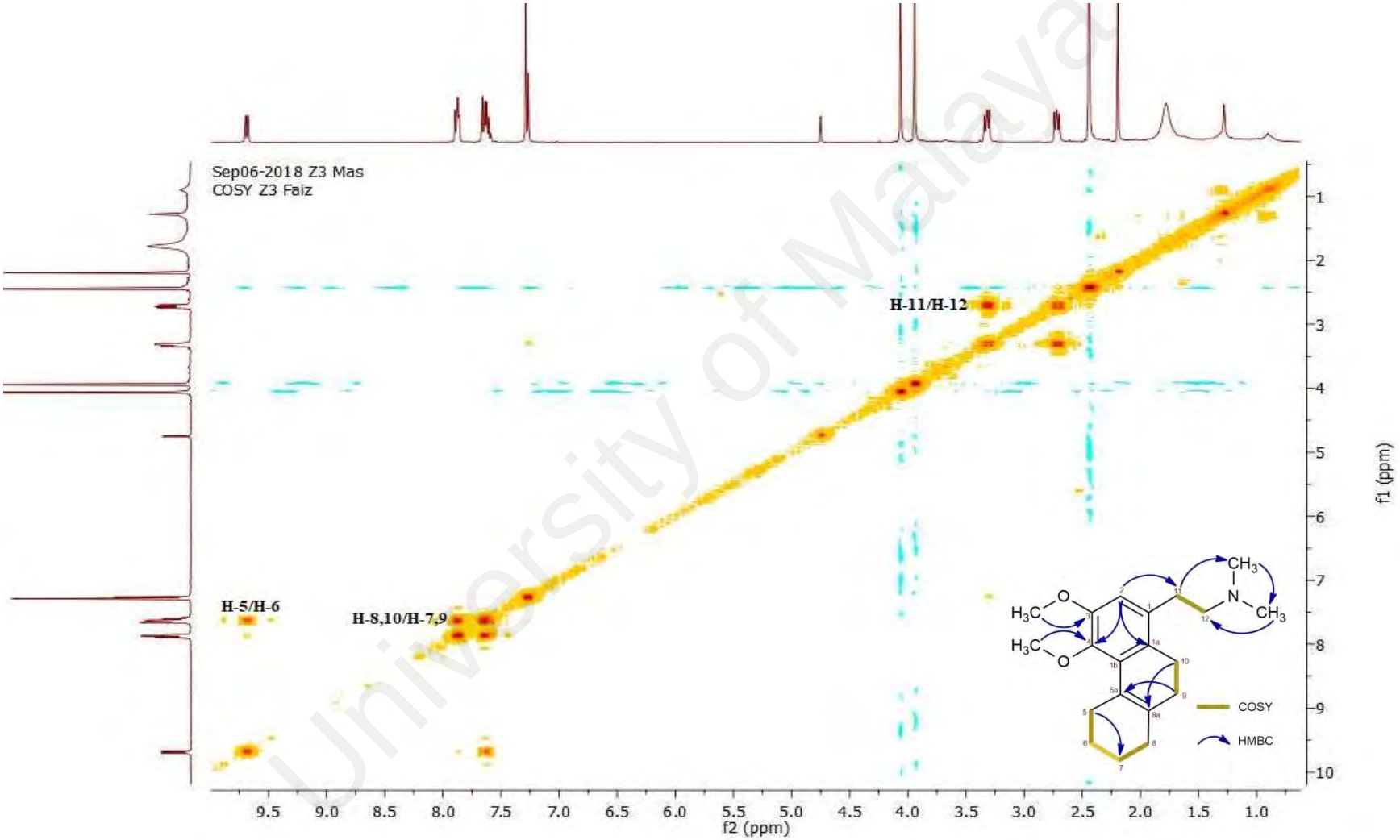

Figure 4.34: COSY spectrum of **3**.

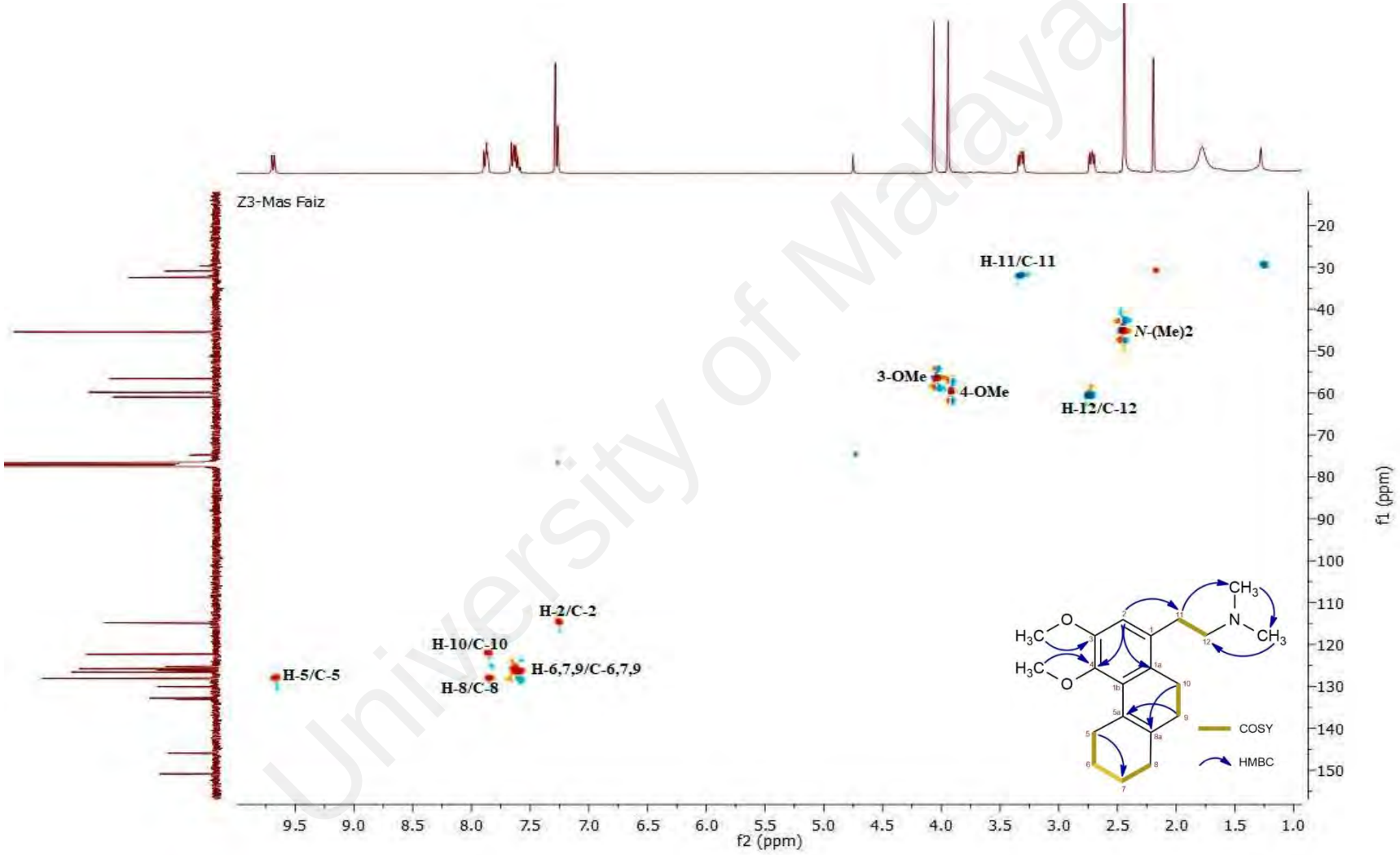

Figure 4.35: HSQC spectrum of **3**.

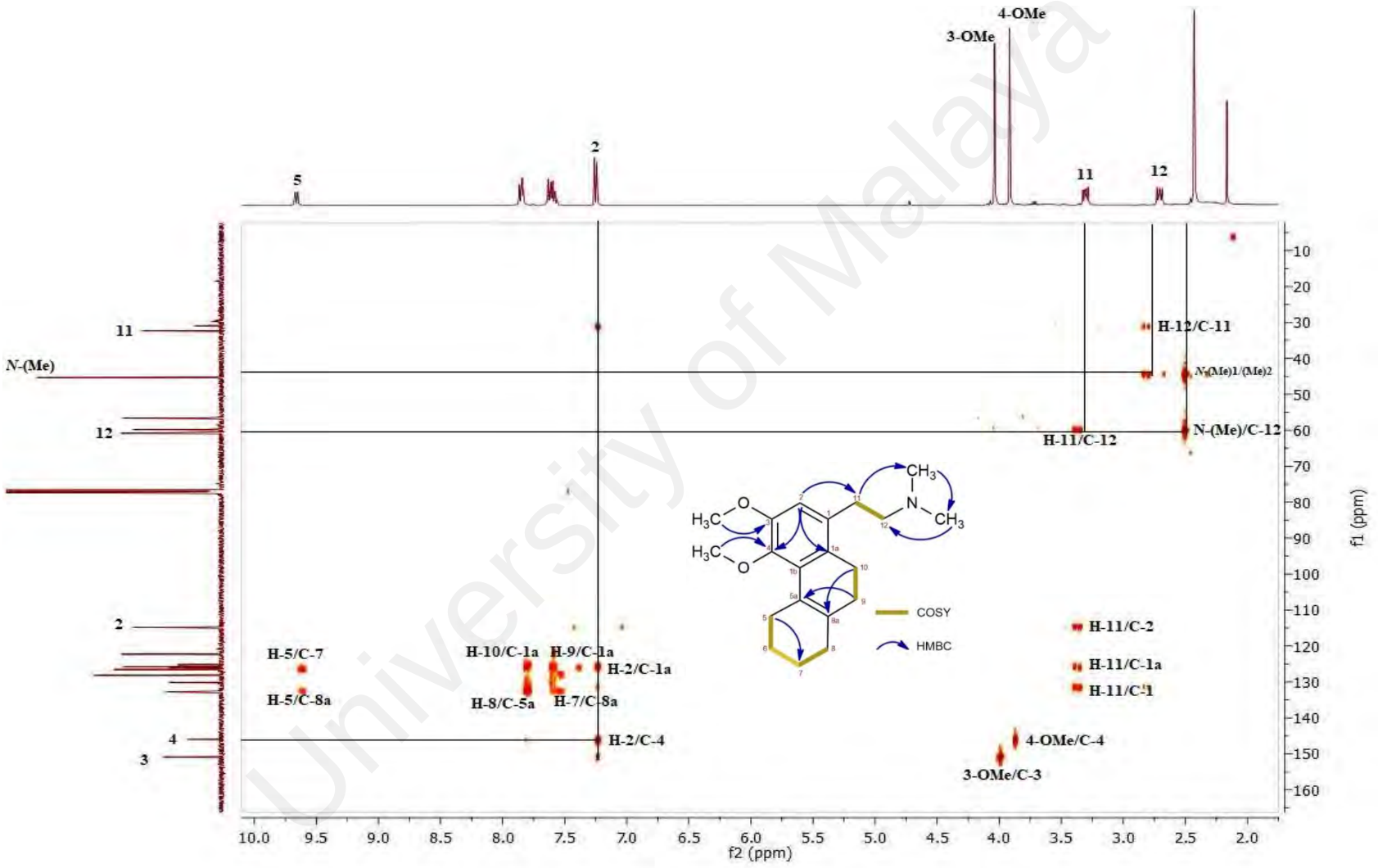

Figure 4.36: HMBC spectrum of **3**.

4.2.4 2-Hydroxyatherosperminine **4**

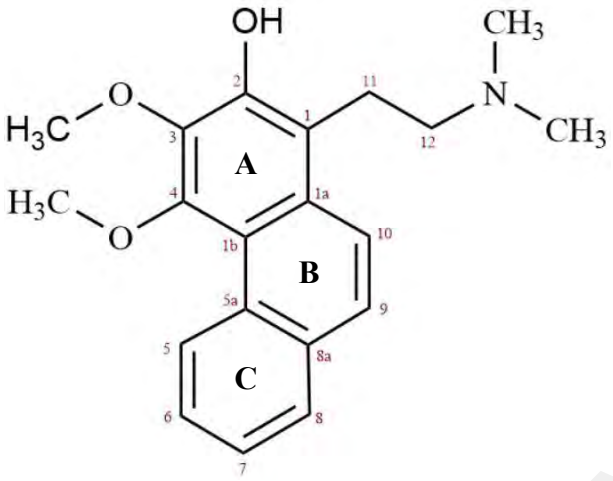

IUPAC: 1-(2-(dimethylamino) ethyl)-3,4-dimethoxyphenanthren-2-ol

Compound **4** was obtained as a brownish amorphous solid with zero optical rotation on plane polarized light. The MS spectrum (Figure 4.38) showed a pseudomolecular ion peak at m/z 326.17 $[M+H]^+$ corresponding to the molecular formula $C_{20}H_{23}NO_3$ with 10 degrees of unsaturation. It is a functional group isomer of compound **2** where they have the same molecular mass but with a different arrangement of the oxygen atom. The FTIR spectrum (Figure 4.39) displayed a significant broad and intense vibrational band at 3412 cm^{-1}, which is a characteristic peak for the hydroxyl group (-OH). While other absorption peaks showed a similar trend like compound **3** as they were derived from the same phenanthrene type alkaloid.

The ^{1}H-NMR (Figure 4.40) and ^{13}C-NMR (Figure 4.41) spectrums of compound **4** were relatively similar to compound **2** and **3**. Alike features could be observed from their spectrums confirming that there were close structural relationships between all of these compounds. The only noticeable difference in the ^{1}H-NMR spectrum of compound **4** was the absence of H-2 proton which should be resonating at δ 7.24. Instead, the H-2 was substituted with a hydroxyl group (-OH) group at position C-2. DEPT-135 spectrum (Figure4.42) revealed no C-2 peak as it was a quaternary carbon. Overall proton-carbon

interpretations from the 2D-NMR experiments have led to the conclusion that the compound **4** is 2-hydroxyatherosperminine. The short-range and long-range correlations are shown in a graphical manner in Figure 4.37 below.

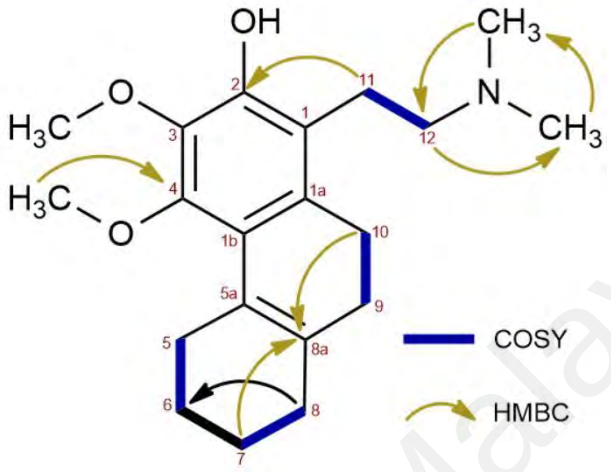

Figure 4.37: ^{1}H-^{1}H and ^{1}H-^{13}C correlations observed in COSY and HMBC spectra of **4**.

Table 4.6: NMR spectroscopy parameters and values of **4** (Awang *et al.*, 2008).

	^{1}H NMR	**HSQC**	**DEPT-135**	**HMBC**	**Literature**
Position	**δ_H, pattern, *J* (Hz)**	**δ_C**	**Type ^{13}C**	**neighbor**	**δ_H, pattern**
1	-	130.10	Q	3, 12, 1b, 10	-
1a	-	125.22	Q	2, 9, 5a, 11	-
1b	-	126.08	Q	3, 5, 8a, 10	-
2	-	148.80	Q	1a, 4, 11	-
3	-	150.80	Q	1b, 1, 3-OMe	-
4	-	145.90	Q	1a, 2, 4-OMe	-
5	9.4174, *d*, J_o=8.0	128.13	CH	1b, 8a, 7	9.67, *d*
5a	-	132.70	Q	6, 8, 9, 1a, 4	-
6	7.5975-7.6442, *m*	126.53	CH	5a, 8	7.56-7.64, *m*
7	7.5975-7.6442, *m*	126.53	CH	5, 8a	7.56-7.64, *m*
8	7.8569-7.8925, *m*	128.13	8	6, 5a, 9	7.84-7.86, *dd*,
8a	-	132.90	Q	5, 7, 10, 1b	-
9	7.5975-7.6442, *m*	125.77	CH	1a, 5a, 8	7.56-7.64, *m*
10	7.8569-7.8925, *m*	122.31	CH	1, 1b, 8a	7.86-7.90 *d*
11	3.3612, *t*, J_v= 8, J_g= 15.2	22.70	(-CH_2)	2, 1a	3.26-3.34, *m*
12	2.8081, *t*, J_v= 8.2, J_g= 15.8	56.70	(-CH_2)	1, *N*-Me	2.65-2.70, *m*
3 –OMe	4.0640, *s*	59.90	CH_3	3	4.04, *s*
4 – OMe	3.8318, *s*	57.20	CH_3	4	3.92, *s*
N-$(Me)_2$	2.3927, *s*	4	CH_3	11, 12	2.41, *s*

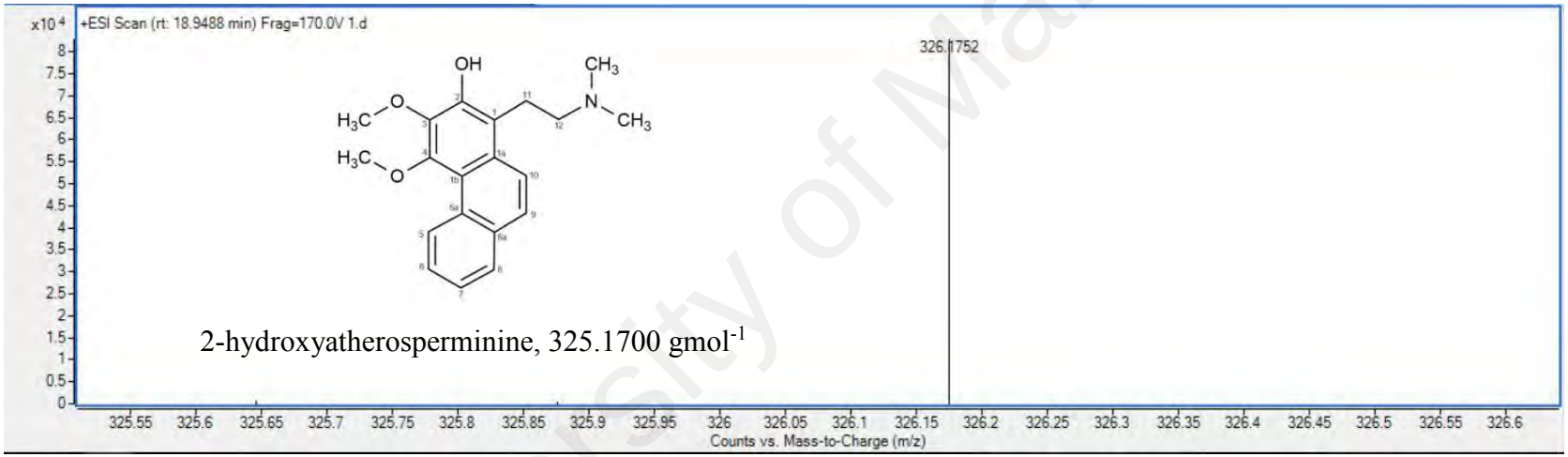

Figure 4.38: MS spectrum of **4** at *m/z* 326.1752.

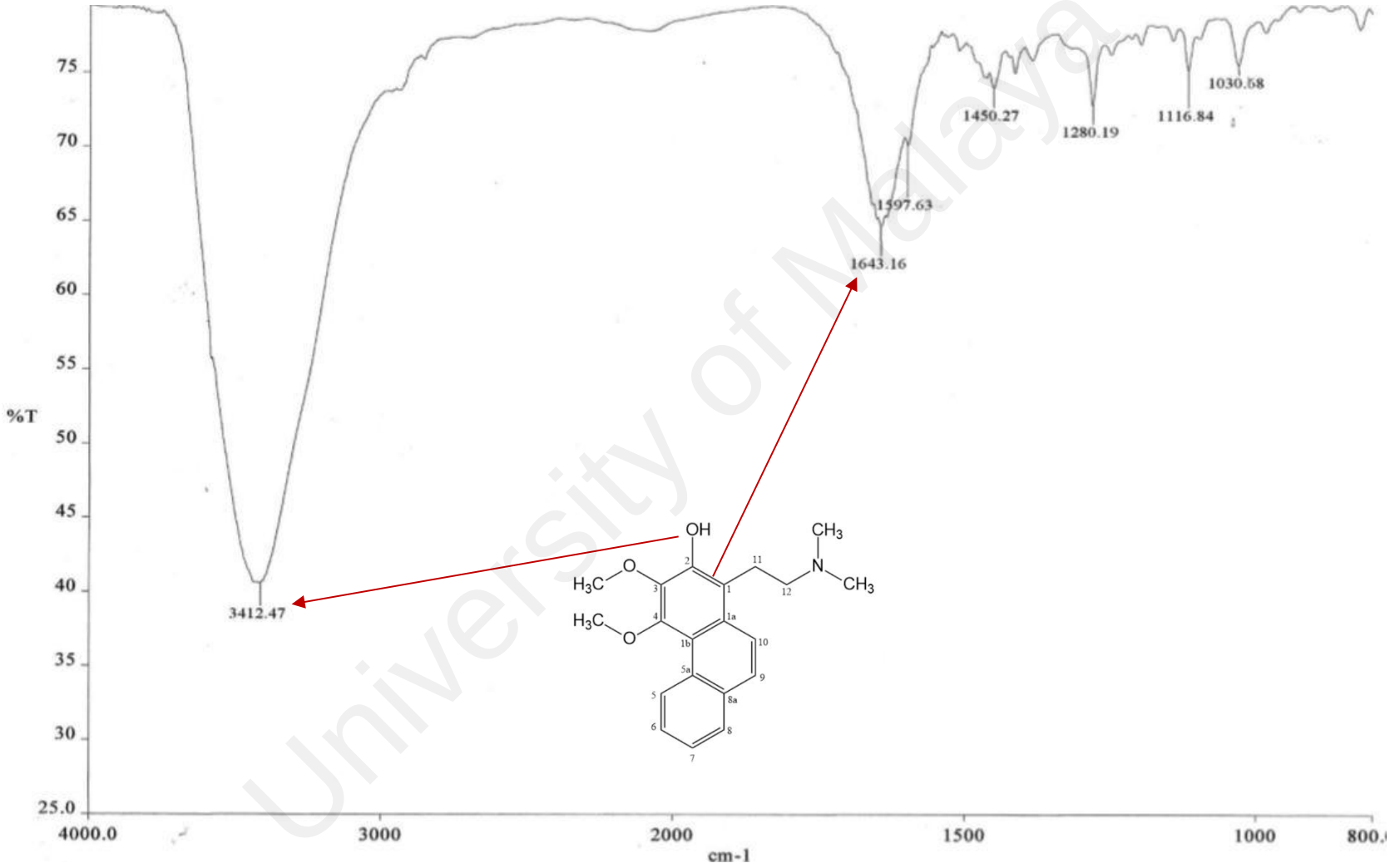

Figure 4.39: FTIR spectrum of **4**.

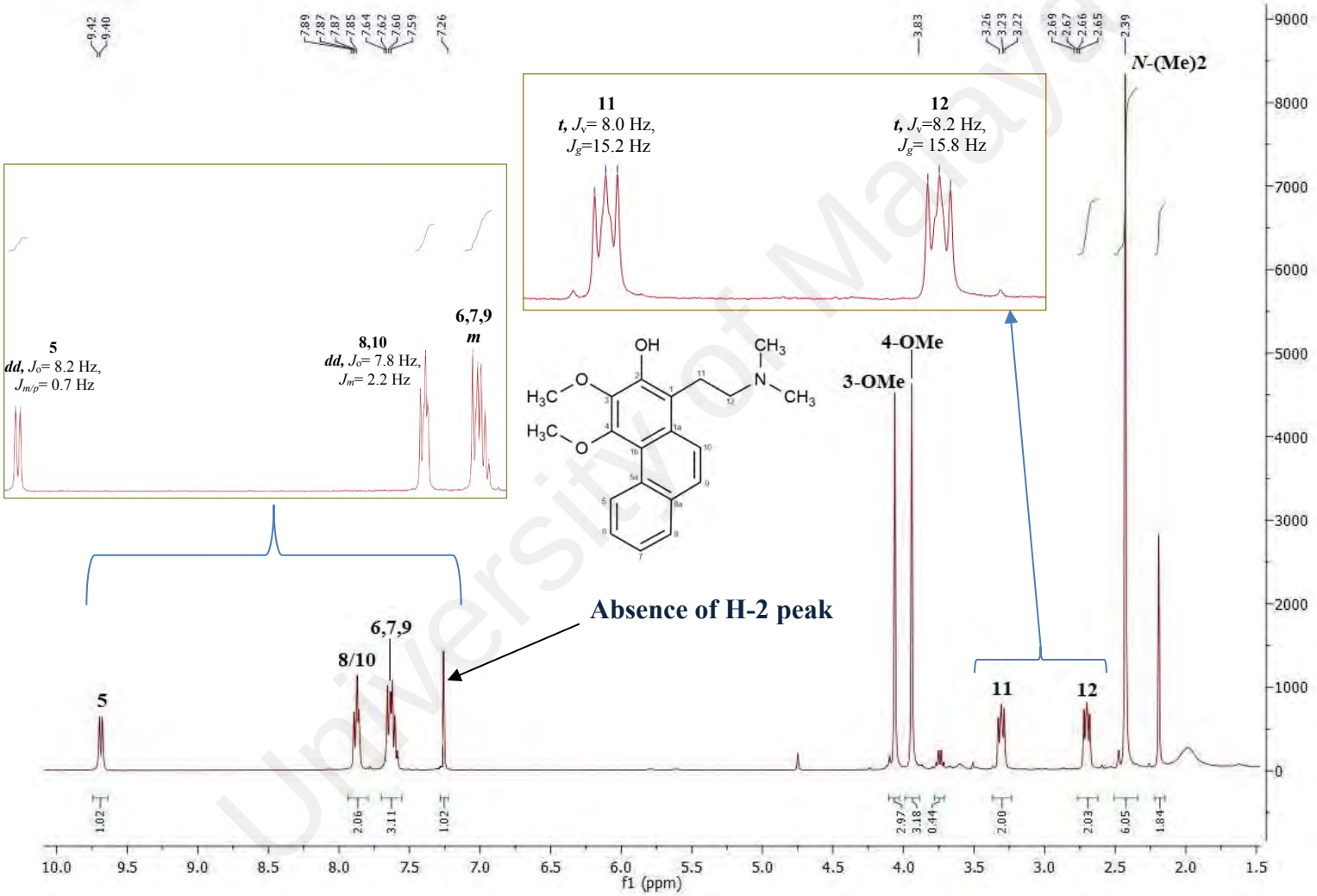

Figure 4.40: ^{1}H NMR spectrum of **4**.

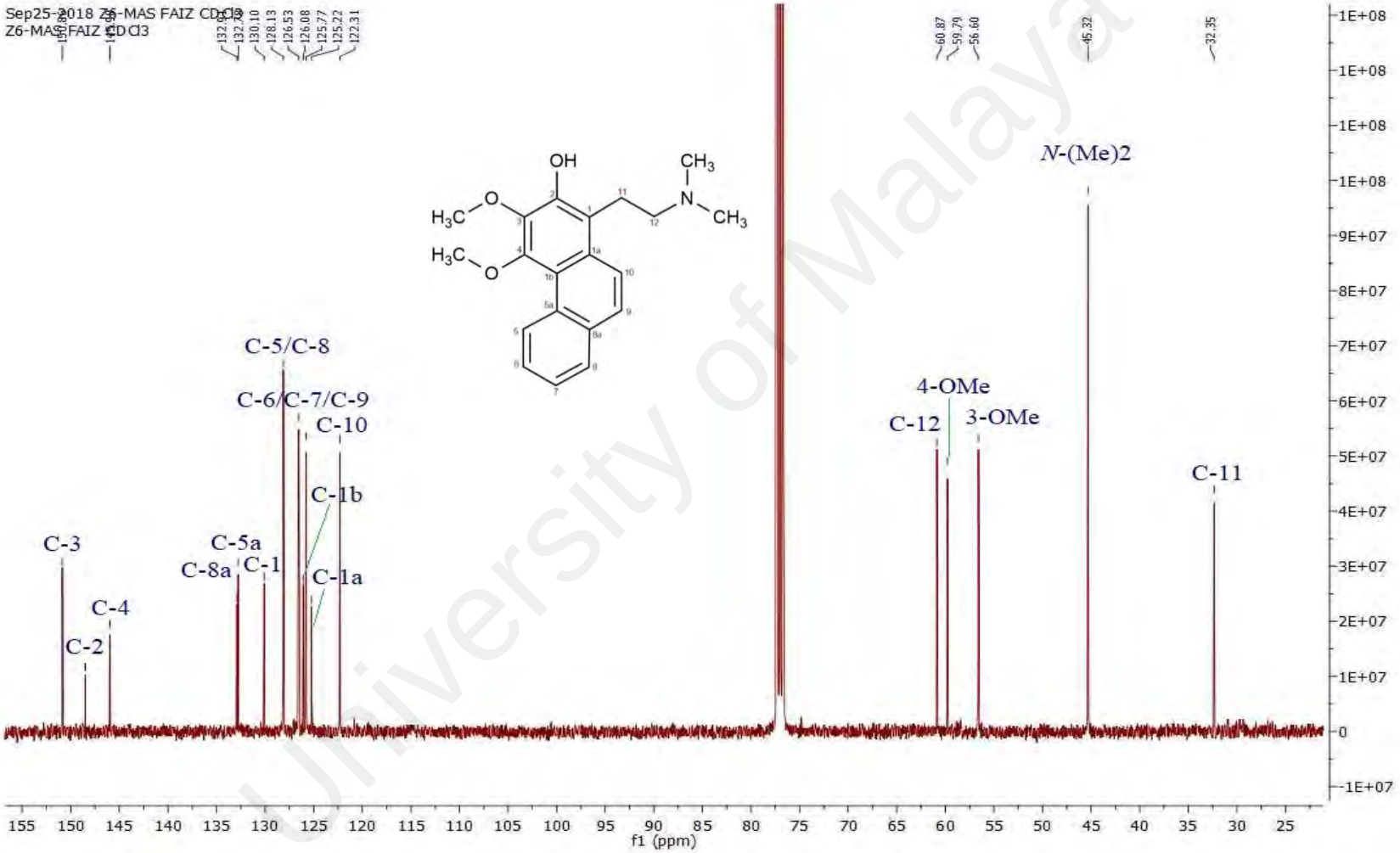

Figure 4.41: ^{13}C NMR spectrum of **4**.

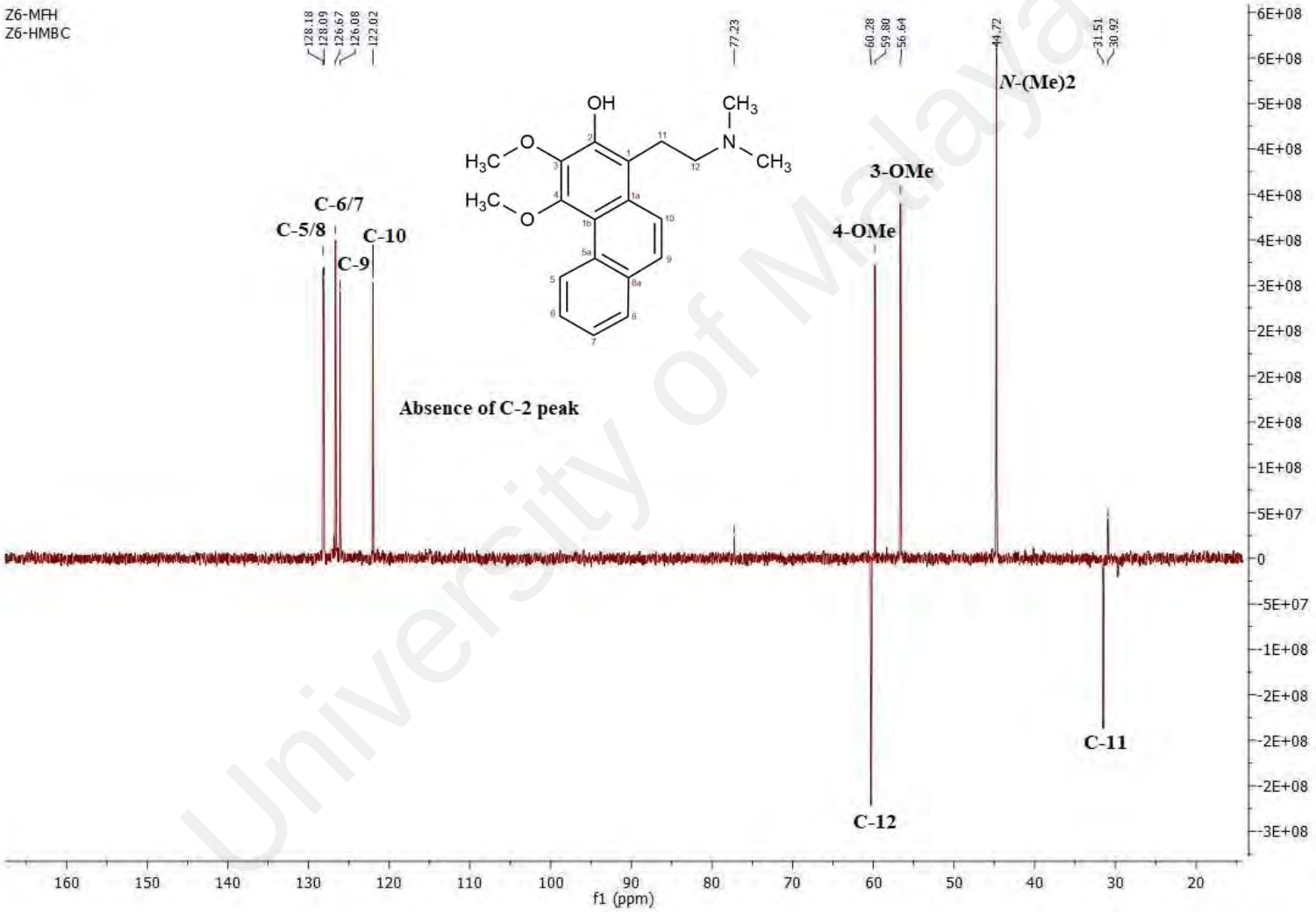

Figure 4.42: DEPT-135 spectrum of **4**.

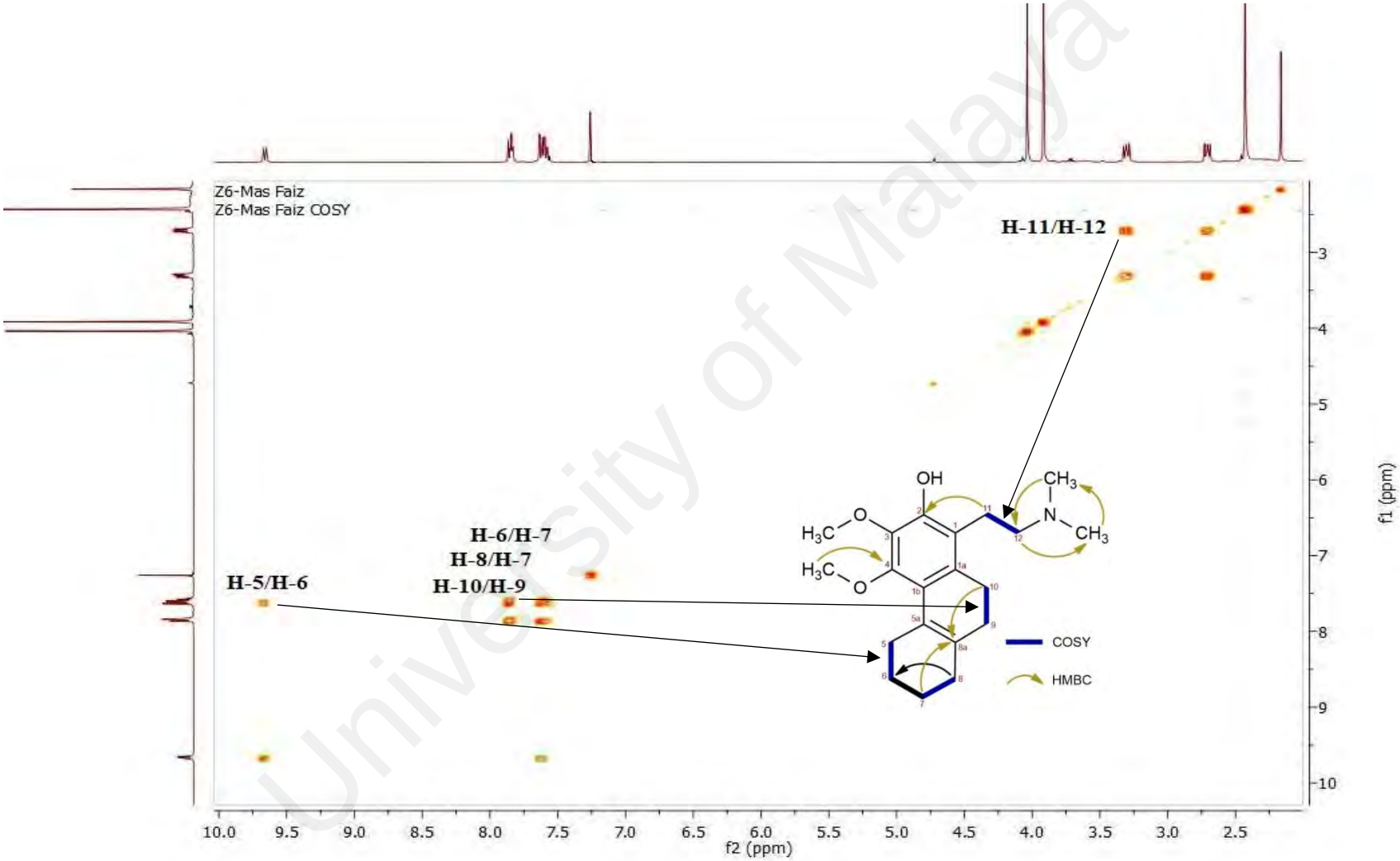

Figure 4.43: COSY spectrum of **4**.

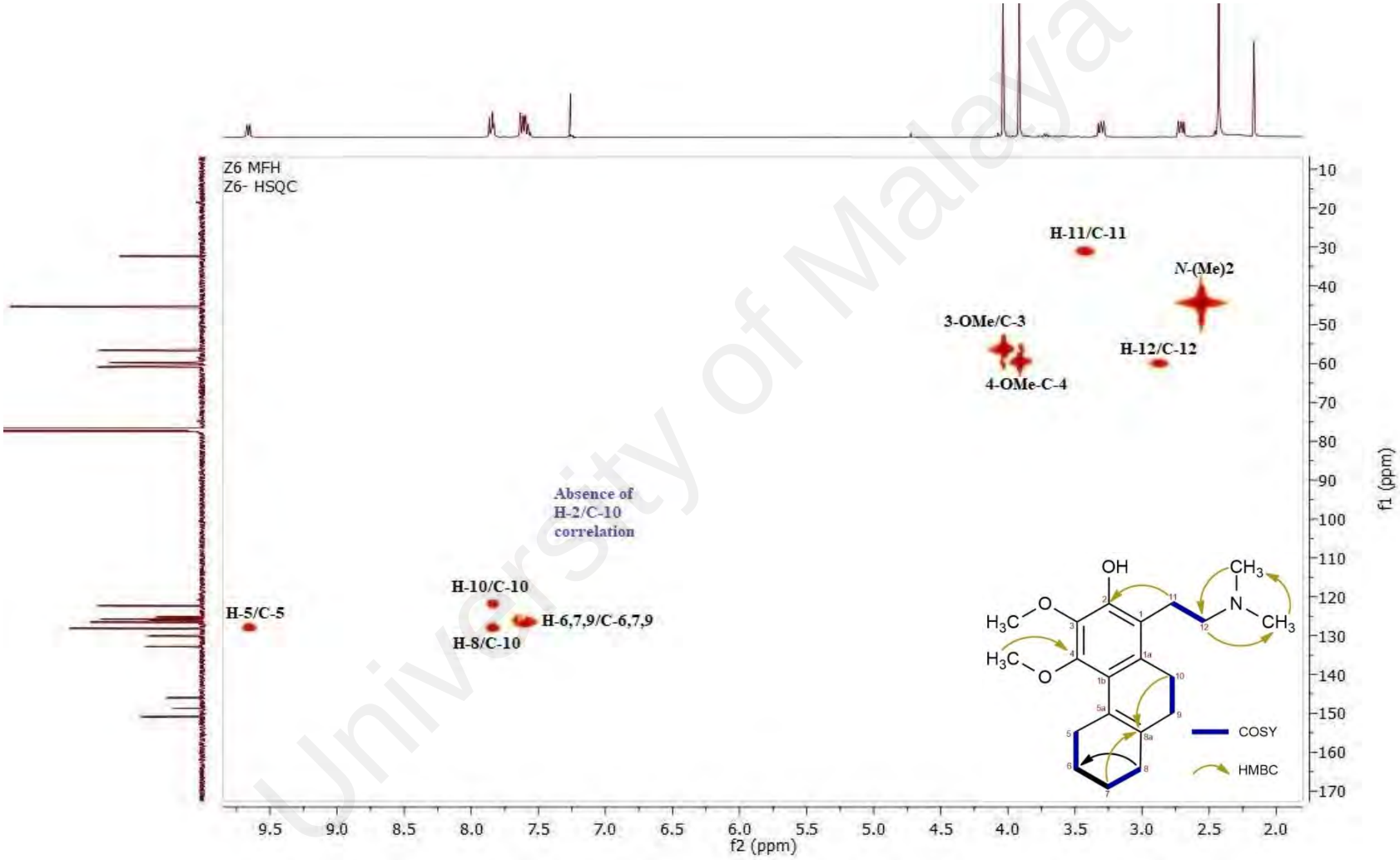

Figure 4.44: HSQC spectrum of **4**.

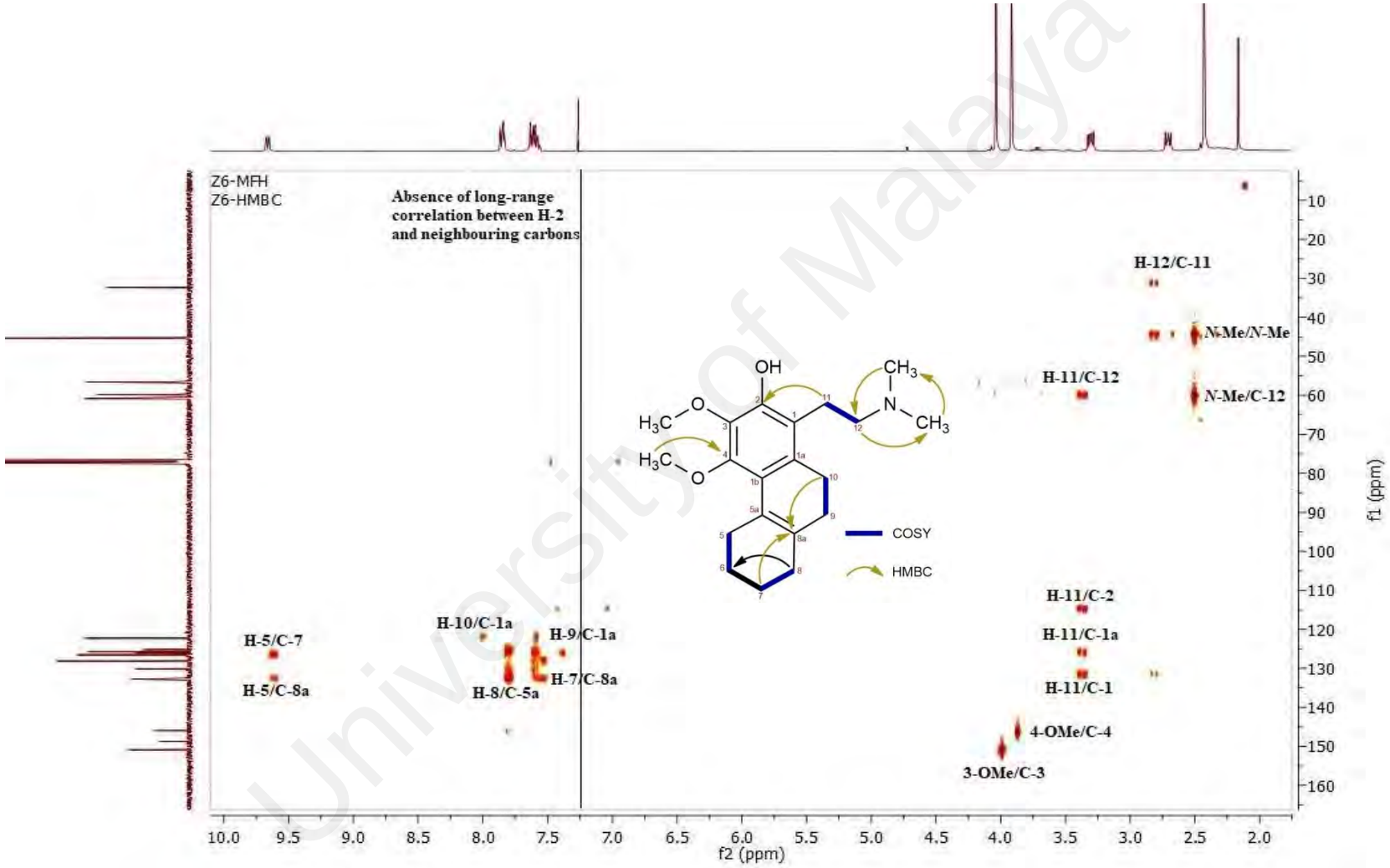

Figure 4.45: HMBC spectrum of **4**.

4.2.5 Argentinine **5**

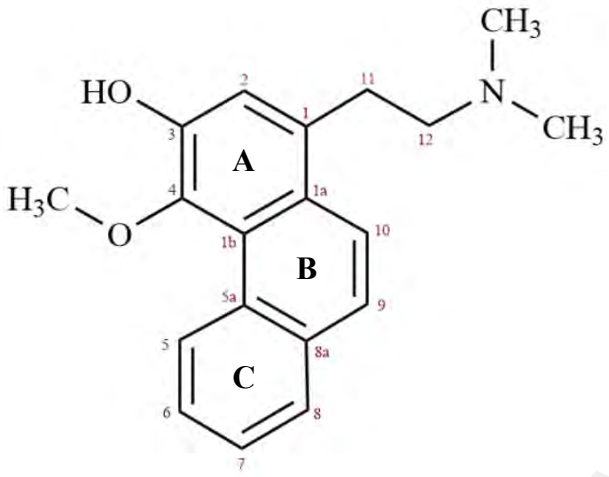

IUPAC: 1-(2-(dimethylamino) ethyl)-4-methoxyphenanthren-3-ol

Compound **5** was attained as an optically inactive brownish amorphous with a pseudomolecular ion peak at *m/z* 296.1627 in the LCMS-IT-TOF spectrum (Figure 4.47), compatible to the molecular formula of $C_{19}H_{21}NO_2$ with 10 degrees of unsaturation. The compound also exhibited UV absorptions at λ_{max} 218, 260, 305 and 345 nm which are the characteristic absorption peaks for phenanthrene type alkaloid. Broad vibrational band occurring at υ_{max} 3440 cm^{-1} indicated that the compound was associated with hydroxyl (-OH) group while having other functional groups stretching appeared to be similar to compound **2, 3** and **4** (Figure 4.48).

The ^{1}H-NMR spectrum (Figure 4.49) indicated the presence of singlets at δ 2.39 (6H) and δ 3.76 (3H) which corresponded to *N*-$(Me)_2$ and 4-OMe, respectively. H-12 and H-11 resonated as triplets at δ 2.66 (J_g= 14.5 Hz, J_v= 5.2 Hz) and δ 3.23 (J_g= 14.5 Hz, J_v= 5.2 Hz) with two proton integration. In the aromatic region, two coupled protons at δ 7.59 (1H, *d*, *J*= 9.4 Hz) and δ 7.85 (1H, *d*, *J*= 9.4 Hz) is a characteristic of an AB system corresponding to H-9 and H-10 in the phenanthrene ring system, were detected. The most deshielded proton at δ 9.41 (1H, *d*, *J*= 7.4 Hz) was best assigned to H-5 due to its unique *ortho* to H-6 and *meta* to H-7. This signal was consistent for all of the compound **2, 3** and

4 due to the presence of methoxy groups at C-3 and C-4 that resulted in an uplifted shift of the H-5 resonance peak to more than δ 9.0. Since most phenanthrene alkaloids have methoxy and/or hydroxyl groups substituted at position C-3 and C-4, they pulled the electron clouds surrounding H-5 simultaneously appreciably shifting the signal towards the downfield region. This is a specific characteristic for phenanthrene alkaloid. Plus, having H-2 appearing as singlet confirmed that C-3 and C-4 were substituted. The aromatic protons (H-6, H-7, and H-9) were observed as multiplets at the region between δ 7.59 – 7.64.

The COSY spectrum of compound **5** (Figure 4.52) has made possible for the assignment of the aromatic protons where there are cross peaks observable for H-5/H-6, H-7/H-8 and H-10/H-9. The positions of proton H-11 and H-12 were confirmed by the correlation found between them. The ^{13}C-NMR (Figure 4.50) and DEPT-135 (Figure 4.48) spectrums displayed a total of nineteen carbons which coincide best with the molecular formula $C_{19}H_{21}NO_2$. It is worthy to take note that the aromatic carbons C-3 and C-4 resonated at higher chemical shifts due to the presence of substituent effects from the electronegative groups such as methoxyl and hydroxyl groups. C-11 peak appeared at the lower field as compared to C-12 due to the fact the C-11 was located adjacent to *N* atom. The HSQC (Figure 4.53) and HMBC (Figure 4.54) experiments further confirmed the structure of compound 5 as argentinine by the distinctive proton-carbon correlations. The graphical representation for the short-range and long-range coupling is shown in Figure 4.46. All the combined spectroscopic techniques have allowed us to determine compound **5** as argentinine.

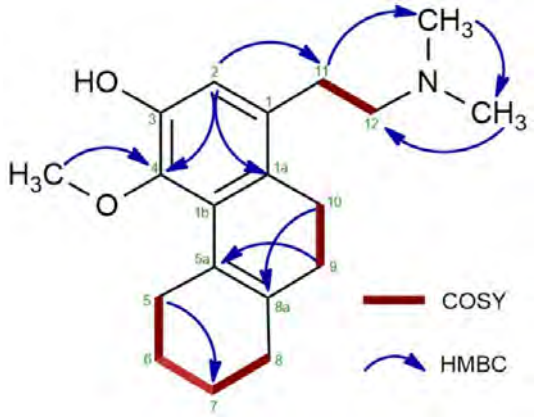

Figure 4.46: ^{1}H-^{1}H and ^{1}H-^{13}C correlations observed in COSY and HMBC spectra of **5**.

Table 4.7: NMR spectroscopy parameters and values of **5** (Casabuono & Pomilio, 1997; Kuck, Albónico *et al.* , 1967).

	^{1}H NMR	**HSQC**	**DEPT-135**	**HMBC**	**Literature**
Position	**δ_H, pattern, *J* (Hz)**	**δ_C**	**Type ^{13}C**	**neighbor**	**δ_H, pattern**
1	-	129.33	Q	3, 12, 1b	-
1a	-	124.37	Q	2, 4, 9, 5a,	-
1b	-	125.30	Q	3, 1, 5, 8a,	-
2	7.2305, *s*	117.56	Q	1a, 4, 11	7.24, *s*
3	-	147.71	Q	1, 3-OMe	-
4	-	142.72	Q	1a, 4-OMe	-
5	9.4154, *d*, J_o=7.4	128.26	CH	1b, 8a, 7	9.56, *dd*
5a	-	132.75	Q	6, 8, 9, 1a,	-
6	7.5875-7.6442, *m*	126.73	CH	5a, 8	7.58-7.65, *m*
7	7.5875-7.6442, *m*	126.73	CH	5, 8a	7.58-7.65, *m*
8	7.8453-7.8925, *m*	127.32	CH	6, 5a, 9	7.86-7.89, *m*
8a	-	133.72	Q	5, 10, 1b	-
9	7.5875-7.6442, *m*	126.54	CH	1a, 5a, 8	7.58-7.65, *m*
10	7.8453-7.8925, *m*	122.61	CH	1, 1b, 8a	7.86-7.86, *m*
11	3.2332, *t*, *J*= 8.0	31.48	(-CH_2)	2, 1a	3.32, *t*
12	2.6671, *t*, *J*= 8.0	60.52	(-CH_2)	1, *N*-Me	2.71, *t*
4 – OMe	3.8318, *s*	60.14	CH_3	4	3.92, *s*
N-$(Me)_2$	2.3927, *s*	45.11	CH_3	11, 12	2.41, *s*

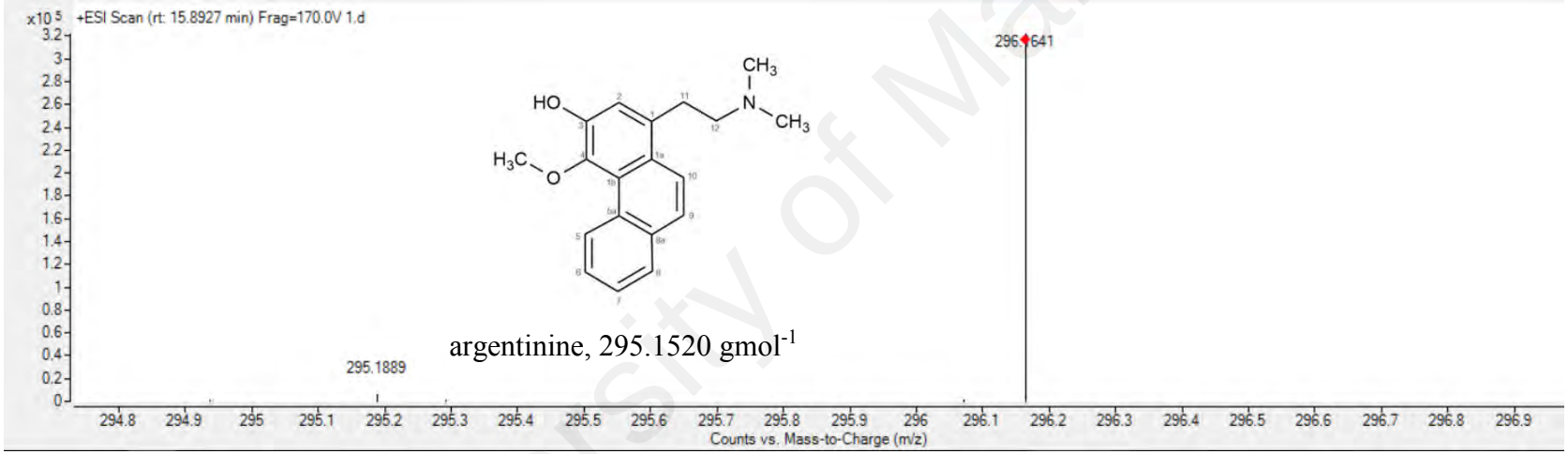

Figure 4.47: MS spectrum of **5** at *m/z* 296.1641.

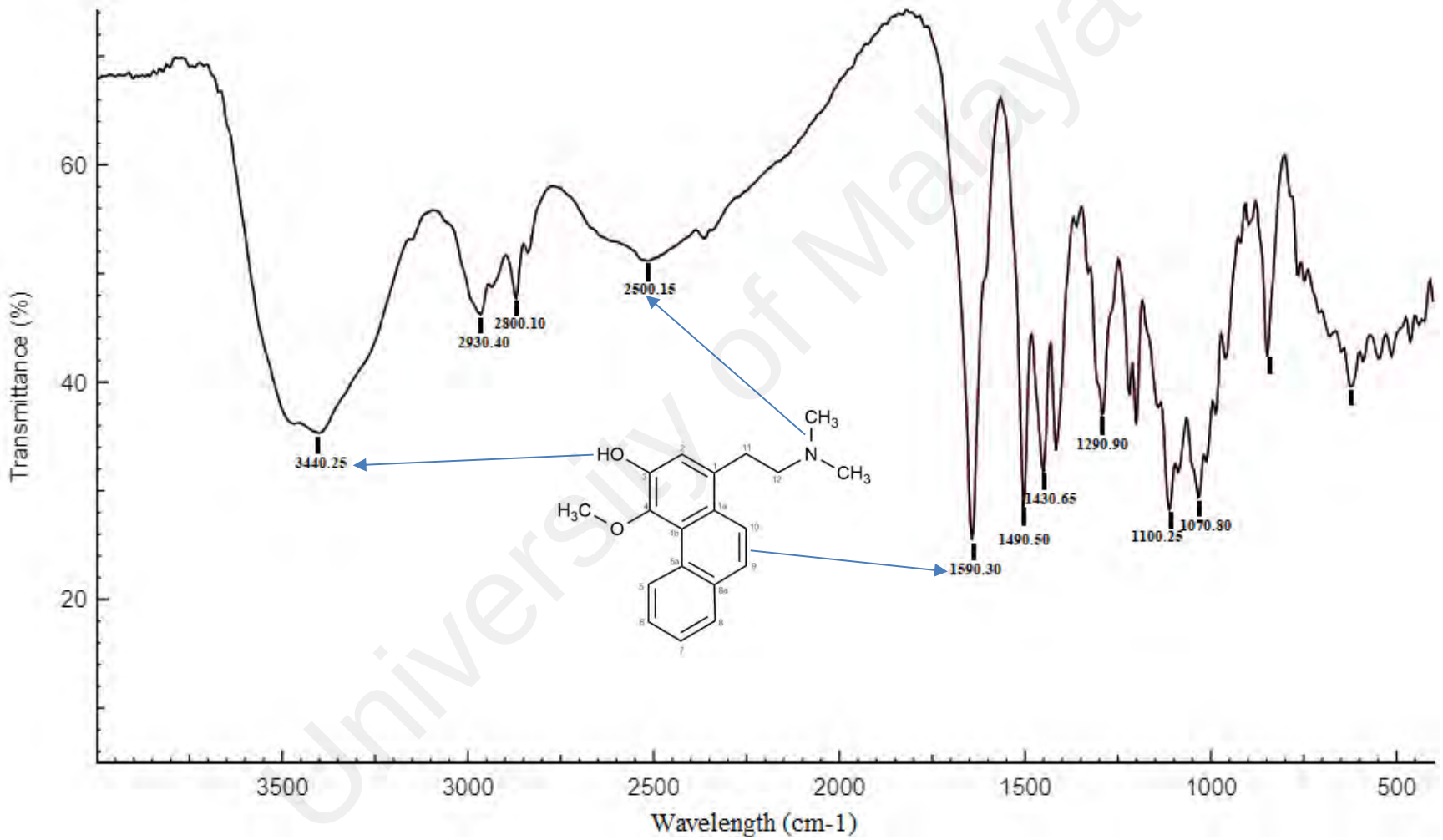

Figure 4.48: FTIR spectrum of **5**.

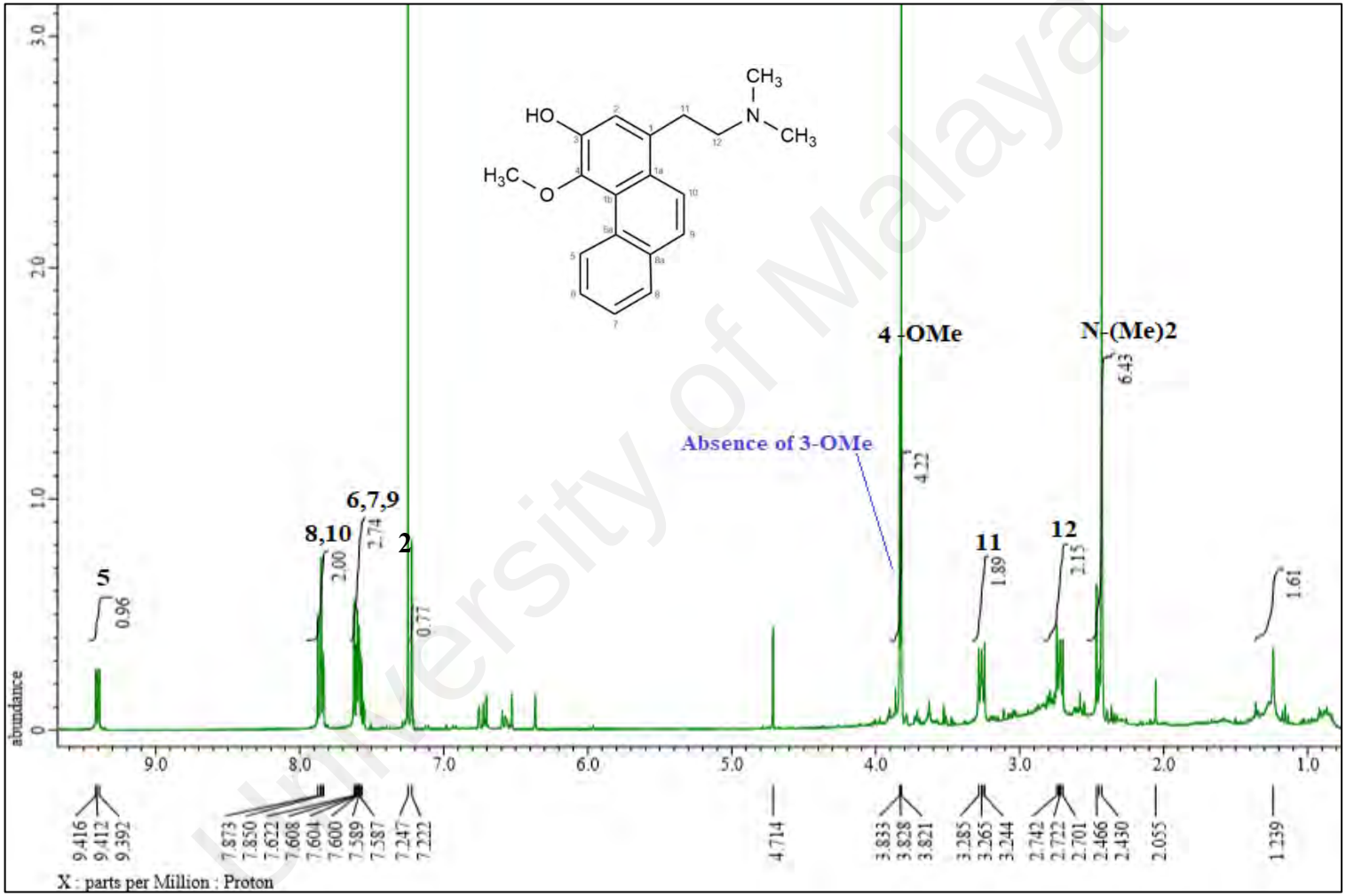

Figure 4.49: ^{1}H NMR spectrum of **5**.

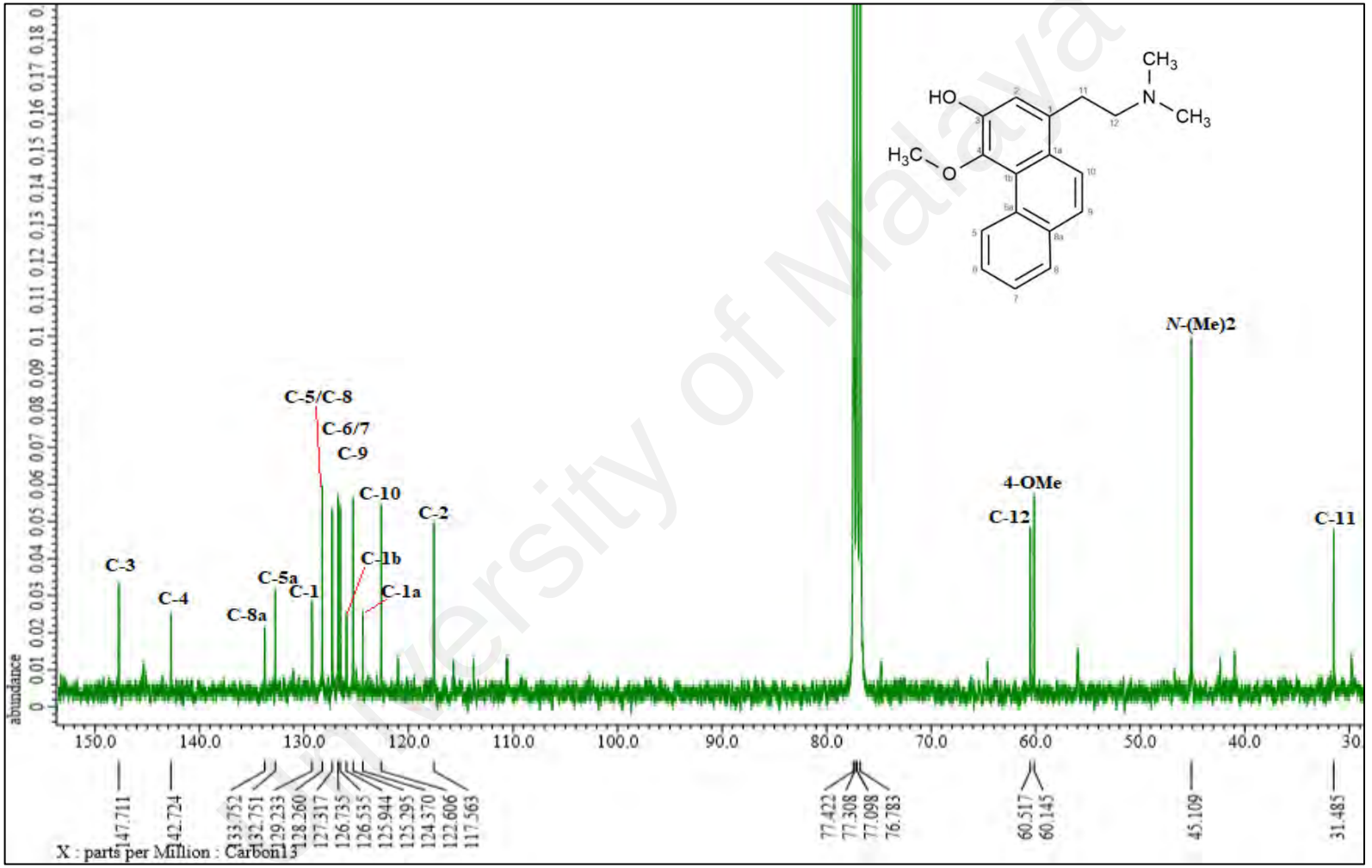

Figure 4.50: ^{13}C NMR spectrum of **5**.

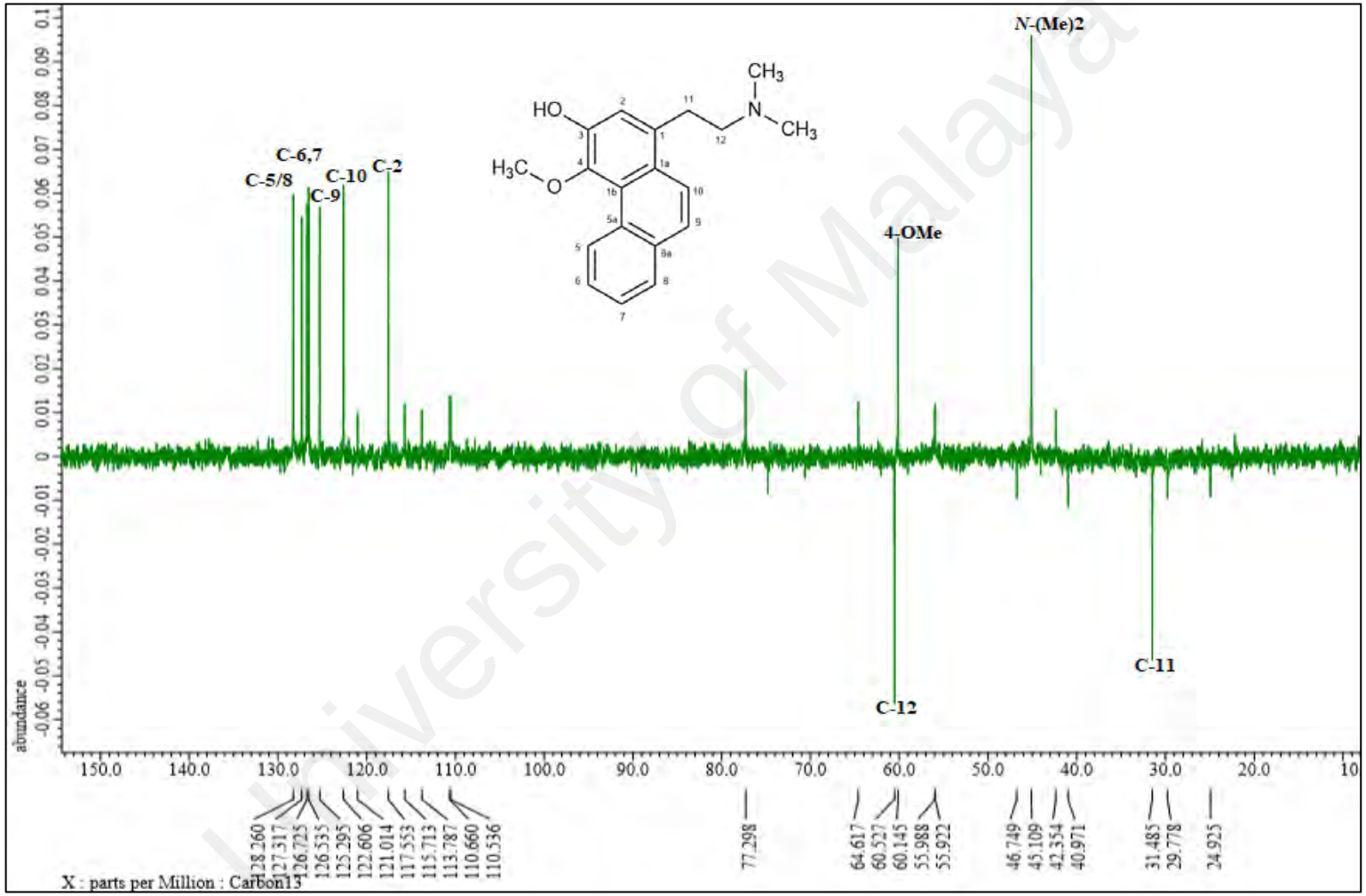

Figure 4.51: DEPT-135 spectrum of **5**.

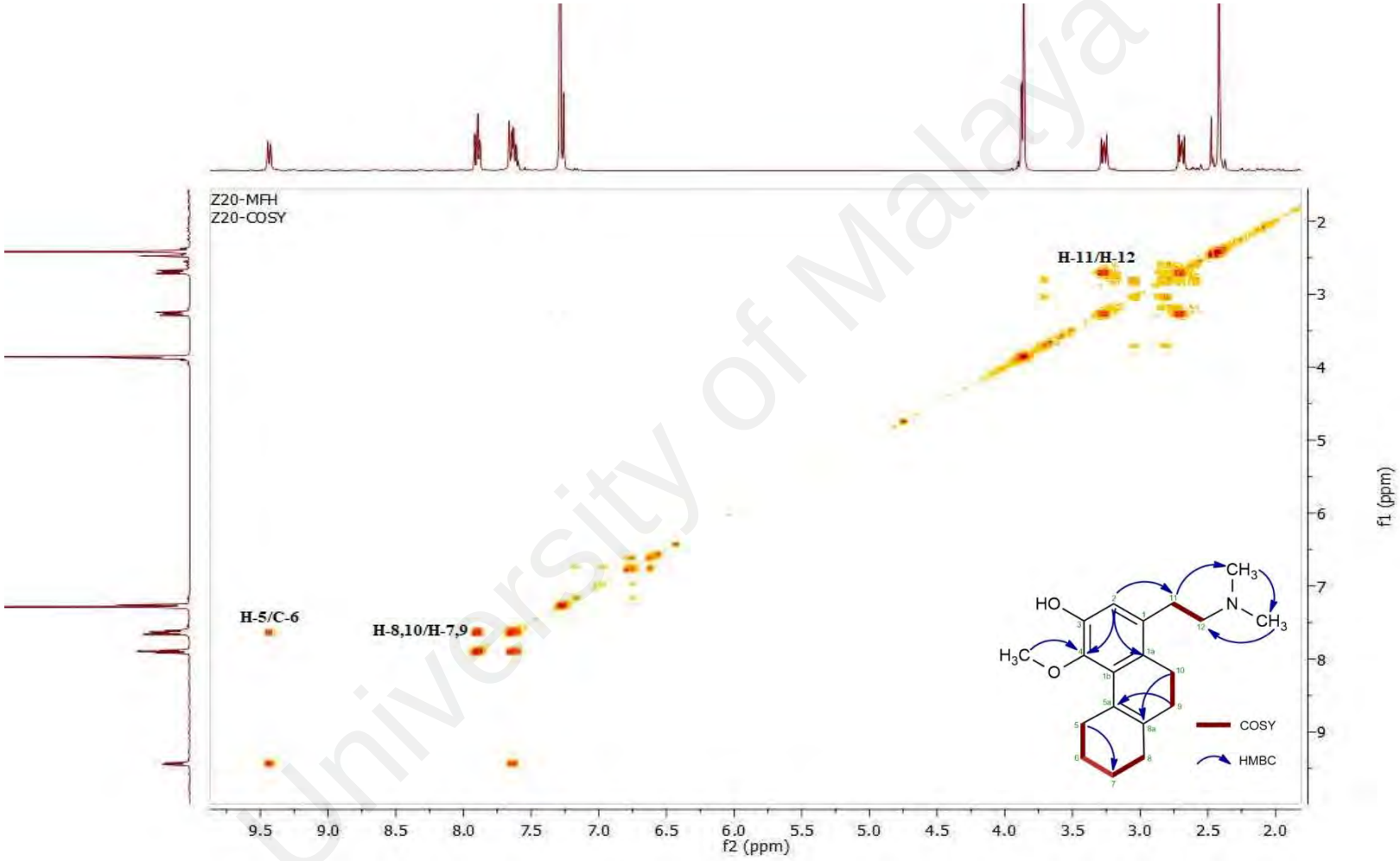

Figure 4.52: COSY spectrum of **5**.

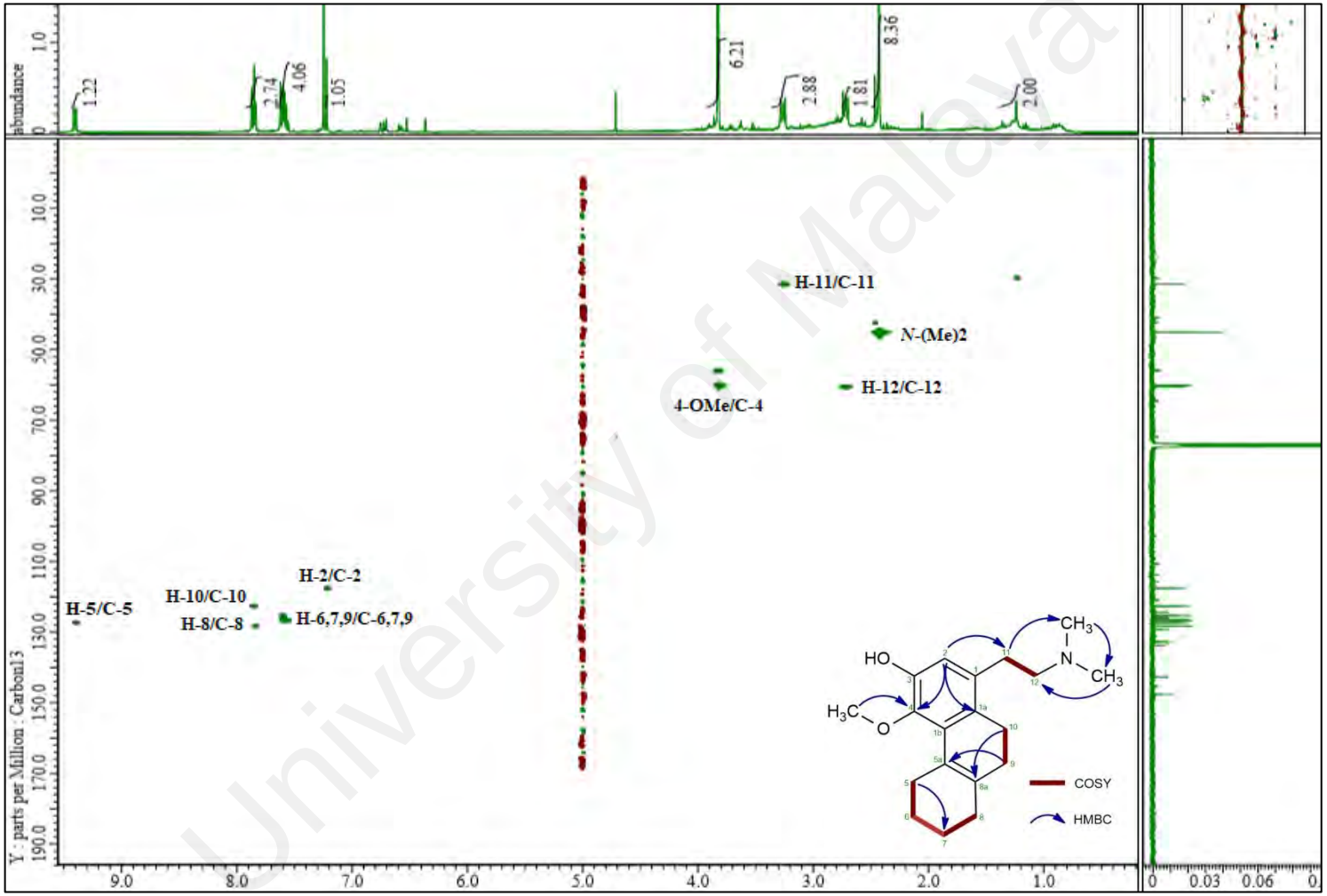

Figure 4.53: HSQC spectrum of **5**.

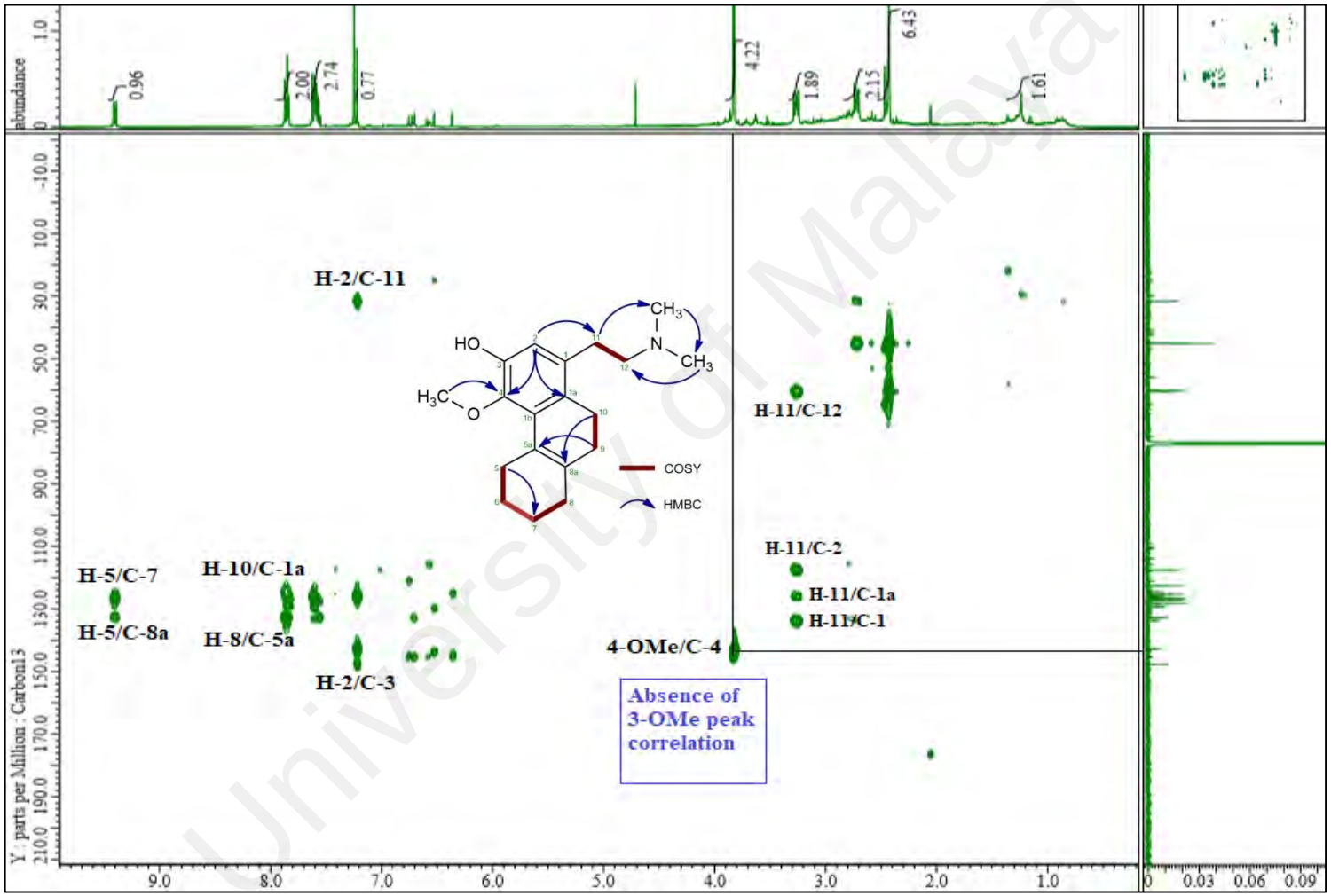

Figure 4.54: HMBC spectrum of **5**.

4.2.6 (+)-*N*-methyllaurotetanine **6**

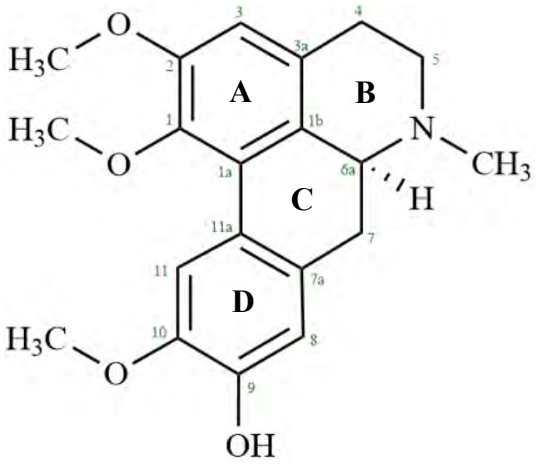

IUPAC:

(S)-1,2,10-trimethoxy-6-methyl-5,6,6a,7-tetrahydro-4H-dibenzo[de,g]quinolin-9-ol

Compound **6** was purified as an active dark brown amorphous solid with optical rotation, $[\alpha]_D^{27} = +45^o$ (c= 0.01, methanol). The positive LCMS-IT-TOF spectrum (Figure 4.56) exhibited a pseudomolecular ion peak, $[M+H]^+$ at *m/z* 342.1854 (calculated for $C_{20}H_{24}NO_4$, 342.1700) associated with the molecular formula $C_{20}H_{23}NO_4$ that is consistent with 10 degrees of unsaturation. The UV spectrum showed maximum absorptions at λ_{max} 227, 250 and 301 nm which were typical for an aporphine moiety, thus suggesting a 1, 2, 9, 10-tetrasubtituted aporphine skeleton. From the FTIR spectrum (Figure 4.57), we could observe vibrational bands at υ_{max} 3120 (broad and wide; -OH stretching), 1600 (moderate; C=C stretch), 1444 (moderate; =C-H stretch) 1371 (moderate; C-N stretch) and 1258 (sharp and intense; C-O stretch) cm^{-1} suggested all the relevant functional groups on the skeletal structure of **6**.

The ^{1}H-NMR spectrum (Figure 4.58) of compound **6** showed three aromatic singlets at δ 6.58, δ 6.81 and δ 8.06 at three isolated environments, most likely on C-3, C-8 and C-11, respectively. Three distinctive methoxy signals were observed at δ 3.65, δ 3.86 and δ 3.90 corresponding to C-1, C-2 and C-10 of the upfield region of the spectrum. However, a significant difference between compound **6** and **7** was clarified by the

presence of a sharp intense singlet peak of *N*-Me at δ 2.55 in the ^{1}H-NMR spectrum of **6**. H-6a has a rather shielded position at δ 2.97 as compared to the corresponding compound **7** was due to the electron donating substituent effect of the latter *N*-Me adjacent to H-6a. The assignment for all the vicinal protons H-4/H-5 and H-6a/H-7 were made successful by the interpretation of COSY spectrum (Figure 4.61). The graphical illustration for all the relationships between relevant protons and carbons is shown in Figure 4.55.

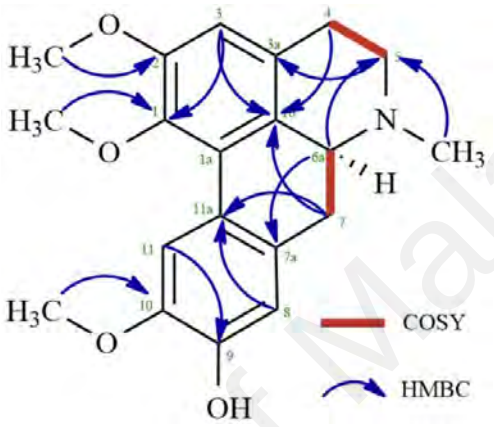

Figure 4.55: ^{1}H-^{1}H and ^{1}H-^{13}C correlations observed in COSY and HMBC spectra of **6**.

The ^{13}C NMR experiment (Figure 4.59) along with DEPT-135 spectrum (Figure 4.60) revealed the presence of twenty carbon signals which validated the molecular formula proposed above. The *N*-Me carbon resonated at δ 31.1 which was apparent in compound **6** but not for compound **7**. The HSQC spectrum (Figure 4.62) has verified the positions for each of the protons on their respective carbons. The HMBC spectrum (Figure 4.63) provided clear correlations between H-3/C-4, H-7/C-8 thus supporting the connectivity of ring A to ring B and C. Ring D was confirmed to be connected to ring C by the cross peak between H-7/C-11a and H-6a/C-7a. In a nutshell, the interpretation of all the complementary spectrums and techniques has concluded that compound **6** is (+)-*N*-methyllaurotetanine.

Table 4.8: NMR spectroscopy parameters and values of **6** (Ian R C Bick *et al.*, 1972; Castro-Saavedra *et al.*, 2016).

	^{1}H NMR	**HSQC**	**DEPT-135**	**HMBC**	**Literature**
Position	**δ_H, pattern, *J* (Hz)**	**^{13}C**	**Type ^{13}C**	**neighbor**	**δ_H, pattern**
1	-	144.7	Q	1-OMe, 3	-
1a	-	127.1	Q	11, 6a	-
1b	-	127.8	Q	4, 3, 7	-
2	-	152.8	Q	2-OMe	-
3	6.5812, *s*	110.2	-CH	1, 1b, 4	6.59, *s*
3a	-	127.4	Q	5, 6a	-
4	**H_a**: 3.19, *dd*, J_v=9.5, J_g=15.6 **H_b**: 2.68, *m*	29.8	$-CH_2$	1b , 5 , 3	H_a= 3.20, *dd* H_b= 2.64, *m*
5	**H_a**: 3.04, *J*= 3.6 **H_b**: 2.54, *dd*, J_v=9.5, J_g=16.0	43.2	$-CH_2$	3a , 6a	H_a=3.00, *d* H_b= 2.55, *dd*
6a	3.05, *m*	52.5	Q	5 , 7a 1a	2.99, *m*
7	**H_a**: 2.48, *m* **H_b**: 2.96, *dd*, *J*= 4.1, J_g=16.2	38.9	CH	1b , 4a	H_a= 2.58, *m* H_b= 2.97, *m*
7a	-	128.2	Q	1a , 6a	-
8	6.81, *s*	114.1	8	4a , 10 , 7	6.80, *s*
9	-	145.3	Q	11 , 7a	-
10	-	145.7	Q	4a , 8	-
11	8.09, *s*	111.3	CH	9 , 7a ,1a	8.06, *s*
11a	-	123.5	Q	1 , 1a	-
1 - OMe	3.65, *s*	60.3	CH_3	1a , 2	3.65, *s*
2 - OMe	3.86, *s*	56.2	CH_3	1 , 3	3.87, *s*
10 - OMe	3.90, *s*	55.9	CH_3	9 , 11	3.90, *s*
N-Me	2.55, *s*	31.0	CH_3	5 , 6a	2.54, *s*

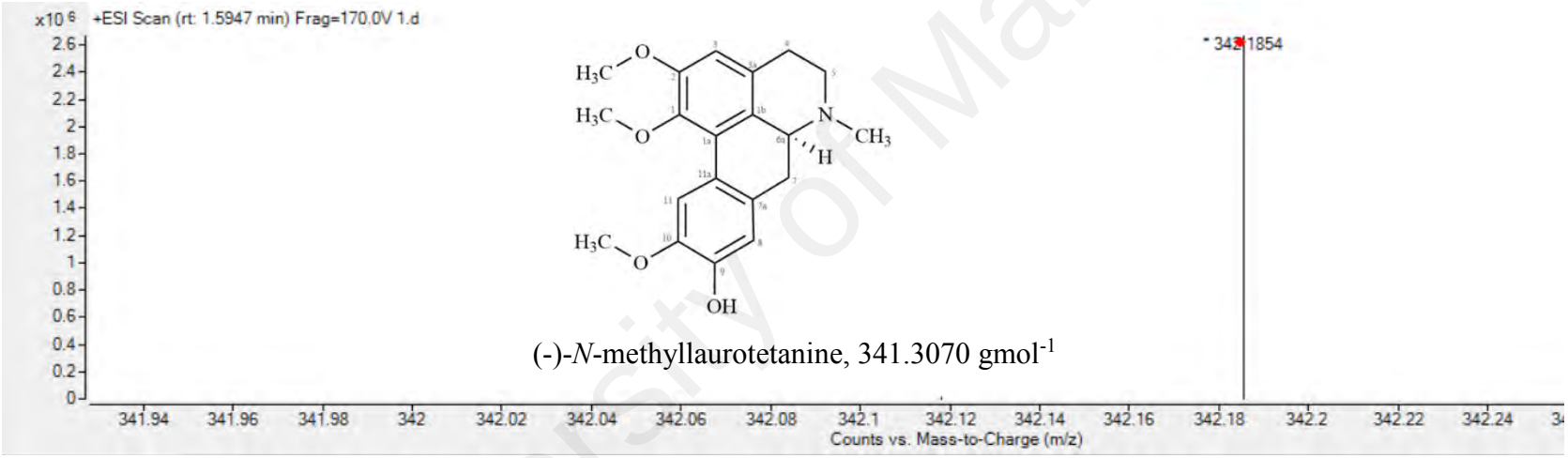

(-)-*N*-methyllaurotetanine, 341.3070 gmol^{-1}

Figure 4.56: MS spectrum of **6** at *m/z* 342.3070.

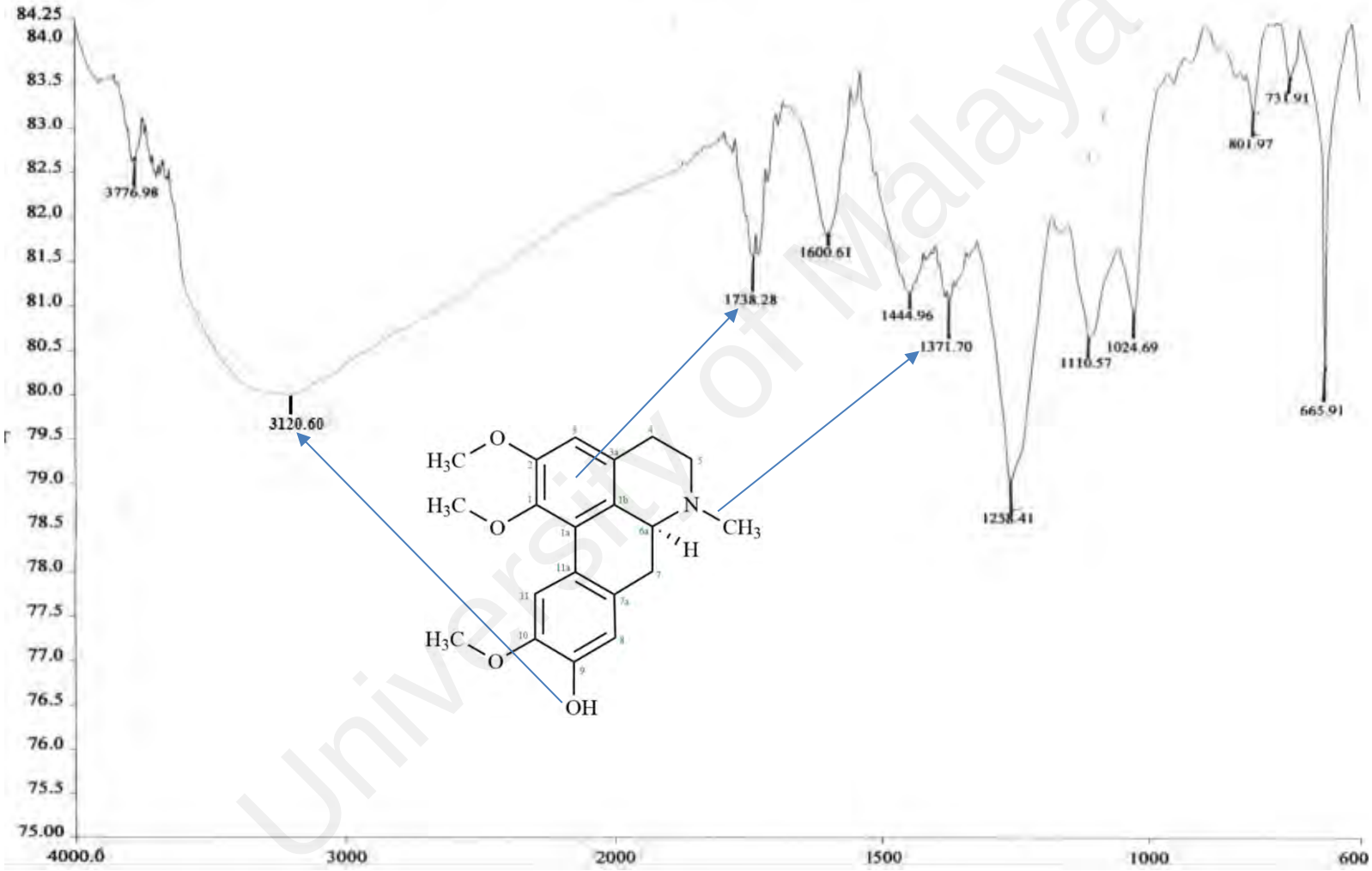

Figure 4.57: FTIR spectrum of **6**.

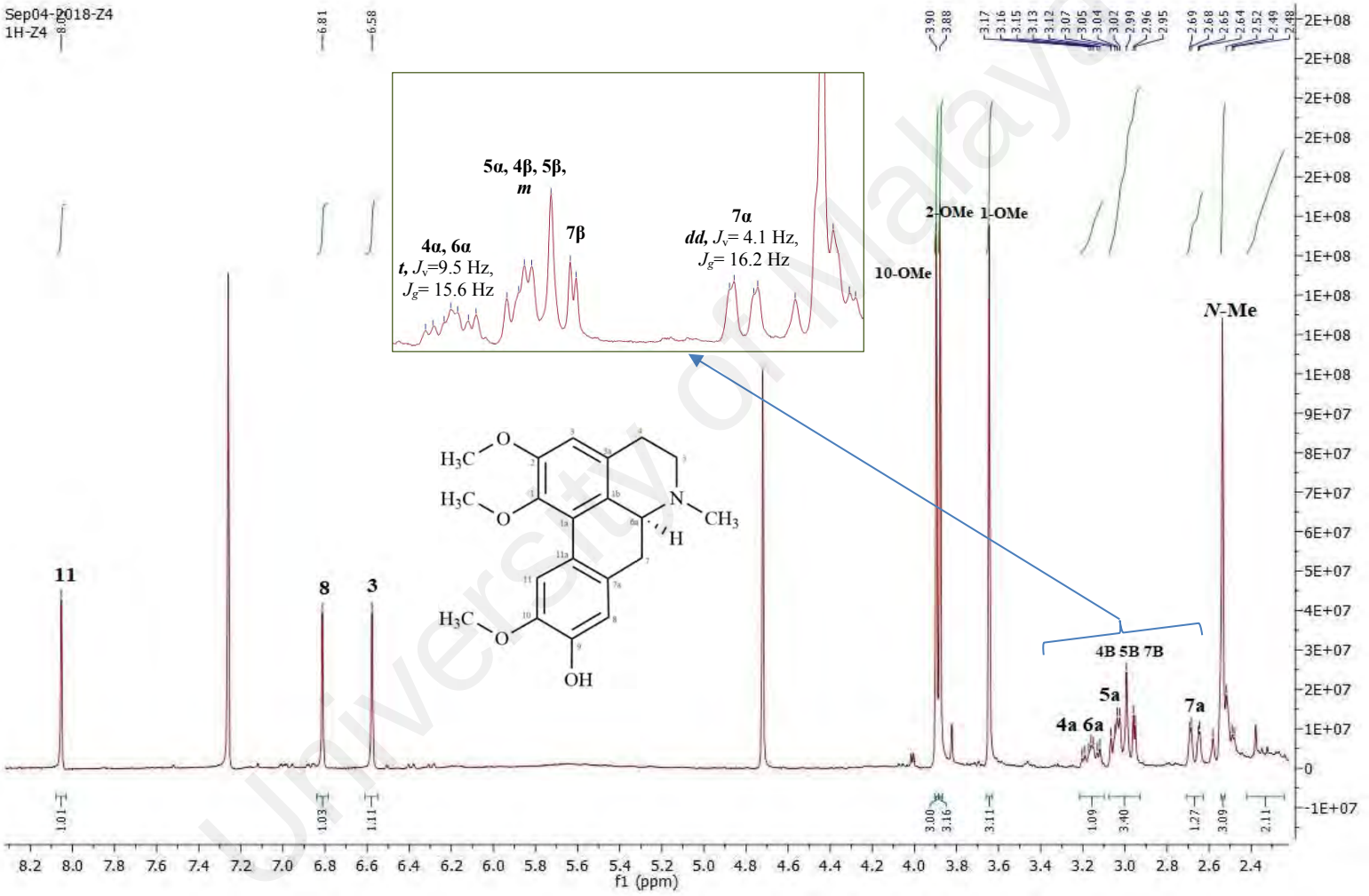

Figure 4.58: ^{1}H NMR spectrum of **6**.

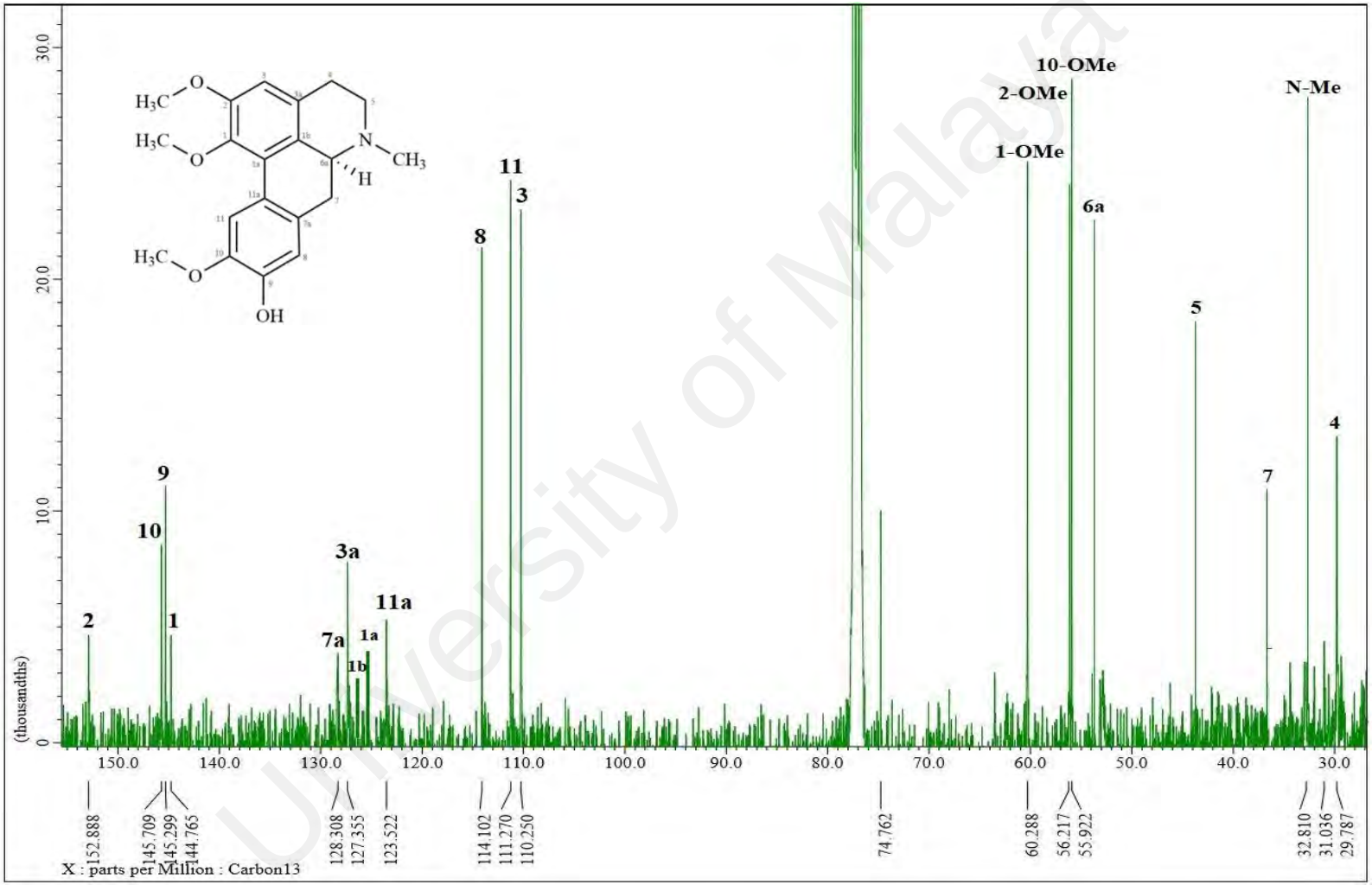

Figure 4.59: ^{13}C NMR spectrum of **6**.

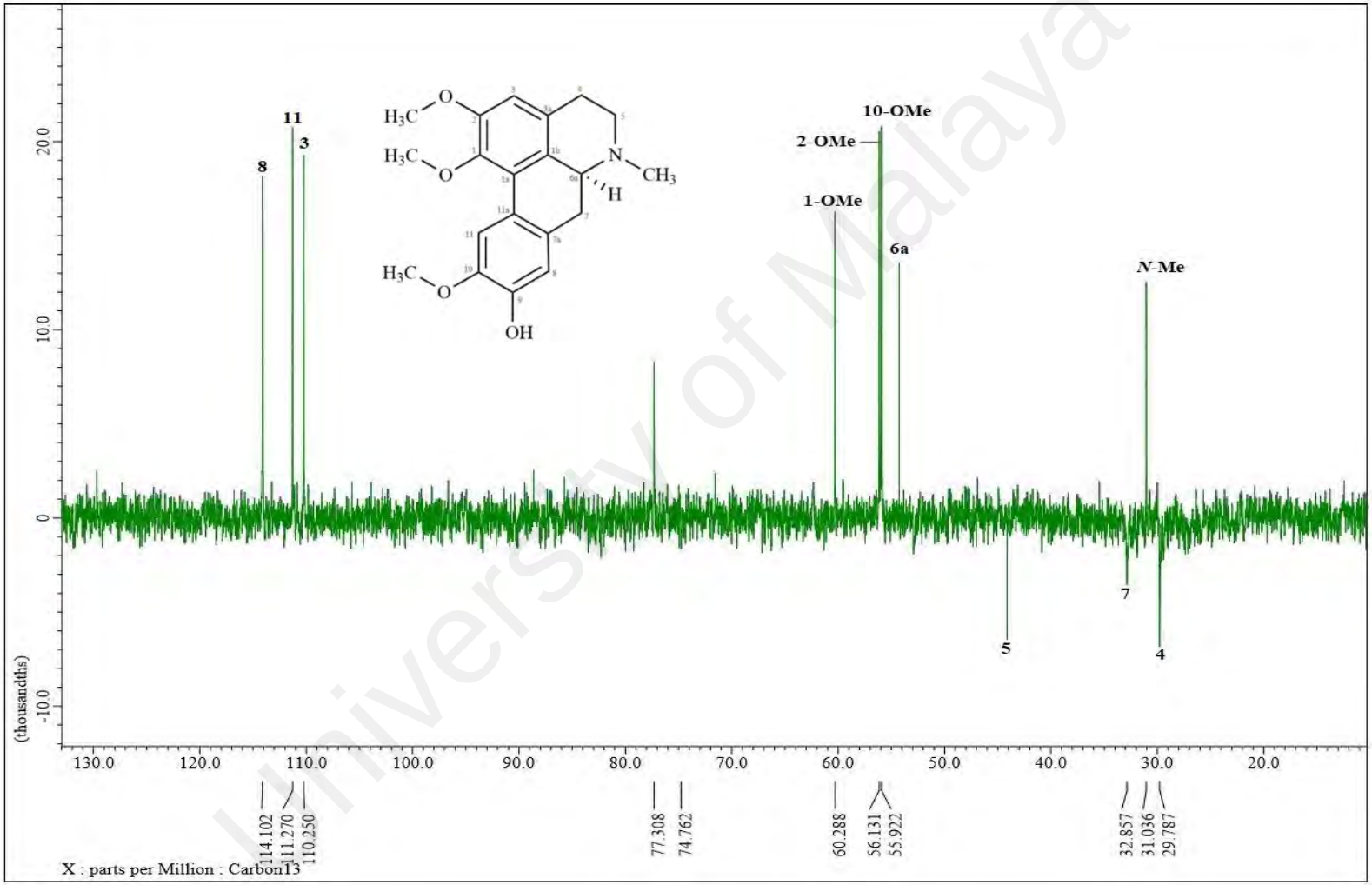

Figure 4.60: DEPT-135 spectrum of **6**.

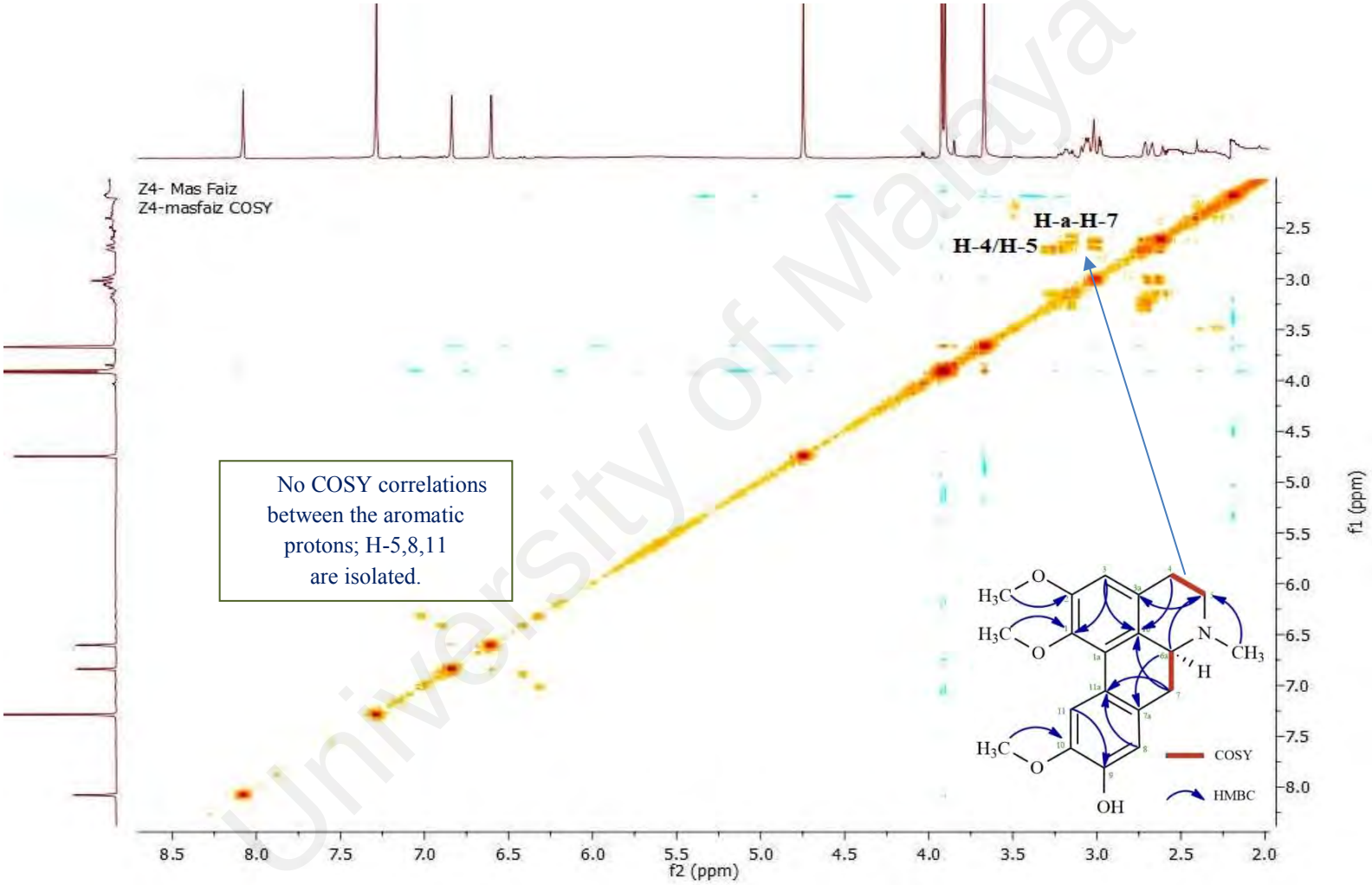

Figure 4.61: COSY spectrum of **6**.

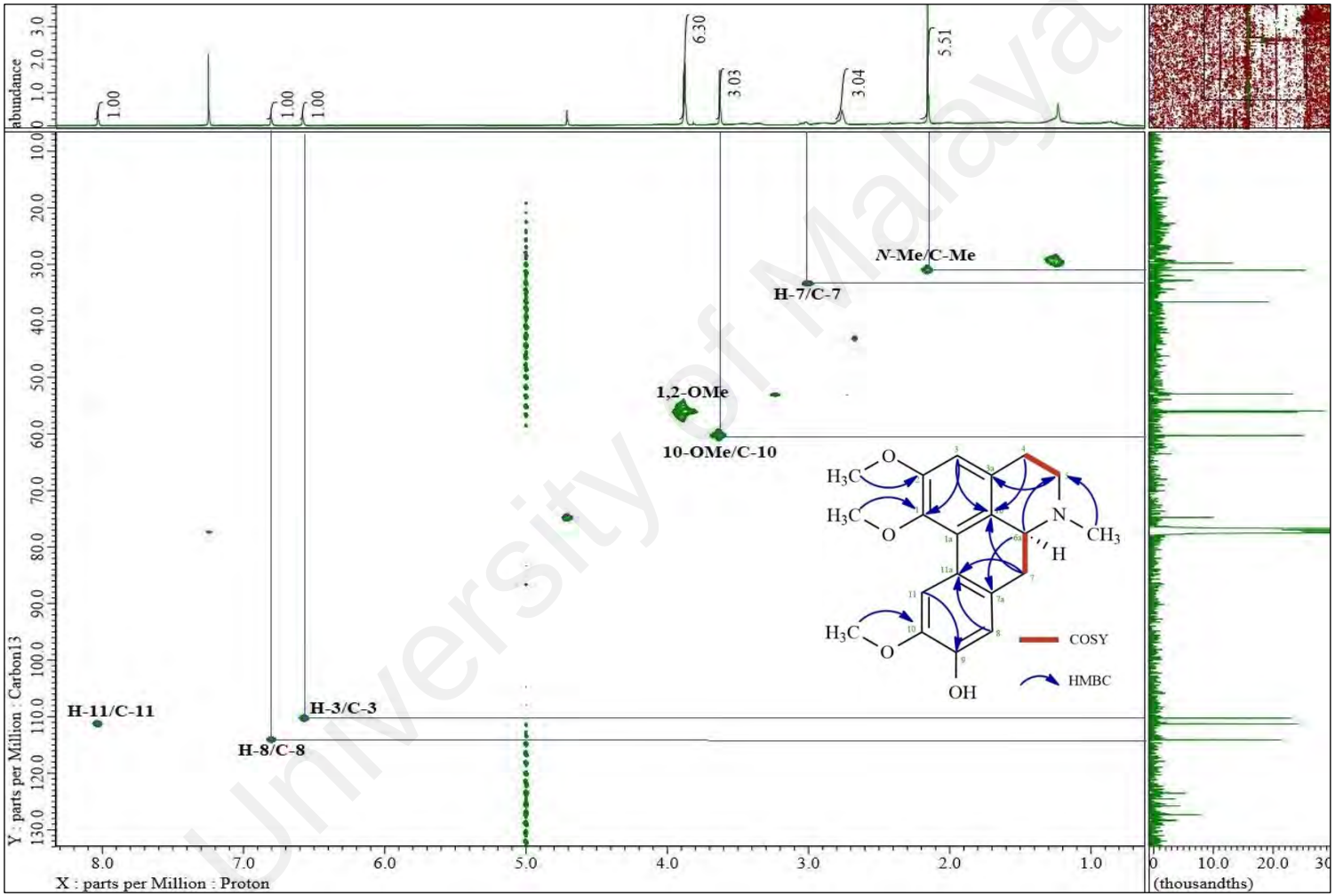

Figure 4.62: HSQC spectrum of **6**.

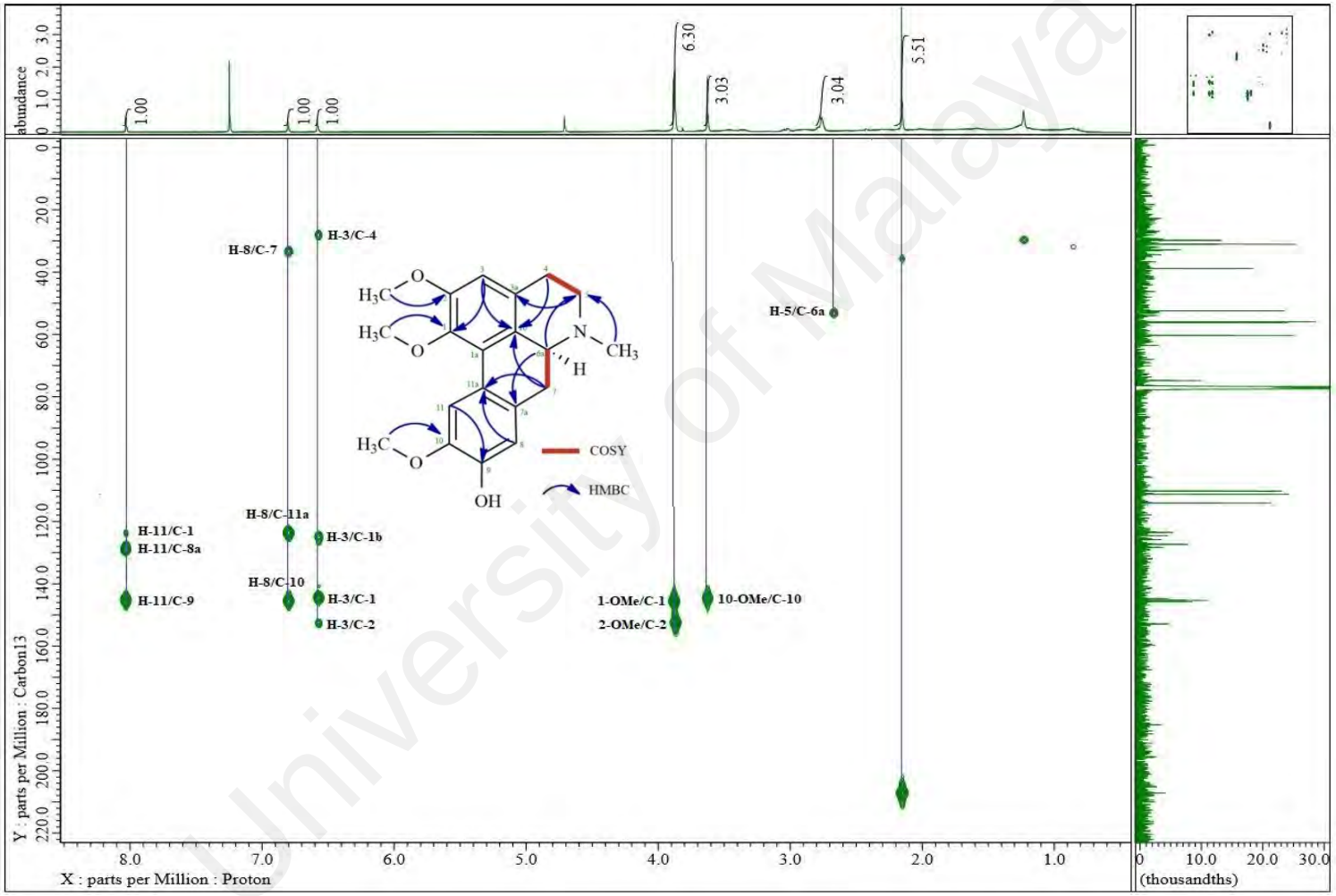

Figure 4.63: HMBC spectrum of **6.**

4.2.7 (+)-Laurotetanine **7**

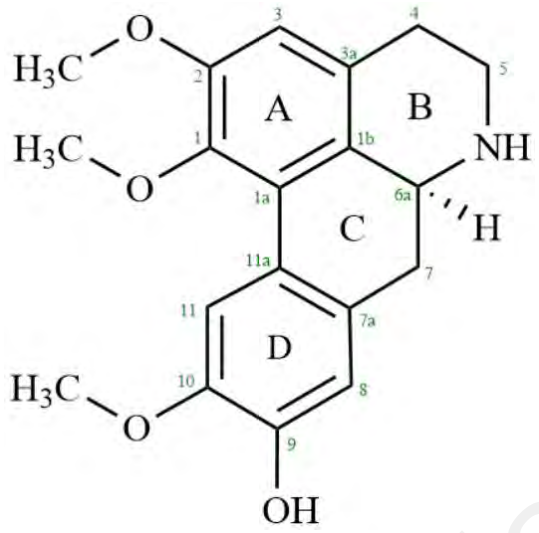

IUPAC: (S)-1,2,10-trimethoxy-5,6,6a,7-tetrahydro-4H-dibenzo[de,g]quinolin-9-ol

Compound **7** was obtained as an optically active dark brown amorphous solid with $[\alpha]_D^{25}$= +37° (c= 0.01, Methanol). The positive LCMS-IT-TOF spectrum (Figure 4.65) exhibited a pseudomolecular ion peak, $[M+H]^+$ at *m/z* 328.1882 which is associated with the molecular formula $C_{19}H_{21}NO_4$ agreeable to 10 degrees of unsaturation. The UV spectrum showed maximum absorptions at λ_{max} 227, 248,280 and 301 nm which were typical for an aporphine moiety, thus suggesting a 1, 2, 9, 10-tetrasubtituted aporphine skeleton. The IR absorption bands at υ_{max} 3429 (-OH stretching), 2920 (C-H stretch), 2097 (N-H stretch), 1653 (C=C stretch), 1464 (=C-H stretch) and 1238 (C-O stretch) cm^{-1} indicated all the relevant functional groups on the skeletal structure (Figure 4.66).

The ^{1}H-NMR spectrum (Figure 4.67) of compound **7** displayed a total of twenty-three proton integrations with twenty of them located in the high field region and three aromatic protons in the lower field region of the spectra. Three distinctive methoxyl group signals were seen at δ 3.65 (1-OMe), δ 3.88 (2-OMe) and δ 3.90 (10-OMe). 1-OMe appeared to be at the most upfield position compared to the other two since its protons were shielded by the anisotropic effect of ring D. The aliphatic protons (H-4a,4b, H-5a,5b, H-6a, H-

7a,7b) resonated as overlapping multiplets at the region between δ 2.64 – 3.16, experiencing similar chemical environment. H-6a of compound **7** formed a slightly deshielded resonance peak as compared to compound **6** as the adjacent secondary amine is not methyl-substituted. Hence, it behaved as an electron-withdrawing substituent. The three isolated aromatic protons; H-3, H-8 and H-11 formed three separate singlet signals further downfield at δ 6.58, δ 6.81 and δ 8.06, respectively. H-11 has the highest chemical shift because of the deshielding magnetic anisotropic effect to ring D, electron withdrawal substituent effect of the adjacent 10-OMe and also the electron affinity of the nearby electronegative 1-OMe on ring A.

Carbon signals from ^{13}C-NMR spectrum (Figure 4.68) supported by DEPT-135 spectrum (Figure 4.69) have disclosed a total of three methyls, three methylenes, four methines and nine quaternary carbons in the molecule, consistent with the molecular structure proposed. The four downfield carbon peaks at δ 152.1, δ 145.3, δ 144.9 and δ 144.3, could be attributed to C-2, C-10, C-9 and C-1 because of their aromatic oxygen substituted nature (C=C-O-). The three methylene carbons resonated at δ 30.9, δ 33.8, δ 43.2 were assigned accordingly to C-4, C-7 and C-5, while the methine carbon (C-6a) was coordinated at δ 53.2.

Long-range correlation deduced from the HMBC spectrum (Figure 4.71) indicated that ring C was fused to ring D through C-7a and C-1a junction. Furthermore, the connectivity of ring A with ring B was clearly observed *via* the correlation between H-3 to C-4 and H-3 to C-1b, respectively. The HMBC cross peaks between 1-OMe/C-1, 2-OMe/C-2 and 10-OMe/C-10 confirmed the placements of the methoxyl groups at their respective carbons. The graphical assignments for all the cross peaks generated are depicted in Figure 4.64. Thorough analysis of the combined techniques has led to the elucidation of **7** as (+)-laurotetanine.

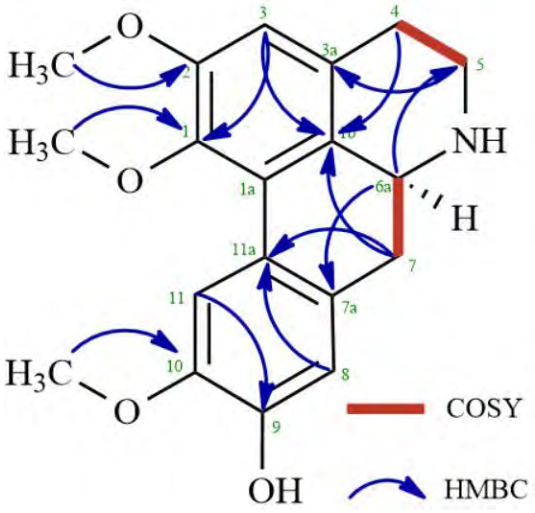

Figure 4.64: ^{1}H-^{1}H and ^{1}H-^{13}C correlation observed in COSY and HMBC spectra of **7**.

Table 4.9: NMR spectroscopy parameters and values of **7** (I Ralph C Bick et al., 1981; Castro-Saavedra et al., 2016).

	^{1}H NMR	**HSQC**	**DEPT-135**	**HMBC**	**Literature**
Position	**δ_H, pattern, *J* (Hz)**	**^{13}C**	**Type ^{13}C**	**neighbor**	**δ_H, pattern**
1	-	144.3	Q	1-OMe, 3	-
1a	-	127.1	Q	11, 6a	-
1b	-	123.8	Q	4, 3, 7	-
2	-	152.2	Q	2-OMe	-
3	6.5812, *s*	110.3	-CH	1, 1b, 4	6.59, *s*
3a	-	127.1	Q	5, 6a	-
4	**H_a**: 2.68, *dd*, J_v= 3.6, J_g=13.2 **H_b**: 3.19	29.7	-CH_2	1b , 5 , 3	H_a= 2.64, *dd* H_b= 3.18, *m*
5	**H_a**: 2.64, *J*= 3.6 **H_b**: 3.04, *dd*, J_v=6.0, J_g=12.5	53.2	-CH_2	3a , 6a	H_a=2.65, *d* H_b= 3.03, *dd*
6a	3.10, *m*	62.50	Q	5 , 7a 1a	2.97, *m*
7	**H_a**: 2.38, *m* **H_b**: 2.96, *dd*, J_v= 4.1, J_g= 14.7	33.9	CH	1b , 4a	H_a= 2.48, *m* H_b= 2.95, *m*
7a	-	130.2	Q	1a , 6a	-
8	6.81, *s*	113.9	8	4a , 10 , 7	6.80, *s*
9	-	144.9	Q	11 , 7a	-

10	-	145.4	Q	4a , 8	-
11	8.06, *s*	111.2	CH	9 , 7a ,1a	8.06, *s*
11a	-	123.9	Q	1 , 1a	-
1 - OMe	3.65, *s*	60.2	CH_3	1a , 2	3.65, *s*
2 - OMe	3.88, *s*	55.8	CH_3	1 , 3	3.87, *s*
10 - OMe	3.90, *s*	56.1	CH_3	9 , 11	3.90, *s*

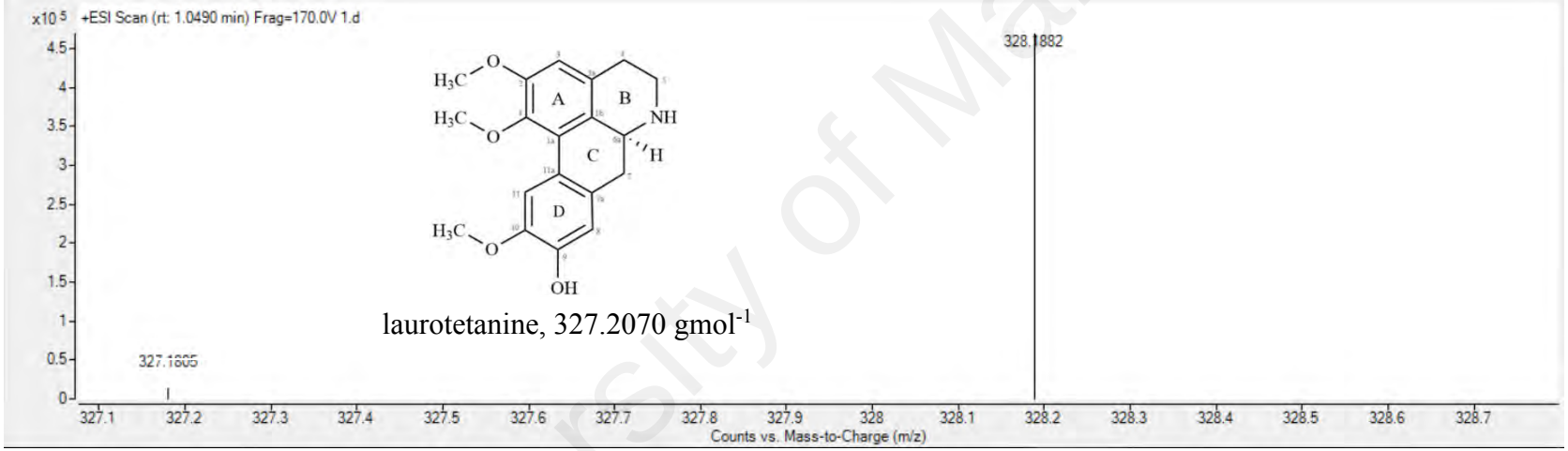

Figure 4.65: MS spectrum of **7** at *m/z* 328.1882.

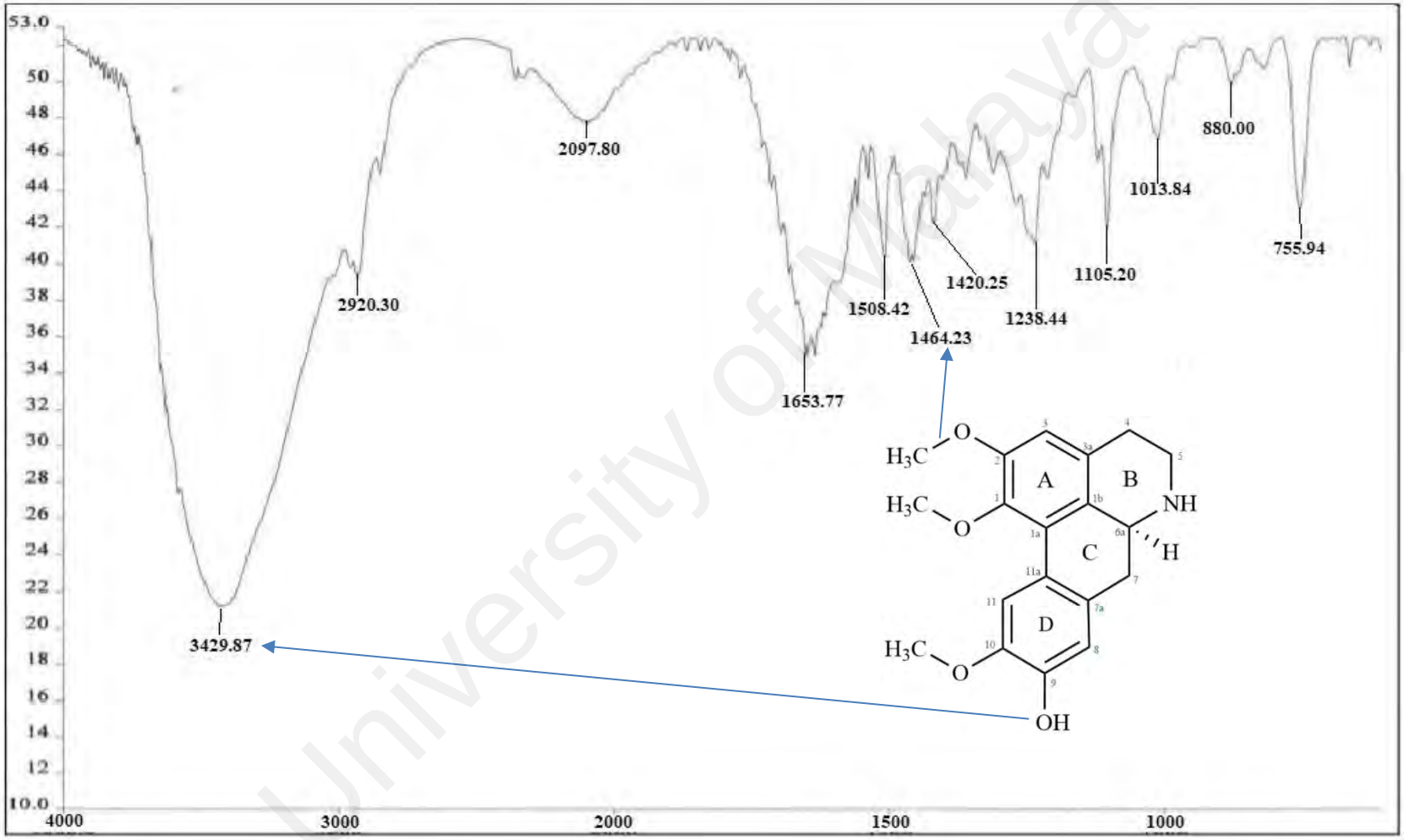

Figure 4.66: FTIR spectrum of **7**.

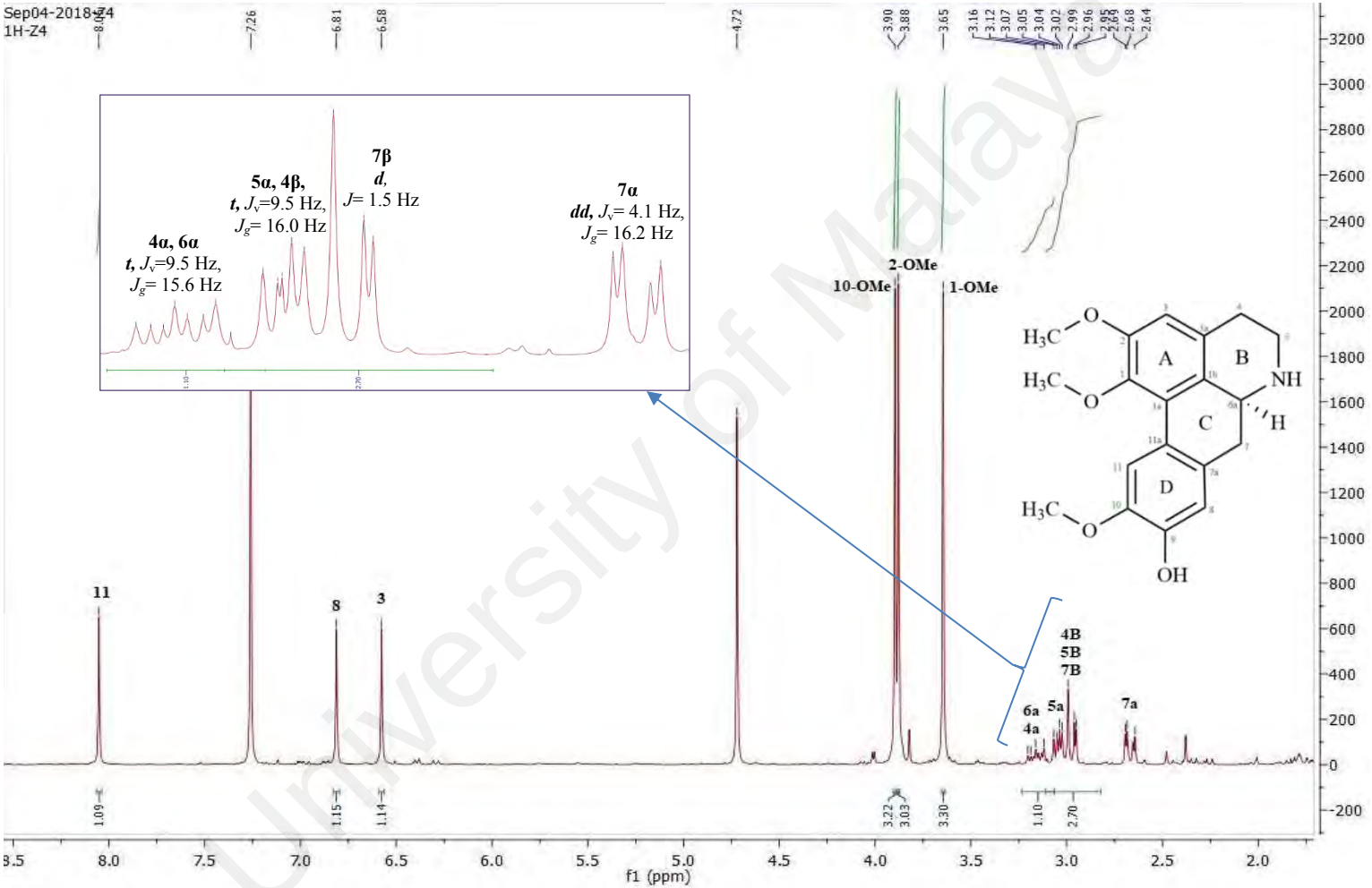

Figure 4.67: ^{1}H-NMR spectrum of **7**.

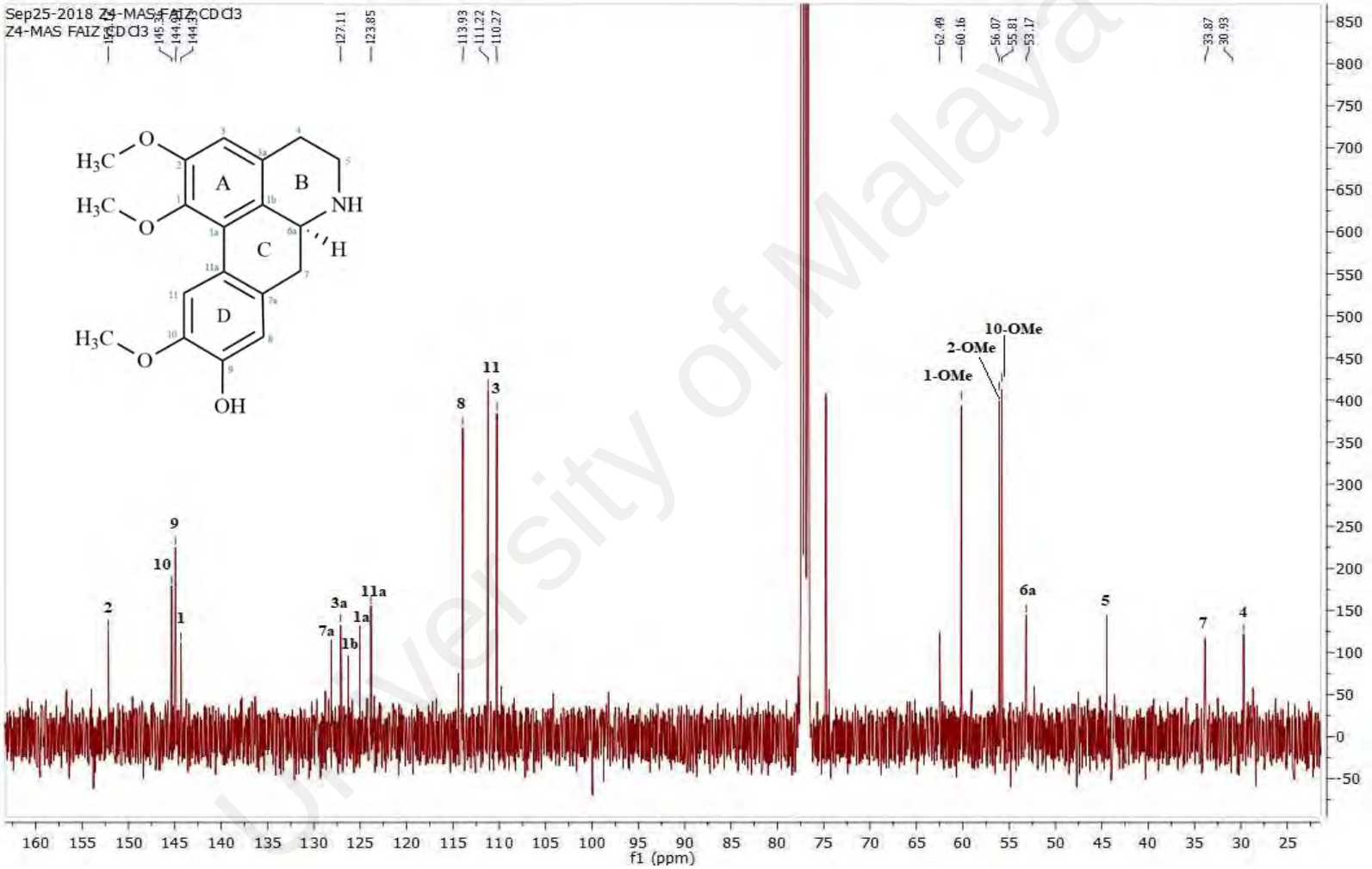

Figure 4.68: ^{13}C-NMR spectrum of **7**.

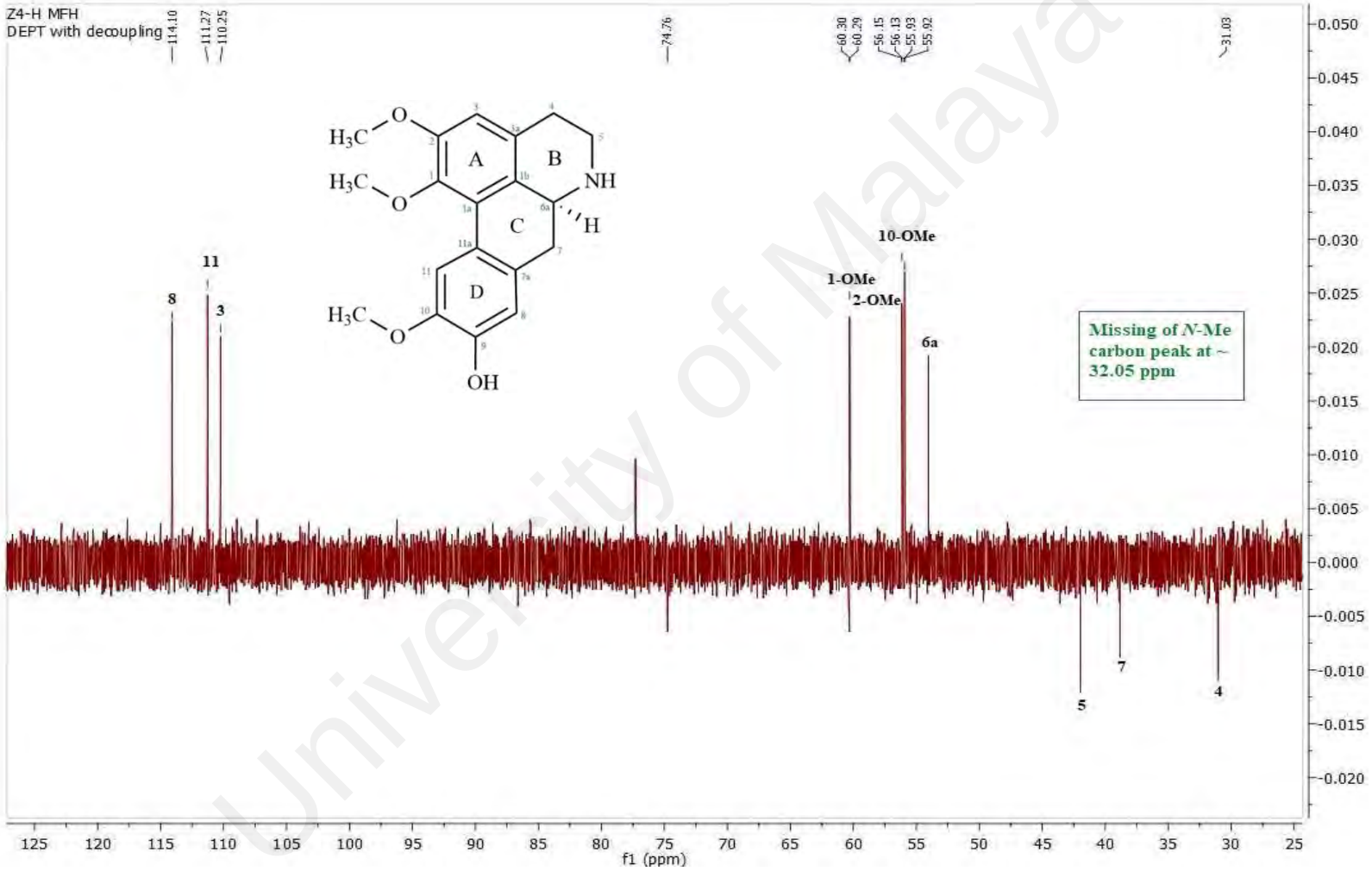

Figure 4.69: DEPT-135 spectrum of **7**.

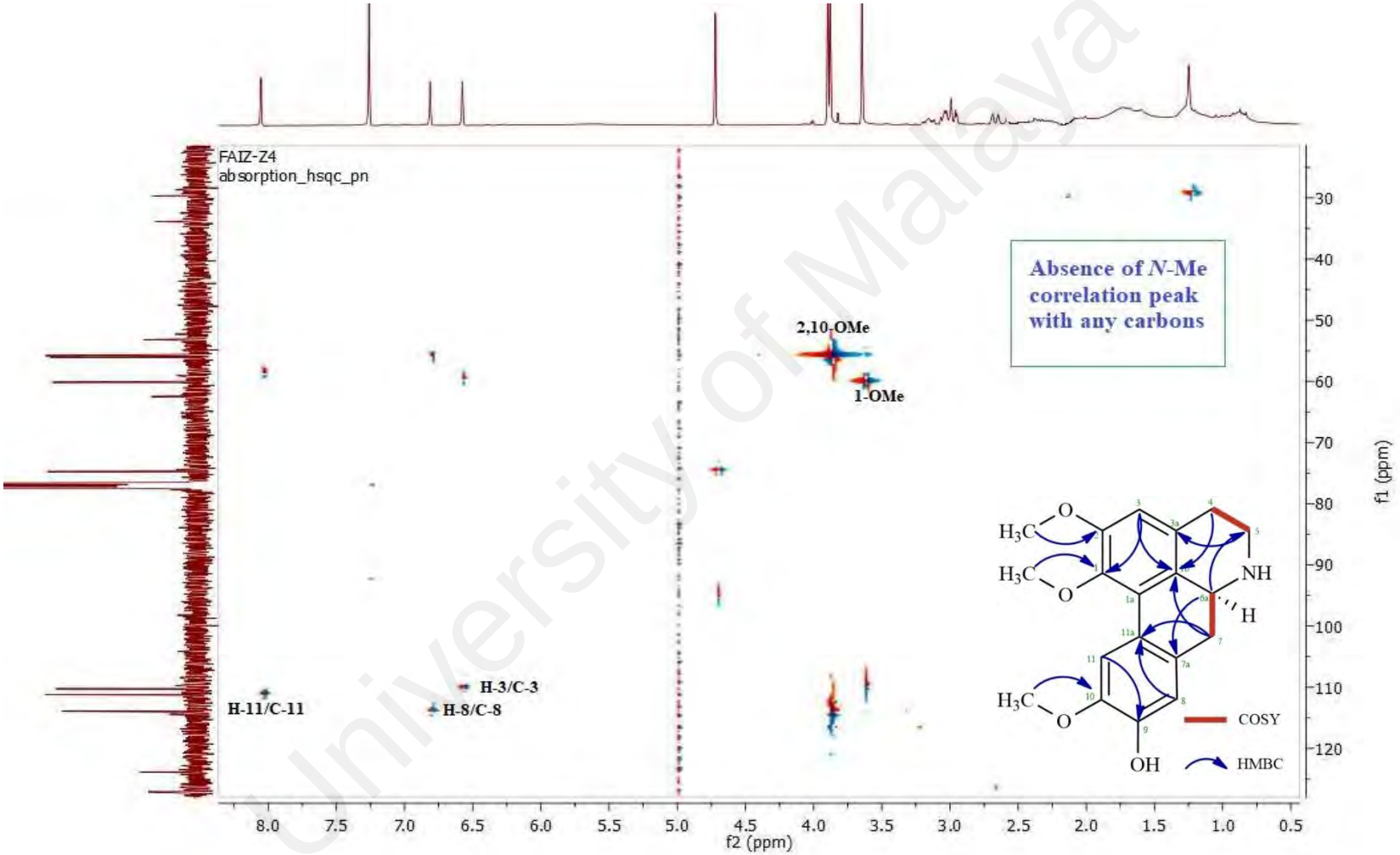

Figure 4.70: HSQC spectrum of **7**.

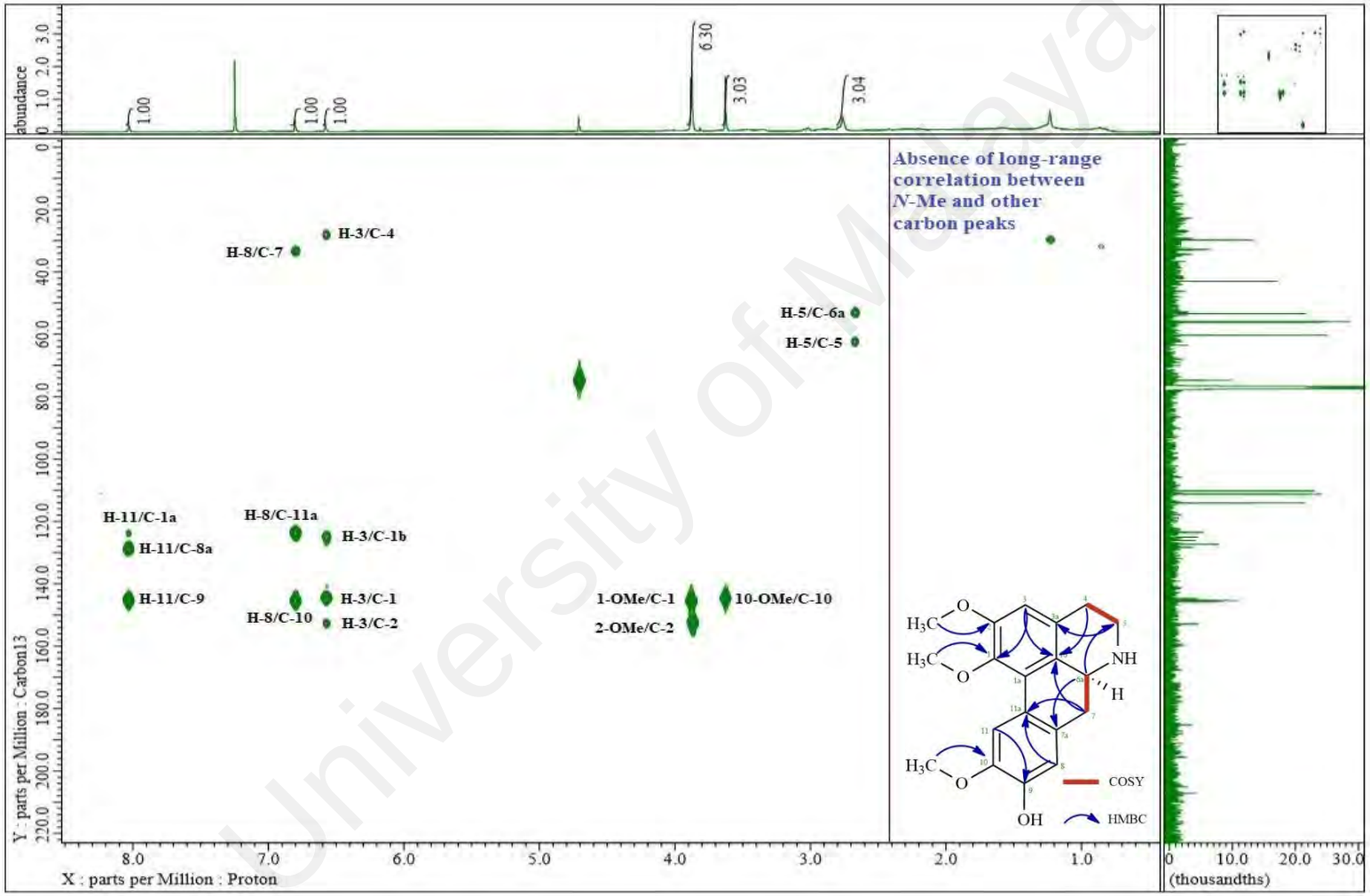

Figure 4.71: HMBC spectrum of **7**.

4.3 Corrosion inhibition study of *Cryptocarya nigra*

The corrosion inhibition experiments were done at the School of Chemical Sciences, University Science Malaysia, Penang. CNHE, CNDE, CNME and three pure compounds; *N*-methylisococlaurine **1**, atherospermine **3** and *N*-methyllaurotetanine **6** isolated from CNDE were tested for their potential as green corrosion inhibitors. Studies were carried out *via* electrochemical method which consists of electrochemical impedance study (EIS) and potentiodynamic dynamic (PDP). Each step was done in duplicate to ensure reproducibility of the results. The inhibitor solutions were prepared into 10, 50, 100, 200, 500 and 1000 ppm by mixing different concentrations of the samples with the appropriate amount of 1.M hydrochloric acid solution. The results obtained are provided below.

4.3.1 Electrochemical impedance study (EIS)

This study was performed to investigate the amount of current flow and the resistance value occurring on the MS surface with and without the presence of inhibitors. The open-circuit potential, E_{ocp} for each of the experiment conducted was first examined for 10 minutes to obtain a steady current reading on the mild steel surface. All the processes involved in the electrical response of the system were fitted against an equivalent Randle CPE circuit model (Figure 4.72) and illustrated as Nyquist plots in Figure 4.73-4.78. Solution resistance (R_s) describes the ohmic resistance while the charge-transfer resistance (R_{ct}) represents the inhibitor's resistance towards oxidation of the metal surface and it is inversely proportional to the corrosion rate. Pure double layer capacitor (C_{dl}) is replaced by a constant phase element (CPE) to justify the semicircle shape of the Nyquist plot (Jüttner, 1990). A useful rule of thumb is that, the higher the diameter of the Nyquist plot, the higher the R_{ct} value, hence the higher the inhibition efficiency of a given inhibitor. All the electrical values after the fitting procedure are tabulated in Table 4.10.

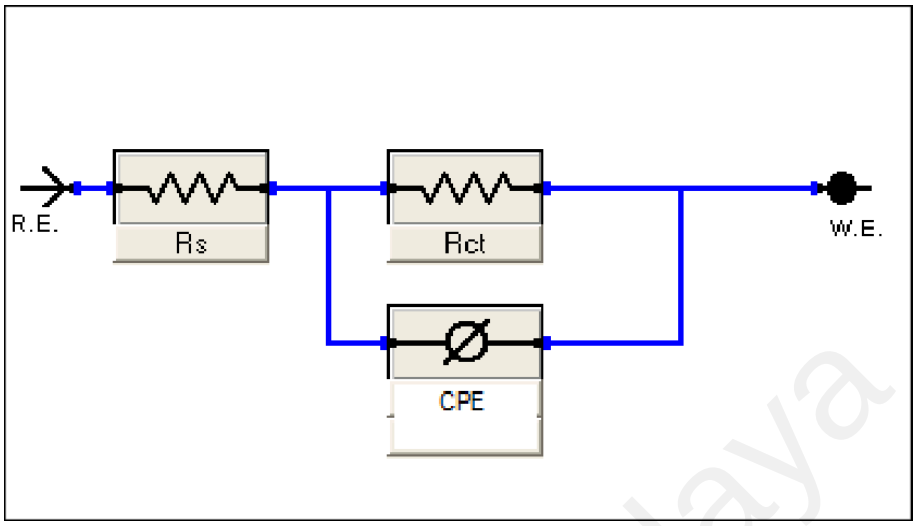

Figure 4.72: The Randle's CPE equivalent circuit used to fit the impedance data.

Table 4.10: Impedance corrosion parameters for all the studied inhibitors on MS in 1M HCl medium.

Inhibitor	Conc. (ppm)	R_s (Ω)	R_{ct} (Ω)	n	CPE (μF cm^{-2})	IE (%)
-	0	1.345	40.53	0.9550	939.8	-
CNHE	10	2.997	42.11	0.7552	822.50	3.75
	100	2.228	54.82	0.6235	735.40	26.06
	200	2.115	66.82	0.7070	722.16	39.34
	500	2.445	85.34	0.7100	601.45	52.50
	1000	2.205	83.70	0.6485	630.42	51.57
CNDE	10	2.299	114.6	0.7480	785.12	64.63
	100	2.682	201.7	0.8422	528.68	79.09
	200	2.107	296.5	0.8826	415.54	86.33
	500	2.702	453.0	0.8248	249.73	**91.05**
	1000	2.737	400.0	0.8375	360.80	89.86
CNME	10	2.228	58.38	0.8602	810.57	30.57
	100	2.238	188.60	0.8522	659.27	78.51
	200	2.150	268.12	0.7562	509.21	84.88
	500	2.680	326.50	0.9210	454.83	87.58
	1000	2.465	301.20	0.8960	472.60	86.54
1	100	2.895	86.2	0.741	628.4	52.98
	200	2.924	129.3	0.792	53405	68.65
	500	2.735	181.7	0.874	412.6	77.70
	1000	2.697	277.5	0.890	258.4	85.40
3	100	2.890	77.1	0.543	771.2	47.46
	200	2.772	129.4	0.768	569.4	68.67
	500	2.769	184.7	0.681	395.4	78.05
	1000	2.766	268.6	0.630	265.3	84.91
6	100	2.740	77.8	0.810	623.6	47.90
	200	2.723	104.3	0.594	600.5	61.14
	500	2.682	195.6	0.599	496.3	79.27
	1000	2.056	338.7	0.602	188.4	**88.05**

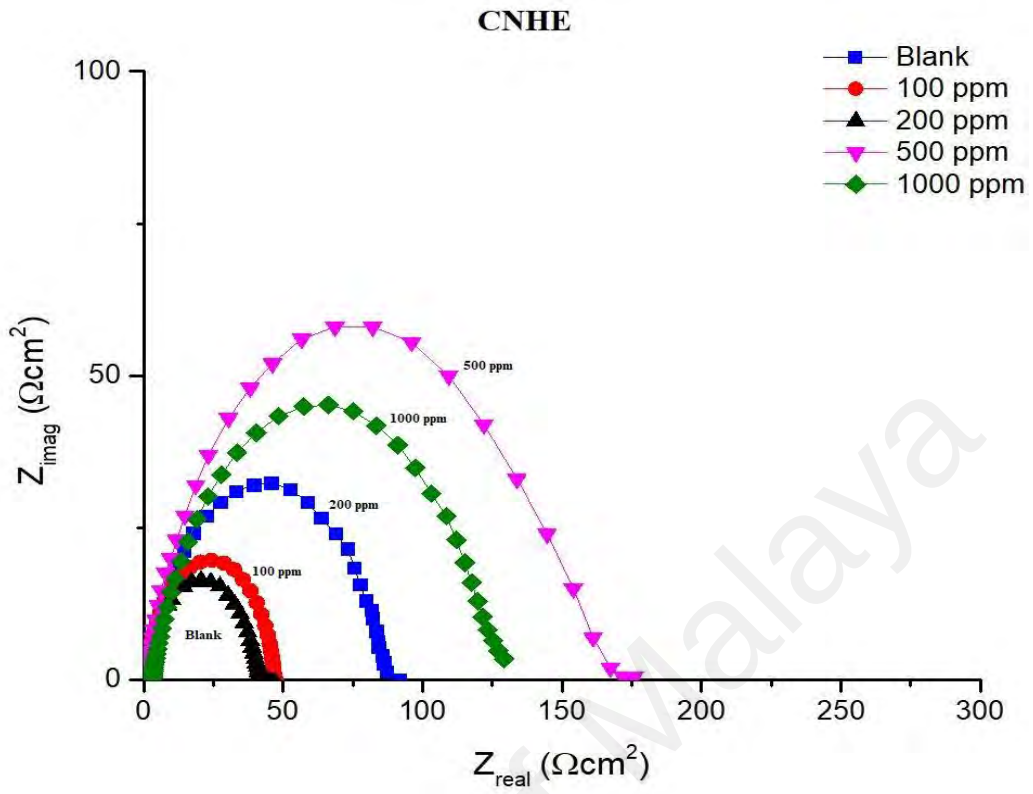

Figure 4.73: Nyquist plots for all concentrations of CNHE in 1M HCl at 303 K.

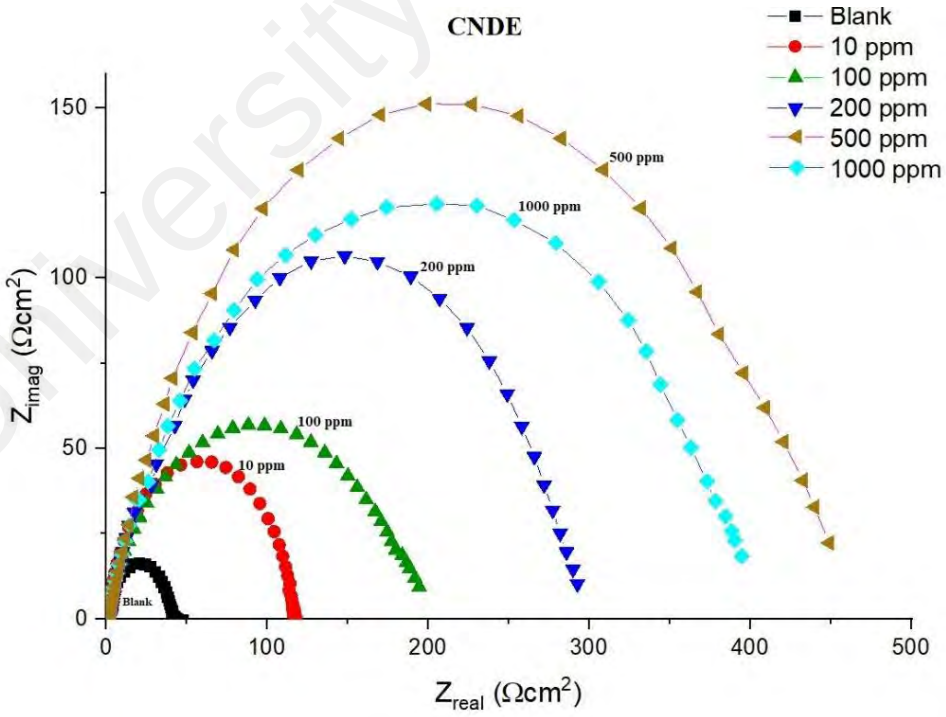

Figure 4.74: Nyquist plots for all concentrations of CNDE in 1M HCl at 303 K.

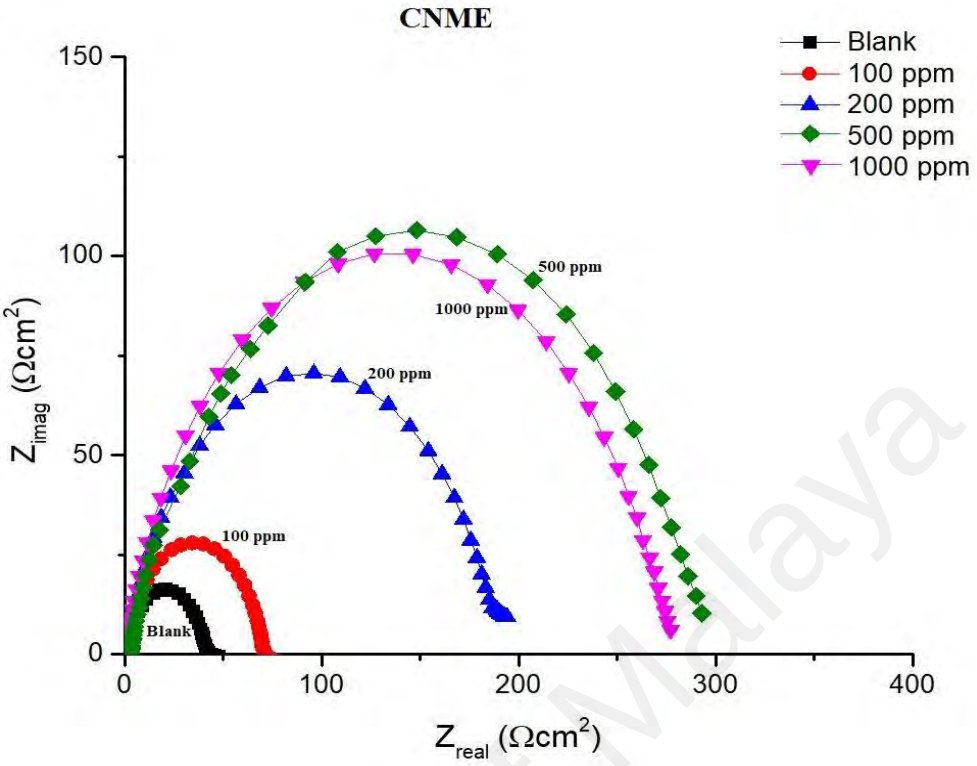

Figure 4.75: Nyquist plots for all concentrations of CNME in 1M HCl at 303 K.

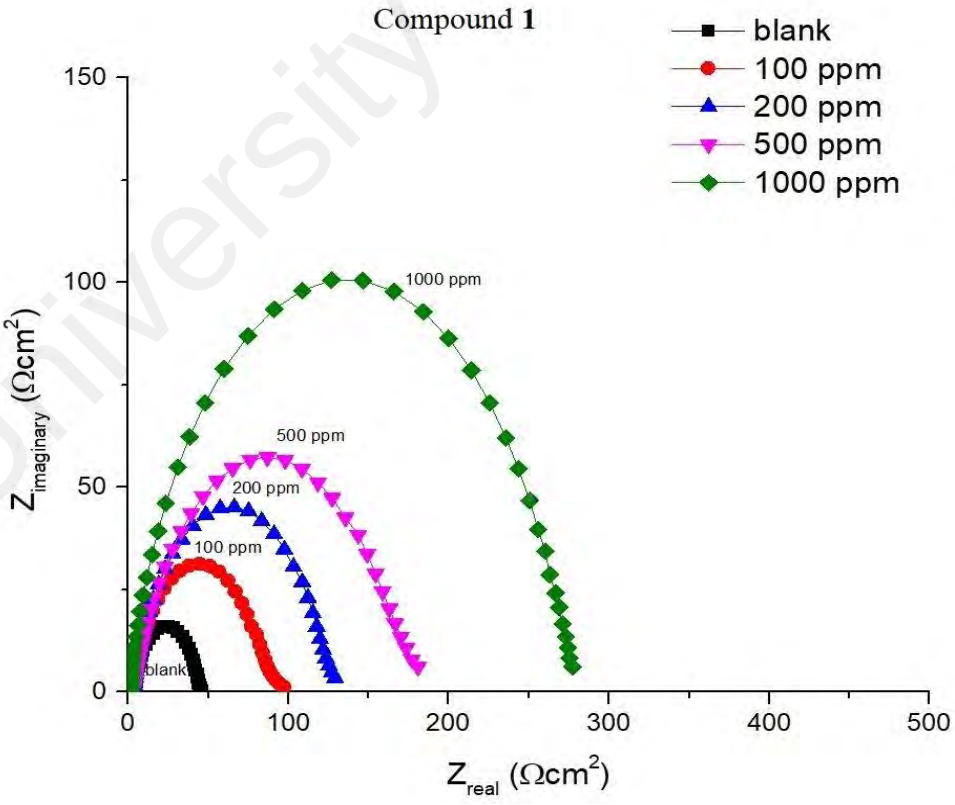

Figure 4.76: Nyquist plots for all concentrations of **1** in 1M HCl at 303 K.

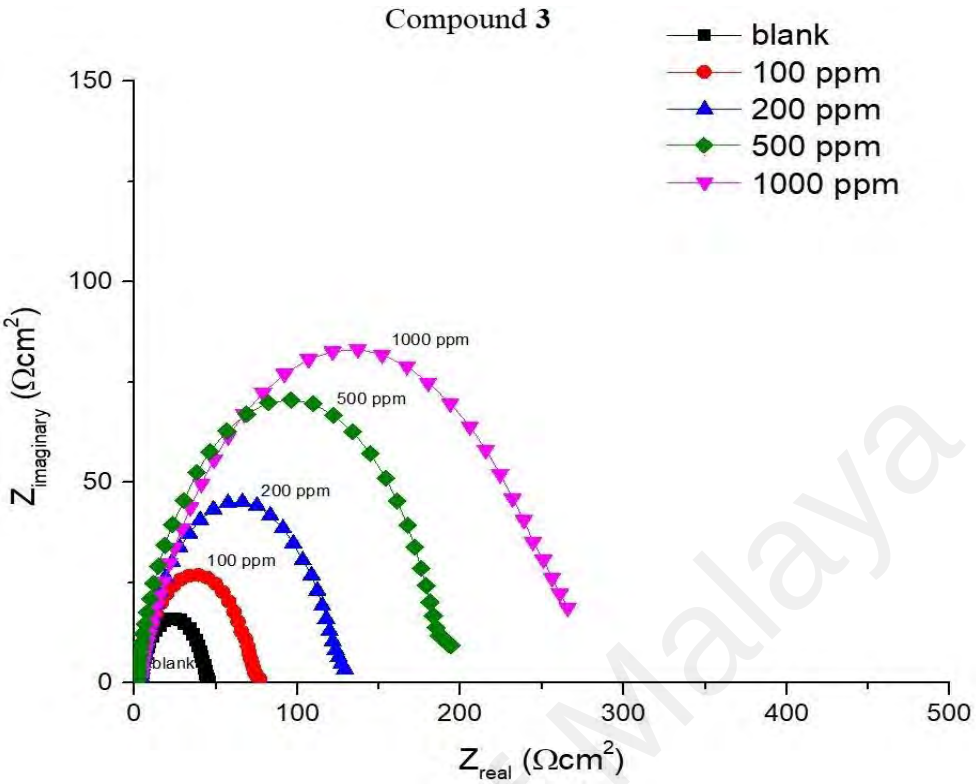

Figure 4.77: Nyquist plots for all concentrations of **3** in 1M HCl at 303 K.

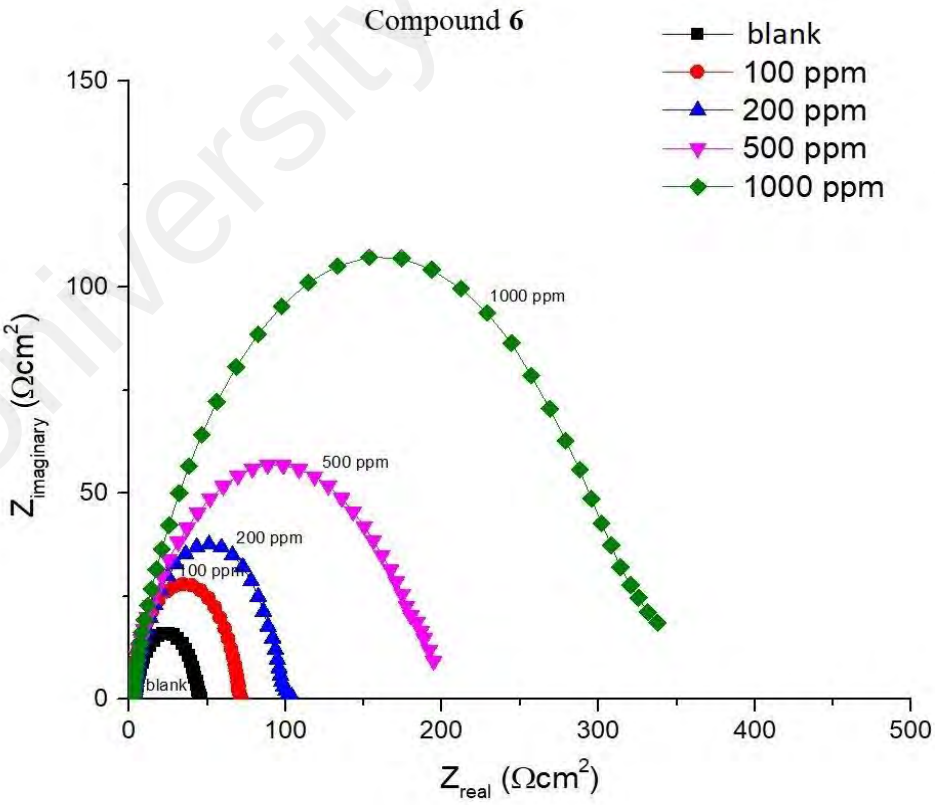

Figure 4.78: Nyquist plots for all concentrations of **6** in 1M HCl at 303 K.

Based on Table 4.10, CNDE showed 91.08 % of inhibition performance at 500 ppm which was the highest compared to CNHE and CNME. The Nyquist plot for CNDE is depicted in Figure 4.74. It could be observed that the diameter of Nyquist plots increased upon increasing inhibitors concentration. This could correspond to the strengthening of the inhibitive film on mild steel surface (Hussin, Jain Kassim *et al.*, 2016). From the Ohmic Law where V=IR, the higher the resistance value (R_{ct}), the lower the electrical current (I) flow, therefore a lower number of electrons being transferred across the metal surface. Lower electron transfer across the surface suggested that the metal dissolution process (oxidation of iron) were being inhibited [(Mathina & Rajalakshmi, 2016)]. The inhomogeneity of the metal surface resulted in lower values of n ($0.5 < n < 1$; depressed semicircle capacitive loop). The maintained semicircle shapes of the Nyquist plots over the experiments indicated that the corrosion inhibition process occurs through a charge transfer mechanism (Satapathy, Gunasekaran, Sahoo *et al.*, 2009). CNDE acted as a concentration independent inhibitor with low optimum concentration value of 500 ppm as compared to the pure alkaloids. This is because CNDE is made up from a combination of compounds, therefore, forming a bulkier solution. Above 500 ppm, CNDE showed less IE % because the inhibitors were replaced by water molecules or chloride ions (Cl^-) when the solution is above its critical concentration (Inzunza *et al.*, 2013).

In the other hand, the pure alkaloids displayed concentration-dependent inhibition patterns with increasing IE % up until 1000 ppm as they have not reached their optimum concentrations. They have higher saturation points above 1000 ppm as compared to their extract (CNDE) due to the less bulk solution formed individually by them (Raja, Qureshi, Abdul Rahim *et al.*, 2013; Wang *et al.*, 1999). Table 4.10 revealed that **6** showed 88.05 % of inhibition performance at 1000 ppm which was the highest compared to **1** and **3**. The Nyquist plots for each of the alkaloid were shown in Figure 4.76-4.78). The increase

in R_{ct} and decrease in CPE values upon addition of **6** indicated reduction in the corrosion rate with the formation of adsorbed protective film on the metal-solution interface. The inhibition action suppresses both the CPE and corrosion current density (i_{corr}) by replacing water molecules present on the working electrode surface by the inhibitors (Crawford, Barmatov *et al.*,2016). The corrosion process was mainly controlled by the charge transfer mechanism and characterized by a single relaxation time constant. No change in inhibition mechanism was observed throughout the whole test period upon addition of the alkaloids (Amin, Khaled, Mohsen, & Arida, 2010).

To sum things up, all alkaloidal inhibitor solutions showed less R_{ct} values than that of their parent extract, CNDE. The presence of many other constituents in the extract itself may have synergistically improved its corrosion inhibition efficiency simultaneously strengthening the adsorption of crude extracts over the MS surface (Raja, Fadaeinasab, *et al.*, 2013).

4.3.2 Potentiodynamic polarization study (PDP)

This experiment was carried out to gain knowledge on the reaction kinetics and the type of corrosion inhibition action of the studied inhibitors on the MS surface. Only one anodic (metal dissolution reaction) and two cathodic (hydrogen evolution and dissolved oxygen reduction) are expected in an aerated acidic solution (Bandy, 1980). The obtained polarization curves for MS in 1M HCl in the absence and presence of different concentrations of inhibitors are shown in Figure 4.79-4.84. Gradient lines at the cathodic and anodic over potentials of the experimental Tafel plots were extrapolated by using Gamry Echem Analyst software version 5.50. The results obtained for IE % of the inhibitors using PDP technique were in close agreement with those obtained using the EIS technique.

From Table 4.11, CNDE showed 82.64 % of IE % at the concentration of 500 ppm which was the highest as compared to CNHE and CNME. Figure 4.80 displayed the Tafel curves before and after the introduction of various concentrations of CNDE. The E_{corr} values were shifted (± 40 - 100 mV) majorly in the anodic direction simultaneously causing the anodic Tafel slope (β_a) to increase, while the value of cathodic Tafel slopes (β_c) to remain constant confirming that only metal dissolution reaction was reduced by surface blocking effect of the inhibitor (Keleş, 2011; Yıldız, Döner, *et al.* 2014). The oxidation of Fe to Fe^{2+} was being suppressed indicated by the inclining values of β_a , thus inhibiting corrosion process. Furthermore, the addition of CNDE reduced the values of current density (i_{corr}) while decreasing the polarization resistance (R_P) which eventually led to the reduction in corrosion rate (CR) (Chetouani, Hammouti, Benhadda, & Daoudi, 2005).

Table 4.11: Polarization corrosion parameters for all the studied inhibitors on MS in 1M HCl medium.

Inhibitor	Conc. (ppm)	E_{corr} (mV)	I_{corr} ($\mu A\ cm^{-2}$)	R_p ($k\Omega\ cm^2$)	β_a ($mV\ dec^{-1}$)	βc ($mV\ dec^{-1}$)	CR (m/Y)	IE (%)
-	0	-494	0.2594	72.20	77.8	96.8	3.07	-
CNHE	10	-489	0.2534	74.2	78.4	97.0	2.99	2.30
	100	-483	0.2390	87.5	95.4	97.4	2.82	7.86
	200	-477	0.2050	98.2	91.0	94.6	2.42	20.97
	500	-466	0.1863	114.3	96.7	99.6	2.20	28.16
	1000	-474	0.2058	104.8	95.0	104.3	2.43	20.64
CNDE	10	-454	0.1582	134.4	87.9	110.6	1.87	39.00
	100	-482	0.1008	210.5	104.9	91.5	1.19	61.13
	200	-480	0.0672	315.9	106.9	90.3	0.80	74.06
	500	-355	0.0450	485.5	113.3	90.6	0.53	**82.64**
	1000	-424	0.0544	395.7	108.3	91.4	0.64	79.03
CNME	10	-476	0.2079	94.7	74.8	115.2	2.45	19.85
	100	-453	0.1047	193.4	90.8	96.1	1.23	59.60
	200	-468	0.0851	243.8	93.8	97.5	1.00	67.18
	500	-456	0.0630	356.6	112.4	96.3	0.74	75.65
	1000	-435	0.0778	281.5	99.6	102.3	0.92	70.00
1	100	-479	0.1558	87.4	59.9	65.8	1.84	39.94
	200	-467	0.1080	124.9	60.8	63.6	1.27	58.34
	500	-456	0.0778	173.6	60.1	64.4	0.92	60.02
	1000	-458	0.0520	267.4	57.1	72.8	0.61	69.96
3	100	-473	0.2152	71.86	64.1	80.2	2.54	17.10
	200	-467	0.2200	119.5	65.5	805	2.60	15.15
	500	-455	0.1010	192.5	93.2	86.3	1.20	61.03
	1000	-462	0.0741	262.7	95.7	84.5	0.87	71.40
6	100	-465	0.2198	81.8	80.2	85.6	2.60	15.26
	200	-457	0.1806	105.0	86.8	87.9	2.13	30.37
	500	-472	0.0982	186.7	75.7	95.6	1.16	62.12
	1000	-435	0.0692	317.7	100.6	101.7	0.81	**73.35**

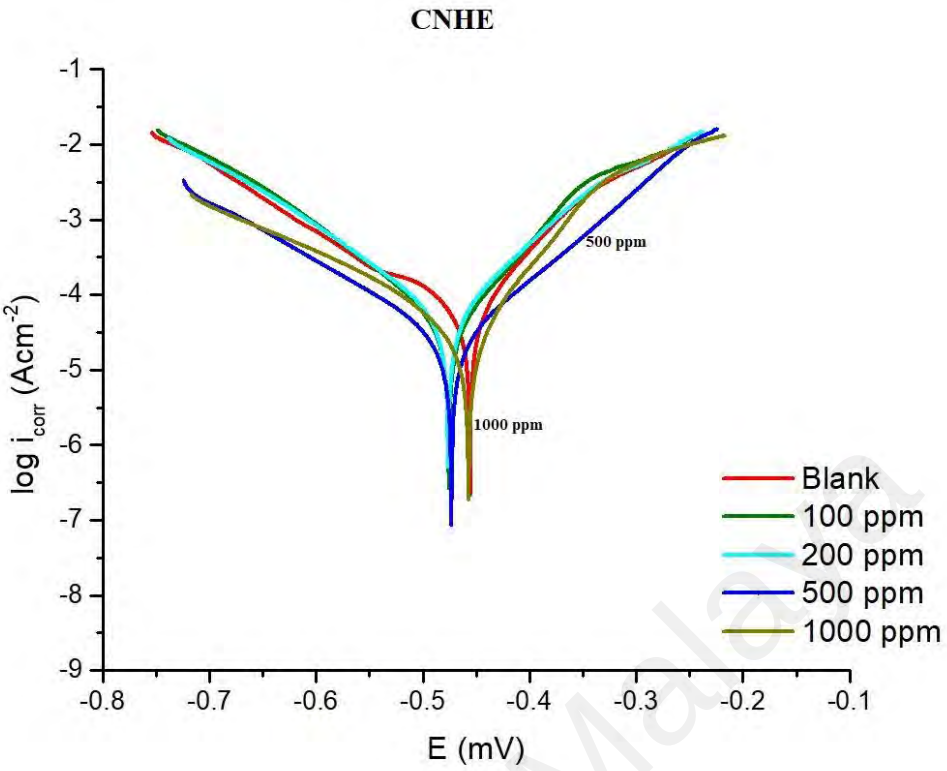

Figure 4.79: Tafel plots for all concentrations of CNHE in 1M HCl at 303 K.

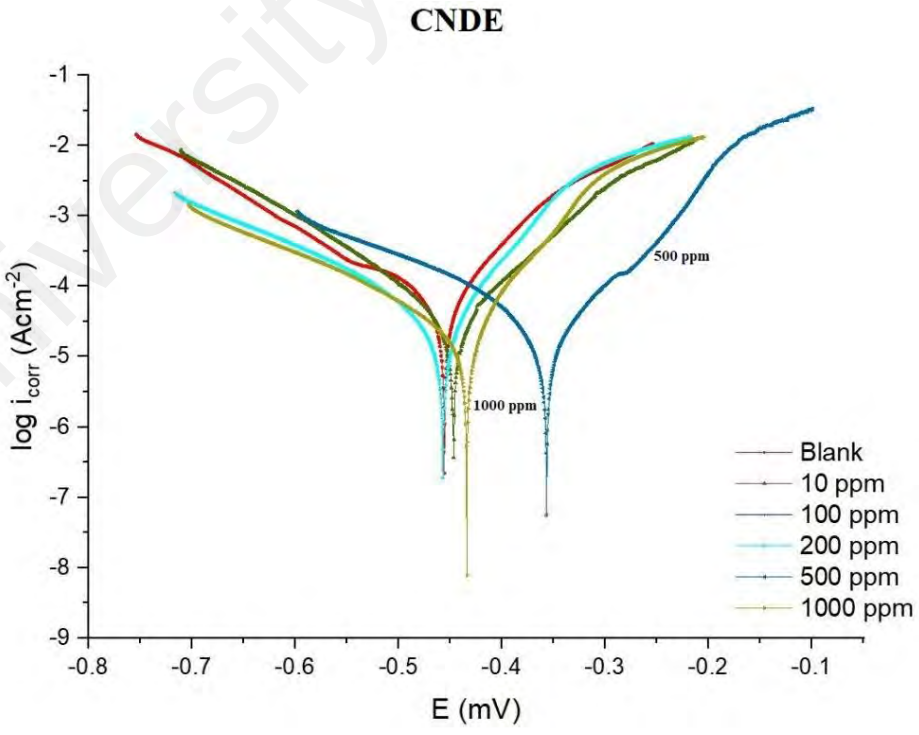

Figure 4.80: Tafel plots for all concentrations of CNDE in 1M HCl at 303 K.

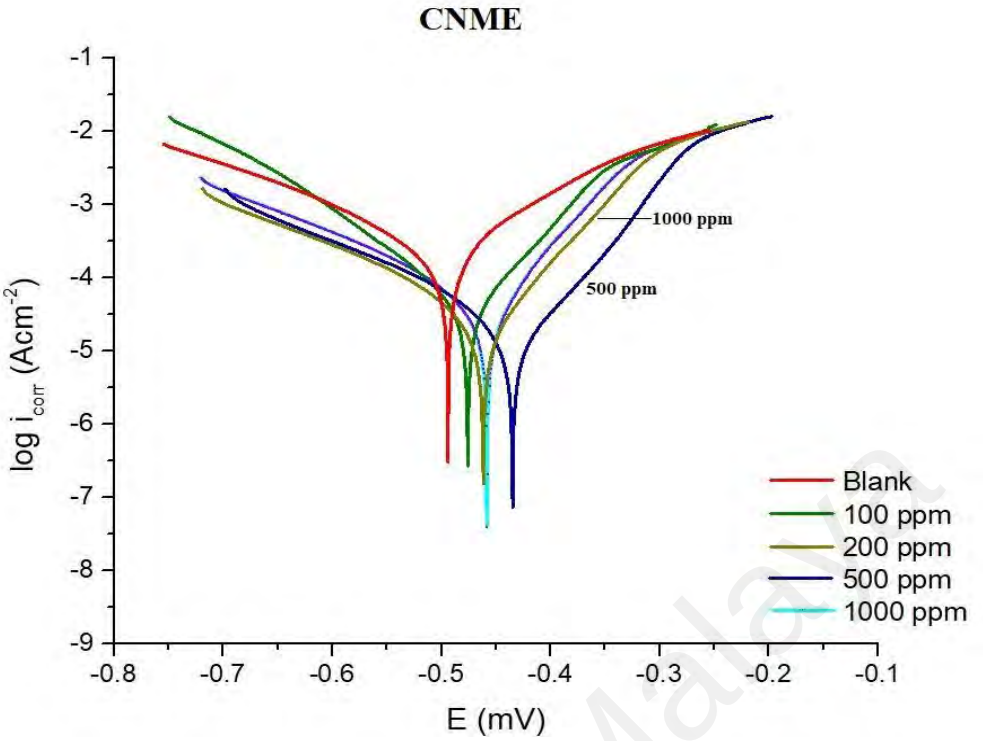

Figure 4.81: Tafel plots for all concentrations of CNME in 1M HCl at 303 K.

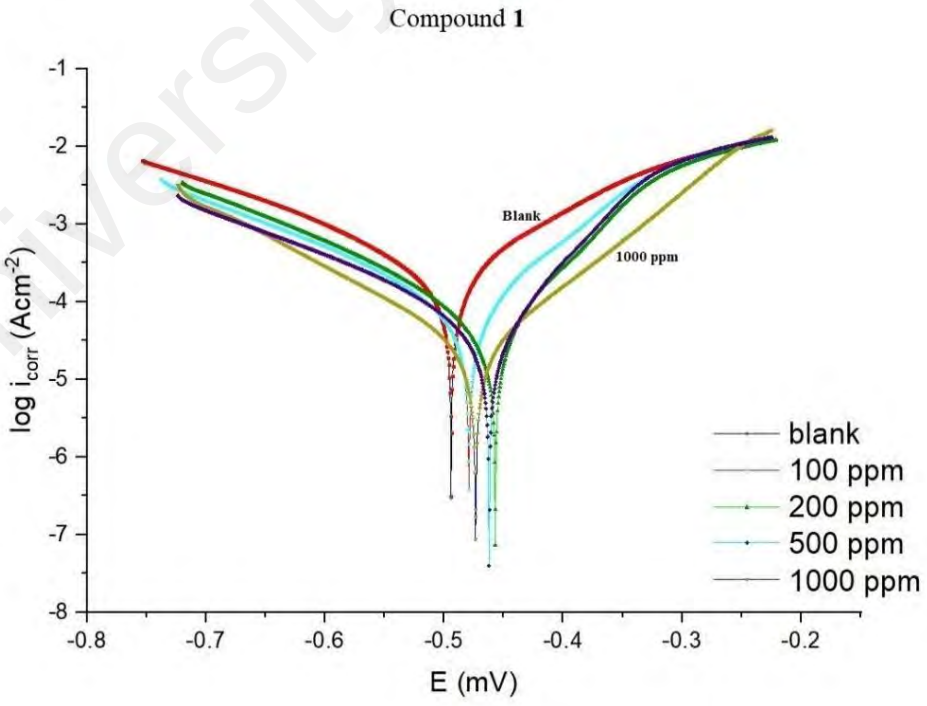

Figure 4.82: Tafel plots for all concentrations of **1** in 1M HCl at 303 K.

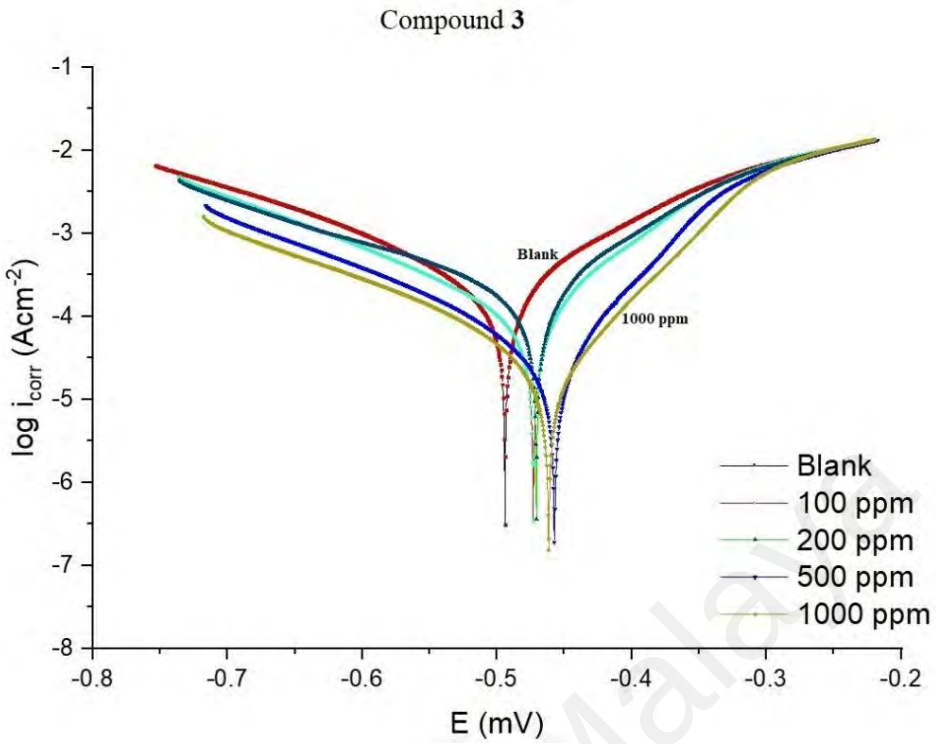

Figure 4.83: Tafel plots for all concentrations of **3** in 1M HCl at 303 K.

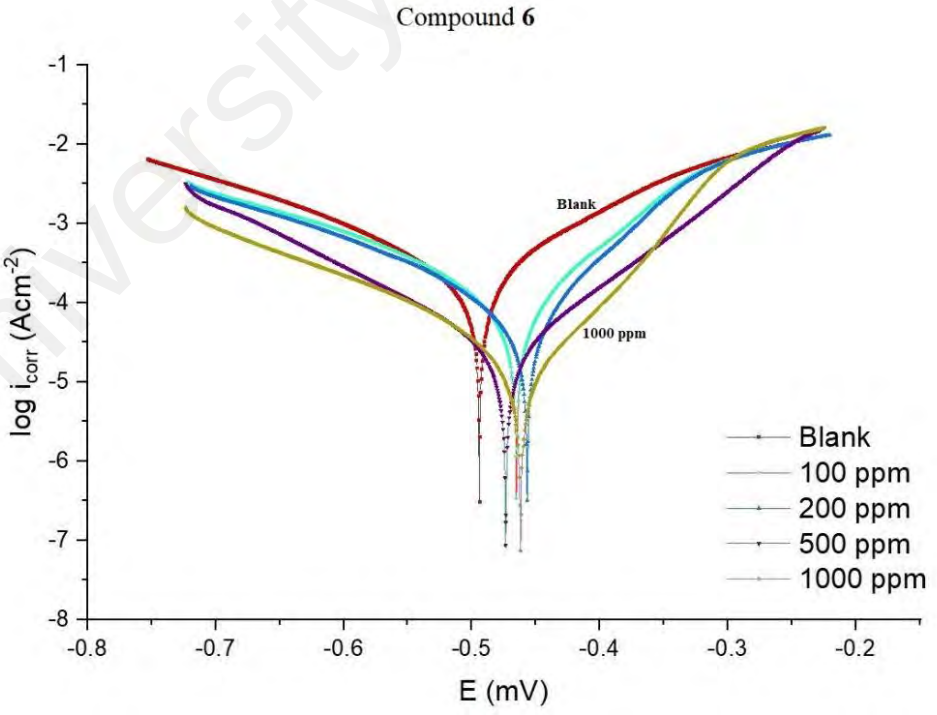

Figure 4.84: Tafel plots for all concentrations of **6** in 1M HCl at 303 K.

The inhibitive actions of all the alkaloidal inhibitor solutions were concentration dependent up until 1000 ppm and resulted in a marked shift in both cathodic and anodic branches of the Tafel plots. The change in the corrosion potential, E_{corr} remained in between $\Delta E = \pm$ 1-30 mV with respect to the blank; therefore, the alkaloids could be classified as a mixed-type inhibitor (Sanaei, Ramezanzadeh *et al.*, 2019). Also, data in Table 4.11 showed that the presence of different alkaloidal concentration did not significantly change the cathodic Tafel slope, β_c relative to the blank. Hence, they were said to exert dominant anodic inhibition by preventing the oxidation of Fe to Fe^{2+} (Hussin, Rahim, Mohamad Ibrahim *et al,* 2013). The results could be visualized from Figure 4.82-4.84. The obtained R_p values showed a similar trend to that of R_{ct} in the impedance results where they appeared the highest at 1000 ppm. The corrosion current (i_{corr}) and potentials (E_{corr}) gradually decreased as the concentration of the inhibitors increased. The protection actions of compound **1**, **3** and **6** were contributed from the electron density of the amine (-N-R_2), hydroxyl (-OH) and methoxyl groups (-OCH_3) (Ostovari, Hoseinieh *et al.*, 2009). The amine groups can donate their lone pair of electrons to the empty *d*-orbitals on the metal surface and forming a uniform layer of protection (Qiang, Zhang *et al.*, 2018; Zhang *et al.*, 2018). **6** showed 73.35 % of IE % which was the highest among the alkaloids. This could be explained based on additional functional groups and the rigidity of its molecular structure. These functional groups acted as possible protonation sites by the acidic media while the rigidity of the molecular structure of **6** ensures better adsorption of the inhibitor on the MS surface (Mohammadi, Hosseini *et al.*, 2016; Olasunkanmi, Kabanda *et al.*, 2016). Altogether, the inhibitive action for these constituents increases in the following order: **1** < **3** < **6**, where the chemical nature of the electrolyte affects the corrosion rate rather than the applied techniques.

4.4 Adsorption isotherm

Corrosion inhibition of mild steel is an exothermic process based on the dependence of ΔG_{ads} on the temperature where increasing reaction temperature will cause desorption of inhibitor from the steel surface (Yamuna & Anthony, 2015). Two adsorption modes are commonly discussed in view of corrosion inhibition which are the chemisorption and physisorption. Generally, physisorption is the electrostatic interaction between the charged molecules (counter ions) against the charged metal surface. Values of ΔG^0_{ads} until -20 kJ mol^{-1} are consistent with the physical adsorption while those lower than -40 kJ mol^{-1} are correlated with the chemisorption (Nnaji *et al.*, 2017; Lai *et al.*, 2017). The nonbonding electron pairs at the electronegative sites may interact with the vacant *d*-orbitals of mild steel to provide a protective chemisorbed film. In the case of the extracts, the absolute values are relatively higher compared to each of the alkaloids, approaching those of chemisorption.

The inhibitive action of *Cryptocarya nigra* extracts towards acid corrosion of mild steel was discussed in view of Langmuir adsorption isotherm. CNDE best fitted the plot, having linearity of R^2 value approximately 0.9997. The strength and stability of the adsorbed layer formed by CNDE could also be evaluated from the higher ΔG_{ads} value as compared to the other extracts. ΔG_{ads} values calculated from the adsorption process was -28.2 $kJmol^{-1}$ which signified that the molecules were adsorbed on the steel surface through comprehensive physisorption and chemisorption interaction. The negative values of ΔG_{ads} ensure the stability and spontaneity of the adsorbed layer on the electrode surface (Prabakaran, Kim *et al.*, 2016; Tezeghdenti, Etteyeb, Dhouibi *et al.*, 2017). Comparison between different adsorption isotherm plots for CNDE was extrapolated in Figure 4.85-4.87. Results for all the Langmuir adsorption isotherms are tabulated Table 4.12.

Table 4.12: Langmuir adsorption isotherm parameters for CNDE and three pure alkaloids.

	CNDE	**1**	**3**	**6**
R^2	0.9997	0.9991	0.9952	0.9991
y-intercept	0.0399	0.0484	0.0703	0.2909
K_{ads} value	25.0627	20.6612	14.2248	3.4376
ΔG_{ads} (J mol^{-1})	**-28,232.95**	-17 746.44	-16 806.12	**-13 228.41**

Thermodynamic parameters of the adsorption process were calculated, and all the three alkaloids were found out to be spontaneously adsorbed onto the MS through predominant electrostatic interaction where their calculated ΔG were less than -20 $kJmol^{-1}$ as tabulated in Table 4.12. The ΔG values indicated that the alkaloids adsorbed on the MS surface through dominantly physisorption mechanism (Cao *et al.*, 2014). The results obtained from the fitting on Langmuir plot in Figure 4.88-4.90 showed good agreement with the results from the electrochemical method, where **6** provided better protection for mild steel against pitting corrosion in 1M HCl solution having the highest R^2 value of 0.9991. A higher value of ΔG_{ads} showed that the inhibitors were spontaneously adsorbed on the MS surface preferably through chemisorption mechanism (Ramdani *et al.*, 2016). IE % of these compounds were directly proportionated to their concentration and molecular weights.

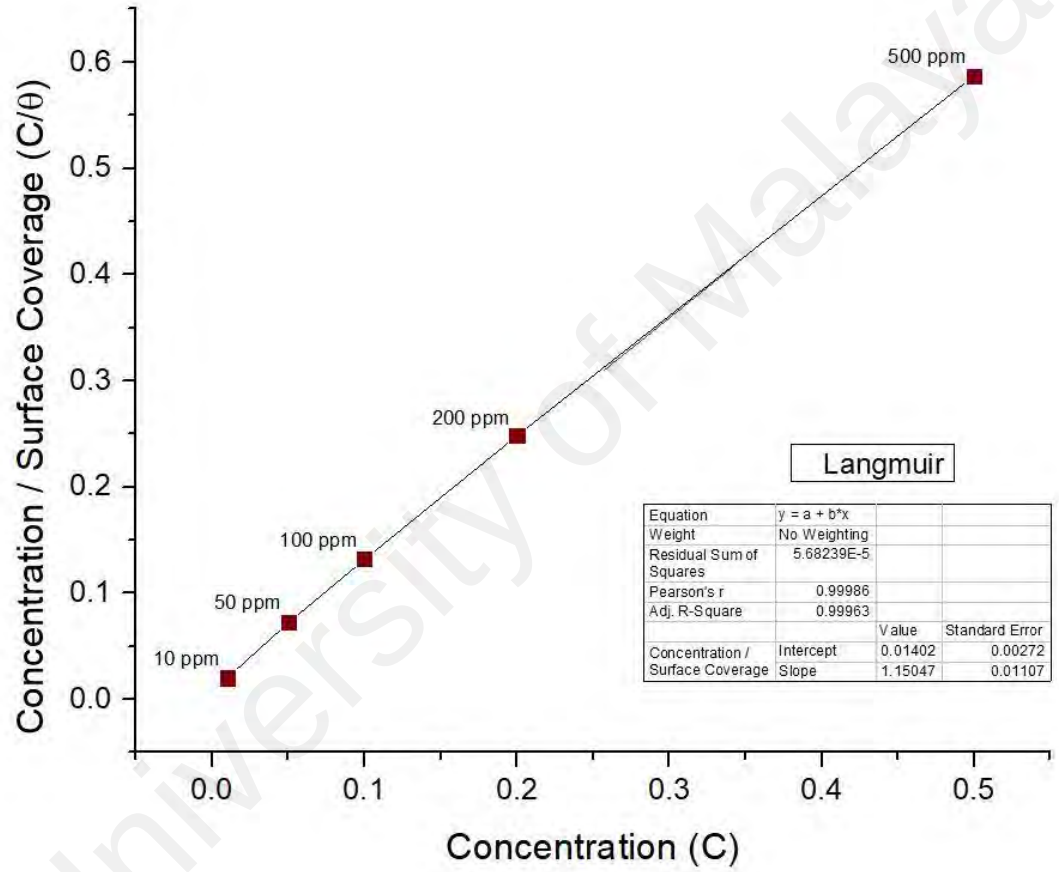

Figure 4.85: Langmuir adsorption isotherm for all concentrations of CNDE on MS in 1M HCl at 303 K.

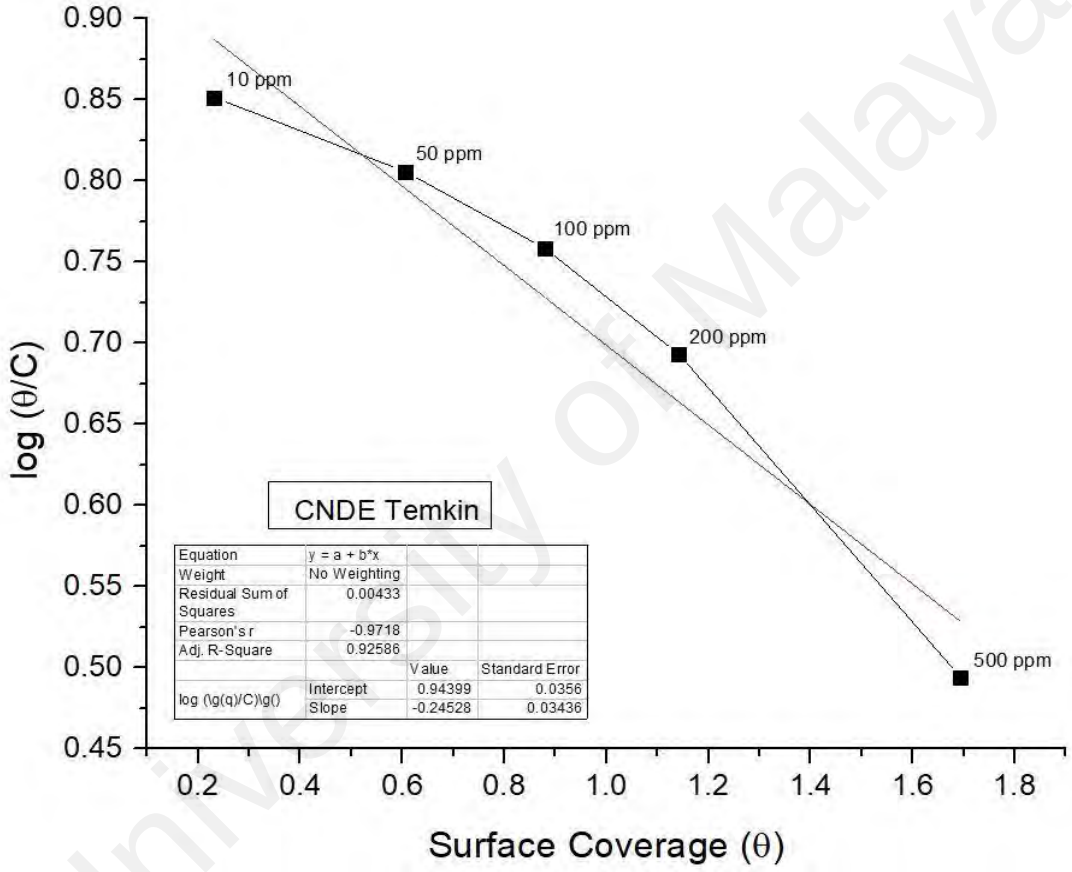

Figure 4.86: Temkin adsorption isotherms for all concentrations of CNDE on MS in 1M HCl at 303 K.

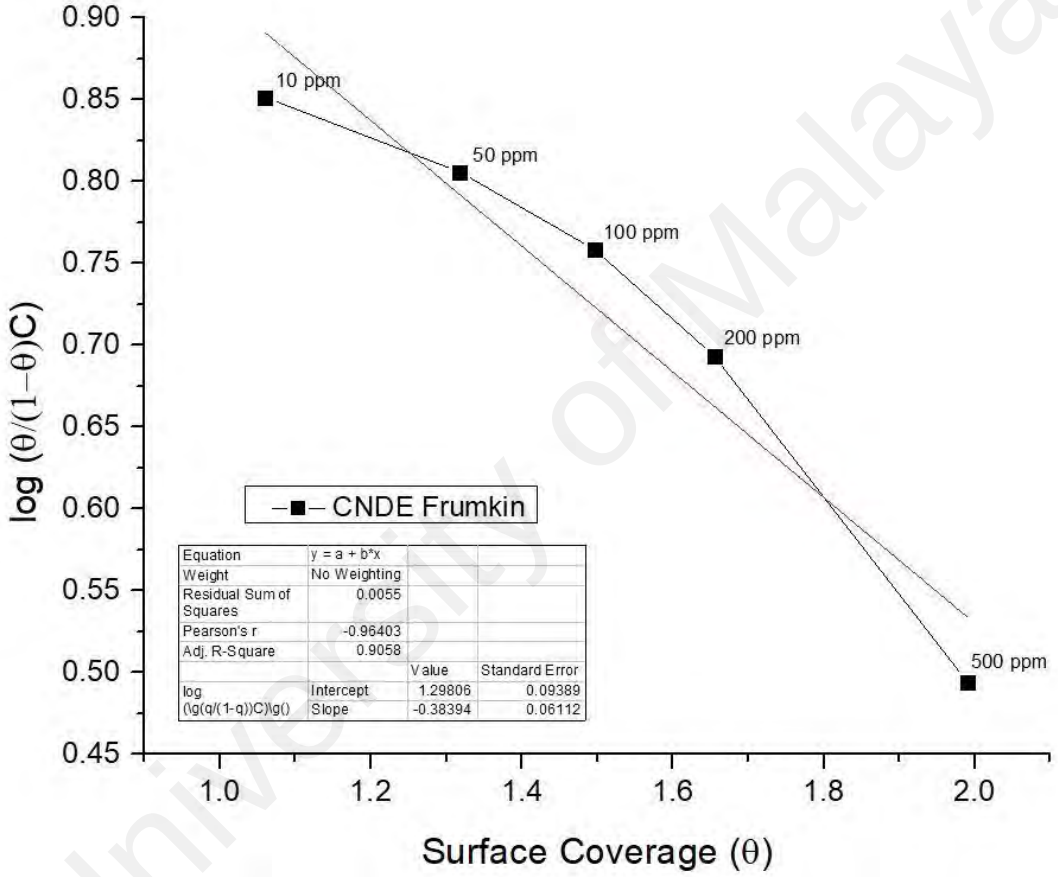

Figure 4.87: Frumkin adsorption isotherms for all concentrations of CNDE on MS in 1M HCl at 303 K.

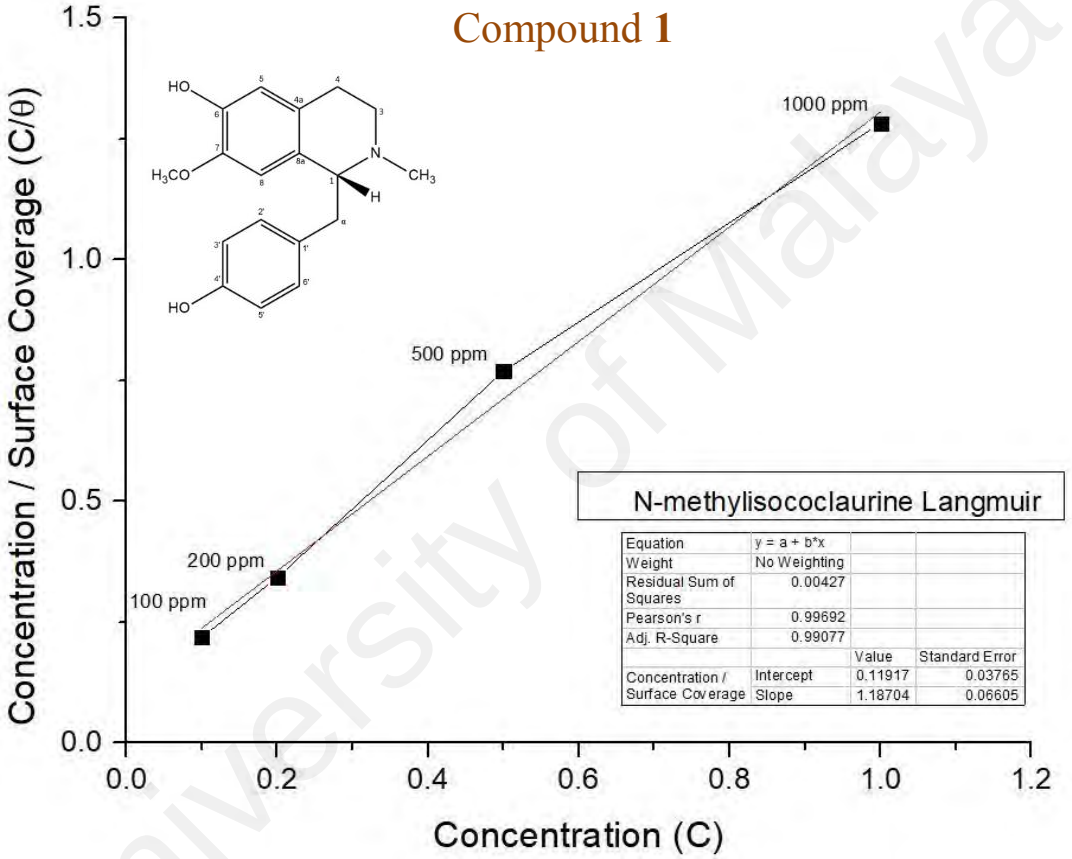

Figure 4.88: Langmuir adsorption isotherm for **1** on MS in 1M HCl at 303 K.

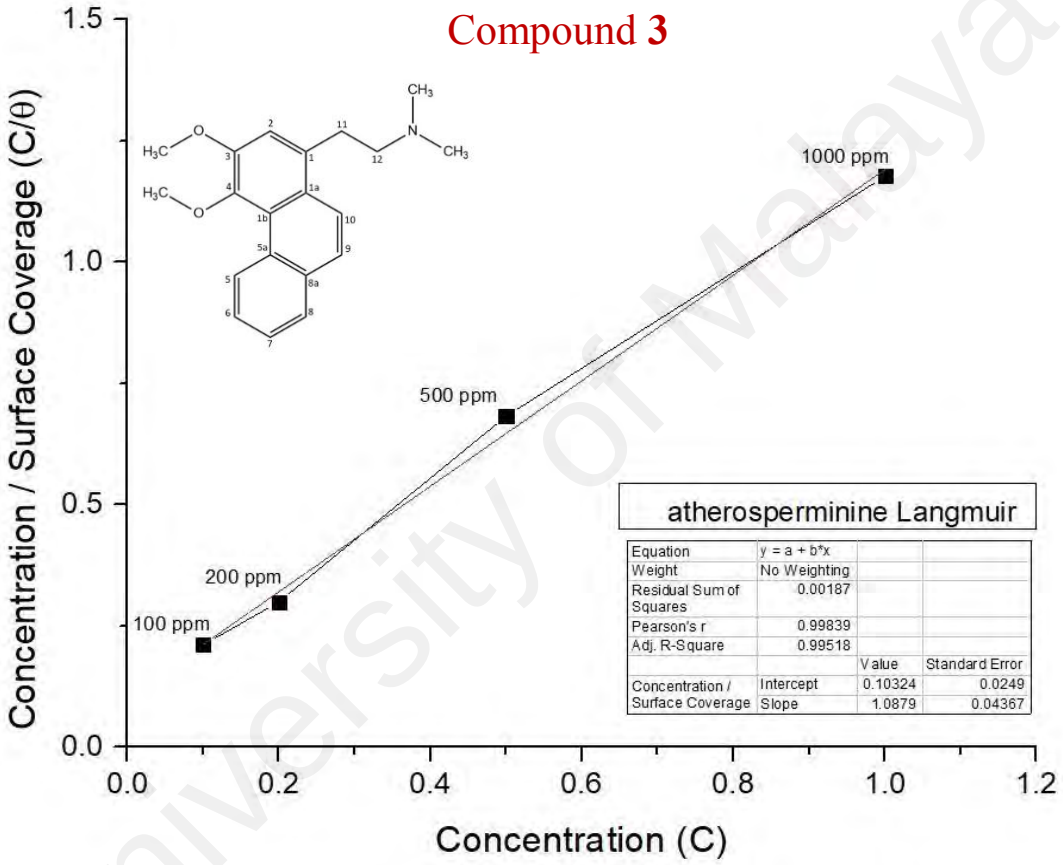

Figure 4.89: Langmuir adsorption isotherm for **3** on MS in 1M HCl at 303 K.

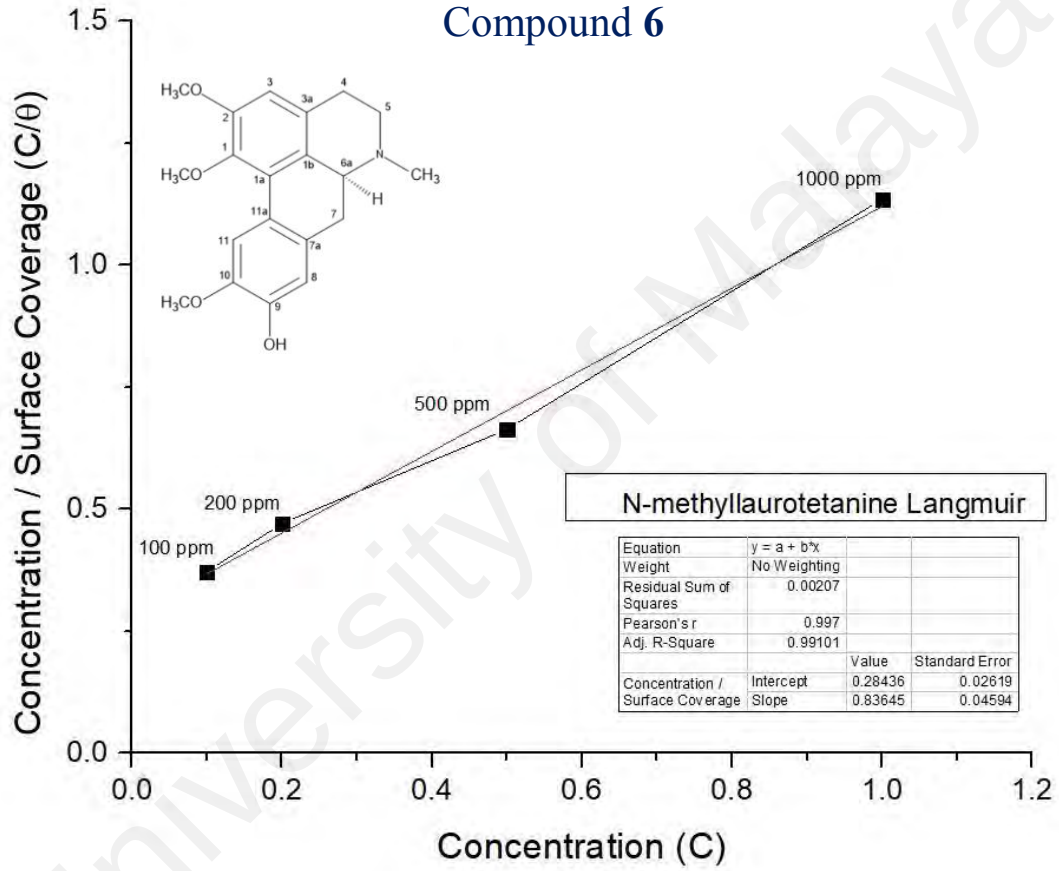

Figure 4.90: Langmuir adsorption isotherm for **6** on MS in 1M HCl at 303 K.

4.5 Proposed mechanism of inhibition

CNDE consist of a variety of constituents, therefore, it displayed a higher ΔG_{ads} value indicating that the inhibition mechanism proceeds towards chemisorption. This mode of adsorption is the result of donor-acceptor interaction between the free electron pairs of heteroatoms and π electrons of multiple bonds from the combination of constituents with the vacant *d*-orbitals of iron (Burkitbayeva, Argimbayeva *et al.*, 2016). The synergistic effect resulted from the multiple components formed a better and stronger interaction of adsorption on the surface of the mild steel. The inhibition mechanism of the pure alkaloids considers the total molecular structure of the inhibitor and the spatial relationship of different functional groups. The more electron donor groups introduced, particularly substituents with conjugated systems will improve the corrosion inhibition efficiency of inhibitor derivatives (Olasunkanmi *et al.*, 2016).

When these structures are incorporated with multiple fused aromatic or aliphatic rings, additional substituents as such protonatable amine or hydroxyl groups may improve their solubilities in the aqueous corrosive fluid. If nitrogen is protonated, the counter anion, Cl^- will enhance the adsorption of compounds. Linked quaternary nitrogen-containing groups can be more effective as a corrosion inhibitor than a molecule containing a single such group. A linking group containing carbon and hydrogen atoms can serve to make the molecule more hydrophobic, which can also enhance effectiveness as a corrosion inhibitor (Hamdan, Suryanto *et al.*, 2018; Saha, Murmu *et al.*, 2019).

In the case of the studied alkaloids, the inhibition effects of the respective compound were governed by the interaction between π electrons of phenyl rings and *p*-electrons from the electron donor groups (N and O) with the vacant *d*-orbitals of Iron through which they form insoluble, stable and uniform thin film on MS surface (Crawford *et al.*, 2016). The results shown by EIS, PDP and adsorption isotherm fitting clearly deduced that the

inhibition mechanism for all studied inhibitors involves blocking of mild steel surface *via* adsorption at the metal-solution interface. The adsorption of inhibitors was influenced by the nature, temperature and morphology of the metal as well as the chemical structure of the inhibitors (Kosari *et al.*, 2014). The values of IE % depend essentially on the electron density at the active centre(s) of the inhibitor molecule. The thermodynamic parameters in Table 4.12 proven that the adsorption of alkaloids on the MS surface in 1M HCl were more towards physisorption than chemisorption. The physisorption of these alkaloids arose from the electrostatic interactions between the protonated electronegative sites and the charged surface of iron (ii) chloride, $(Fe^{2+}\ Cl^{-})_{ads}$ (Benarioua, Mihi *et al.*, 2019; Odewunmi, Umoren *et al.*, 2015).

The comparison between different spatial adsorption interactions of **1**, **3** and **6** on mild steel surface are discussed in Figure 4.91-4.93 below. For **1**, a phenyl ring is interconnected with the isoquinoline moiety through the α-carbon which is sp^3 hybridized and can freely rotate. This free bond rotation causes a weak momentary interaction of π- and nonbonding lone pair electrons of oxygen on the phenyl ring with the vacant *d*-orbitals of iron. Consequently, resulting in a lower IE %. For alkaloid **3**, a *N,N*-dimethylethanamino group is attached to the phenanthrene moiety and the carbon at position 11 and 12 are sp^3 hybridized. The link between these two carbons is freely to rotate, hence inducing rotation of the amino group. This eventually leads to a weak momentary electrostatic interaction between the protonated amino group and $(FeCl^{-})_{ads}$ species on the mild steel surface (Sulaiman, Onawole *et al.*, 2019). Therefore, attaining a low IE % value.

However, for alkaloid **6**, the three methoxyl and 1 hydroxyl groups on the aporphine structure were aligned in the same direction as a result, forming the highest electron density over a specific area. The arrangements of the functional groups in a rigid structure

aided the effectiveness of the adsorption process of **6** on the mild steel surface. Aromatic compounds with the cyclic delocalized π-electron system are susceptible to electron delocalization in acidic media (Singh, Ebenso *et al.*, 2016). The importance of the planarity shape of the benzene ring is described by the orbital approach. Owing to the trigonal planar shape of carbons having sp^2 hybridized orbitals, the rings of **6** are flat and there was no possibility for free rotation of bond to occur (Stefanoni, Angst, & Elsener, 2018). This flatness property permits the overlapping of the *p*-orbitals in a systematic staggered arrangement indirectly forming a stable monolayer of protection (A. Singh *et al.*, 2018). Formation of a smooth homogenous monolayer by **6** on the MS surface has led to higher surface coverage, Θ (Figure 4.94) thus making the IE % of the alkaloid the highest as compared to the other two (Sadeghi Erami *et al.*, 2019).

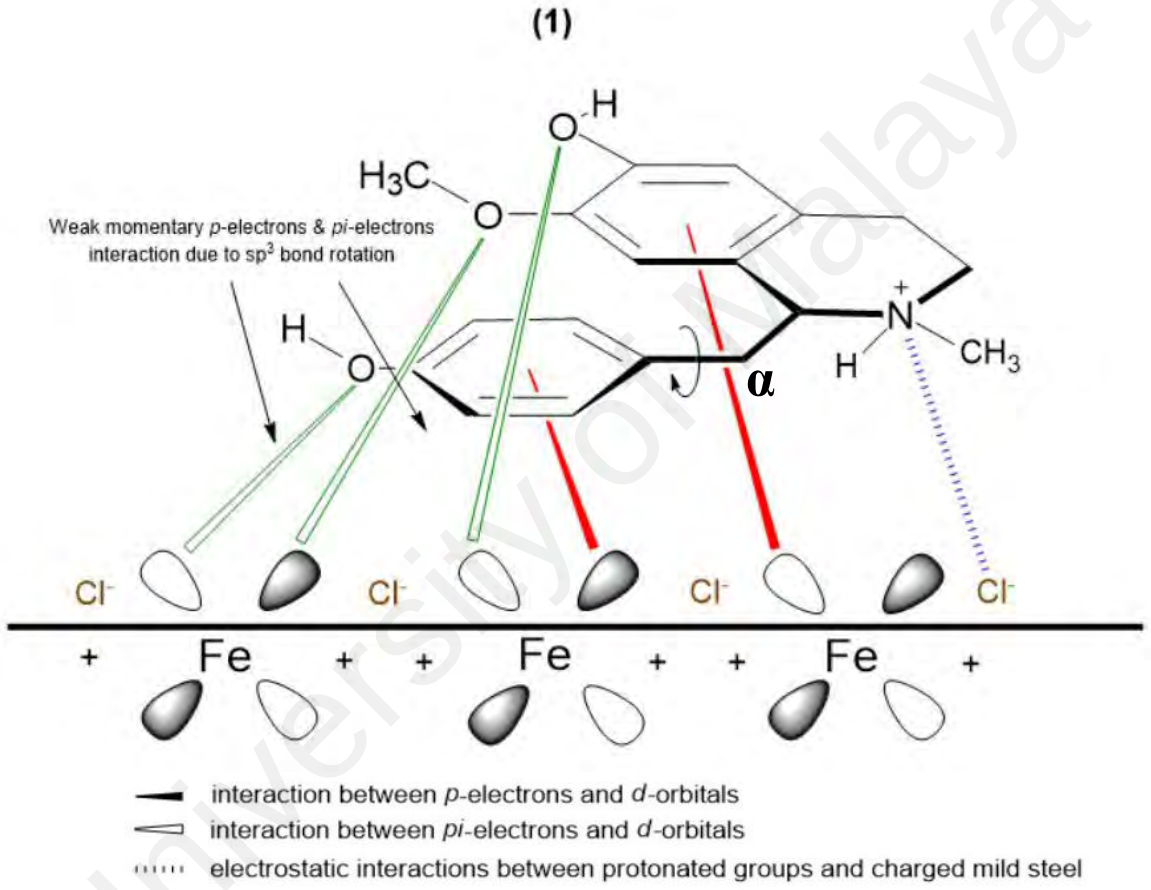

Figure 4.91: Different spatial adsorption interactions of **1** on mild steel surface.

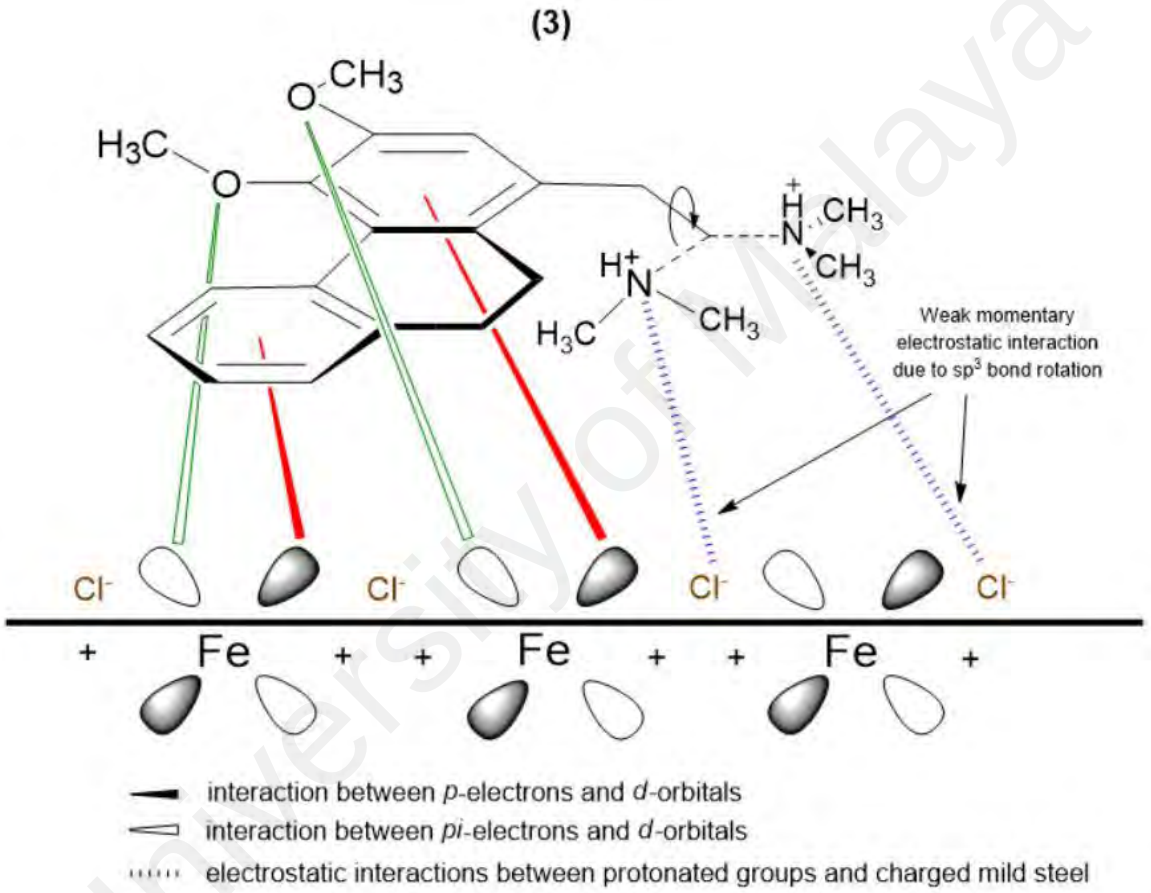

Figure 4.92: Different spatial adsorption interactions of **3** on mild steel surface.

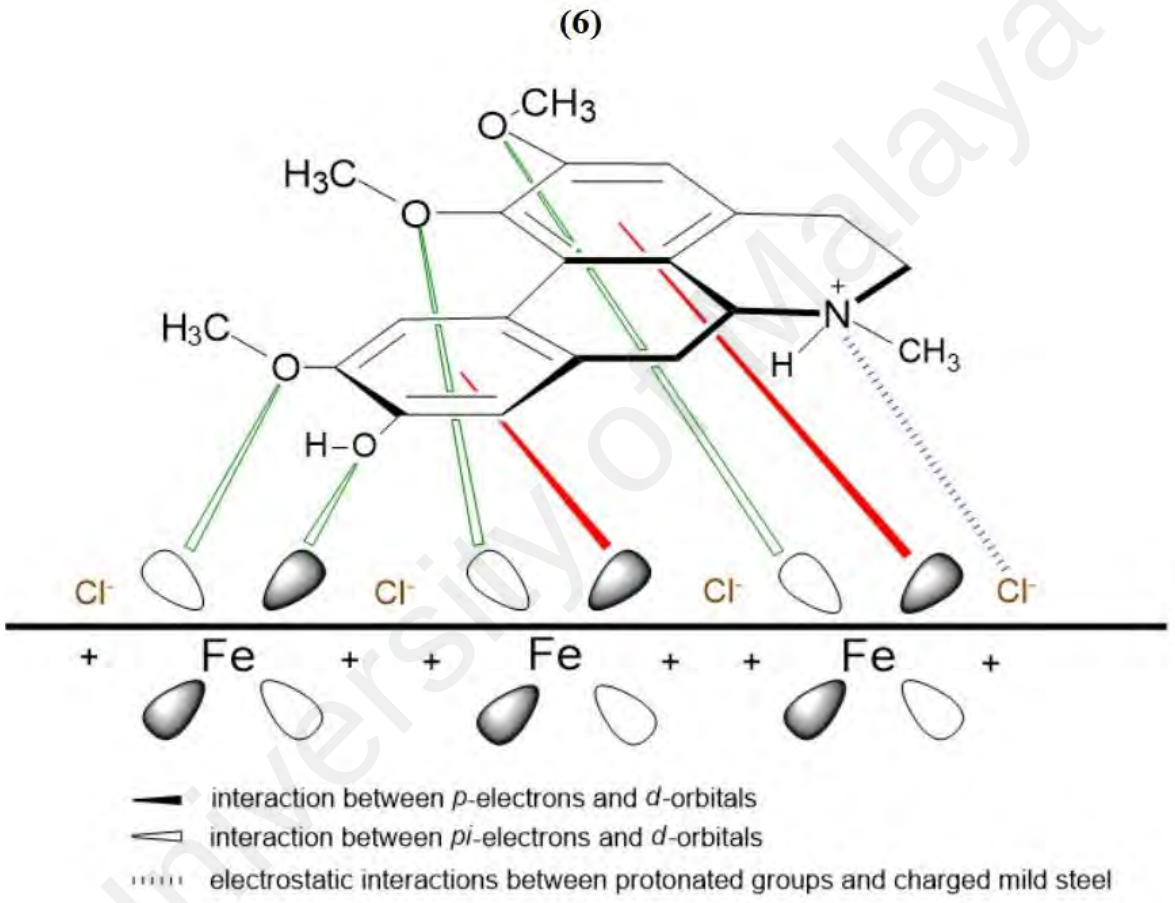

Figure 4.93: Different spatial adsorption interactions of **6** on mild steel surface.

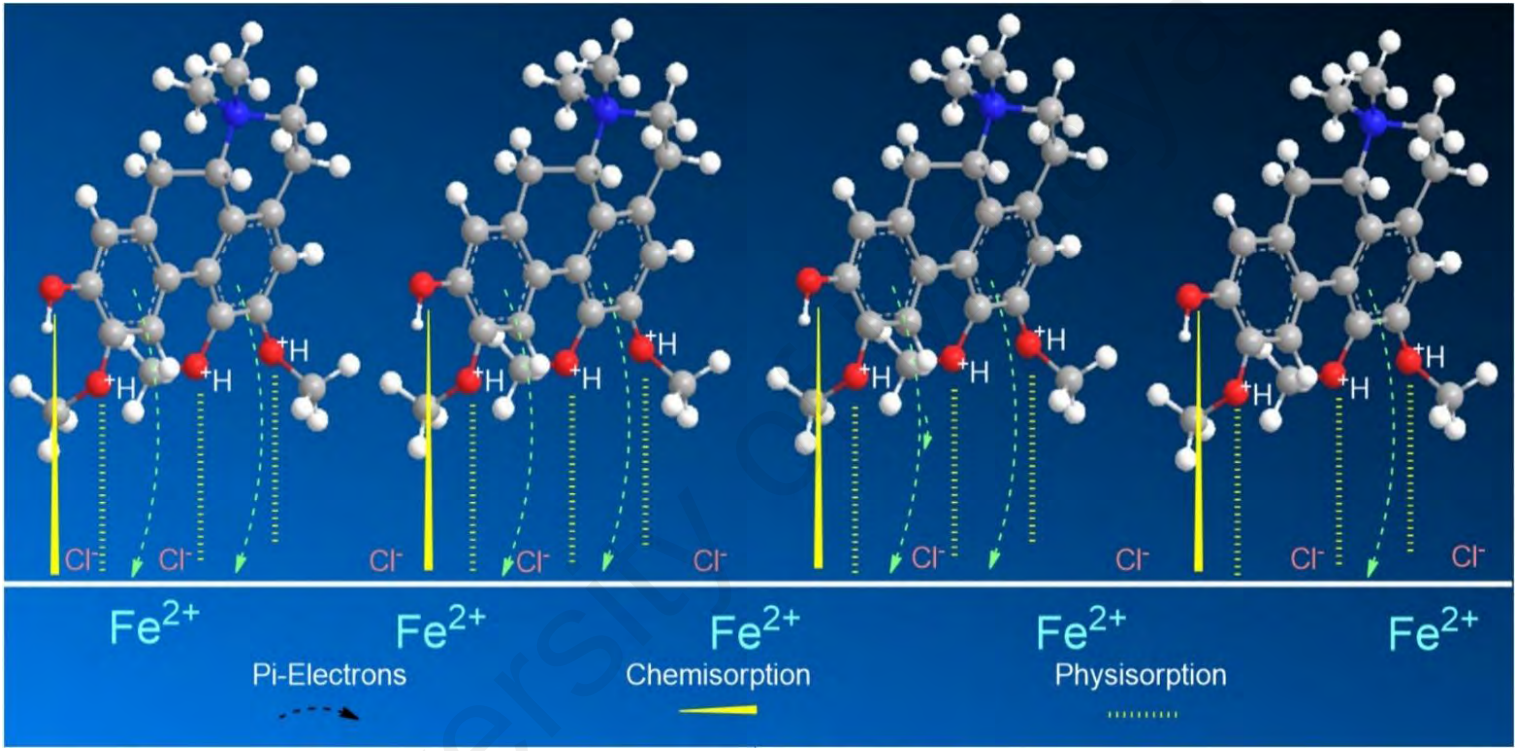

Figure 4.94: Staggered and systematic arrangement of **6** on the MS surface.

The proposed formation of Fe^{2+}-**6** complex was accomplished by a coordinative bond from the nonbonding lone pair electrons on the oxygen atom towards the Fe^{2+} as shown in Figure 4.95. The deprotonation of the hydroxyl group by the existing Cl^- species present in the 1M HCl media causes a resonance effect onto the aromatic ring (Donnelly, Downie *et al.*, 1978). This effect was generated due to electron donating substituents on the ring that causes the delocalization of π-electrons. The stabilization of the π-electrons created an excess positive charge on the oxygen atom of the adjacent *ortho*-located methoxyl group (Figure 4.96).

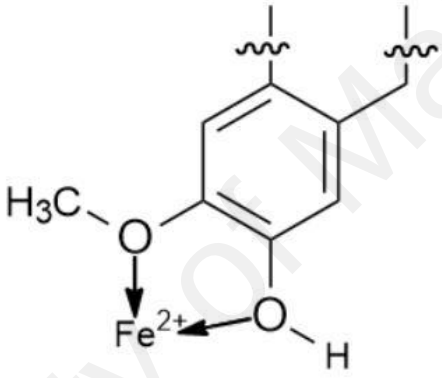

Figure 4.95: Structural formula for the Fe^{2+}-**6** complex.

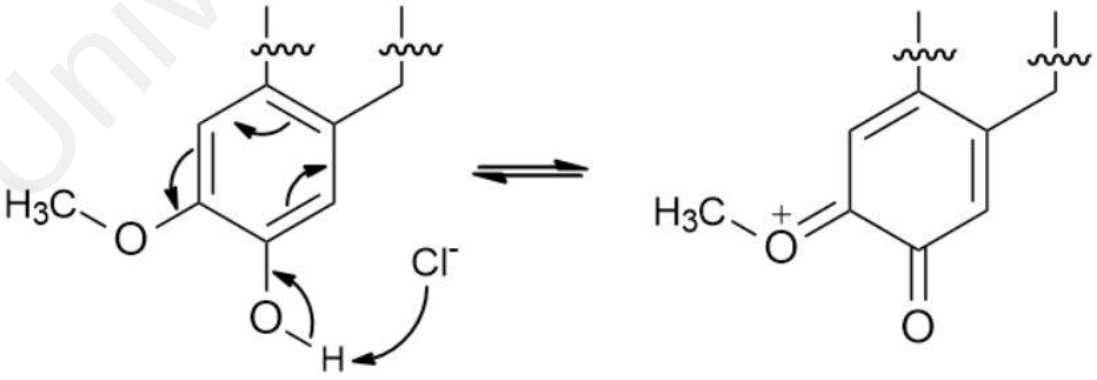

Figure 4.96: Electron delocalization on alkaloid **6** due to resonance effect.

4.6 Surface analysis

The surface morphology of MS due to corrosion process was examined under SEM analysis along with EDX to determine the elemental compositions on the surface before and after the exposure to the corrosive media with and without the inhibitors. Figure 4.97 displays an array of the SEM-EDX micrographs recorded for (a) polished mild steel, (b) without any inhibitors, (c) with the presence of 1000 ppm **CNDE**, and (d) with the presence of 1000 ppm **6**. No sign of corrosion action has taken place on the polished mild steel surface looking from Figure 4.97 (a).

Figure 4.97 (b) revealed that without any inhibitive actions the surface of MS appeared to be highly corroded with areas of localized corrosion. However, in the presence of 500 ppm CNDE in Figure 4.97 (c) the corrosion activity was suppressed as seen from the decrease in localized corrosion areas. This is due to the adsorption of inhibitors on the mild steel surface forming a monolayer of protection against corrosion activity (Jevremović, Singer, Nešić *et al.*, 2013).

Table 4.13: The percentage of elements for each specimen obtained from the energy dispersive X-ray spectroscopy (EDX) analysis after 24 h immersion in 1M HCl.

Sample	Element (% wt)			
	Fe	O	C	Cl
(a) Untreated Polished Mild Steel	99.4	-	0.13	-
(b) Mild Steel in 1M HCl	50.5	41.7	3.2	2.7
(c) Mild Steel in 500 ppm CNDE	82.8	10.2	5.1	1.2
(d) Mild Steel in 1000 ppm **2**	76.2	16.6	6.3	1.5

In Table 4.13, elemental analysis of corroded sample (Figure 4.97 (b)) using energy dispersive X-ray spectroscopy (EDX) revealed the percentage of chlorine (Cl) and oxygen (O) were immense due to the formation of adsorptive ferrous chloride $(FeCl_2)_{ads}$ which

can further oxidize to form ferric hydroxide ($Fe(OH)_3$) and oxyhydroxides (FeOOH) (Faustin, Maciuk *et al.*, 2015; Gupta, Verma *et al.*, 2016). In the case of MS immersed in 1M HCl with CNDE inhibitor, only trace amount of Cl^- and O were detected indicating that the corrosion process has been inhibited significantly. The presence of CNDE as corrosion inhibitors has decreased the oxygen reduction process hence reducing corrosion rate. The decreased in oxygen value shows the effectiveness of this inhibitor.

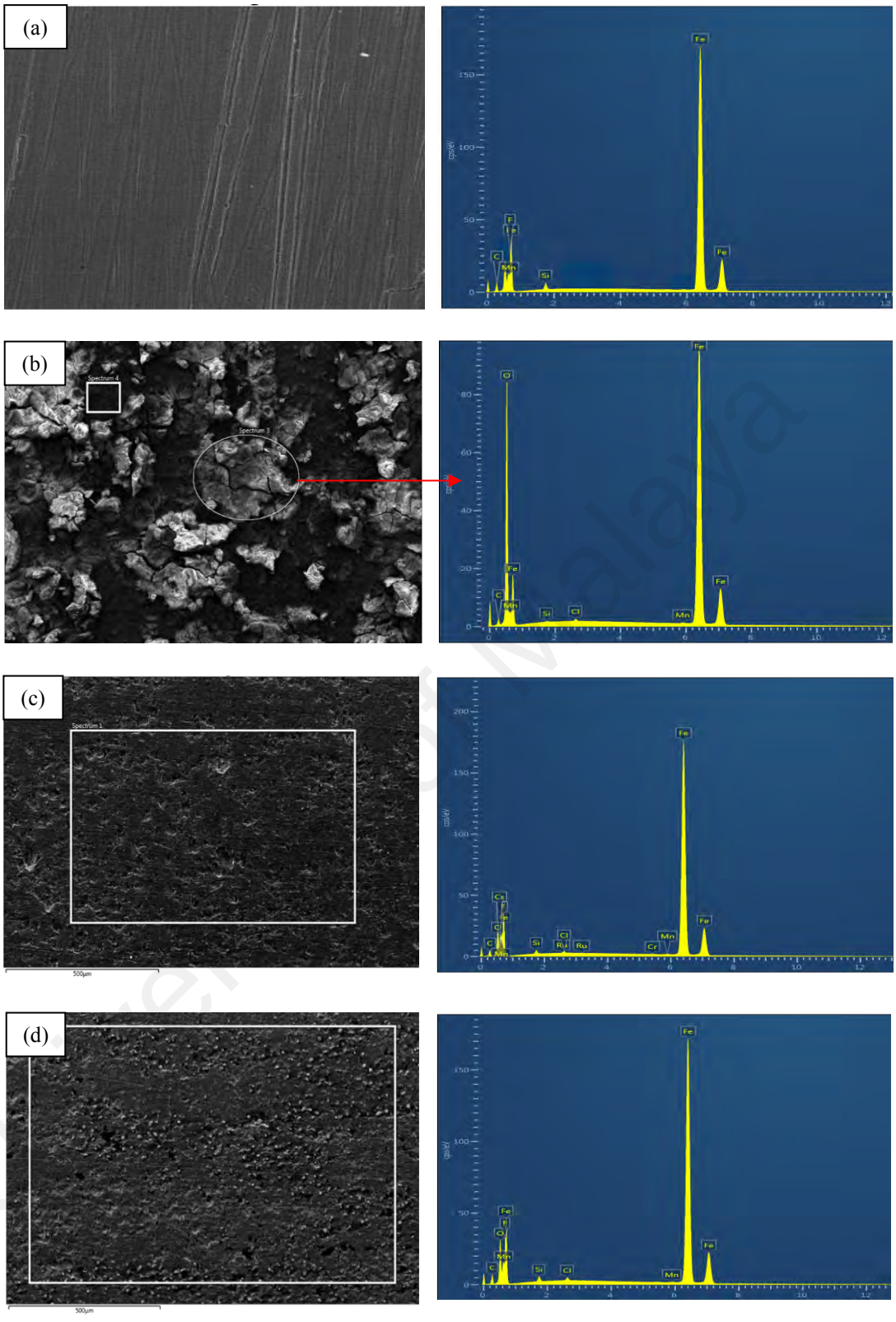

Figure 4.97: SEM micrographs for (a) polished MS, (b) corroded MS, (c) MS with the presence of 500 CNDE, (d) with the presence of 1000 ppm **6**. All at the magnification of 500 X.

Alkaloid **6** exhibited positive impact in preventing corrosion on mild steel as shown in SEM micrograph displayed in Figure 4.97 (d). The percentage of Fe is higher than that of the corroded sample with only less than 10% of oxygen and chlorine elements. The excess negative charge resulted from the adsorption of Cl^- promotes electrostatic interaction with cations (protonated alkaloids). The protonated inhibitor molecules will adsorb on the mild steel surface via chloride ions which form an interconnecting bridge upon replacement of chloride and water molecules. Electrostatic interaction was believed to occur between the protonated molecules and $(FeCl^-)_{ads}$ species at anodic sites.

Overall, surface analysis using scanning electron microscope (SEM) proved a significant improvement on the morphology of the mild steel plates in the presence of an optimum concentration of CNDE and **6** inhibitors.

CHAPTER 5: CONCLUSION

This chapter will summarize all the outlines, sequential steps and results obtained throughout this eventful coursework. First, the *Cryptocarya nigra* species was collected at Hutan Ulu Sat, Machang, Kelantan by the phytochemical group and stored in the Herbarium of University of Malaya. The bark part of the species was later assigned as KL 5272. Mayer's test was conducted on a portion of the sample to detect the level of alkaloidal content and a positive result was obtained indicated by the formation of mild white precipitate. Owing to this, approximately 2.5 kg of the sample was extracted using three different solvents of gradual increasing polarity by conventional cold percolation method to give hexane (CNHE), dichloromethane (CNDE) and methanol extracts (CNME).

In the expanding global interest to search for a new potential source of green corrosion inhibitors, the three crude extracts were studied for their corrosion inhibition activity on mild steel in 1M HCl *via* electrochemical impedance study (EIS), potentiodynamic polarization experiment (PDP) and scanning electron microscope-energy dispersive x-ray (SEM-EDX). Altogether, CNDE showed the highest inhibition efficiency of 91.05 % for EIS and 82.64 % for PDP. This promising result has led to the need for the identification of the chemical constituents of CNDE using liquid chromatography mass spectrometer-ion trap- time of flight (LCMS-IT-TOF). Various chemical constituents as seen from the LC profile of CNDE may have synergistically prevented corrosion on mild steel.

Next, 11.5 g of CNDE was concentrated by acid-base extraction to give 17 % of yield recovery. It was then separated and fractionated through extensive column chromatography (CC) over silica gel using dichloromethane and methanol solvent system as the mobile phase. The eluents were further separated on thin layer chromatography (TLC) plates and sprayed with dragendorff's reagent for detection of alkaloids. The

orange spots having the same R_f values on the TLC plates were pooled together into smaller subfractions. The combined groups were then purified separately and successfully in stages to obtain seven compounds named (+)-*N*-methylisococlaurine **1**, atherosperminine-*N*-oxide **2**, atherosperminine **3**, 2-hydroxyatherosperminine **4**, argentinine **5**, (+)-*N*-methyllaurotetanine **6** and (+)-laurotetanine **7**. on preparative thin layer chromatography (PTLC). The structures of the isolated compounds were elucidated with the aid of spectroscopic methods such as 1D NMR (^{1}H, ^{13}C and DEPT), 2D NMR (COSY, NOESY, HSQC, HMBC) and FTIR spectroscopy.

Keen to investigate the components responsible for the compelling corrosion inhibition activity of CNDE, three of the pure compounds; **1**, **3**, and **6** were analyzed under EIS and PDP. Experiments were conducted over a range of inhibitor concentrations starting from 100 ppm to 1000 ppm over duplicate assessment to allow reproducibility of results. Compound **6** displayed potent inhibition efficiency for both methods with 88.05 % and 73.35 %, respectively. This admirable outcome could be attributed to the rigidity of the aporphine skeletal structure, despite having the highest number of functional groups in a systematic one-direction arrangement.

Though CNDE acted as an anodic type (ΔE_{corr}> +30 mV) concentration independent inhibitor with optimum concentration of 500 ppm, on the other hand, compound **6** behaved as a mixed typed (ΔE_{corr}< +30 mV) concentration-dependent inhibitor until 1000 ppm. The inhibition mechanism for both inhibitors was governed by the charge-transfer mechanism observable from the maintain semi-circle shapes of the Nyquist plots (EIS). They showed predominant inhibitory effects on the anodic reaction sites of the corrosion process indicated by the increasing values of β_a of the Tafel slopes (PDP). The oxidation of Fe to Fe^{2+} was significantly reduced which led to the decrease in the corrosion rates of mild steel.

The adsorption isotherm for CNDE and 6 best fitted against the Langmuir plot with the linearity (R^2) of more than 0.9990. The adsorbed species formed insoluble complexes, Fe^{2+}-**3** upon the interaction with the metal lattice. Overall interpretation of the adsorption isotherms suggested that CNDE and **6** formed a monolayer of protection on the mild steel surface through prevalent physisorption mechanism as the ΔG_{ads} calculated were -28.2 and -13.2 $kJmol^{-1}$, respectively. Finally, SEM micrographs exhibited considerable surface morphological improvements upon addition of optimum concentrations of CNDE and **6**. Further supported with the elemental compositions retrieved from the EDX result, all said and done, both subjects could be best referred as reliable green corrosion inhibitors.

Theoretical predictions for the pure compounds were in good agreement with the retrieved experimental results in the following order: *N*-methyllaurotetanine **6** > atherosperminine **3** > *N*-methylisococlaurine **1**. The comparative study by means of inhibition efficiency for all the electrochemical tests performed on the extracts and alkaloids has come to a satisfactory term. In a nutshell, all the analytical data collected in were in accordance with one another therefore *Cryptocarya nigra* could be utilized a new potential source of green corrosion inhibitor. (Abdel-Gaber, Abd-El-Nabey, Sidahmed, El-Zayady, & Saadawy, 2006)

CHAPTER 6: REFERENCES

Abd El Haleem, S. M., Abd El Wanees, S., Abd El Aal, E. E., & Farouk, A. (2013). Factors affecting the corrosion behaviour of aluminium in acid solutions. I. Nitrogen and/or sulphur-containing organic compounds as corrosion inhibitors for Al in HCl solutions. *Corrosion Science*, *68*, 1–13.

Al-Tameme, H. J. M. (2016). Systematics study of *Frankenia L*. (Frankeniaceae) in Iraq. *Research Journal of Pharmaceutical, Biological and Chemical Sciences*, *7*(1), 1232–1241.

Alvarez-Rivera, G., Ballesteros-Vivas, D., Parada-Alfonso, F., Ibañez, E., & Cifuentes, A. (2019). Recent applications of high resolution mass spectrometry for the characterization of plant natural products. *TrAC Trends in Analytical Chemistry*, *112*, 87–101.

Amin, M. A., Khaled, K. F., Mohsen, Q., & Arida, H. A. (2010). A study of the inhibition of iron corrosion in HCl solutions by some amino acids. *Corrosion Science*, *52*(5), 1684–1695.

Awang, K., Hadi, A. H. A., Saidi, N., Mukhtar, M. R., Morita, H., & Litaudon, M. (2008). New phenantrene alkaloids from *Cryptocarya crassinervia*. *Fitoterapia*, *79*(4), 308–310.

Bahrami, M. J., Hosseini, S. M. A., & Pilvar, P. (2010). Experimental and theoretical investigation of organic compounds as inhibitors for mild steel corrosion in sulfuric acid medium. *Corrosion Science*, *52*(9), 2793–2803.

Bandy, R. (1980). The simultaneous determination of tafel constants and corrosion rate—a new method. *Corrosion Science*, *20*(8), 1017–1028.

Barouni, K., Bazzi, L., Salghi, R., Mihit, M., Hammouti, B., Albourine, A., & El Issami, S. (2008). Some amino acids as corrosion inhibitors for copper in nitric acid solution. *Materials Letters*, *62*(19), 3325–3327.

Benarioua, M., Mihi, A., Bouzeghaia, N., & Naoun, M. (2019). Mild steel corrosion inhibition by Parsley (*Petroselium Sativum*) extract in acidic media. *Egyptian Journal of Petroleum*, *28*(2), 155-159.

Bick, I. R. C., Preston, N. W., & Potier, P. (1972). Alkaloids of *Cryptocarya odorata* (Lauraceae). *Bulletin de La Societe Chimique de France*, (12), 4596–4597.

Bick, I. R. C., Sevenet, T., Sinchai, W., Skelton, B. W., & White, A. H. (1981). Alkaloids of *Cryptocarya longifolia*: x-ray crystal structure of thalifoline and longifolonine. *Australian Journal of Chemistry*, *34*(1), 195–207.

Bourgaud, F., Gravot, A., Milesi, S., & Gontier, E. (2001). Production of plant secondary metabolites: a historical perspective. *Plant Science*, *161*(5), 839–851.

Burkitbayeva, B. D., Argimbayeva, A. M., Rakhymbay, G. S., Beisenova, G. S., & Avchukir, K. (2016). Nitrogen-containing inhibitors and their link to their protective mechanism with molecular structure. *International Journal of Biology and Chemistry;* Vol 9 No 1 (2016)*: International Journal of Biology and Chemistry*.

Cao, Z., Tang, Y., Cang, H., Xu, J., Lu, G., & Jing, W. (2014). Novel benzimidazole derivatives as corrosion inhibitors of mild steel in the acidic media. Part II: Theoretical studies. *Corrosion Science*, *83*, 292–298.

Casabuono, A. C., & Pomilio, A. B. (1997). Alkaloids from endophyte-infected *Festuca argentina* 1. Dedicated to Professor Eduardo G. Gros on the occasion of his 65th anniversary.1. *Journal of Ethnopharmacology*, *57*(1), 1–9.

Castro-Saavedra, S., Fuentes-Barros, G., Tirapegui, C., Acevedo-Fuentes, W., Cassels, B. K., Barriga, A., & Vilches-Herrera, M. (2016). Phytochemical analysis of alkaloids from the Chilean endemic tree *Cryptocarya alba*. *Journal of the Chilean Chemical Society*, *61*(3), 3076–3080.

Cave, A., Leboeuf, M., Moskowitz, H., Ranaivo, A., Bick, I. R. C., Sinchai, W., … Cabalion, P. (1989). Alkaloids of *Cryptocarya phyllostemon*. *Australian Journal of Chemistry*, *42*(12), 2243–2263.

Chetouani, A., Hammouti, B., Benhadda, T., & Daoudi, M. (2005). Inhibitive action of bipyrazolic type organic compounds towards corrosion of pure iron in acidic media. *Applied Surface Science*, *249*(1), 375–385.

Christenhusz, M. J., & Byng, J. W. (2016). The number of known plants species in the world and its annual increase. *Phytotaxa*, *261*(3), 201-217.

Cooke, R. G., & Haynes, H. F. (1954). Alkaloids of *Cryptocarya angulata* and *Cryptocarya triplinervis*. *Australian Journal of Chemistry*, *7*, 99–103.

Crawford, L. P., Barmatov, E. B., Hughes, T. L., & Ho, M. Y. (2018). Corrosion Inhibition. *U.S. Patent Application No. 15/566,529*.

Custodio, D. L., & Junior, V. F. da V. (2014). Lauraceae alkaloids. *RSC Advances*, *4*(42), 21864–21890.

Donnelly, B., Downie, T. C., Grzeskowiak, R., Hamburg, H. R., & Short, D. (1978). The effect of electronic delocalization in organic groups R in substituted thiocarbamoyl RCSNH2 and related compounds on inhibition efficiency. *Corrosion Science*, *18*(2), 109–116.

Eddy, N. O. (2009). Ethanol extract of *Phyllanthus amarus* as a green inhibitor for the corrosion of mild steel in H2SO4. *Portugaliae Electrochimica Acta*, *27*(5), 579–589.

Faustin, M., Maciuk, A., Salvin, P., Roos, C., & Lebrini, M. (2015). Corrosion inhibition of C38 steel by alkaloids extract of *Geissospermum* laeve in 1M hydrochloric acid: Electrochemical and phytochemical studies. *Corrosion Science*, *92*, 287–300.

Gao, D., Wang, Z., Zhu, P., & Ye, W. (2011). Isolation and characterization of new set of microsatellite loci in *Cryptocarya chinensis*. *Guangxi Zhiwu*, *31*(1), 39–42.

Gillanders, L., Williams, S., Ryan, G., & Trout, J. F. (2016). Barrier coating corrosion control methods and application systems for interior piping systems. Pipe Restoration Technologies. *U.S. Patent No. 9,446,429*. Washington, DC: U.S. Patent and Trademark Office.

Gomes-Bezerra, K. M., Gomes, S. M., SILVEIRA, C. E. D. S., & Soares-Silva, L. H. (2018). Leaf epidermal descriptors applied to the taxonomy of Lauraceae, including new anatomical characters. *Phytotaxa*, *358*(1), 49-66.

Grundmeier, G., Schmidt, W., & Stratmann, M. (2000). Corrosion protection by organic coatings: electrochemical mechanism and novel methods of investigation. *Electrochimica Acta*, *45*(15), 2515–2533.

Gupta, N. K., Verma, C., Quraishi, M. A., & Mukherjee, A. K. (2016). Schiff's bases derived from l-lysine and aromatic aldehydes as green corrosion inhibitors for mild steel: Experimental and theoretical studies. *Journal of Molecular Liquids*, *215*, 47–57.

Hamdan, A. B., & Haider, F. I. (2018, January). Study on tea leaves extract as green corrosion inhibitor on mild steel in hydrochloric acid solution. In *IOP Conference Series: Materials Science and Engineering* (Vol. 290, No. 1, p. 012086). IOP Publishing.

Hussin, M. H., Jain Kassim, M., Razali, N. N., Dahon, N. H., & Nasshorudin, D. (2016). The effect of *Tinospora crispa* extracts as a natural mild steel corrosion inhibitor in 1M HCl solution. *Arabian Journal of Chemistry*, *9*, S616–S624.

Hussin, M. H., & Kassim, M. J. (2011). The corrosion inhibition and adsorption behavior of *Uncaria gambir* extract on mild steel in 1M HCl. *Materials Chemistry and Physics*, *125*(3), 461–468.

Hussin, M. H., Rahim, A. A., Mohamad Ibrahim, M. N., & Brosse, N. (2013). Physicochemical characterization of alkaline and ethanol organosolv lignins from oil palm (*Elaeis Guineensis*) fronds as phenol substitutes for green material applications. *Industrial Crops and Products*, *49*, 23–32.

Ikeuba, I., Ita, B. I., Okafor, P. C., Ugi, B. U., & Kporokpo, E. B. (2015). Green corrosion inhibitors for mild steel in H2SO4 solution: Comparative study of flavonoids extracted from the crude extract og *Gongronema Latifoliunm*. *Protection of Metals and Physical Chemistry of Surfaces*, *51*(6), 1043–1049.

Inzunza, R. G., Salas, B. V., Wiener, M. S., Beltran, M. C., Koytchev, R. Z., Stilianova, M. S., … Gaynor, J. T. (2013). Aqueous extract of Creosote bush (*Larrea tridentata*) leaves as green inhibitor for carbon steel in hydrochloric acid solution. *International Journal of Electrochemical Science*, *8*(5), 6433–6448.

Jevremović, I., Singer, M., Nešić, S., & Mišković-Stanković, V. (2013). Inhibition properties of self-assembled corrosion inhibitor talloil diethylenetriamine imidazoline for mild steel corrosion in chloride solution saturated with carbon dioxide. *Corrosion Science*, *77*, 265–272.

Ji, G., Anjum, S., Sundaram, S., & Prakash, R. (2015). *Musa paradisica* peel extract as green corrosion inhibitor for mild steel in HCl solution. *Corrosion Science*, *90*, 107–117.

Juliawaty, L. D., Kitajima, M., Takayama, H., Achmad, S. A., & Aimi, N. (2000). A 6-substituted-5,6-dihydro-2-pyrone from *Cryptocarya strictifolia*. *Phytochemistry*, *54*(8), 989–993.

Jüttner, K. (1990). Electrochemical impedance spectroscopy (EIS) of corrosion processes on inhomogeneous surfaces. *Electrochimica Acta*, *35*(10), 1501–1508.

Kanniah, K. D., Tan, K. P., Cracknell, A. P., Huete, A. R., Idris, N. H., Lau, A. M. S., … Ahmad, A. (2018). Assessment of biophysical properties of Royal Belum tropical forest, Malaysia. *Singapore Journal of Tropical Geography*, *39*(1), 90–106.

Kaur, G., Kapoor, A., & Kaur, G. (2015). Ethnopharmacological review of traditional herbal plants for anticancer activity. *World Journal of Pharmacy and Pharmaceutical Sciences*, *4*(9), 244–264.

Keleş, H. (2011). Electrochemical and thermodynamic studies to evaluate inhibition effect of 2-[(4-phenoxy-phenylimino)methyl]-phenol in 1M HCl on mild steel. *Materials Chemistry and Physics*, *130*(3), 1317–1324.

Khan, G., Newaz, K. M. S., Basirun, W. J., Ali, H. B. M., Faraj, F. L., & Khan, G. M. (2015). Application of natural product extracts as green corrosion inhibitors for metals and alloys in acid pickling processes- a review. *International Journal of Electrochemical Science*, *10*(8), 6120–6134.

Kosari, A., Moayed, M. H., Davoodi, A., Parvizi, R., Momeni, M., Eshghi, H., & Moradi, H. (2014). Electrochemical and quantum chemical assessment of two organic compounds from pyridine derivatives as corrosion inhibitors for mild steel in HCl solution under stagnant condition and hydrodynamic flow. *Corrosion Science*, *78*, 138–150.

Krishnan, M., Subramanian, H., Dahms, H.-U., Sivanandham, V., Seeni, P., Gopalan, S., … Rathinam, A. J. (2018). Biogenic corrosion inhibitor on mild steel protection in concentrated HCl medium. *Scientific Reports*, *8*(1), 2609.

Kuck, A. M., Albónico, S. M., Deulofeu, V., & Escalante, M. G. (1967). Alkaloids from *Argentine Fagara* species. *Phytochemistry*, *6*(11), 1541–1550.

Kurniadewi, F., Juliawaty, L. D., Syah, Y. M., Achmad, S. A., Hakim, E. H., Koyama, K., … Takahashi, K. (2010). Phenolic compounds from *Cryptocarya konishii*: their cytotoxic and tyrosine kinase inhibitory properties. *Journal of Natural Medicines*, *64*(2), 121–125.

Lai, C., Xie, B., Zou, L., Zheng, X., Ma, X., & Zhu, S. (2017). Adsorption and corrosion inhibition of mild steel in hydrochloric acid solution by S-allyl-O,O′-dialkyldithiophosphates. *Results in Physics*, *7*, 3434–3443.

Lim, A. L., Haron, N. W., Yong, K. T., & Wong, M. M. (2010). Notes on some plant collections from Bachok and several forest reserves in Kelantan. *Malaysian Journal of Science*, *29*, 47-54.

Lin, F.-W., Wu, P.-L., & Wu, T.-S. (2001). Alkaloids from the leaves of *Cryptocarya chinensis* HEMSL. *Chemical & Pharmaceutical Bulletin*, *49*(10), 1292–1294.

Lu, S.-T., Wu, Y.-C., & Leou, S.-P. (1985). Alkaloids of formosan *Fissistigma* and Goniothalamus species. *Phytochemistry*, *24*(8), 1829–1834.

Madkour, L. H., Kaya, S., Kaya, C., & Guo, L. (2016). Quantum chemical calculations, molecular dynamics simulation and experimental studies of using some azo dyes as corrosion inhibitors for iron. Part 1: Mono-azo dye derivatives. *Journal of the Taiwan Institute of Chemical Engineers*, *68*, 461–480.

Marzorati, S., Verotta, L., & Trasatti, S. (2019). Green corrosion inhibitors from natural sources and biomass wastes. *Molecules*, *24*(1), 48.

Mathina, A., & Rajalakshmi, R. (2016). Corrosion inhibition of mild steel in acid medium using *Canna indica* as green corrosion inhibitor. *Rasayan Journal of Chemistry*, *9*(1), 56–66.

Mo, S., Luo, H.-Q., & Li, N.-B. (2016). Plant extracts as "green" corrosion inhibitors for steel in sulphuric acid. *Chemical Papers*, *70*(9), 1228–1237.

Mohammadi, A., Hosseini, S. M. A., Bahrami, M. J., & Shahidi, M. (2016). Corrosion inhibition of mild steel in acidic solution by apricot gum as a green inhibitor. *Progress in Color, Colorants and Coatings*, *9*(2), 117–134.

Murmu, M., Saha, S. K., Murmu, N. C., & Banerjee, P. (2019). Effect of stereochemical conformation into the corrosion inhibitive behaviour of double azomethine based Schiff bases on mild steel surface in 1 mol L−1 HCl medium: An experimental, density functional theory and molecular dynamics simulation study. *Corrosion Science*, *146*, 134–151.

Nasrullah, A., Zahari, A., Mohamad, J., & Awang, K. (2013). Antiplasmodial alkaloids from the bark of Cryptocarya nigra (Lauraceae). *Molecules*, *18*(7), 8009-8017.

Newman, R. C., & Sieradzki, K. (1999). Corrosion Science. *MRS Bulletin*, *24*(7), 12–15.

Nnaji, N. J. N., Ujam, O. T., Ibisi, N. E., Ani, J. U., Onuegbu, T. O., Olasunkanmi, L. O., & Ebenso, E. E. (2017). Morpholine and piperazine based carboxamide derivatives as corrosion inhibitors of mild steel in HCl medium. *Journal of Molecular Liquids*, *230*, 652–661.

Odewunmi, N. A., Umoren, S. A., Gasem, Z. M., Ganiyu, S. A., & Muhammad, Q. (2015). l-Citrulline: An active corrosion inhibitor component of watermelon rind extract for mild steel in HCl medium. *Journal of the Taiwan Institute of Chemical Engineers*, *51*, 177–185.

Olasunkanmi, L. O., Kabanda, M. M., & Ebenso, E. E. (2016). Quinoxaline derivatives as corrosion inhibitors for mild steel in hydrochloric acid medium: Electrochemical and quantum chemical studies. *Physica E: Low-Dimensional Systems and Nanostructures*, *76*, 109–126.

Omar, H., Hashim, N., Zajmi, A., Nordin, N., Abdelwahab, S., Azizan, A., ... & Ali, H. (2013). Aporphine alkaloids from the leaves of *Phoebe grandis* (Nees) Mer. (Lauraceae) and their cytotoxic and antibacterial activities. *Molecules*, *18*(8), 8994-9009.

Ostovari, A., Hoseinieh, S. M., Peikari, M., Shadizadeh, S. R., & Hashemi, S. J. (2009). Corrosion inhibition of mild steel in 1M HCl solution by henna extract: A comparative study of the inhibition by henna and its constituents (Lawsone, Gallic acid, α-d-Glucose and Tannic acid). *Corrosion Science*, *51*(9), 1935–1949.

Parthipan, P., Narenkumar, J., Elumalai, P., Preethi, P. S., Usha Raja Nanthini, A., Agrawal, A., & Rajasekar, A. (2017). Neem extract as a green inhibitor for microbiologically influenced corrosion of carbon steel API 5LX in a hypersaline environments. *Journal of Molecular Liquids*, *240*, 121–127.

Patel, D. A. D. (2017). Synthesis of new flavanoid and chalcone derivatives as antimicrobial agent by green chemistry approach. *21st Annual Green Chemistry & Engineering Conference, Reston, VA, United States, June 13-15*, GC+E-220. American Chemical Society.

Peter, A., Obot, I. B., & Sharma, S. K. (2015). Use of natural gums as green corrosion inhibitors: an overview. *International Journal of Industrial Chemistry*, *6*(3), 153–164.

Prabakaran, M., Kim, S.-H., Hemapriya, V., & Chung, I.-M. (2016). Evaluation of polyphenol composition and anti-corrosion properties of *Cryptostegia grandiflora* plant extract on mild steel in acidic medium. *Journal of Industrial and Engineering Chemistry*, *37*, 47–56.

Qiang, Y., Zhang, S., Tan, B., & Chen, S. (2018). Evaluation of Ginkgo leaf extract as an eco-friendly corrosion inhibitor of X70 steel in HCl solution. *Corrosion Science*, *133*, 6–16.

Raja, P. B., Fadaeinasab, M., Qureshi, A. K., Rahim, A. A., Osman, H., Litaudon, M., & Awang, K. (2013). Evaluation of Green Corrosion Inhibition by Alkaloid Extracts of *Ochrosia oppositifolia* and Isoreserpiline against Mild Steel in 1 M HCl Medium. *Industrial & Engineering Chemistry Research*, *52*(31), 10582–10593.

Raja, P. B., Qureshi, A. K., Abdul Rahim, A., Osman, H., & Awang, K. (2013). *Neolamarckia cadamba* alkaloids as eco-friendly corrosion inhibitors for mild steel in 1M HCl media. *Corrosion Science*, *69*, 292–301.

Ramawat, K. G., Dass, S., & Mathur, M. (2009). The chemical diversity of bioactive molecules and therapeutic potential of medicinal plants. In *Herbal drugs: ethnomedicine to modern medicine* (pp. 7-32). Springer, Berlin, Heidelberg.

Ramdani, M., Elmsellem, H., Haloui, B., Elkhiati, N., Layachi, M., Mesfioui, A., … El Mahi, B. (2016). *Gracilaria bursa-pastoris* as eco-friendly corrosion inhibitor for mild steel in 1 M HCl media. *Pharma Chemica*, *8*(1), 330–337.

Ribeiro, D. V, & Abrantes, J. C. C. (2016). Application of electrochemical impedance spectroscopy (EIS) to monitor the corrosion of reinforced concrete: A new approach. *Construction and Building Materials*, *111*, 98–104.

Richard, T., Temsamani, H., Cantos-Villar, E., & Monti, J.-P. (2013). Chapter Two - Application of LC–MS and LC–NMR Techniques for Secondary Metabolite Identification. In D. B. T.-A. in B. R. Rolin (Ed.), *Metabolomics Coming of Age with its Technological Diversity* (Vol. 67, pp. 67–98).

Sadeghi Erami, R., Amirnasr, M., Meghdadi, S., Talebian, M., Farrokhpour, H., & Raeissi, K. (2019). Carboxamide derivatives as new corrosion inhibitors for mild steel protection in hydrochloric acid solution. *Corrosion Science*, *151*, 190–197.

Saeed, M. T., Saleem, M., Usmani, S., Malik, I. A., Al-Shammari, F. A., & Deen, K. M. (2019). Corrosion inhibition of mild steel in 1 M HCl by sweet melon peel extract. *Journal of King Saud University - Science*.

Saidi, N., Hadi, A. H. A., Awang, K., & Mukhtar, M. R. (2009). Aphorpine alkaloids from bark of *Cryptocarya ferrea*. *Indonesian Journal of Chemistry*, *9*(3), 461-465.

Sanaei, Z., Ramezanzadeh, M., Bahlakeh, G., & Ramezanzadeh, B. (2019). Use of Rosa canina fruit extract as a green corrosion inhibitor for mild steel in 1M HCl solution: A complementary experimental, molecular dynamics and quantum mechanics investigation. *Journal of Industrial and Engineering Chemistry*, *69*, 18–31.

Sastri, V. S. (2012). *Green corrosion inhibitors: theory and practice* (Vol. 10). John Wiley & Sons.

Satapathy, A. K., Gunasekaran, G., Sahoo, S. C., Amit, K., & Rodrigues, P. V. (2009). Corrosion inhibition by *Justicia gendarussa* plant extract in hydrochloric acid solution. *Corrosion Science*, *51*(12), 2848–2856.

Saxena, A., Prasad, D., Haldhar, R., Singh, G., & Kumar, A. (2018). Use of *Saraca ashoka* extract as green corrosion inhibitor for mild steel in 0.5 M H2SO4. *Journal of Molecular Liquids*, *258*, 89–97.

Schwabe, K. A., Carson, R. T., DeShazo, J. R., Potts, M. D., Reese, A. N., & Vincent, J. R. (2014). Creation of Malaysia's Royal Belum State Park: A Case Study of Conservation in a Developing Country. *The Journal of Environment & Development*, *24*(1), 54–81.

Singh, A., Ansari, K. R., Haque, J., Dohare, P., Lgaz, H., Salghi, R., & Quraishi, M. A. (2018). Effect of electron donating functional groups on corrosion inhibition of mild steel in hydrochloric acid: Experimental and quantum chemical study. *Journal of the Taiwan Institute of Chemical Engineers*, *82*, 233–251.

Singh, P., Ebenso, E. E., Olasunkanmi, L. O., Obot, I. B., & Quraishi, M. A. (2016). Electrochemical, Theoretical, and Surface Morphological Studies of Corrosion Inhibition Effect of Green Naphthyridine Derivatives on Mild Steel in Hydrochloric Acid. *The Journal of Physical Chemistry C*, *120*(6), 3408–3419.

Stefanoni, M., Angst, U. M., & Elsener, B. (2018). Electrochemistry and capillary condensation theory reveal the mechanism of corrosion in dense porous media. *Scientific Reports*, *8*(1), 7407.

Sulaiman, K. O., Onawole, A. T., Faye, O., & Shuaib, D. T. (2019). Understanding the corrosion inhibition of mild steel by selected green compounds using chemical quantum based assessments and molecular dynamics simulations. *Journal of Molecular Liquids*, *279*, 342–350.

Suzuki, Y., Saito, Y., Goto, M., Newman, D. J., O'Keefe, B. R., Lee, K.-H., & Nakagawa-Goto, K. (2017). *(−)*-Neocaryachine, an Antiproliferative Pavine Alkaloid from *Cryptocarya laevigata*, Induces DNA Double-Strand Breaks. *Journal of Natural Products*, *80*(1), 220–224.

Tezeghdenti, M., Etteyeb, N., Dhouibi, L., Kanoun, O., & Al-Hamri, A. (2017). Natural products as a source of environmentally friendly corrosion inhibitors of mild steel in dilute sulphuric acid: Experimental and computational studies. *Protection of Metals and Physical Chemistry of Surfaces*, *53*(4), 753–764.

Thakur, B. K., Anthwal, A., Rawat, D. S., Rawat, B., Rashmi, & Rawat, M. S. M. (2012). A review on genus *Alseodaphne*: phytochemistry and pharmacology. *Mini-Reviews in Organic Chemistry*, *9*(4), 433–445.

Verma, C., Ebenso, E. E., Bahadur, I., & Quraishi, M. A. (2018). An overview on plant extracts as environmental sustainable and green corrosion inhibitors for metals and alloys in aggressive corrosive media. *Journal of Molecular Liquids*, *266*, 577–590.

Verma, C., Ebenso, E. E., & Quraishi, M. A. (2017). Ionic liquids as green and sustainable corrosion inhibitors for metals and alloys: An overview. *Journal of Molecular Liquids*, *233*, 403–414.

Verpoorte, R., & Memelink, J. (2002). Engineering secondary metabolite production in plants. *Current Opinion in Biotechnology*, *13*(2), 181–187.

Wan, O. W. N. N., Liew, S. Y., Khaw, K. Y., Murugaiyah, V., Litaudon, M., & Awang, K. (2016). Cholinesterase inhibitory activity of isoquinoline alkaloids from three *Cryptocarya* species (Lauraceae). *Bioorganic & Medicinal Chemistry*, *24*(18), 4464–4469.

Wan Othman, W. N. N., Liew, S. Y., Khaw, K. Y., Murugaiyah, V., Litaudon, M., & Awang, K. (2016). Cholinesterase inhibitory activity of isoquinoline alkaloids from three *Cryptocarya* species (Lauraceae). *Bioorganic & Medicinal Chemistry*, *24*(18), 4464–4469.

Wan Othman, W. N. N., Sivasothy, Y., Liew, S. Y., Mohamad, J., Nafiah, M. A., Ahmad, K., … Awang, K. (2017). Alkaloids from *Cryptocarya densiflora* (Lauraceae) and their cholinesterase inhibitory activity. *Phytochemistry Letters*, *21*, 230–236.

Wang, K. W., & Ge, Y. C. (2018). New Analogues of Aporphine Alkaloids. *Mini reviews in medicinal chemistry*, *18*(19), 1590-1602.

Wang, D., Li, S., Ying, Y., Wang, M., Xiao, H., & Chen, Z. (1999). Theoretical and experimental studies of structure and inhibition efficiency of imidazoline derivatives. *Corrosion Science*, *41*(10), 1911–1919.

Wang, S. S., & Frankel, G. S. (2017). Fundamental Study of Corrosion Preventive Compounds: Part I—Formulation and Characterization. *Corrosion*, *74*(4), 444-456.

Wu, X., Ding, W., Zhong, J., Wan, J., & Xie, Z. (2013). Simultaneous qualitative and quantitative determination of phenolic compounds in *Aloe barbadensis* Mill by liquid chromatography–mass spectrometry-ion trap-time-of-flight and high performance liquid chromatography-diode array detector. *Journal of Pharmaceutical and Biomedical Analysis*, *80*, 94–106.

Wu, Y.-C., Kao, S.-C., Huang, J.-F., Duh, C.-Y., & Lu, S.-T. (1990). Two phenanthrene alkaloids from *Fissistigma glaucescens*. *Phytochemistry*, *29*(7), 2387–2388.

Yamuna, J., & Anthony, N. (2015). *Citrus sinensis* L. leaf extract as an efficient green corrosion inhibitor for mild steel in aqueous medium. *International Journal of ChemTech Research*, *7*(1), 37–43.

Yıldız, R., Döner, A., Doğan, T., & Dehri, İ. (2014). Experimental studies of 2-pyridinecarbonitrile as corrosion inhibitor for mild steel in hydrochloric acid solution. *Corrosion Science*, *82*, 125–132.

Zahari, A., Ablat, A., Sivasothy, Y., Mohamad, J., Choudhary, M. I., & Awang, K. (2016). In vitro antiplasmodial and antioxidant activities of bisbenzylisoquinoline alkaloids from *Alseodaphne corneri* Kosterm. *Asian Pacific Journal of Tropical Medicine*, *9*(4), 328–332.

Zhang, K., Yang, W., Yin, X., Chen, Y., Liu, Y., Le, J., & Xu, B. (2018). Amino acids modified konjac glucomannan as green corrosion inhibitors for mild steel in HCl solution. *Carbohydrate Polymers*, *181*, 191–199.